Investigating the Behaviour of Short-Span FRP-Reinforced Glulam Beams

by

Yannick Vetter

A thesis

presented to the University of Waterloo

in fulfillment of the

thesis requirement for the degree of

Master of Applied Science

in

Civil Engineering

Waterloo, Ontario, Canada, 2022

Author's Declaration

I hereby declare that I am the sole author of this thesis. This is a true copy of the thesis, including any required final revisions, as accepted by my examiners.

I understand that my thesis may be made electronically available to the public.

Abstract

The broader availability of engineered wood products has generated a resurgence of wood used as a construction material over the past few decades. To further promote the use of timber, a solution aimed at increasing the structural capacity of aging or deficient members must be developed. The use of externally bonded fibre reinforced polymer (FRP) sheets has been the subject of various studies that have produced encouraging results.

This study was conducted to determine the effects of the reinforcement quantity and orientation on the flexural response of short-span FRR-reinforced glulam beams. Special consideration was given to the depth-to-span ratio and the effect of partially and fully confined reinforcement configurations on the observed failure modes. A total of thirty glulam beams were tested under four-point loading with the load at failure, midspan deflection, strain distribution and failure mode being recorded and used to quantify the effect of the reinforcement. In addition to the experimental program, a non-linear model was developed to predict the flexural resistance of unreinforced and reinforced beams. Individual component testing was performed to determine the characteristic strengths of the materials needed as input for the model.

Results for the simple tension and U-shaped reinforced glulam beams demonstrated increases in resistance and stiffness compared to the control specimens; however, the combination of the span-to-depth ratio and insufficient development length caused shear failures. The undesired failure mode was addressed through the use of transversely applied FRP sheets. The addition of FRP hoops located in the shear regions of the bending member helped increase the resistance by factors ranging up to 1.17 and contained the failure to allow for some post-peak resistance. FRP sheets providing tension reinforcement at the midspan and confinement in the shear spans were also investigated as means of partially confined beams aimed at addressing the question of retrofitting members that have accessibility issues and has shown to prevent undesirable failure modes while also providing some level of post-peak resistance compared to conventional retrofitting schemes. Fully confined beams were also the subject of this investigation to better understand the effect of the quantity of reinforcement and to use a comparison to unconfined beams. The effect of beam depth was considered by replicating certain reinforcement configurations on larger cross-sectional beams, with results demonstrating consistent results. The material model used to generate the resistance curves was shown to generate a model to experimental strength value ratio of 0.92.

Acknowledgements

I would like to thank my supervisor, Dr. Daniel Lacroix, for his guidance and support throughout my time at the University of Waterloo. I would like to extend my gratitude towards certain individuals that have played an important role in the completion of this project. A special thank you to Maxime Cléroux and Peter Volcic for all the laughs and time spent helping me complete my experimental tests.

To my partner Noelle, I am grateful for your love and unwavering belief in me during these last two years. Above all, I would like to thank my parents and sister for the encouragement and support throughout my entire life, none of this could have been possible without you.

Table of Contents

Author's Declaration ii

Abstract iii

Acknowledgements iv

List of Figures ix

List of Tables xiii

Chapter 1 Introduction 1

  1.1 General 1

  1.2 Research Needs 2

  1.3 Research Objectives 4

  1.4 Scope 5

  1.5 Thesis Organization 5

Chapter 2 Literature Review 7

  2.1 General 7

  2.2 Wood as a Construction Material 7

  2.3 Mass Timber 9

    2.3.1 Glued-Laminated (Glulam) Timber 11

  2.4 Fibre Reinforced Polymers (FRPs) 12

  2.5 FRP-Reinforced Glulam 14

    2.5.1 The Need for Reinforcement 14

    2.5.2 Compression Reinforcement 14

    2.5.3 Shear Reinforcement 15

    2.5.4 Flexural Reinforcement 16

    2.5.5 Predicting the Flexural Response of FRP-Reinforced Glulam Beams 26

2.6 Summary 29

Chapter 3 Experimental Program 31

3.1 General 31

3.2 Description of the Unreinforced Specimens 31

3.3 Description of the Reinforced Specimens 33

3.3.1 FRP Information and Application Process 33

3.3.2 Reinforcement Configurations – Stage 1 35

3.3.3 Reinforcement Configurations – Stage 2 36

3.4 Summary of Test Matrix 42

3.5 Test Setup and Instrumentation 43

3.5.1 Material Properties – Component Test 43

3.5.2 Full Scale Four-Point Bending Tests 47

Chapter 4 Experimental Results 49

4.1 General 49

4.2 Component Tests 49

4.2.1 Wood Compression Coupons 49

4.2.2 Wood Tension Coupons 51

4.2.3 FRP Tension Coupons 52

4.3 Characterization of Failure Modes for the Beams 55

4.3.1 Unreinforced Glulam Beams 56

4.3.2 Reinforced Glulam Beams 58

4.4 Flexural Performance of Glulam Beams 68

4.4.1 Unreinforced Glulam Beams 68

4.4.2 Reinforced Glulam Beams 70

4.4.3 Effect of the Reinforcement Configuration 72

4.4.4 Summary of Bending Test Results 75

Chapter 5 Analytical Model for Bending Strength 77

5.1 General 77

5.2 Idealized Stress-Strain Relationship 77

5.2.1 Size Effects 78

5.3 Moment Curvature Analysis 82

5.3.1 Unreinforced Beams 83

5.3.2 Reinforced Beams 86

5.4 Development of Resistance Curves 89

5.4.1 Derivation of the Displacement Equation for Linear Elastic Materials 89

5.4.2 Beam Displacements of Nonlinear Materials 91

5.4.3 General Procedure 92

5.5 Material Model Verification 93

Chapter 6 Discussion 97

6.1 General 97

6.1 Behaviour of Unreinforced Glulam Beams 97

6.2 Effects of Simple Tension and U-shaped GFRP Reinforcement 98

6.3 Effect of Transverse GFRP Reinforcement 104

6.4 Effect of Beam Depth 111

6.5 Modelling the Behaviour of Unreinforced and Reinforced Glulam Beams 115

6.5.1 Effect of FRP Reinforcement on the Strain Distribution 115

6.5.2 Predicting the Behaviour of Unreinforced Beams 116

6.5.3 Predicting the Behaviour of Reinforced Beams 118

Chapter 7 Conclusions......125

7.1 Summary and Conclusions......125

Recommendations for Future Work......126

References......128

Appendices......135

Appendix A Test Results of Wood Compression Coupons......135

Appendix B Test Results of Wood Tension Coupons......138

Appendix C Test Results of FRP Tension Coupons......141

Appendix D Failure Progression of Unreinforced and Reinforced Glulam Beams......147

Appendix E Derivation of Displacement Equations for Resistance Curve......178

Appendix F Force Displacement and Strains......182

List of Figures

Figure 1.1 - Example of Confinement Accessibility Restrictions for Glulam Beams 3
Figure 2.1 - Three Main Axes of Wood 7
Figure 2.2 - Cellular Structure of Wood 8
Figure 2.3 - Glulam Beam 12
Figure 2.4 - Typical Stress-Strain Curves for FRPs and Mild Steel 13
Figure 2.5 - U-shaped CFRP Reinforcement 17
Figure 2.6 - Orientation of CFRP Reinforcement Sheets 18
Figure 2.7 - Reinforcement Configurations for Beams Subjected to Blast Loading 19
Figure 2.8 - Simple Tension: FRP Delamination and Wood Splintering Failure 20
Figure 2.9 - U-shaped with Confinement: Shear Region Failure 21
Figure 2.10 - Fully Confined Reinforcement Configurations 22
Figure 2.11 - Full Confinement: Failure Modes 23
Figure 2.12 - Wood Stud Reinforcement Configurations 24
Figure 2.13 - Wood Stud Failure Modes 24
Figure 2.14 - Effect of Reinforcement on the Strength of Wood Specimens 25
Figure 2.15 - Local Reinforcement of Existing Timber Beams 25
Figure 2.16 - Stress-strain Relationship of Wood 26
Figure 2.17 - Procedure for Moment-Curvature Analysis 27
Figure 2.18 - Reinforced Beam Equilibrium 27
Figure 2.19 - Resistance Curve Comparison Between Experimental and Numerical Modelling 28
Figure 2.20 - Moment Curvature Analysis for Beams with Applied Axial Load 29
Figure 3.1 - Initial Beam Deformities 31
Figure 3.2 - Beam Cross-sections 32
Figure 3.3 - Application Procedure for the FRP Sheets 34
Figure 3.4 - Reinforcement Schemes 1 Through 4 35
Figure 3.5 - Reinforcement Schemes 5 and 6 37
Figure 3.6 - Reinforcement Schemes 7 and 8 38
Figure 3.7 - GFRP Fabric Cutout for R9 and R10 39
Figure 3.8 - Reinforcement Schemes 9 and 10 40
Figure 3.9 - Reinforcement Scheme 11 41

Figure 3.10 - Reinforcement Scheme 12 42
Figure 3.11 - Wood Coupons 44
Figure 3.12 - Wood Coupon Tests 45
Figure 3.13 - FRP Coupons 46
Figure 3.14 - FRP Coupon Test 46
Figure 3.15 - Static Bending Test Setup 48
Figure 4.1 - Representative Compression Failures of Wood Coupons 49
Figure 4.2 - Compression Coupon Test 50
Figure 4.3 - Tension Coupon Test 52
Figure 4.4 - FRP Coupon Failure 53
Figure 4.5 - Representative Stress-Strain Curves for FRP Coupons 54
Figure 4.6 - Idealized Resistance Curve and Terminology 56
Figure 4.7 - Splintering Tension Failure of Unreinforced Beams 57
Figure 4.8 - Cross-grain Tension Failure of Unreinforced Beams 57
Figure 4.9 - Compression Folds on Unreinforced Beams 57
Figure 4.10 - Simple Tension Failure of Unreinforced Beams 58
Figure 4.11 - Horizontal Shear Failures for R1 Beams 59
Figure 4.12 - Stress Concentration Failure for R1 Beams 59
Figure 4.13 - Representative Failure Mode for R2 Beams 60
Figure 4.14 - Representative Failure Modes for R3 Beams 61
Figure 4.15 - Representative Failure Mode for Reinforcement Scheme 4 61
Figure 4.16 - Representative Failure Mode for Reinforcement Scheme 5 62
Figure 4.17 - Representative Failure Mode for Reinforcement Scheme 6 63
Figure 4.18 - Representative Failure Mode for Reinforcement Scheme 7 64
Figure 4.19 - Representative Failure Mode for Reinforcement Scheme 8 65
Figure 4.20 - Representative Failure Mode for Reinforcement Scheme 9 65
Figure 4.21 - Representative Failure Modes for Reinforcement Scheme 10 66
Figure 4.22 - Representative Failure Modes for Reinforcement Scheme 11 67
Figure 4.23 - Representative Failure Modes for Reinforcement Scheme 12 68
Figure 4.24 - Resistance Curves of Unreinforced Glulam Beams 69
Figure 4.25 - Resistance Curves of Reinforced Beams in Stage 1 72

Figure 4.26 - Resistance Curves of Reinforced [100] Beams in Stage 2 74
Figure 4.27 - Resistance Curves of Reinforced [160] Beams in Stage 2 75
Figure 5.1 - Stress Distribution Proposed by Buchanan (1990) 78
Figure 5.2 - Experimental Stress-Strain Curves for the Wood Coupons.. 80
Figure 5.3 - Glulam Input Stress-Strain Relationship 81
Figure 5.4 - FRP Input Stress-Strain Relationship 82
Figure 5.5 - Unreinforced Glulam: Distribution of Strain, Stress, and Forces Prior to Compression Yielding 83
Figure 5.6 - Unreinforced Glulam: Distribution of Strain, Stress, and Forces Post Compression Yielding 84
Figure 5.7 - Representative Moment-Curvature Analysis of Unreinforced Beams 85
Figure 5.8 - Reinforced Glulam: Distribution of Strain, Stress, and Forces Prior to Compression Yielding 86
Figure 5.9 - Reinforced Glulam: Distribution of Strain, Stress, and Forces Post Compression Yielding 87
Figure 5.10 - Representative Moment-Curvature Analysis of Reinforced Beams 89
Figure 5.11 - Beam Diagrams for the Derivation of the Deflection Equation 90
Figure 5.12 - Curvature Diagram of Yielded Beams.. 91
Figure 5.13 - Slope and Displacement Diagrams of Yielded Beams 92
Figure 5.14 - Representative Moment-Curvature and Resistance Curve for Unreinforced Beams 93
Figure 5.15 - Comparison of Model to Published (Lacroix 2017) Resistance Curves 96
Figure 6.1 - Behaviour of Unreinforced Glulam Beams 98
Figure 6.2 - Comparison of Initial Failure to Failure at P_{max} for the U-02 98
Figure 6.3 - Horizontal Shear Failure of R2-01.. 100
Figure 6.4 - Comparison of Simple Tension and U-shaped Reinforcement Configurations............. 101
Figure 6.5 - Stress Concentration Failure of R1-01.. 103
Figure 6.6 - Transverse Reinforcement Provided in Stage 2... 104
Figure 6.7 - Confinement Effect of GFRP Hoops 106
Figure 6.8 - Contained Wood Damage 107
Figure 6.9 - Post-Peak Behaviour of Fully Confined Beams 107
Figure 6.10 - Comparison of Tail Reinforcement to Simple Tension 108

Figure 6.11 - Failure Mode Comparison of Tail Reinforcement to Simple Tension.......................... 109
Figure 6.12 - R9 Results Compared to Simple Tension and Unreinforced Beam Averages.............. 110
Figure 6.13 - Bond Failure 111
Figure 6.14 - Reinforcement Schemes Investigated on the [160] Beams.. 112
Figure 6.15 - Representative Failure Modes for the [160] Beams 113
Figure 6.16 - Resistance Curves of Reinforced [160] Beams in Stage 2 114
Figure 6.17 - Prediction of Unreinforced Beams 117
Figure 6.18 - Prediction of Reinforced Beams in Stage 1 119
Figure 6.19 - Prediction of R5 and R6 Beams in Stage 2.. 120
Figure 6.20 - Prediction of R9 and R10 Beams in Stage 2.. 121
Figure 6.21 - Prediction of R7 Beams in Stage 2 122
Figure 6.22 - Prediction of R11 and R12 Beams in Stage 2.. 123

List of Tables

Table 3.1 - Manufacturer Design Values for the Epoxy and FRP Composite Material 33
Table 3.2 - Experimental Test Matrix Summary 43
Table 4.1 - Static Test Results of Compression Coupons 51
Table 4.2 - Static Test Results of Tension Coupons 52
Table 4.3 - Static Test Results of FRP Tension Coupons 54
Table 4.4 - Summary of Flexural Test Results of Unreinforced Beams 69
Table 4.5 - Summary of Flexural Test Results of Reinforced Beams in Stage 1 70
Table 4.6 - Summary of Flexural Test Results of Reinforced Beams in Stage 2 71
Table 4.7 - Experimental Test Results Summary 76
Table 5.1 - Model Input Strengths 80
Table 5.2 - Model Input Strengths for Lacroix (2017) 94
Table 5.3 - Comparison of Model Predictions to Lacroix (2017) Results 95
Table 6.1 - Effect of Simple Tension and U-shaped GFRP Reinforcement 99
Table 6.2 - Effect of Transverse GFRP Reinforcement 105
Table 6.3 - Unreinforced and Reinforced Bending Stiffnesses for [160] Beams in Stage 2 112
Table 6.4 - Effect of Beam Depth on Bending Stiffness 114
Table 6.5 - Wood Tensile Failure Strain 116
Table 6.6 - Comparison of Model to Experimental Results for Unretrofitted Beams 117
Table 6.7 - Comparison of Model to Experimental Results for Retrofitted Beams in Stage 1 118
Table 6.8 - Comparison of Model to Experimental Results for R5 and R6 Beams in Stage 2 120
Table 6.9 - Comparison of Model to Experimental Results for R9 and R10 Beams in Stage 2 121
Table 6.10 - Comparison of Model to Experimental Results for R11 and R12 Beams in Stage 2 122
Table 6.11 - Summary of Model to Experimental Strength Ratios 124

Chapter 1
Introduction

1.1 General

The resurgence of timber within the construction industry has been heavily influenced by the development and commercialization of mass timber products, such as glued-laminated timber (glulam), dowel-laminated timber (GLT), and cross-laminated timber (CLT). These mass timber products have allowed for the use of wood to move away from conventional light-frame low-rise residential and commercial structures to much larger structures typically reserved to concrete and steel. Initiatives from the Government of Canada encouraging the use of wood, such as the Green Construction through Wood (GCWood) program (Canada, 2020) have contributed to an uptake in mass timber bridges (e.g., Mistissini Bridge, Albanel Bridge) and tall mass timber buildings (e.g., Brock Commons, Origine, Wood Innovation and Design Centre) across Canada, and globally (e.g., Mjøstårne, The Tree, Forte). Other means of promoting the use of the material have been carried out, with the province of British Columbia, Canada, and some European countries going as far as requiring the consideration of the material in any new government funded structures (Nelson, 2020; Province of British Columbia, 2009). In comparison to dimensional lumber (i.e., stick-frame), engineered wood and mass timber products have more reliable strength properties and good fire performance (i.e., predictable charring rate), in addition to being an environmentally friendly alternative to concrete and steel. With the buildings and construction industry accounting for near 40% of the global energy-related carbon emissions (Lei Win, 2021), there is a growing shift of focus in the industry being placed on reducing emissions and general pollution, thereby contributing to further interest into incorporating mass timber products in the Canadian infrastructure. Wood is a renewable construction material which absorbs and stores carbon dioxide (CO_2) during its growth. Incorporating more wood in our infrastructure contributes to a reduction in global emissions through its smaller carbon footprint and carbon sequestration (Green & Taggart, 2017).

The newest editions of the National Building Code of Canada (NBCC) and International Building Code (IBC) brought forward significant updates related to the use of wood, including the construction of encapsulated mass timber buildings up to 12- and 18-storeys, respectively (International Code Council, 2021; NRCC, 2022), which was previously limited to 6-storeys. The latter has been possible due to significant research efforts leading to design provisions for CLT used in platform construction in the

Canadian wood design code (Canadian Standards Association, 2019a), and new design guides for CLT structures (Karacabeyli & Gagnon, 2019) and mass timber bridges (Moses & Brown and Co., 2017).

1.2 Research Needs

Despite the significant progress towards the development of design provisions and guides for mass timber buildings, one area that has been trailing is the adoption of hybrid glulam beams reinforced with fibre-reinforced polymers (FRPs) in buildings and mass timber bridges. Since 2007, more than 50 mass timber bridges have been built across Canada (NRC, 2021). The high tensile strength and stiffness of the FRPs can contribute to a reduction of the glulam beam size, an increase in span lengths, and can be used as a reinforcing material in the case of rehabilitation. To this date, there are no design guidelines in the CSA O86 “Engineering Design in Wood” nor the CSA S6 “Canadian Highway Bridge Design Code” for glulam beams reinforced with FRPs (Canadian Standards Association, 2019a, 2019b). In the CSA S6, the guidelines related to FRP and wood address the rehabilitation of timber stringers, which fundamentally, behave differently from glulam. Furthermore, the existing design guidelines relate to the retrofitting of in-situ members, rather than the design of hybrid FRP-reinforced wood products.

The use of FRP sheets or bars as tension reinforcement has been studied over the last few decades and stems from the encouraging results gathered through experimental tests done on concrete specimens (e.g., El-Hacha & Rizkalla, 2004; Ritchie et al., 1990; Schober et al., 2015). Promising results, demonstrating significant strength and stiffness increases, have been reported by researchers investigating the flexural behaviour of FRP-reinforced timber specimens (e.g., Gentile et al., 2002; Johns & Lacroix, 2000; D. Lacroix & Doudak, 2020a; Plevris & Triantafillou, 1992; Raftery & Harte, 2011).

Although simple tension reinforcement has shown potential to improve the strength and stiffness of timber and glulam beams, it does not contribute to increased ductility with the failure being sudden and brittle (Dorey & Cheng, 1996b; Hernandez et al., 1997). Recently, Lacroix and Doudak (2020) investigated the effects of using bidirectional glass FRP (GFRP) in various arrangements providing confinement on the post-peak behaviour of glulam beams under simulated blast loading and have shown that ductility ratios up to 3.6 can be attained. Furthermore, researchers have employed a material predictive model that relies on the moment-curvature analysis to determine the force displacement (i.e., resistance curves) of the FRP-reinforced glulam beams (Gentile et al., 2002; Lacroix & Doudak, 2018; Lacroix & Doudak, 2020). Finite element models have also been employed successfully to predict the global response of FRP-reinforced glulam beams (Glisovic et al., 2017). Despite the significant research efforts regarding the behaviour of FRP-reinforced glulam beams, the limited information regarding the bond behaviour between the two materials has resulted in the majority of material models assuming a perfect bond. Furthermore, full confinement of a beam to provide additional ductility (Lacroix, 2017) is not always possible due to the overall cost of the material and installation for larger members or in the event where there is restricted access to the member thereby preventing the application of full confinement (Figure 1.1).

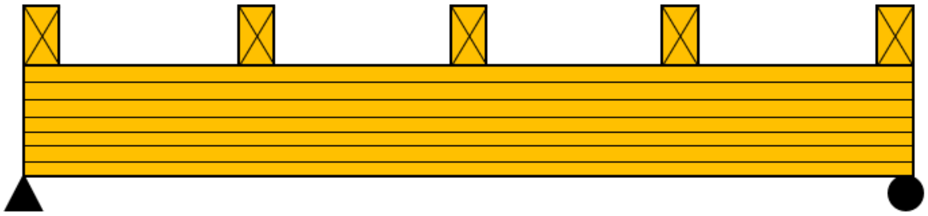

Figure 1.1 - Example of Confinement Accessibility Restrictions for Glulam Beams

With an increasing number of mass timber bridges, it is not unreasonable to foresee that some of these bridges will require rehabilitation or retrofitting near the end of their design service life. While several research programmes on the behaviour of FRP-reinforced glulam beams have been undertaken (e.g., Buell & Saadatmanesh, 2005; Gentile et al., 2002; Johns & Lacroix, 2000b; Yang et al., 2016), there is a lack of research in the behaviour of FRP-reinforced glulam beams and how to increase the overall behaviour to eliminate undesirable failure modes when full confinement is not an option. There are several limitations with the current approaches to modelling. In order to promote the adoption of FRP-reinforced wood (i.e., timber, glulam) beams as feasible retrofitting options, additional research is required to investigate the effects of providing FRP to enhance the flexural strength and stiffness as well as ductility on the global behaviour and undesired failure modes (e.g., FRP de-bonding, shear).

Currently, the Canadian Highway Bridge Code (Canadian Standards Association, 2019b) accounts for the FRP reinforcement of timber stringers by increasing the allowable bending stress used in design calculations. The lack of available literature on the topic has required authorities to conservatively increase the bending capacity of reinforced timber, while completely omitting the stiffness increase of FRP-reinforced glulam bending members.

1.3 Research Objectives

The overarching aim of the research program is to investigate the behaviour of unreinforced and FRP-reinforced glulam beams as well as to understand the limitations of the reinforcement configurations experimentally and analytically. Of particular interest, this study aims to develop reinforcement schemes that will provide improved ductility in cases where there is restricted access and compare it to the behaviour of traditional reinforcement schemes as well as when fully confined. More specifically, the goals of the current thesis are to:

1. Investigate the effects of providing simple tension and U-shaped GFRP reinforcement as well as the effect of varying the reinforcement thickness on the flexural response of reinforced glulam beams relative to unreinforced glulam beams.
2. Develop and implement reinforcement schemes that eliminate undesirable failure modes using a combination of unidirectional and bidirectional GFRP fabrics when providing tension reinforcement only for beams with restricted access and to experimentally investigate their performance.
3. Evaluate the performance of the reinforcement schemes for beams with restricted access and to compare it to that of fully confined beams using unidirectional and bidirectional GFRP fabrics.
4. Develop a non-linear material model capable of predicting the complete flexural resistance curve of unreinforced and reinforced glulam beams by improving over existing approaches. Validate the developed material model using published experimental data and compare the numerical values to the experimental curves.
5. Provide guidance on the assumptions related to the development of analytical resistance curves for FRP-reinforced glulam beams and limitations depending on the reinforcement scheme, FRP fabric utilized, beam cross-section size, and span. The findings from the current research program will be compared to existing design guidelines and, where appropriate, recommendations for analysis and design will be provided.

1.4 Scope

These research objectives are met through the following steps:

- Detailed literature review on the behaviour of the wood material and FRP-reinforced glulam specimens subjected to bending;
- Wood and FRP coupon testing to establish the strength values to be used in the material model;
- Testing of five unreinforced glulam beams to establish the baseline resistance curves;
- Testing of nine glulam beams reinforced with simple tension and U-shaped reinforcement to determine the effect of varying GFRP thickness on the flexural response;
- Testing of sixteen FRP-reinforced beams containing some level of transverse reinforcement to compare the flexural response to both the unreinforced and unconfined beams;
- Analytically generating the resistance curves and comparing them to the experimental test results;
- Discussing the results of the failed beams by comparing their resistance and stiffness and proposing future work recommendations.

1.5 Thesis Organization

This thesis is organized into the following seven chapters:

Chapter 1 introduces the topic of mass timber. A brief introduction of the material explaining its relevance in today’s construction industry is presented, followed by the research needs and objectives set forth in this research program.

Chapter 2 presents a detailed literature review. The main topics covered in this section include the use of wood as a construction material, a detailed review of mass timber, FRPs, the need for reinforced glulam, compression, shear and flexural strengthening of timber, and proposed models used to predict the flexural behaviour.

Chapter 3 discusses the experimental program and the methods used. This includes the description of the glulam specimens and the instrumentation, the procedure followed to apply the FRP reinforcement, and a summary of the test matrix.

Chapter 4 presents the experimental results of the coupon and four-point bending tests introduced in Chapter 3. It includes a section characterizing the failure modes observed during the four-point bending tests.

Chapter 5 introduces the material properties and equations used to develop the moment-curvature and resistance curve models.

Chapter 6 discusses the results of both the experimental and analytical programs.

Chapter 7 summarizes the findings and proposes potential future work.

Chapter 2

Literature Review

2.1 General

The purpose of this chapter is to introduce the background information pertaining to wood, specifically when used as a building material. As a shift in focus is being placed on reducing the amount of pollution created by the construction industry, sustainable materials (e.g., wood) are picking up steam amidst growing environmental consciousness. Trees have been used in construction for centuries, and the natural behaviour of the material needs to be well understood if timber is to stand a chance when compared to the more conventional building materials. Wood mechanics, the benefits of mass timber, and research from literature are presented in this section to help validate the growing interest surrounding the material in the construction industry.

2.2 Wood as a Construction Material

Trees are biologically produced, and they are one of the oldest structural materials. Wood is an orthotropic material, meaning that the mechanical properties are dependent on the direction of the load relative to the orientation of the grain. Three main axes are established when looking at Figure 2.1, the longitudinal axis is referred to as the parallel-to-grain direction, while both the radial and tangential axes are referred to as perpendicular-to-grain direction. The variability of the material, in terms of size and strength, stems from the fact that trees are naturally growing in different environments and require different needs. Needs such as water, nutrients, and the structural strength required to resist the imposed environmental forces all affect the overall growth.

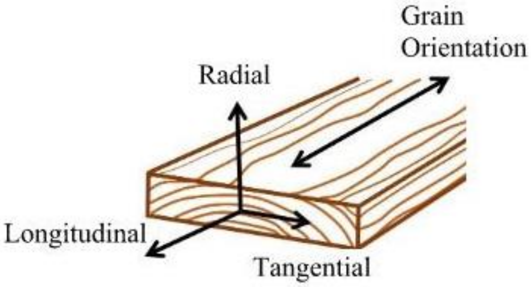

Figure 2.1 - Three Main Axes of Wood

*Reproduced from Legg & Bradley (2016)

The material is composed of wood fibres, which are made up of cellulose and resemble a bundle of small, elongated hollow straws. The fibres run parallel to the length of the tree and are held together through the help of lignin found in between the wood fibres (Ramage et al., 2017). The idealized cellular structure is depicted in Figure 2.2, showing the fibre walls having different densities representing the heartwood and sapwood layers. The heartwood, representing the period of slow growth where the tree is not requiring as much water, is characterized by the thicker cell fibres while the sapwood is characterized by the thin celled fibres, representing a period of fast growth where the wider fibres facilitate the transportation of water (Ramage et al., 2017).

Wood is also hygroscopic, meaning that it will absorb and release moisture to maintain equilibrium with its surrounding environment. Moisture is stored in the wood as bound water within the fibre cell walls and as free water within the cell cavities which are held together through capillary forces. When the wood material is subjected to a change in moisture content, it is the free water that initially regulates the change (i.e., leaves or enters the cells) thereby allowing the material to reach its equilibrium moisture content. The change in moisture causes shrinkage or expansion in the perpendicular-to-grain direction in the order of 1% for every 5% deviation in moisture content (Green & Taggart, 2017).

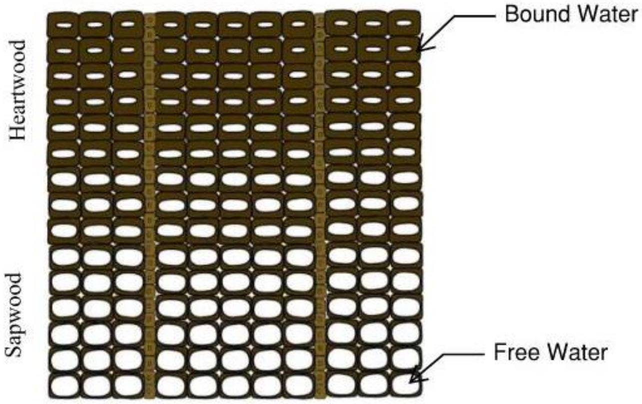

Figure 2.2 - Cellular Structure of Wood

*Reproduced from Ramage et al. (2017)

Natural and seasoning defects are other factors that play a role in the materials variability and their type, size, and location are crucial to the damage they can cause. Natural defects such as knots, compression zones, and non-linear grain direction occur during the growth of the material and are associated with the environmental conditions present during the growth of the tree. Natural defects can induce stress concentrations in the members who are not always visible on the exterior faces.

Seasoning defects are the result of the variability associated with milling practices, causing dimensional defects on both the cross-sectional (e.g., checks and splits) and longitudinal (e.g., warping or bowing) faces of the dressed members. Milling defects can result in dimensional variations and based on their orientation can be further amplified once the members are loaded.

In order to provide guidance to engineers and simplify the member selection process, a list of stress grades was developed based on the different species and defects. In Canada, all lumber is graded in accordance with the National Lumber Grades Authority (NLGA) *Standard Grading Rules for Canadian Lumber* (NLGA, 2017) whereas the United States has multiple grading agencies based on geographical location.

The design strength of structural timber is calculated in accordance with design standards (e.g., CSA O86, NDS, Eurocode 5), which set forth the equations used to determine the member capacities (Canadian Standards Association, 2019a). These design standards provide reference design values for the modulus of elasticity and stresses (parallel- and perpendicular-to-grain direction) obtained by full-scale experimental tests conducted on the species reported (Barrett & Lau, 1994). Wood experiences the highest resistance when loaded axially in the parallel-to-grain direction. Conversely, wood is weakest when loaded perpendicular-to-grain, with design standards omitting the perpendicular-to-grain tension stress values for solid timber members.

2.3 Mass Timber

Advances in technology have allowed for the development of various engineered wood products (EWPs), which have revolutionized the use of dimensional lumber in the construction industry. These relatively new products aim to address some of the disadvantages surrounding conventional light-frame timber when compared to concrete and steel. Examples of EWPs include glued-laminated timber (glulam), cross-laminated timber (CLT), dowel laminated timber (DLT), nail-laminated timber (NLT), and laminated veneer lumber (LVL). Engineered wood is defined as wood-based structural members fabricated using wood strands, fibres, and/or veneers together (e.g., plywood, OSB) to create light weight products with remarkably high strength and performance (Naturally Wood, 2022). Mass Timber is defined as large cross-sectional members made-up of smaller, dimensional lumber, fixed together using various fasteners (e.g., glue, dowels, nails) to create dimensionally stable structural members with less variability than the sawn timber equivalent (Naturally Wood, 2022).

Through both federal and provincial initiatives, the number of mass timber projects completed in Canada increased from 10 projects completed annually in 2007 to 60 projects in 2018 alone for a total of 412 completed projects in 2021 (NRC, 2021). The completion of these projects is in part due to intensive research conducted over the recent years aimed at disproving some of the misconceptions surrounding the material. For example, the 13-storey Origine project located in Quebec underwent rigorous fire and structural testing to justify the adequacy of the glulam post and beam design containing CLT slabs, load-bearing walls, and balloon-framing CLT shear wall system (NRC, 2021).

The fire performance of mass timber elements is a major hurdle for the material and its use in new builds. Recent code adoptions in Canada have permitted the use of encapsulated mass timber for up to 12 stories (NRC, 2020). A 2018 research program conducted by the National Research Council of Canada (NRCC) played a crucial role in quantifying the contributions of mass timber elements exposed to fire (Su et al., 2021). Fire tests were conducted in rooms having partial and full exposure to main structural elements (e.g., glulam beam, columns, and CLT slabs), and the results demonstrated a more controlled burn occurring of the mass timber elements when compared to a more conventional light-frame design. The tests also validated the equations set forth by various standards to determine the charring rate and char depth of burning mass timber elements (Canadian Standards Association, 2019a).

In addition to the enhanced structural capabilities of mass timber, the recent uptake in use of the material is in part due to other key features. In terms of environmental benefits, wood sourced from sustainably renewed forests has the potential to greatly reduce the carbon footprint of a structure. An analysis aimed at comparing the environmental impact of a 160-meter-long bridge constructed using either glulam or reinforced concrete was conducted (Lefebvre & Richard, 2014). The results favoured the glulam beam design, presenting negative carbon emissions which fell at 1,472 tonnes of CO_2 beneath the reinforced concrete alternative. A relatively new concept in the world of mass timber is biophilic design; a notion that relies on having elements and textures of the natural world exposed throughout the building can enhance human health and productivity. A 2010 study demonstrated the stress-reducing potential of exposed wood in the built environment. By comparing the stress levels of university students experiencing the same academic challenges, it was found that the group of students living in rooms with exposed wood experienced lower levels of stress (Fell, 2010). Organizations are constantly looking for ways to improve the well-being of their employees, and with wood gaining popularity and legitimacy in terms of creating a more biophilic environment, companies can add to the conventional fitness program offerings and online mental health resources. The benefits extend beyond creating and enjoyable environment, with evidence suggesting that substantial cost savings resulting from an increase in productivity can be directly related to the employees working environment (Frey, 2020). FPInnovations published a study aimed at relating biophilic design and the pro-health outcomes. Considering Canadians living in urban areas spend around 88% percent of their time indoors, it is important to understand the benefits of exposed wood in buildings. The results revealed encouraging outcomes in terms of patient recovery times and pain perception (Augustin & Fell, 2015). The study also shines a light on the versatility of the material, with biophilic designs utilizing wood with the absence of windows and views which are commonly used to increase natural light and increase the exposure to nature (Augustin & Fell, 2015).

Mass timber also plays an important role in Canada’s economy, working hand in hand with the forestry sector. In 2018, the forest sector contributed $25.8 billion dollars to the Canadian economy, demonstrating the country’s ability to progress the bioeconomy and create demand in the forest sector (NRC, 2021). Mass timber is transforming the construction industry by creating high-performing renewable products that can help address the carbon footprint issue for the construction industry.

2.3.1 Glued-Laminated (Glulam) Timber

Glued-laminated timber, commonly referred to as glulam, is an engineered wood product that dates back to the early 20th century. As shown in Figure 2.3, glulam is composed of multiple laminates that have been milled and dried, allowing for large cross-sectional members that provide similar fire resistance as large solid sawn timber beams, but with increased load capacities and dimensional stability (NRC, 2021). By grading the laminates used in the fabrication process (i.e., removing natural defects), manufacturers are able to reduce some of the variability found in bulky solid sawn timber beams. The ability to create these large cross-sectional members from smaller dimensional lumber also minimizes the tree size required for fabrication.

In Canada, manufacturers must comply with CSA O177 “Qualification Code for Manufacturers of Structural Glued-Laminated Timber” when fabricating glued-laminated timber (CSA, 2015). Based on the fabrication process, the use of the wood material can be optimized, with some special cases deliberately positioning the strongest laminates on the exterior faces to provide optimal bending resistance. The members can also be treated for environmental conditions, cambered, or tapered to again optimize the design and help maintain the life of the structure. A significant amount of research is investing how the use of prefabrication can further increase the use of mass timber (Gasparri &

Aitchison, 2019; Orlowski, 2019; Sartori & Crocetti, 2016). Innovation and technological advances have resulted in improved computer aided machines (e.g., CNC) that allow designers to specify precise dimensions that can be included prior to material delivery. The materials high strength-to-weight ratio, along with reduced construction schedules (i.e., ability to prefabricate panels and connections) are all factors increasing the adoption of the material in the industry.

Figure 2.3 - Glulam Beam

*Reproduced from NRC (2021)

2.4 Fibre Reinforced Polymers (FRPs)

Fibre reinforced polymer (FRP) materials are made-up of two primary raw material constituents. The composite action between high strength fibres and a polymer resin creates the structurally viable construction material commonly used in today's construction, mainly for the reinforcement of existing structural elements. The reinforcing fibres are the main load carrying components of the material; however, their size and filamentary nature prevent them to be used as stand-alone materials. Common types of fibres used in structural engineering applications include aramid, carbon and glass. The polymer resin (i.e., the non-fibrous component) is used to connect the fibres together, allowing for the load transfer as well as providing a level of protection (ACI Committee 440, 2007). Different types of polymer resins exist (e.g., epoxy, vinylester, polyurethane), each comprising their own set of pros and cons. Epoxy resins are most commonly used in structural applications and belong in the same family of epoxies used for concrete crack injection and anchors for concrete. An outstanding corrosion resistance along with minimal shrinkage once cured also gives the epoxy resin an edge in engineering applications (Bank, 2006). Two main manufacturing processes are used to make FRP products. The pultrusion process consists of an automated method producing FRP profiles, bars, and strips that are manufactured off site and are sold pre-cured (Bakis et al., 2002). The wet-layup manufacturing process is completed at the time of application, with the name originating from the in-situ application process of combining the polymer resin and fibres to create the FRP material (Bank, 2006). The fibrous component is sold as a fabric that can be cut and applied along various surface geometries. Prior to its application, the fibres are impregnated with the polymer resin which is then applied to the surface of the reinforced material (Bank, 2006).

Figure 2.4 shows representative stress-strain relationships for carbon (CFRP) and glass (GFRP) reinforced polymers compared to mild steel (ACI Committee 440, 2007). A linear elastic behaviour is experienced for the FRP materials, having a lower stiffness than the steel but exhibiting higher stresses at failure.

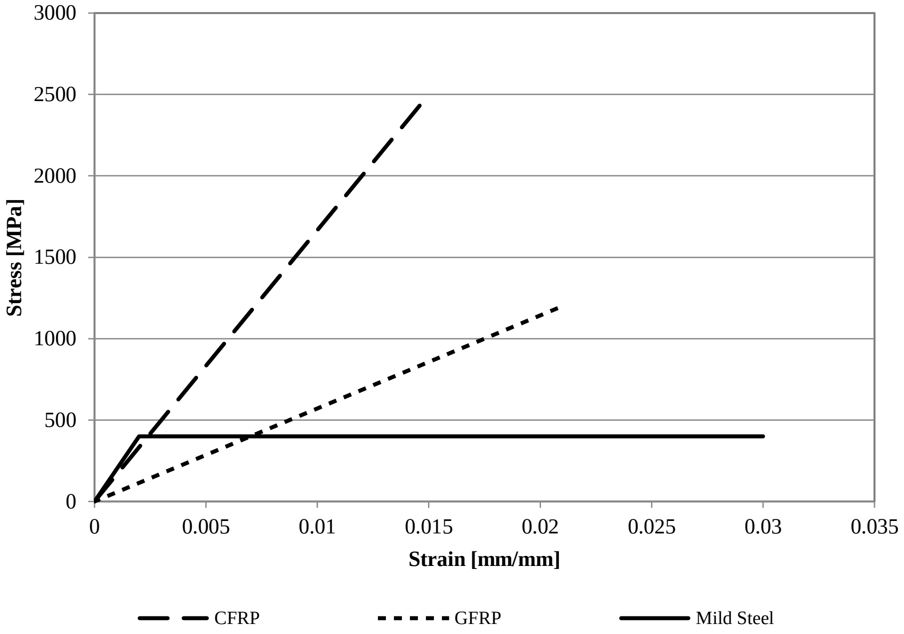

Figure 2.4 - Typical Stress-Strain Curves for FRPs and Mild Steel

*Reproduced from ACI Committee 440 (2007)

2.5 FRP-Reinforced Glulam

Techniques employing various materials to reinforce structural timber elements have been around for decades, with metal-reinforced timber patents dating back to the 1920s (Bulleit, 1984). A literature review of existing retrofit methods for wood (e.g., aluminum and steel plates) was conducted, and the findings stated that many of the metal reinforcement methods were not commercially adaptable. However, it was reported that the use of fibre reinforced polymers (FRPs) was not only successful in strengthening wood members but also stood a better chance for commercial development (Bulleit, 1984). Several years later, the technological advances facilitating the production of the high strength material has shown to become a feasible solution for the reinforcement of timber elements. Research investigating the long-term effects of the FRP-timber composite material has also shown positive results (Aratake et al., 2011; Davids et al., 2008), although extended research regarding this topic is still required to better understand or predict the behaviour and expected life span of the reinforced members.

2.5.1 The Need for Reinforcement

Wood is a natural material which means that in addition to the structural deficiencies (e.g., structural damage, design mistakes, and construction errors) accounted for when using concrete or steel, the material is also susceptible to biodeterioration. The main cause of bio-deterioration in wood is biotic agents (C. Legg & Tingley, 2020). These agents are living organisms (e.g., bacteria, fungi, insects, etc.) that attack the material under ideal conditions and can lead to severe structural damage if not addressed early on. The understanding of fungi decay has led to prevention through design protocols that have constructed and maintained timber bridges with service lives exceeding 100 years (Wacker et al., 2020).

FRP reinforcement has a chance to become extremely useful when engineers are faced with decisions regarding the retrofitting of timber bridges that require increased load carrying capacities. The high-strength material has the ability to increase the load-carrying capacity of existing timber elements in-situ, reducing the time and cost of repairs when compared to a newly designed and constructed structure.

2.5.2 Compression Reinforcement

Although commonly used to reinforce bending members, the use of FRP fabric applied as confinement reinforcement for timber columns has been investigated and has shown potential. Zhang et al. (2012)

investigated the compressive behaviour of FRP-reinforced timber columns containing longitudinal cracks. Comparing the resistance of the retrofitted columns to the control specimens, the results demonstrated that the FRP reinforcement was able to help restore the load-carrying capacity of the timber columns (Zhang et al., 2012).

The use of FRPs to increase the capacity and stiffness of timber columns has also been the subject of past research. Kim & Andrawes (2016) reinforced heavy timber piles and investigated the effect of the reinforcement on specimens exposed to accelerated aging, with results showing capacity increases up to 80% and 35% for the control and aged columns, respectively. The use of various fibre orientation (e.g., 0°, 0/90°, ±45°) was also studied to investigate the effect of the reinforcement configuration on the compressive behaviour of solid sawn timber columns and the results demonstrated both stiffness increases and the localization of damage along the reinforced specimens (O'Callaghan, 2021).

2.5.3 Shear Reinforcement

Akbiyik et al. (2007) studied the effects of various shear reinforcement configurations on severely checked timber beams. To better understand the flexural capacity of the beams, a variety of repair systems were investigated; namely, hex bolts running the entire depth of the stringer, transverse lag screws extending through the entire depth, GFRP and plywood side plates mechanically attached (Akbiyik et al., 2007). All three reinforcement configurations recorded shear stresses that exceeded the load and resistance factor design (LRFD) allowable strength values, with an average increase of 1.29 relative to LRFD design values (Akbiyik et al. 2007). The shear reinforcement in this study was applied to damaged members (i.e., deemed inadequate or loaded to failure in the experimental tests). The use of transverse hex bolts spaced at 610 mm and lag screws spaced at 305 mm along the beam resulted in an 88% recovery of the original strength. The plywood side plates used to reinforce a stringer that was deemed structurally deficient was able to increase the ultimate load by 14.3% and the FRP side plates were able to increase the ultimate load by 91% (Akbiyik et al. 2007).

Hota et al. (2010) investigated the behaviour of retrofitted beams having service lives exceeding 50 years using GFRP sheets. Two types of configurations were considered, namely, Vacuum Bagging and GFRP spray methods. Results demonstrated a 267% increase in stiffness for the specimens reinforced with the FRP using the vacuum method and an increase of 41% for the sprayed on GFRP method when compared to the control specimens (Hota et al., 2010). Svecova and Eden (2004) conducted an experimental program aimed at increasing the flexural and shear strength of timber beams using GFRP bars. The initial reinforcement configuration, consisting of transversely inserted bars, had an average strength increase of 35% compared to the unreinforced beam. A second reinforcement configuration consisting of both transverse and longitudinal bars was analyzed, where an average strength increase of 52% was observed for beams reinforced with both shear and flexure reinforcement compared to those only reinforced for shear.

Gentry (2011) investigated the potential of FRP bars and sheets used as reinforcement for lower-grade wood with the overarching aim being to reduce the variability in wood strengths. A total of 42 unreinforced beams (32 mm x 72 mm x 320 mm) were tested under three-point bending and an average failure load of 23 kN was recorded, with approximately 50% of the specimens failing in shear (Gentry, 2011). The reinforcement configurations consisted of FRP pins drilled and epoxied transversely into the specimen. While all variations of pin spacing and diameter allowed for different failure loads, most of the specimens failed in tension, with the initial failure starting on the tensile laminate near the hole drilled for the pins. The probabilistic distribution from the small-scale test results indicated that the presence of shear reinforcement increased the allowable shear stress design value by 50% or more (Gentry, 2011). Large-scale tests were also completed on timber beams specifically chosen to have finger joints or a lower strength grade. Reinforcement configurations for the large-scale tests varied from having only transverse FRP bars to including some flexural FRP sheets to enhance the bending capacity of the already transversely reinforced sections. Results of the large-scale tests conducted on doubly reinforced glulam beams indicated that the shear pins have a negative effect on the flexural capacity of the beams, which has been attributed to the damage done to the tension laminates when drilling the pin holes (Gentry, 2011). The author concluded that simply adding longitudinal FRP reinforcement benefited the lower-grade beams by reducing the variability and increasing the resistance to the level observed in unreinforced higher-grade beams (Gentry, 2011).

2.5.4 Flexural Reinforcement

The flexural strengthening of timber elements using FRP has been studied more extensively when compared to shear and compression reinforcement. Most of the research aims to improve the bending capacity of the flexural elements by reducing or eliminating the brittle tensile failure observed in unreinforced timber beams (Buell & Saadatmanesh, 2005b; Johns & Lacroix, 2000a; Plevris & Triantafillou, 1992). By providing tension reinforcement, the beams are able to reach the compression yielding/softening strains which result in more ductile load carrying members (Lacroix, 2017).

Experimental tests conducted by (Rosa García et al., 2013) showed promising results for the use of FRP as a reinforcing material for timber beams. The effects of CFRP and basalt FRP (BFRP) on the flexural behaviour of solid sawn timber specimens were investigated. A total of 26 beams with U-shaped FRP sheets (Figure 2.5) were loaded under three-point bending up to failure. The reinforcement quantity and layout differed between reinforcement schemes and was measured in terms of weight per unit area (g/m^2), and the orientation of the fibres (i.e., unidirectional, or bi-directional). Strength increases up to 24% compared to the control beams were recorded, with particular interest being focused on the optimization of the reinforcing material (i.e., obtaining the larger strains to allow the reinforcement to be more engaged) (Rosa García et al., 2013).

(a) U-shape reinforcement (b) Reinforced specimens

Figure 2.5 - U-shaped CFRP Reinforcement

*Reproduced from Rosa García et al. (2013)

Johns & Lacroix (2000) investigated the behaviour of sawn timber specimens reinforced with glass (GFRP) and CFRP. A total of 150 beams were subjected to four-point bending and loaded up to failure. An increase in strength was observed in all reinforced specimens that did not contain significant defects such as cracks or knots. Such increases ranged from 40% to 100% of the unreinforced cases, with the largest increases being present in the beams reinforced with GFRP in a U-shaped configuration (Johns & Lacroix, 2000a). In all configurations, the largest bending resistance increases occurred in the weakest members, experimentally demonstrating that the FRP bridges defects that are present on the timber specimens.

Buell & Saadatmanesh (2005) reinforced dismantled timber bridge beams with CFRP sheets and studied their performance. The solid sawn Douglas Fir beams were 203 mm x 483 mm x 9100 mm and wrapped with different retrofit configurations. The main variable analyzed throughout the experimental program was the direction of application for the CFRP sheets, where both transversely (Figure 2.6a) and longitudinally (Figure 2.6b) applied fabric were compared to determine their practicality and performance. Stiffness increases ranging from 5% to 27% compared to the control beam and bending capacity increases ranging from 40% to 53% for the beams reinforced with sheets extending up to the compression face of the element were observed (Buell & Saadatmanesh, 2005).

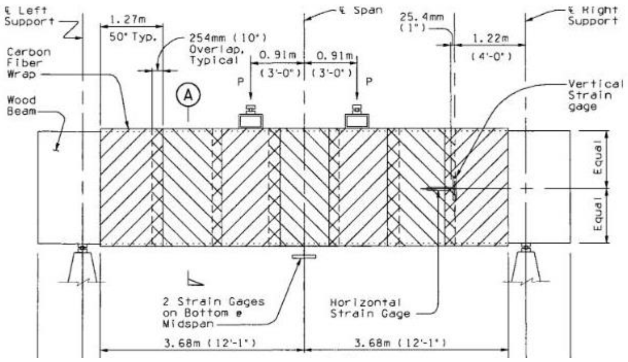

(a) Transversely applied CFRP sheets

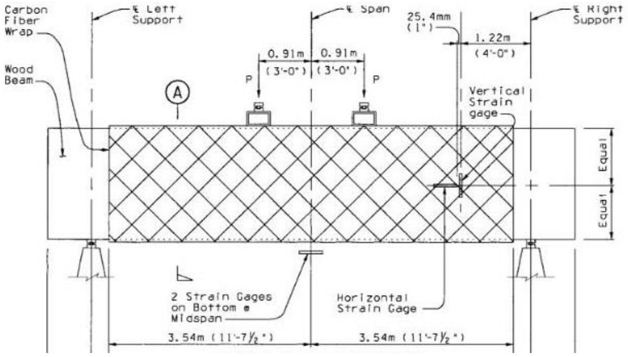

(b) Longitudinally applied CFRP sheets

Figure 2.6 - Orientation of CFRP Reinforcement Sheets

*Reproduced from Buell & Saadatmanesh (2005)

In addition to FRP sheets, near surface mounted (NSM) pultruded FRP bars have also been studied and included in the code (Canadian Standards Association, 2019b). Gentile et al. (2002) retrofitted existing timber bridge stringers using GFRP bars placed longitudinally near the tension face with the goal of providing the same type of tensile reinforcement commonly seen in reinforced concrete beams. Half-scale (100 mm x 300 mm x 4300 mm) and full-scale (200 mm x 600 mm x 10,400 mm) creosote-treated Douglas Fir beams having shear span-to-depth ratios exceeding 5.5 were loaded to failure under four-point bending. The reinforcement increased the ultimate tensile strain of the timber by an average of 64%, showing that the bars helped resist the opening of cracks, as well as confined the local failures and bridged the wood defects. This resulted in a ductile compression failure in the wood rather than the typical brittle failure observed on the tension face of an unreinforced member (Gentile et al., 2002).

An experimental program investigating the flexural resistance of FRP-reinforced glulam beams subjected to static and simulated blast loading was conducted to better understand the material behaviour under high-strain rates (Lacroix & Doudak, 2018). Some of the reinforcement configurations investigated in the study are shown in Figure 2.7, where the commonly known simple tension reinforcement (Figure 2.7a) was included to better understand the associated failure modes. Figure 2.7b depicts the novel reinforcement configuration investigated by the authors which consisted of unidirectional (0°) U-shaped reinforcement along with unidirectional fabric applied at 90º to the wood fibres to act as confinement in the high-bending stress region (i.e., at midspan). The GFRP simple tension reinforcement configuration yielded an average increase in resistance, displacement at maximum resistance and stiffness of 1.35, 1.30 and 1.1, respectively. The U-shaped reinforcement containing midspan confinement experienced greater average increases in resistance, displacement at maximum resistance and stiffness equal to 1.57, 1.62 and 1.12, respectively (Lacroix & Doudak, 2018).

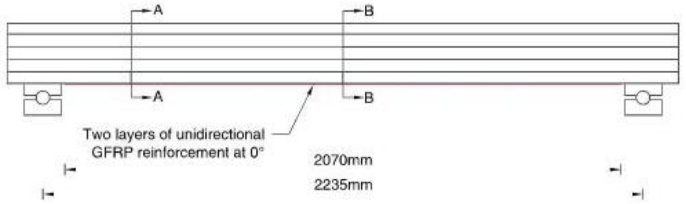

(a) Simple tension reinforcement

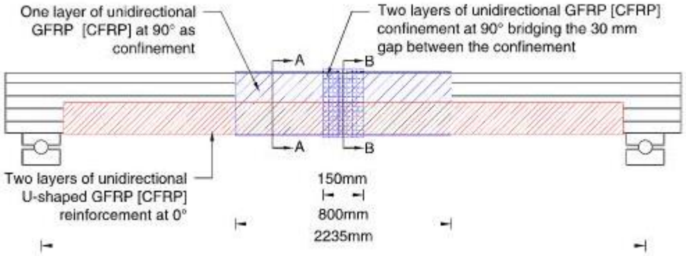

(b) U-shaped reinforcement with midspan confinement

Figure 2.7 - Reinforcement Configurations for Beams Subjected to Blast Loading

*Reproduced from Lacroix & Doudak (2018)

The experimental test results were in line with past observations regarding the delamination failure that occurred for glulam beams reinforced in a simple tension configuration (Dorey & Cheng, 1996a; Hernandez et al., 1997; Sonti et al., 1996). The representative failure modes associated with the simple tension reinforcement configuration are shown in Figure 2.8, where the debonding of the reinforcement sheet is clearly visible. The wood splintering failure, initiating from the tensile laminates and propagating through the entire depth of the beam is also observed in Figure 2.8 (Lacroix & Doudak, 2018).

(a) Example specimen no. 1 (b) Example specimen no. 2

Figure 2.8 - Simple Tension: FRP Delamination and Wood Splintering Failure

*Reproduced from Lacroix & Doudak (2018)

The enhanced reinforcement configuration consisting of midspan confinement did provide adequate resistance in the confined region; however, the increased resistance resulted in failures that occurred outside of the high-bending stress region. As shown in Figure 2.9, both the static and dynamic tests resulted in FRP delamination failures that occurred outside of the confined regions. Although both the simple tension and partially confined configurations investigated by Lacroix & Doudak (2018) experienced some sort of FRP damage, it is important to note that the recorded wood tensile failure strain for the U-shaped reinforced beam containing the midspan confinement was increased by 1.26 and 1.14 when compared to the unreinforced and simple tension reinforced beams, respectively.

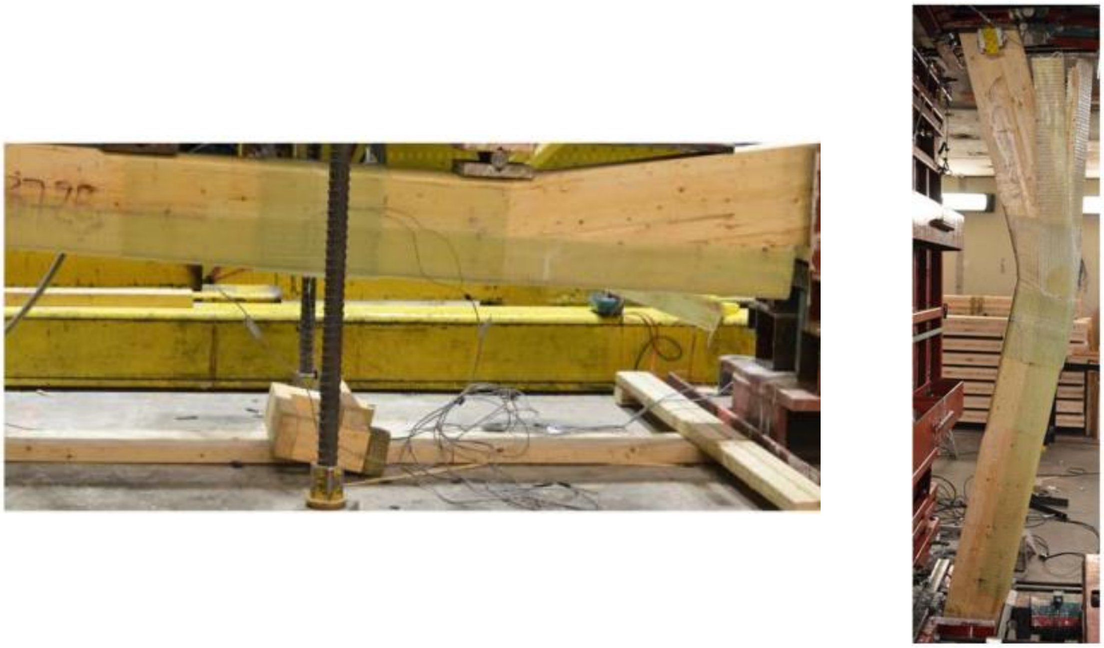

(a) Static loading (b) Dynamic loading

Figure 2.9 - U-shaped with Confinement: Shear Region Failure

*Reproduced from Lacroix & Doudak (2018)

Lacroix and Doudak (2020) investigated the behaviour of FRP-reinforced glulam beams subjected to simulated blast loading by incorporating fully confined reinforcement configurations that extended the entire length of the specimens. The cross-sectional beam sizes did not allow a single FRP sheet to provide full confinement, therefore, the authors designed various reinforcement configurations aimed at providing adequate splice lengths between reinforcement sheets, as shown in Figure 2.10. Increases in resistance and stiffness were observed for all reinforcement configurations along with ultimate displacement increases ranging up to 3.6 times that observed for the unreinforced control beams (Lacroix and Doudak, 2020).

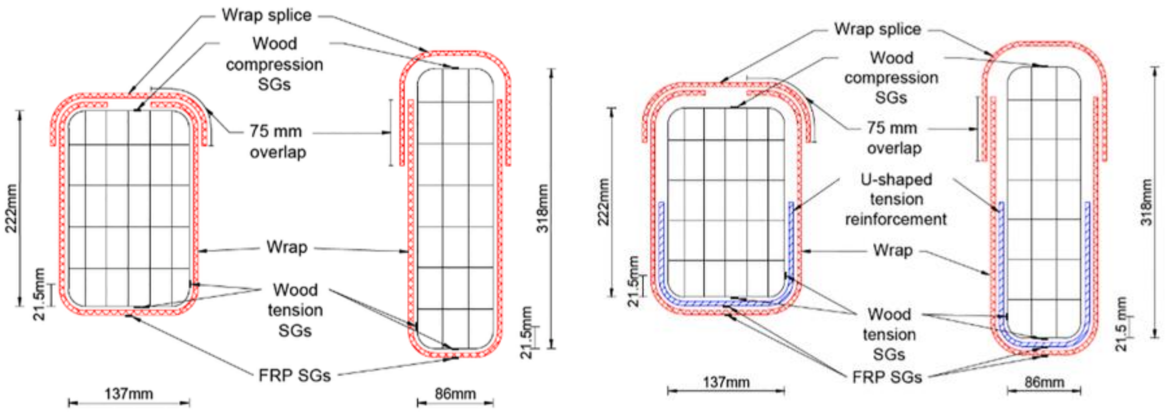

(a) Bidirectional FRP (b) Unidirectional and bidirectional FRP

Figure 2.10 - Fully Confined Reinforcement Configurations

*Reproduced from Lacroix & Doudak (2020)

In terms of failure modes, the dynamic loading played an important part in revealing the path of weakest resistance. As shown in Figure 2.11, two main failure modes were observed for the fully confined glulam beams. An adequate bond between the reinforcing material and the wood was shown to confine the failure to the midspan and affect both the FRP and wood (Figure 2.11b). The high-strain rate loading was also shown to produce unzipping failures (Figure 2.11c). For the unzipping failures, the full confinement provided enough resistance to minimize the wood damage shown in the unreinforced specimens (Figure 2.11a); however, the delamination of the FRP characterized the ultimate failure. Lacroix and Doudak (2020) reported an average increase in wood tensile failure strain of 1.2 in the FRP-reinforced specimens compared to the un-reinforced specimens. The value is consistent with the 1.17 value reported by Lacroix and Doudak (2018) when utilizing unidirectional FRPs. It is also consistent with the value provided in the Canadian bridge design code (Canadian Standards Association, 2019b) which proposes values of 1.1 and 1.2 for Select Structural and No.1 grades, respectively.

(a) Unreinforced – Wood splintering failure

(b) FRP and wood rupturing

(c) Unzipping failure

Figure 2.11 - Full Confinement: Failure Modes

*Reproduced from Lacroix & Doudak (2020)

Lacroix et al. (2021) experimentally investigated the flexural performance of FRP-reinforced wood studs with and without the presence of FRP confinement. The four reinforcement configurations investigated are shown in Figure 2.12. The beams reinforced with two layers of simple tension reinforcement increased in resistance, displacement at maximum resistance and stiffness by average factors of 1.09, 1.29 and 1.02, respectively (Lacroix et al., 2021). The two layer U-shaped reinforced beams resulted in average increases of 1.60, 3.16 and 1.26 for the resistance, displacement at maximum resistance and stiffness, respectively (Lacroix et al., 2021). The addition of FRP confinement (Figure 2.12c and d) provided enough reinforcement to further increase the resistance by factors of 1.50 and 1.29 for the simple tension and U-shaped reinforced beams, respectively, when compared to the unconfined beams.

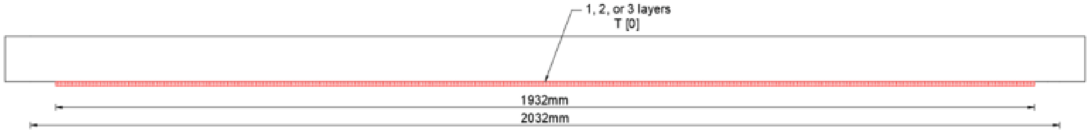

(a) Simple tension

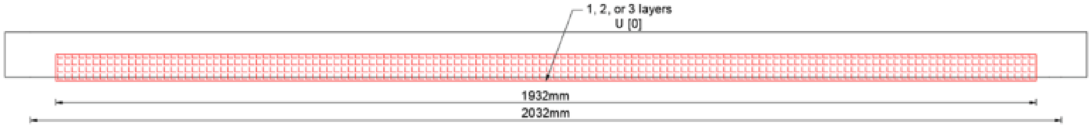

(b) U-shaped

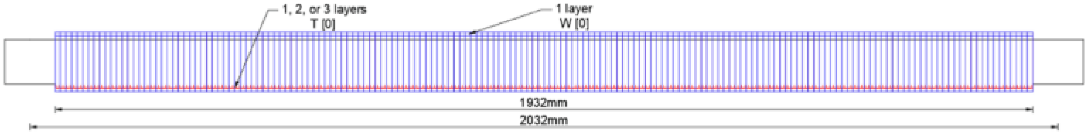

(c) Simple tension and confinement

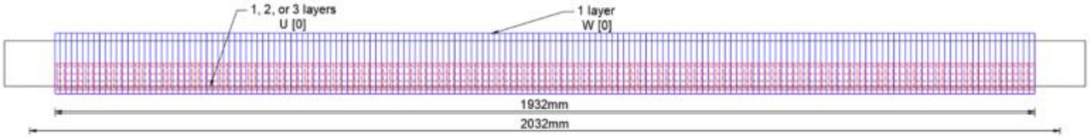

(d) U-shaped and confinement

Figure 2.12 - Wood Stud Reinforcement Configurations

*Reproduced from Lacroix et al. (2021)

The failure modes associated with the reinforcement configurations are shown in Figure 2.13. The simple tension reinforcement was observed to de-bond due to the failed wood pushing on the reinforcement (Figure 2.13a) whereas wood splintering and compression yielding was observed for the U-shaped reinforced beam (Figure 2.13b), and a localized failure was observed for the confined beams (Figure 2.13c).

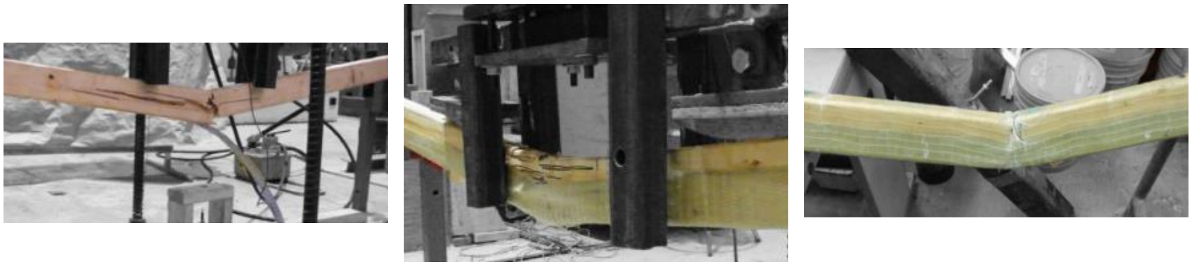

(a) Simple tension: FRP delamination

(b) U-shaped: Wood splintering and compression yielding

(c) Confined: Localized damage

Figure 2.13 - Wood Stud Failure Modes

*Reproduced from Lacroix et al. (2021)

Lacroix et al. (2021) also conducted an analysis aimed at addressing the theory that the lower-grade wood benefits the most from the reinforcement, originally discussed by Johns & Lacroix (2000). Figure 2.14 clearly demonstrates that the weaker beams experienced strength increases of two times that of their unreinforced sister specimens. In comparison, the stronger beams experienced lower strength increases.

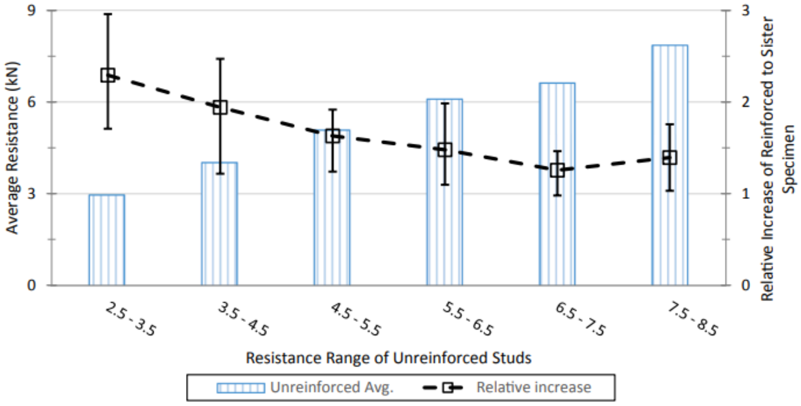

Figure 2.14 - Effect of Reinforcement on the Strength of Wood Specimens

*Reproduced from Lacroix et al. (2021)

When considering various retrofitting techniques or designs, the optimization of the reinforcing material remains an important factor in the decision process. Corradi et al. (2021) conducted research that focuses on the local reinforcement of existing timber bridges. Experimental tests have shown that the presence of defects (e.g., knots) on the tensile face within the high-bending regions can reduce the bending capacity by roughly 35% when compared to non-deficient specimens (Corradi et al., 2021). By applying the CFRP sheets solely around the defects and maintaining proper development length (Figure 2.15), the authors reported that the FRP contributed to reducing the deficiencies from the 35% without FRP to a 20% decrease in strength when FRP is applied over the defects compared to non-deficient specimens, thereby increasing the performance by 15% (Corradi et al., 2021).

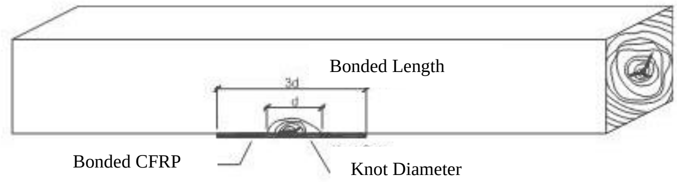

Figure 2.15 - Local Reinforcement of Existing Timber Beams

*Reproduced from Corradi et al. (2021)

2.5.5 Predicting the Flexural Response of FRP-Reinforced Glulam Beams

The reinforcement of wood (i.e., timber and glulam) beams has created a need for material models capable of analytically predicting their flexural behaviour. A material model for wood was originally developed based on a linear elastic tension and bilinear compression behaviour (Buchanan, 1990). As shown in Figure 2.16, the tension behaviour is assumed to be linear elastic up to an ultimate stress, f_t, and strain, ε_{tu}, while the compressive behaviour behaves in a linear elastic manner up to a yield stress, f_c, and strain, ε_y, before decreasing linearly to its ultimate stress, f_{cu}, and strain, ε_{cu}.

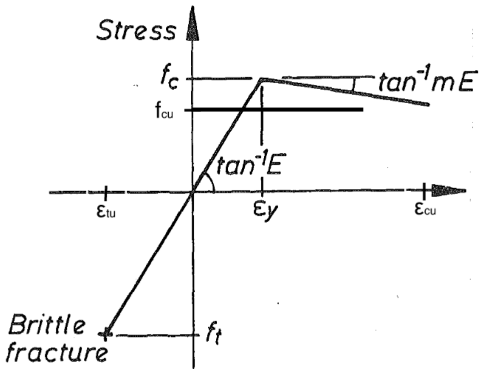

Figure 2.16 - Stress-strain Relationship of Wood

*Reproduced from Buchanan (1990)

The bilinear behaviour of the material promotes the use of moment-curvature analyses, capable of incorporating the non-linear portion of the stress-strain relationship. The ASTM D7199 “Establishing Characteristic Values for Reinforced Glued-Laminated Timber (Glulam) Beams Using Mechanics-Based Models” standard (ASTM, 2012) establishes a procedure that can be used to determine the moment-curvature data of reinforced glulam beams (Figure 2.17).

Gentile et al. (2002) developed a computer program to predict the flexural behaviour of FRP-reinforced beams. The initial program, as proposed by Buchanan (1990), underestimated the strength capabilities. Upon further investigation, the ultimate tensile strains in the wood reinforced with FRP were observed to be 64% larger than the modelled allowed (i.e., unreinforced wood) (Gentile et al. 2002). In order to address the fact that wood tensile failure strains are higher in wood reinforced with FRP, the authors incorporated a modification factor, α_m, designed to increase the tensile rupture strain values based on experimental results. The calibrated model was able to predict bending strength values that were within 2.8% of the experimental strengths (Gentile et al. 2002).

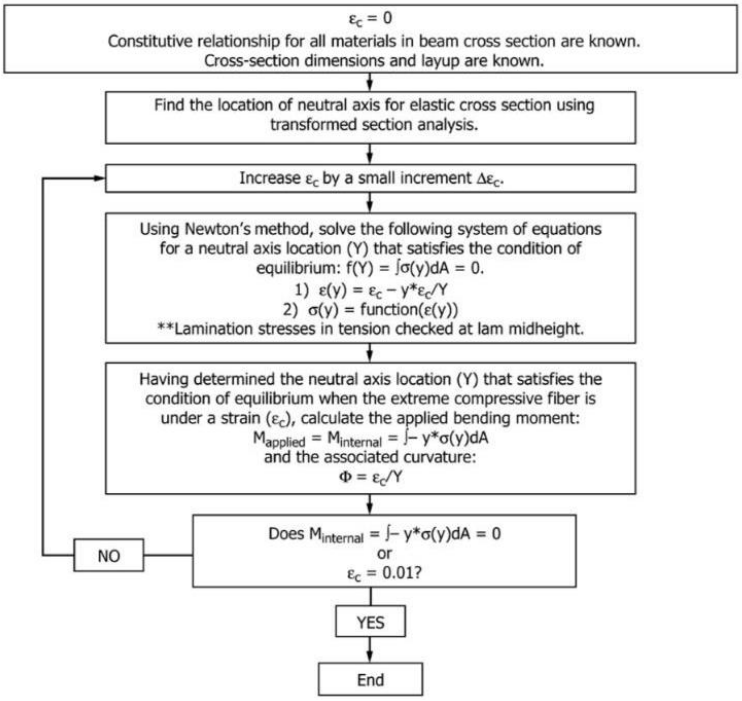

$\varepsilon_c = 0$

Constitutive relationship for all materials in beam cross section are known.

Cross-section dimensions and layup are known.

Find the location of neutral axis for elastic cross section using transformed section analysis.

Increase ε_c by a small increment $\Delta\varepsilon_c$.

Using Newton's method, solve the following system of equations for a neutral axis location (Y) that satisfies the condition of equilibrium: $f(Y) = \int\sigma(y)dA = 0$.

1) $\varepsilon(y) = \varepsilon_c - y*\varepsilon_c/Y$

2) $\sigma(y) = \text{function}(\varepsilon(y))$

**Lamination stresses in tension checked at lam midheight.

Having determined the neutral axis location (Y) that satisfies the condition of equilibrium when the extreme compressive fiber is under a strain (ε_c), calculate the applied bending moment:

$M_{applied} = M_{internal} = \int - y*\sigma(y)dA$

and the associated curvature:

$\Phi = \varepsilon_c/Y$

Does $M_{internal} = \int - y*\sigma(y)dA = 0$ or $\varepsilon_c = 0.01$?

Figure 2.17 - Procedure for Moment-Curvature Analysis

*Reproduced from ASTM (2012)

Other research programs have adequately modelled their results using the non-linear stress-strain relationship and modification factor, α_m. Lacroix and Doudak (2020) reinforced glulam beams subjected to both static and dynamic loading. Using the strain, stress and force profile depicted in Figure 2.18, the authors were able to extract model to experimental ratios of 0.99 and 1.02 for the maximum load and the displacement at maximum load, respectively.

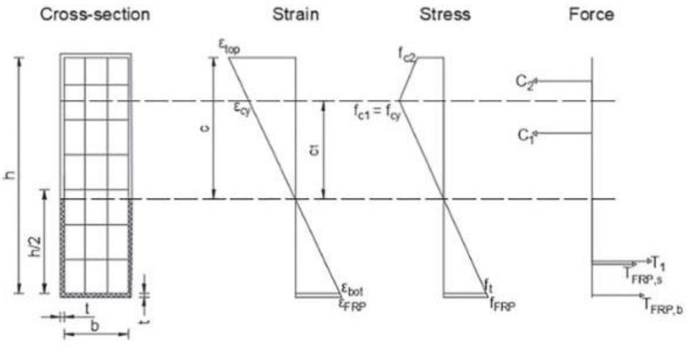

Figure 2.18 - Reinforced Beam Equilibrium

*Reproduced from Lacroix & Doudak (2020)

In addition to analytical material models used to perform moment-curvature analyses, other researchers have considered the use of more computer intensive processes to determine the flexural response of glulam beams (Glisovic et al., 2017; Raftery & Harte, 2013). Finite element modelling (FEM) conducted by Glisovic et al. (2017), incorporating the orthotropic behaviour of timber, required the input data of nine independent constants (e.g., three moduli of elasticity, three shear moduli and three Poisson's ratios). The resistance curves presented in Figure 2.19, shows both the experimental and FEM results of unreinforced (Figure 2.19a) and reinforced (Figure 2.19b) glulam beams. The FEM analysis was shown to adequately predict the behaviour and resulted in an average numerical to experimental ratios of 1.02, 0.99 and 1.00 for the maximum capacity, maximum midspan deflection and bending stiffness (Glisovic et al., 2017).

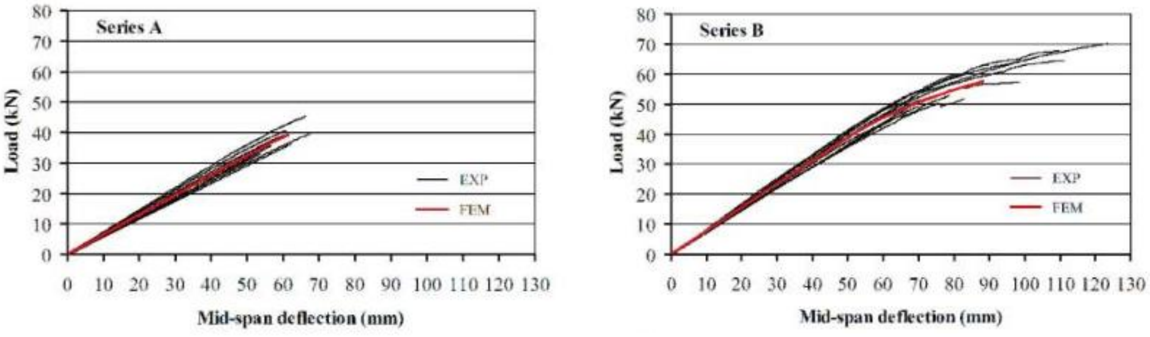

(a) Unreinforced beams (b) Reinforced beams

Figure 2.19 - Resistance Curve Comparison Between Experimental and Numerical Modelling

*Reproduced from Glisovic et al. (2017)

Plevris & Triantafillou (1992) conducted experimental and analytical work on wood beams having FRP reinforcement applied along the tensile laminate of the beam. By considering different reinforcement ratios (i.e., area of reinforcement to the area of wood), the authors were able to determine that reinforcement ratios exceeding 3% did not proportionally benefit from the added reinforcement when compared to the increases observed for ratios less than 3% (Plevris &Triantafillou, 1992).

More recently, the effects of varying wood tensile to compressive modulus of elasticity on the flexural behaviour of glulam beams have been the subject of various studies. A numerical study investigating different wood tension to compression modulus of elasticity ratios along with different axial loads showed that both factors had a significant impact on the out-of-plane flexural response (Lacroix, 2017; Lacroix et al., 2018). The analysis results shown in Figure 2.20 are consistent with the observations made by Buchanan (1990), where an increase in axial load resulted in a decrease in moment capacity.

The study shows the importance of the material properties in predicting the flexural response of wood elements, and thus, should also be investigated on FRP-reinforced timber and glulam members.

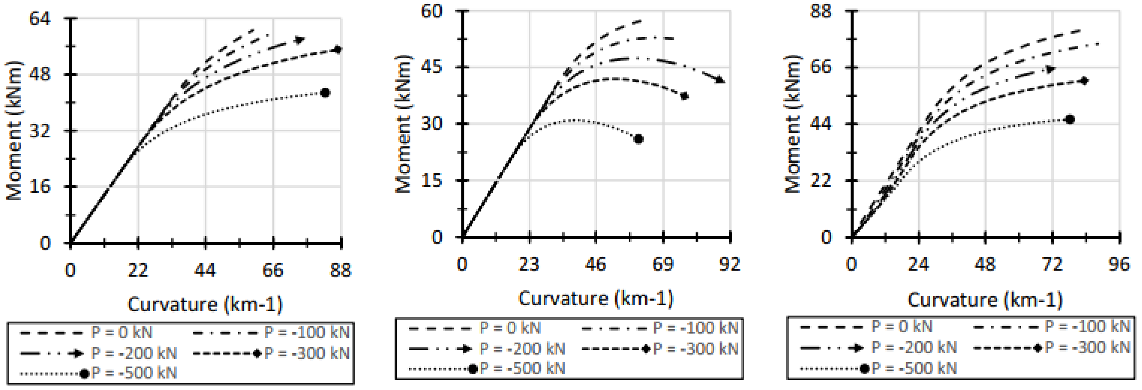

(a) Case 1 – $E_{wt} = E_{wc}$; m = 0.01 (b) Case 2 – $E_{wt} = E_{wc}$; m = 0.2 (c) Case 3 – $E_{wt} = 2E_{wc}$; m = 0.01

Figure 2.20 - Moment Curvature Analysis for Beams with Applied Axial Load

*Reproduced from Lacroix et al. (2018)

2.6 Summary

The literature review has highlighted the need for understanding the behaviour of FRP-reinforced wood products under flexure. Despite significant research investigating the compressive, shear, and flexural behaviour of FRP-reinforced wood elements, little research has been dedicated to preventing undesirable failure modes (e.g., premature de-bonding of FRP tension reinforcement) aside from providing full-length confinement. Furthermore, there are currently no design guidelines in the Canadian highway bridge code nor in the Engineering in wood (Canadian Standards Association, 2019a, 2019b) with regards to the design of FRP-reinforced glulam elements.

The literature has shown that significant increases in resistance and stiffness can be attained by providing FRP reinforcement. It was also observed to reduce the variability, bridge defects, and contribute to an increased wood tensile failure strain. Furthermore, in cases where full-length confinement is used to reinforce the members, significant post-peak resistance was reported.

Despite the significant improvements provided by the FRP, little research has been directed at preventing undesirable failure modes by least invasive retrofitting techniques nor to the various assumptions in predicting the flexural strength. Thus far, recommendations have been to avoid simple tension reinforcement due to the lack of ductility; however, in cases where members need to be retrofitted, full access to a member may not be possible to allow for full confinement. Further research is required to understand the effects of cross-section size to span, alternate reinforcing schemes for members with accessibility restrictions, failure modes, and finally in investigating the limitations of the material models in predicting the flexural behaviour.

Chapter 3

Experimental Program

3.1 General

This chapter describes the experimental program investigating the flexural response of unreinforced and FRP-reinforced glulam beams under static loading. The experimental program can be divided into two phases consisting of tests on:

1. Components (e.g., wood, FRP coupons) subjected to uniaxial loading to determine the material properties for input in the analytical program.
2. Unreinforced and reinforced beams subjected to static four-point bending.

A total of thirty glulam beams were tested statically under four-point bending in addition to forty-eight coupon tests on the wood and FRP in order to determine the respective material properties. The following sections describes the test specimens, experimental test setups, and protocols.

3.2 Description of the Unreinforced Specimens

Glulam specimens of stress grade 20f-EX were used in this experimental program and were obtained from a single supplier in which two different cross-sections were considered. Initial deformities were present on the beams, such as rounded or uneven edges (Figure 3.1a), uneven laminate widths (Figure 3.1b), and splits (Figure 3.1c). These deformities were removed by means of dressing using a planer and jointer.

(a) Rounded edges (b) Uneven laminate widths (c) Damaged laminates

Figure 3.1 - Initial Beam Deformities

Final cross-sectional dimensions of 69 mm x 100 mm and 69 mm x 160 mm were chosen for both beams, as they allowed a common size for the dressed beams (i.e., free of initial deformities). The two cross-sections result in depth to width ratios of 1.45:1 (i.e., 69 mm x 100 mm) and 2.3:1 (i.e., 69 mm x 160 mm) and were chosen to investigate the effects of depth to width ratio on the flexural response of unreinforced and FRP-reinforced glulam beams. Figure 3.2 shows representative samples of the two cross-section sizes after dressing the beams to their final sizes.

(a) 69 mm x 100 mm (b) 69 mm x 160 mm

Figure 3.2 - Beam Cross-sections

The nomenclature of the specimens is based on the beam depth, with [100] beams having a depth of 100 mm and [160] beams having a depth of 160 mm. [100] specimens are made up of three laminates pressed and glued together on their flat face (Figure 3.2a) while [160] beam specimens have a total of five laminates (Figure 3.2b). The specimen lengths were determined in accordance with ASTM D198 “Standard Test Methods of Static Tests of Lumber in Structural Sizes” (ASTM, 2021b). According to the standard, a minimum shear span to depth (a/d) ratio of 4 allows for the evaluation of flexural properties (ASTM, 2021b). Therefore, total beam lengths of 1,355 mm and 2,280 mm were chosen for the [100] and [160] beams. The lengths allowed for shear and design spans of 400 mm and 1,200 mm for the [100] beams, and shear and design spans of 640 mm and 1,920 mm for the [160] beams. Prior to testing, the specimens were stored in a humidity chamber which allowed the specimens to maintain their required moisture content. The average moisture content of the 20f-EX glulam was 11.2% with a coefficient of variation of 0.11. The average density of the beams was determined to be 442 kg/m^3 with a coefficient of variation of 0.06.

3.3 Description of the Reinforced Specimens

A total of six different glass FRP (GFRP) reinforcement configurations were investigated to enhance the flexural behaviour of glulam beams under four-point bending. The testing of the reinforced beams is divided into two distinct stages. The first stage had the objective of investigating the effects of reinforcement ratio when unidirectional GFRP is applied as simple tension and U-shaped (i.e., up to mid-depth) on the stiffness and strength of the reinforced glulam beams. The retrofit configurations investigated in the second stage were determined following the completion of stage 1 and had for objective of further enhancing the behaviour of the glulam beams by addressing any premature or undesirable failure modes observed in stage 1. The following sections describes the procedure used to apply the reinforcing material, details on the reinforcement configurations, and instrumentation.

3.3.1 FRP Information and Application Process

The epoxy and GFRP used in this study were acquired from Simpson Strong-Tie. A two-part epoxy polymer resin was used due to its high modulus, high strength, and documented literature demonstrating adequate bond between the GFRP and wood material. The mechanical properties provided by Simpson Strong-Tie are given in Table 3.1. The GFRP fabric was delivered and stored in rolls with a width of 36 inches.

Table 3.1 - Manufacturer Design Values for the Epoxy and FRP Composite Material

Fabric Fibre Orientation	**Fabric Dry Weight (g/m2)**	**Fabric Layer Thickness (mm)**	**Composite Tensile Strength (MPa)**	**Composite Modulus of Elasticity (GPa)**	**Composite Rupture Strain (mm/mm)**
Unidirectional (0°)	915	1.30	390	23	0.017
Bidirectional (0°/90°)	611	0.66	310	17	0.018

Prior to the application of the GFRP, the glulam tension laminate corners were routed using a corner round over bit (12.7 mm radius) to avoid stress concentrations in the FRP extending beyond the bottom face. The application face(s) of the beams were then wire brushed using a grinder to roughen the surface in order to provide a more suitable interface for the bond between the FRP fabric and the glulam.

A calculated 2.4:1 weight ratio of the two-component (part A to part B) epoxy resin was measured and mixed for five minutes at 700 rpm using an electric mixer. Prior to its application, the glulam FRP application face(s) was coated with a thin layer of the epoxy resin mixture using paint rollers (Figure 3.3a). The GFRP fabric was initially saturated with the epoxy resin by means of paint brushes and rib rollers (Figure 3.3b). The impregnated FRP sheet was then lifted and placed onto the epoxy coated glulam beam (Figure 3.3c). Rib rollers were used to remove any air bubbles and improve the bond between the wood and subsequent FRP sheets. Specimens were regularly checked during the first few hours of curing to ensure no air bubbles were forming and that the polymer matrix was setting properly (Figure 3.3d).

(a) Coating the glulam beam (b) Saturating the FRP fabric

(c) Application of the FRP (d) Curing

Figure 3.3 - Application Procedure for the FRP Sheets

3.3.2 Reinforcement Configurations – Stage 1

A total of nine 69 mm x 100 mm x 1355 mm (i.e., [100] beams) 20f-EX glulam beams were tested to failure under static four-point bending. In stage 1, four different schemes focusing on tensile reinforcement, specifically simple and U-shaped tension using unidirectional GFRP, were investigated. Figure 3.4 shows a side and cross-sectional view of the four reinforcement schemes considered in stage 1. Schemes 1 and 2 (Figure 3.4a) consist of two and four layers of unidirectional GFRP applied on the tension face of the glulam beam, respectively. Schemes 3 and 4 (Figure 3.4b) expand on the simple tension configurations of schemes 1 and 2 by extending the unidirectional GFRP reinforcement applied solely to the tension face up to the mid-depth of the beam. The difference between schemes 3 and 4 are the number of layers, where scheme 3 had two layers and scheme 4 had four layers of U-shape reinforcement. The cross-sections describing the different reinforcement schemes displayed in this chapter show a gap between the FRP and the wood to better differentiate between the two materials and to clearly show the location of the strain gauges.

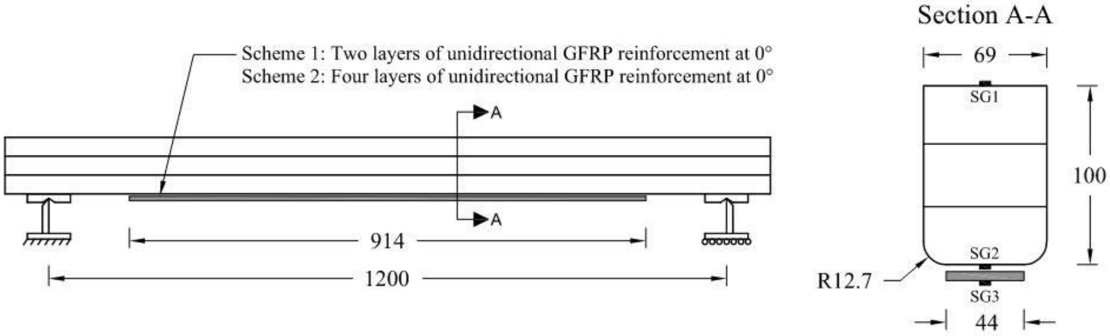

(a) Reinforcement schemes 1 and 2

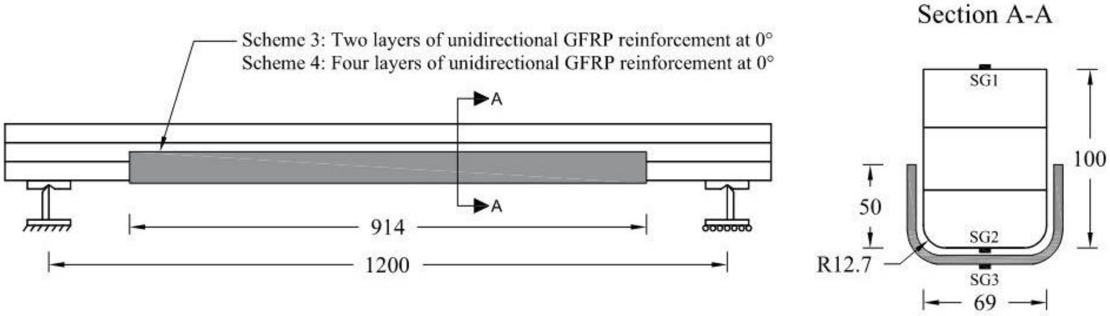

(b) Reinforcement schemes 3 and 4

Figure 3.4 - Reinforcement Schemes 1 Through 4

Strain gauges were instrumented at midspan of each reinforced bending specimen, measuring the wood compressive strain, wood tensile strain and FRP tensile strain. The strain gauges located on the glulam beam were applied prior to the application of the reinforcement, while the gauge measuring the tensile strain of the FRP was applied once the reinforcement had hardened. A pair of specimens were tested for each reinforcement configuration and thickness, with the addition of a third specimen tested having the two layers of unidirectional GFRP along the tensile face (i.e., reinforcement scheme 1).

3.3.3 Reinforcement Configurations – Stage 2

A total of twelve 69 x 100 x 1355 mm^3 (i.e., [100] beams) and four 69 x 160 x 2280 mm^3 (i.e., [160] beams) 20f-EX glulam beams were tested to failure under static four-point bending loads. The addition of shear reinforcement in the form of partial or full confinement was investigated in stage 2. Reinforcement schemes 5 and 6 consisted of unidirectional GFRP reinforcement applied to the tensile face of the beams along with 50.8 mm wide GFRP hoops applied transversely confining the beam and ends of the simple tension reinforcement (Figure 3.5). The pair of reinforcement schemes are identical with the sole difference being the type of fabric used for the hoops. Unidirectional hoops were chosen for reinforcement scheme 5 (Figure 3.5a), whereas bidirectional hoops were used in reinforcement scheme 6 (Figure 3.5b). It is important to note that the comparison between different hoop fabrics was conducted on beams having both two and four layers of unidirectional simple tension reinforcement. Both variations are depicted in Figure 3.5a and Figure 3.5b, with the note pointing to the longitudinal reinforcement.

Reinforcement schemes 7 and 8 investigated the effect of fully confining the beam longitudinally using 0/90 bidirectional fabric. The beam cross-sectional size (69 mm x 100 mm) allowed for one sheet to be applied longitudinally while also providing adequate overlap length on the compression face (Figure 3.6). Reinforcement scheme 7 (Figure 3.6a) consisted of two layers of unidirectional GFRP sheets applied as U-shape reinforcement along with two layers of 0/90° bidirectional GFRP sheets. Reinforcement scheme 8 (Figure 3.6b) consisted of four layers of 0/90° bidirectional GFRP sheets. The FRP sheets located on the compressive edge of the specimens were held together with 12.7 mm finishing nails. The specimens were left to set with the tension face facing up, with the goal of creating a better bond between the FRP and the glulam's tension fibres (i.e., avoid sagging). The compression face was frequently attended to during the first few hours of curing in order to maintain the bond between the overlapping layer and the glulam.

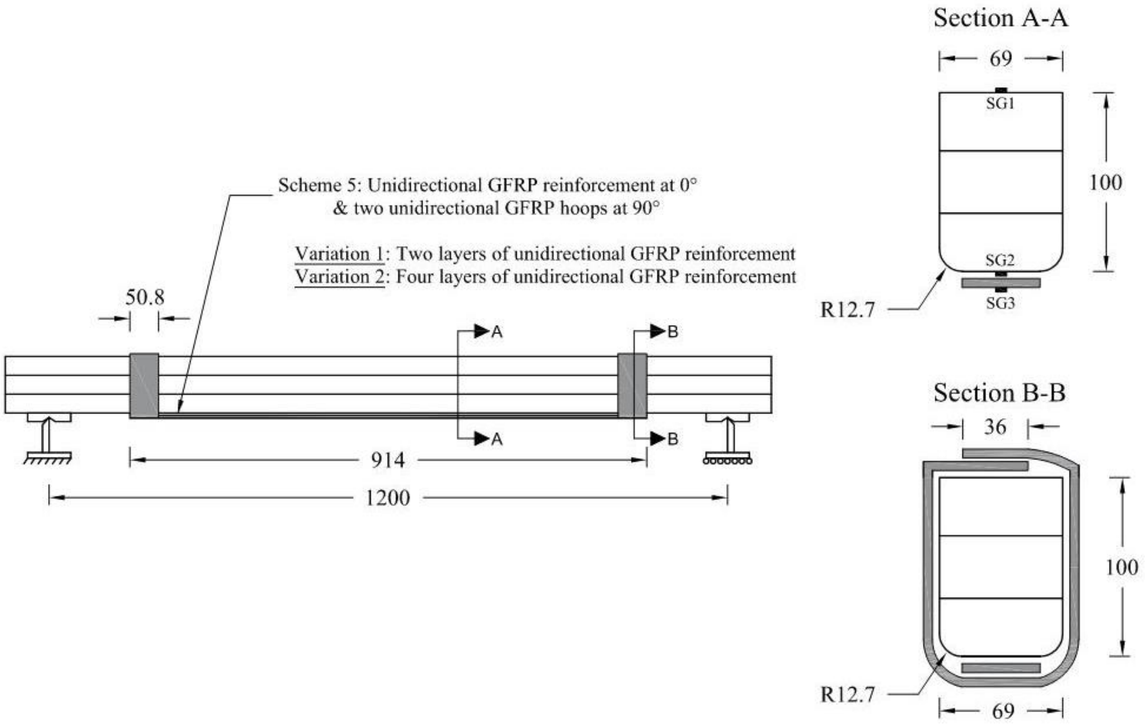

(a) Reinforcement scheme 5

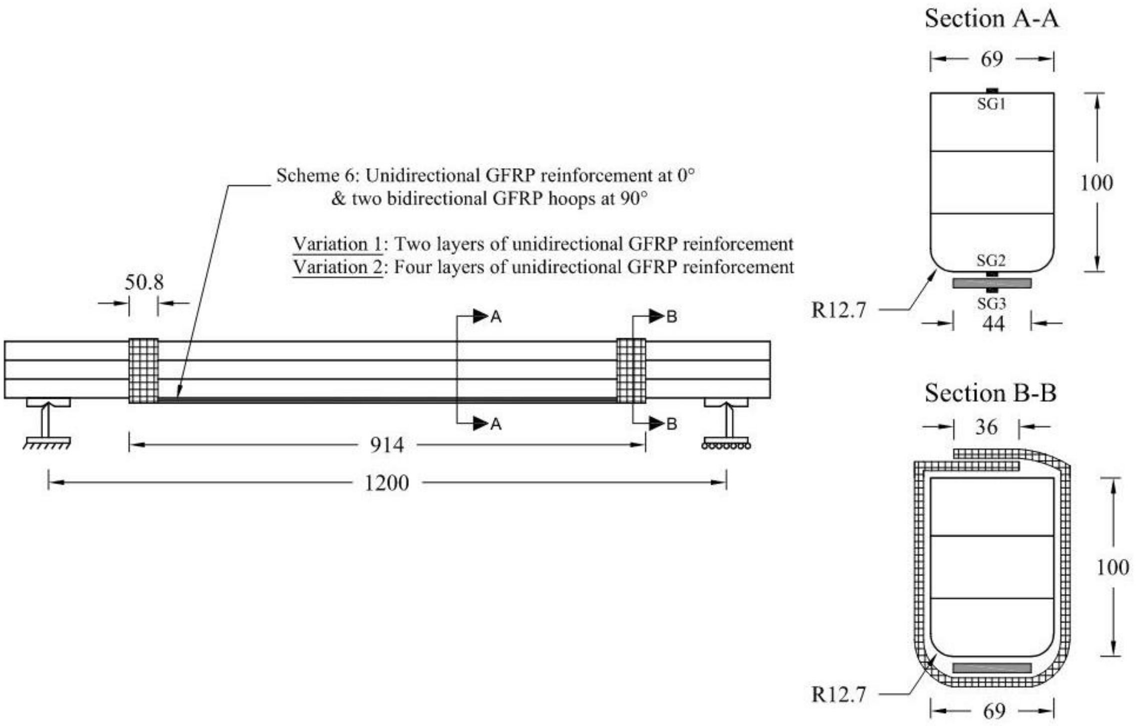

(b) Reinforcement scheme 6

Figure 3.5 - Reinforcement Schemes 5 and 6

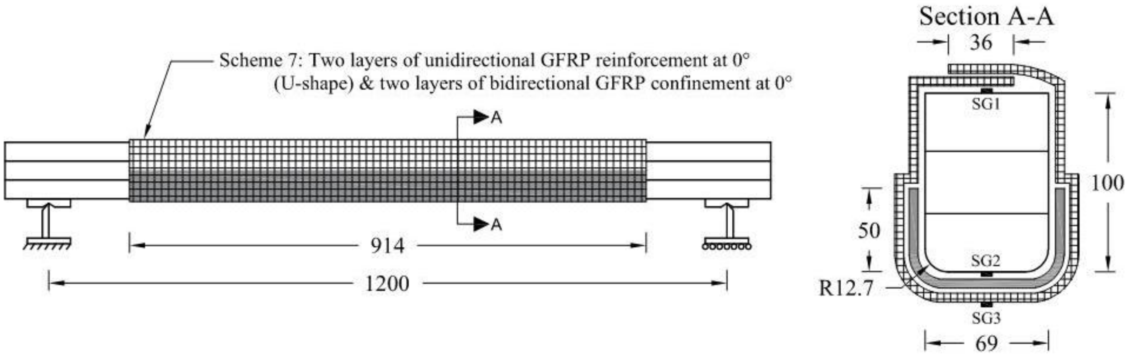

(a) Reinforcement scheme 7

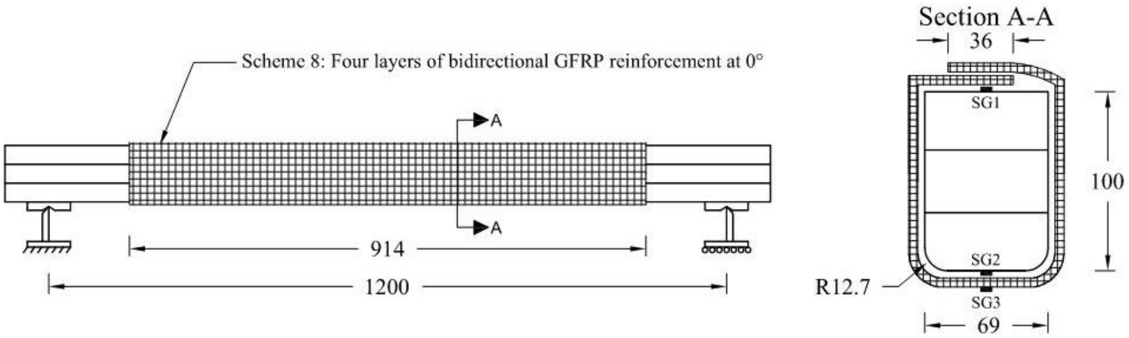

(b) Reinforcement scheme 8

Figure 3.6 - Reinforcement Schemes 7 and 8

Reinforcement schemes 9 and 10 were developed to create an arrangement that provided tension reinforcement at the midspan, all while providing anchoring and/or confinement reinforcement within the shear regions using the same FRP sheet. The purpose of these reinforcement schemes is for cases where confinement is not possible in the maximum region (e.g., main beam supporting purlins on top) such that partial confinement is provided where physically possible. Reinforcement scheme 9 (Figure 3.8a) consisted of two layers of unidirectional GFRP fabric applied as simple tension reinforcement on the tension face of the specimen with the addition of two 0/90° bidirectional GFRP tails, which are FRP sheets emulating a simple tension strip that is anchored through the help of confinement on the beam in the shear region. Figure 3.7 depicts the general fabric cut-out shape used to provide anchoring to the GFRP tails.

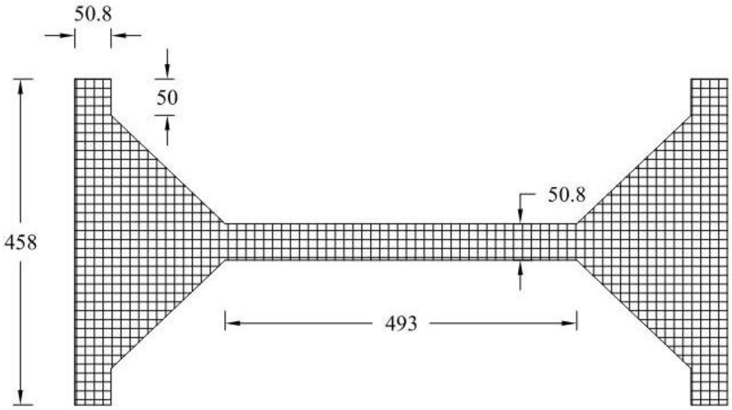

Figure 3.7 - GFRP Fabric Cutout for R9 and R10

The pre-cut GFRP sheets propagated from the tension face up to the compression face of the beam, including overlapping of the reinforcement on the compression face to prevent premature debonding of the tension reinforcement. Reinforcement scheme 10 (Figure 3.8b) consisted of four layers of 0/90° bidirectional GFRP sheets (Figure 3.7) applied such that the overlapping tabs would alternate sides and provide a more symmetrical cross-section.

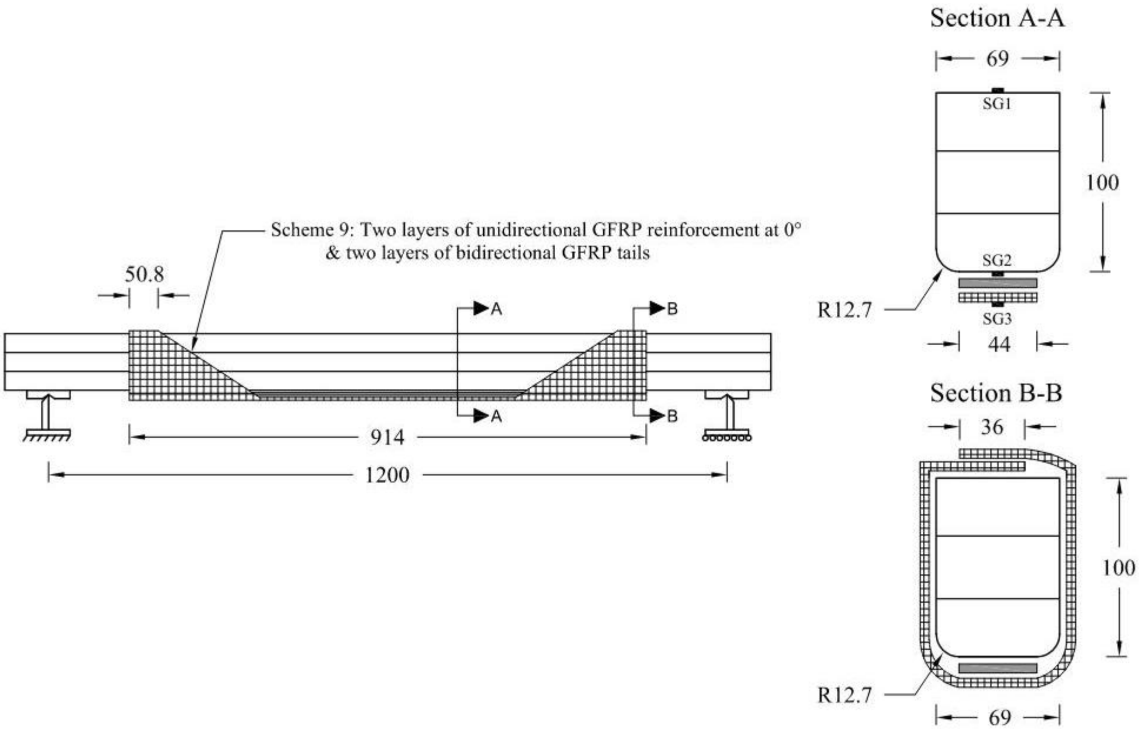

(a) Reinforcement scheme 9

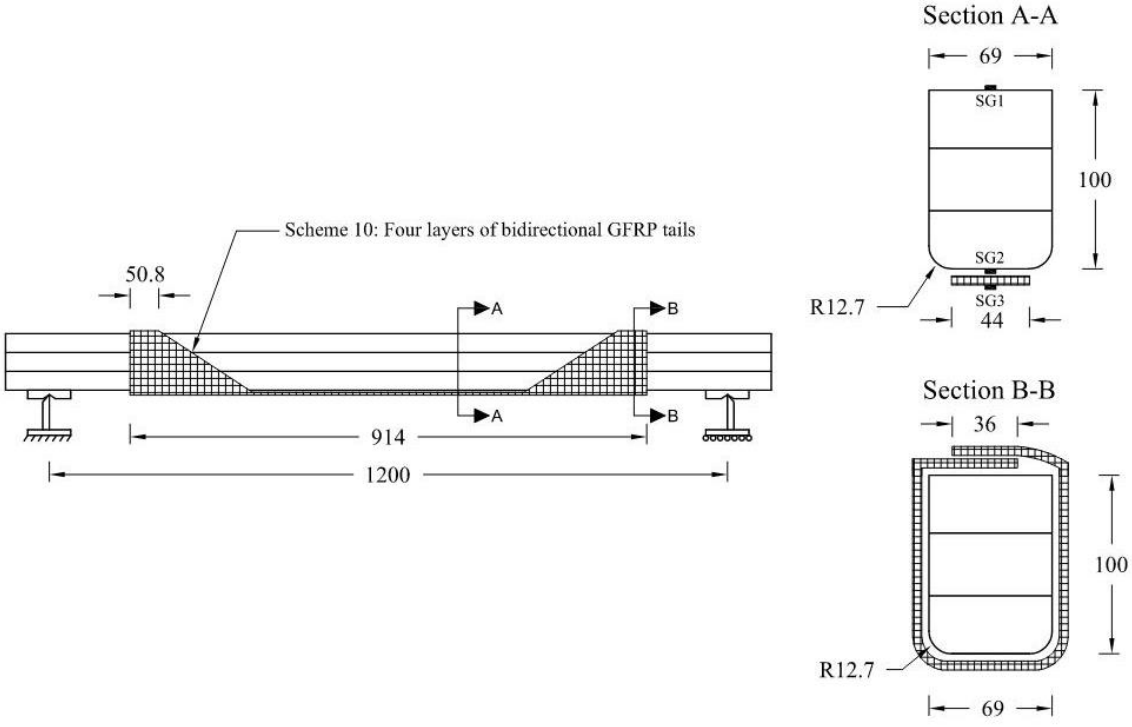

(b) Reinforcement scheme 10

Figure 3.8 - Reinforcement Schemes 9 and 10

Reinforcement schemes 11 and 12 were established for the 69 x 160 x 2280 mm^3 beams. Reinforcement scheme 11 consisted of three layers of unidirectional GFRP sheets applied longitudinally on the tension face of the specimen and four 76.2 mm wide bidirectional GFRP hoops applied transversely confining the beam and the ends of the simple tension reinforcement (Figure 3.9). Scheme 11 was developed to compare the performance of the unidirectional GFRP sheets with transverse hoops, as seen in reinforcement scheme 6 for the [100] beams, on the deeper [160] beams. Due to the longer span associated with the deeper beams, the addition of two extra hoops along with an increased thickness (76.2 mm vs. 50.2 mm) was provided to further enhance the performance.

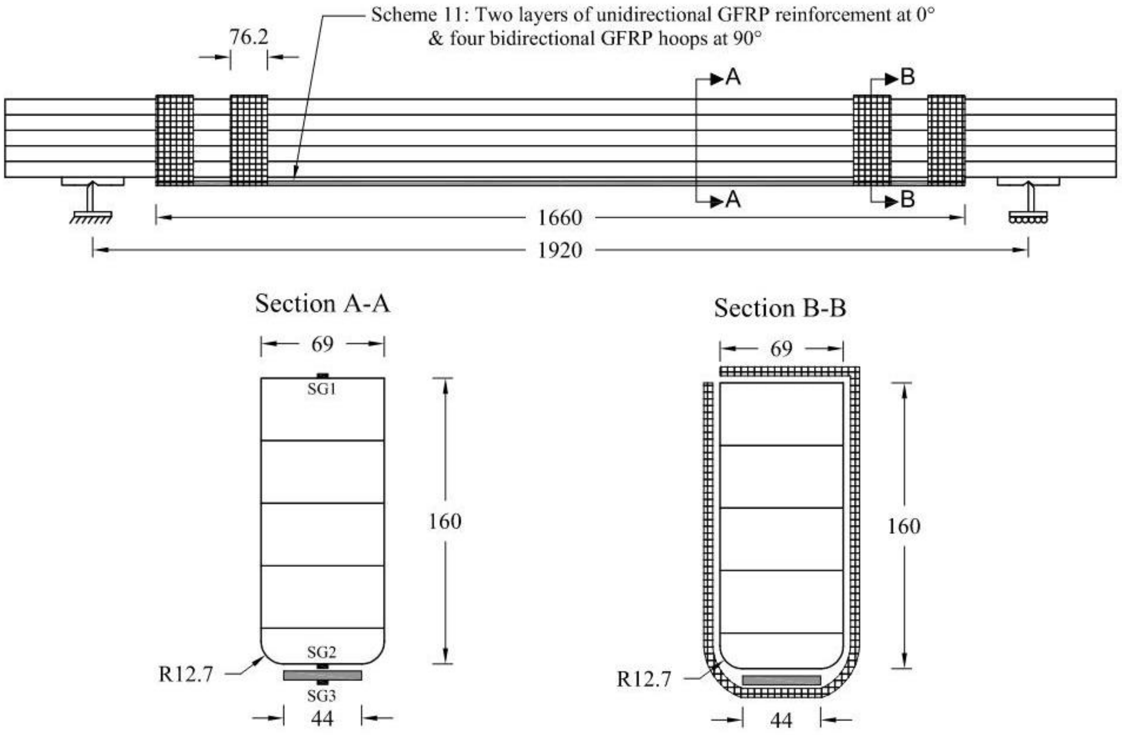

Figure 3.9 - Reinforcement Scheme 11

Reinforcement scheme 12 (Figure 3.10a) is identical to scheme 10 but amplified to six bidirectional GFRP tails to accommodate the larger beam cross-section and length. To avoid an unnecessary amount of FRP fabric on the compression face (i.e., where the fabric overlapped), only one side of the sheet contained the tab that would rest on the compression face and consecutive sheets would be applied from opposite sides to ensure an even bond. Figure 3.10a depicts the GFRP cutout for the larger [160] beams.

The 69 x 160 x 2280 mm^3 beams were also set to cure with the tension face pointing up and the areas containing FRP on the compression face were joined together using rib rollers and rested directly on the sawhorses to adequately bond the sheet to the glulam.

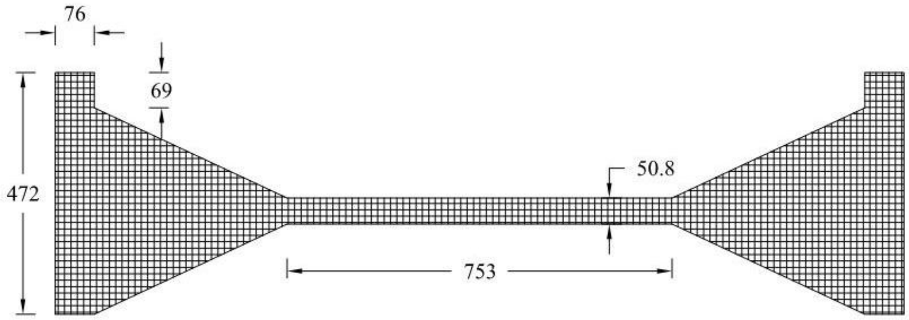

(a) GFRP Fabric Cutout for R12

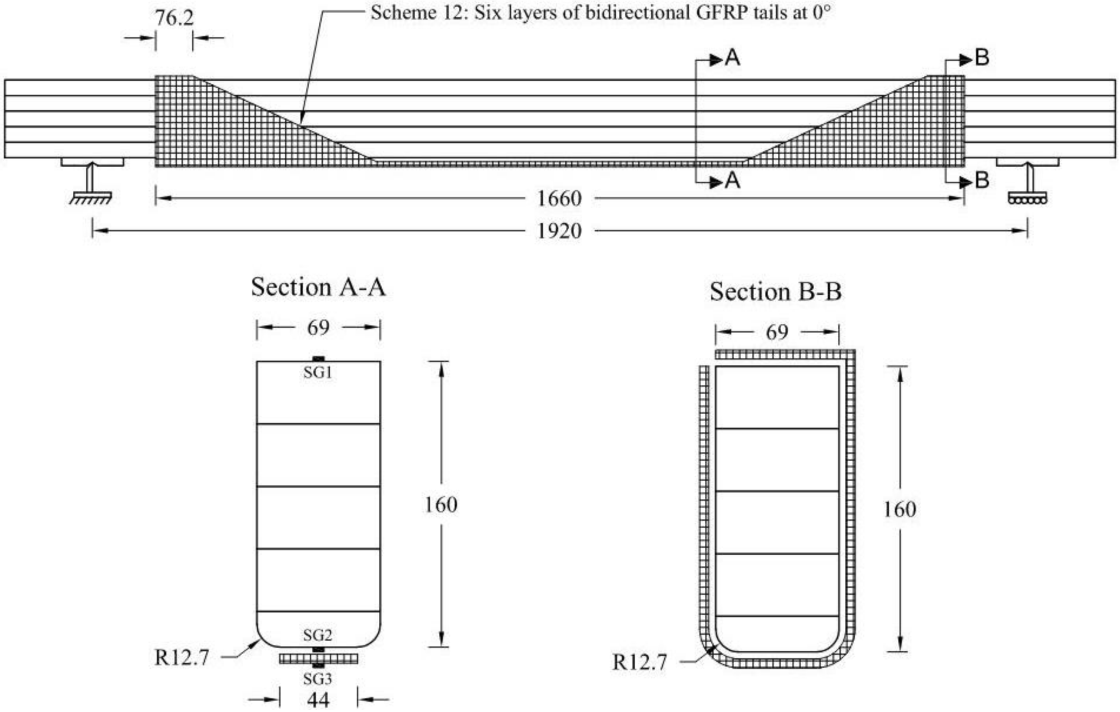

(b) Reinforcement scheme 12

Figure 3.10 - Reinforcement Scheme 12

3.4 Summary of Test Matrix

The summary of the thirty tested glulam specimens is provided in Table 3.2. The naming convention for each glulam beam is **Y&−#**; where “**Y**” refers to the specimen type (**U** for unreinforced and **R** for reinforced), "**&**" represents the reinforcement scheme number (when applicable) and "**#**" represents the specimen number. The depth of the specimen is added in square brackets following the specimen's name to differentiate between [100] beams (69 mm x 100 mm x 1,355 mm) and [160] beams (69 mm x 160 mm x 2,280 mm). The specimen's reinforcement configuration is labelled using a letter denoting the arrangement (**S** for simple tension reinforcement, **U** for U-shaped reinforcement, **H** for hoop reinforcement in the shear region, **C** for full confinement reinforcement, and **TA** for tension reinforcement with confinement anchoring in the shear region), followed by a square bracket containing the fabric fibre orientation. The subscript following the bracket represents the number of layers used in that specific arrangement. The addition of multiple letters represents not only the addition of reinforcement but also the order of application.

Table 3.2 - Experimental Test Matrix Summary

Stage	Specimen Type	Specimen Name	FRP Reinforcement Configuration
1	Unreinforced	U-01 − U-05	-
	Reinforced	R1-01 − R1-03; [100]	$S[0]_2$
		R2-01, R2-02; [100]	$S[0]_4$
		R3-01, R3-02; [100]	$U[0]_2$
		R4-01, R4-02; [100]	$U[0]_4$
2	Reinforced	R5-01; [100]	$S[0]_2$ $H[0]_2$
		R5-02; [100]	$S[0]_4$ $H[0]_2$
		R6-01; [100]	$S[0]_2$ $H[0/90]_2$
		R6-02; [100]	$S[0]_4$ $H[0/90]_2$
		R7-01, R7-02; [100]	$U[0]_2$ $C[0/90]_2$
		R8-01, R8-02; [100]	$C[0/90]_4$
		R9-01, R9-02; [100]	$S[0]_2$ $TA[0/90]_2$
		R10-01, R10-02; [100]	$TA[0/90]_4$
		R11-01, R11-02; [160]	$S[0]_3$ $H[0/90]_2$
		R12-01, R12-02; [160]	$TA[0/90]_6$

3.5 Test Setup and Instrumentation

3.5.1 Material Properties – Component Test

The moment-curvature analysis requires the input of uniaxial stress-strain relationships for the wood and FRP material. The wood tension and compression properties were obtained from clear sample test results completed in accordance with ASTM D143 "Standard Test Methods for Small Clear Specimens of Timber” (ASTM, 2021a). A total of six compression coupons were prepared from extra material using a guided table saw (Figure 3.11a), with final dimensions of 50.8 mm x 50.8 mm x 203 mm. A 500 kN hydraulic test frame loaded the coupons in compression and recorded the applied force (Figure 3.12a). The displacement was recorded using a linear variable displacement transducer (LVDT) and used to calculate the relative change in length (i.e., strain).

(a) Compression

(b) Tension

Figure 3.11 - Wood Coupons

The six wood tension coupons were prepared using a bandsaw outlining the general shape of the specimen and finished on a belt sander to smoothen any irregularities (Figure 3.11b), with a reduced cross section area of 5 mm x 10 mm (ASTM, 2021a). A 10 kN electromechanical frame pulled the coupons until failure and recorded the applied force (Figure 3.12b). The displacement was calculated using a 50.8 mm extensometer placed at midspan and used to calculate the relative change in length as it is loaded to failure.

(a) Compression (b) Tension

Figure 3.12 - Wood Coupon Tests

The FRP tension properties were obtained from coupon test results completed in accordance with ASTM D3039 “Standard Test Method for Tensile Properties of Polymer Matrix Composite Materials” (ASTM, 2014). The FRP coupons were prepared in larger flat sheets and later cut to size once the composite had cured (Figure 3.13a). The coupons were held between aluminum tabs (Figure 3.13) and designed to extend beyond the grips to avoid stress concentrations and unwanted failure modes. All FRP coupons were 25.4 mm wide, and 406 mm long, with varying thicknesses based on the type of layup investigated (ASTM, 2014). A total of six coupons were tested for each of the layups investigated.

(a) Coupon (b) Curing of aluminium tabs

Figure 3.13 - FRP Coupons

The FRP coupons were pulled to failure using a 100 kN hydraulic load frame that recorded the applied force and actuator displacement. A 50.8 mm extensometer was placed at the midspan of the specimens for the beginning of every test and removed before ultimate failure to avoid damage. The general test configuration to determine the FRP stress-strain relationship is shown in Figure 3.14.

Figure 3.14 - FRP Coupon Test

3.5.2 Full Scale Four-Point Bending Tests

A total of five unretrofitted and twenty-five retrofitted glulam beams were tested statically under four-point bending in accordance with ASTM D198-21a "Standard Test Methods of Static Tests of Lumber in Structural Sizes" (ASTM, 2021b). As per the standard, hardwood load-bearing blocks having a radius larger than two times the beam depths were fabricated, and lateral support was provided at the supports even though the depth-to-width ratio never exceed three. A span-to-depth (a/d) ratio of four for both beam sizes was selected in accordance with the ASTM standard (ASTM, 2021b). Simply supported boundary conditions were provided through the use of an anchored pin and roller system (Figure 3.15).

A 500 kN hydraulic load frame with a load cell connected to the actuator was used to load all thirty bending tests. The four 69 x 160 x 2,280 mm^3 glulam beams were pre-loaded to record the bending stiffness prior to the application of the FRP. The unreinforced and reinforced beams were loaded in displacement control until failure, with loading protocols ranging from 3.5 mm/min to 10 mm/min to ensure ultimate failure within five and ten minutes (ASTM, 2021b). During the tests, a data acquisition system recorded the data at a sampling rate of 15 samples per second. The applied load, midspan deflection, and shear free deflection were measured using the frame load cell, a linear position transducer (string pot) and an LVDT in the shear free region, respectively. Additionally, the wood and FRP strains were recorded at midspan using strain gauges. The location of the strain gauges relative to the beams cross-section is visually displayed in Subsection 3.3.2 and 3.3.3.

Prior to testing, weight and moisture readings were taken and documented along with the visual observation of the specimens. Documentation and photographs of the failed specimens were also recorded. Figure 3.15 shows a representation of the actual test setup with all of the instrumentation.

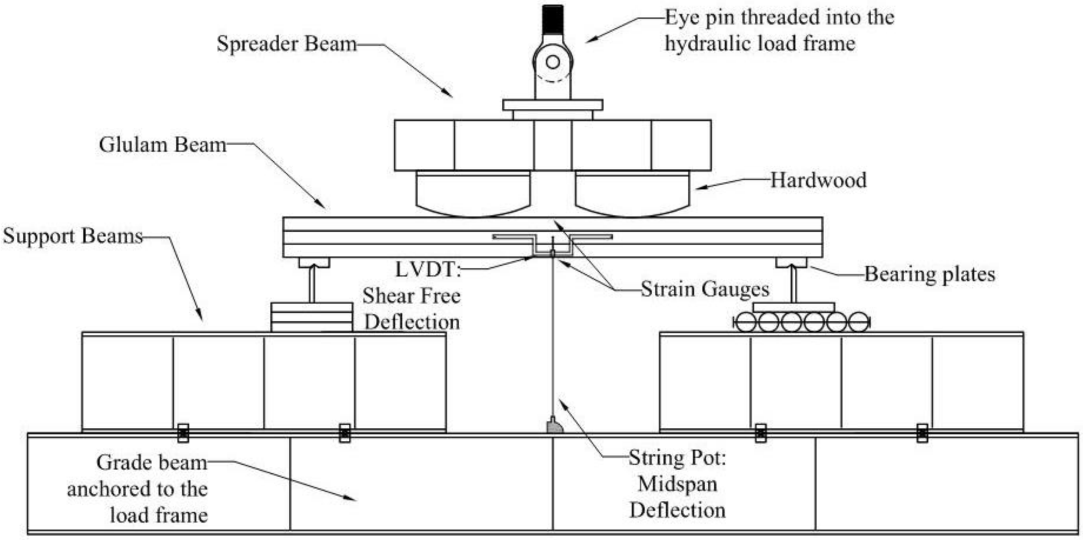

Figure 3.15 - Static Bending Test Setup

Chapter 4

Experimental Results

4.1 General

The experimental results from the static uniaxial component and four-point bending tests are presented in this chapter. A total of six glulam compression coupons, six glulam tension coupons, and thirty-six FRP tension coupons were tested to failure. The flexural test matrix presented in Table 3.2 summarizes the experimental project conducted to determine the flexural behaviour of five unreinforced and twenty-five reinforced 20f-EX glulam beams.

4.2 Component Tests

4.2.1 Wood Compression Coupons

Representative failure modes for the wood compression coupons are shown in Figure 4.1, where the specimens were observed to initially fail due to fibre crushing (Figure 4.1a) with some exhibiting wedge splitting once the yielding strain was exceeded (Figure 4.1b). A representative stress-strain curve for the compression coupon tests is shown in Figure 4.2

(a) Crushing (b) Wedge splitting

Figure 4.1 - Representative Compression Failures of Wood Coupons

From the stress-strain curve shown in Figure 4.2a, it can be seen that the wood behaves linearly until the wood fibres begin to crush, with virtually no visible damage to the specimen at the yield load (Figure 4.2). The wood fibres began to fail once the maximum load was attained, resulting in a decrease in resistance at greater strains. The stress-strain curve for wood in compression can be idealized with a bi-linear curve, which will later be discussed in Chapter 5. It should be noted that the compression coupon tests were displacement controlled at a rate of 0.67 mm/min and terminated once the stress dropped below 75% of the maximum stress or once the strain exceeded 0.02 mm/mm. The compression coupon strain was obtained by using the LVDT displacement (mm) of the cross-head divided by the initial coupon length (mm). The stress-strain curves for all compression coupon specimens can be found in Appendix A.

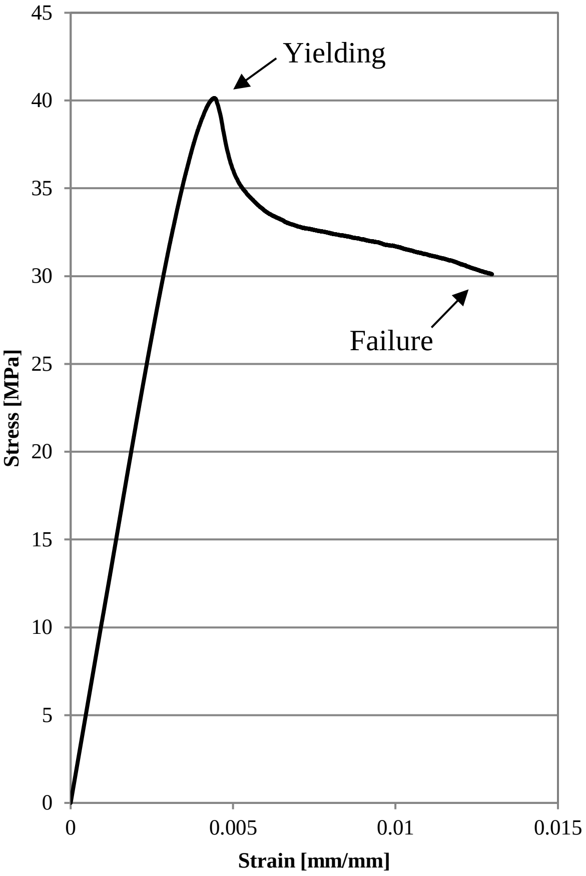

(b) Yielding

(a) Stress-strain behaviour

(c) Failure

Figure 4.2 - Compression Coupon Test

The static test results defining the average material properties of the compression coupons are shown in Table 4.1. The high variation in the failure strain (i.e., ε_{cu}) is due to the fact that the failure criterion was defined as 75% of the yield strength or the 0.02 mm/mm strain limit, whichever occurred first. The 0.02 mm/mm limit corresponded to a point where the specimen could no longer be loaded safely due to torsional forces being applied on the actuator. The material behaved similarly for all the specimens tested and the results show that the difference between ultimate stresses, regardless of the termination condition, are comparable. This is due to the plateau behaviour following the initial loss in strength (Figure 4.2a), showing that the ultimate stress remained within the same range once the initial decrease in stress occurred.

Table 4.1 - Static Test Results of Compression Coupons

Sample Number	MOE[a] (MPa)	f_{cy}[b] (MPa)	ε_{cy}[c] x 10^{-4} (mm/mm)	f_{cu}[d] (MPa)	ε_{cu}[e] x 10^{-4} (mm/mm)
1	10,722	40.1	37.4	30.1	130.0
2	10,467	40.3	38.5	30.0	100.0
3	11,061	41.7	37.7	31.3	142.0
4	10,495	39.1	37.3	30.0	200.0
5	10,717	41.1	38.8	31.7	200.0
6	10,538	39.9	37.9	29.9	163.0
Average	10,667	40.4	37.9	31.2	155.8
Std. Dev	203	0.8	0.4	1.3	36.4
COV	0.02	0.02	0.01	0.04	0.23

[a] Compression modulus of elasticity

[b] Compression yield strength

[c] Compression yield strain

[d] Ultimate compressive strength

[e] Ultimate compressive strain

4.2.2 Wood Tension Coupons

A representative failure mode and corresponding stress-strain curve for the tension coupon tests are shown in Figure 4.3. The required tensile failure occurring within the reduced midspan region was observed for all seven coupons tested (Figure 4.3a). From the stress-strain curve shown in Figure 4.3b, the wood subjected to uniaxial tensile loads behaves linearly up to an ultimate stress and strain.

The tension coupon tests were loaded in displacement control with an actuator head displacement of 1 mm/min and terminated once the fibres had ruptured. The static test results defining the average material properties of the tension coupons are shown in Table 4.2. The stress-strain curves for all tension coupon specimens can be found in Appendix B.

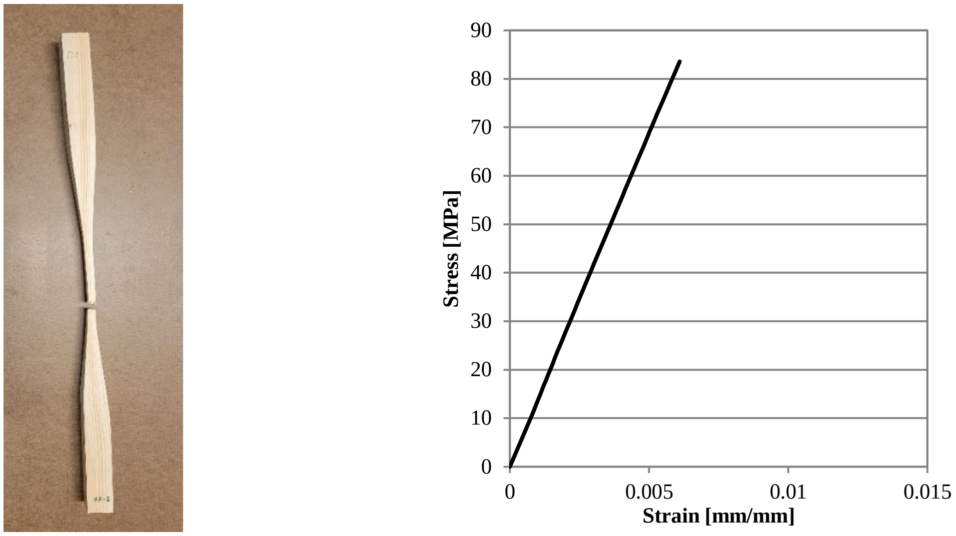

(a) Failure (b) Stress-strain behaviour

Figure 4.3 - Tension Coupon Test

Table 4.2 - Static Test Results of Tension Coupons

Sample Number	MOE^{a} (MPa)	f_{tu}^{b} (MPa)	$\varepsilon_{tu}^{c} \times 10^{-4}$ (mm/mm)
1	13,811	83.6	62.0
2	13,044	75.9	58.0
3	14,510	119.8	87.0
4	12,416	88.5	69.0
5	12,679	96.6	72.0
6	13,266	71.6	56.0
Average	13,288	89.3	67.0
Std. Dev	702	15.9	10.5
COV	0.05	0.18	0.16

[a] Tension modulus of elasticity

[b] Ultimate tensile strength

[c] Ultimate tensile strain

4.2.3 FRP Tension Coupons

The FRP material properties for each lay-up considered in the research program were obtained through tests completed on 406 mm long coupons. Two types of GFRP reinforcement were used and the representative failures can be seen in Figure 4.4. The unidirectional fabric having the majority of fibres running longitudinally from the grips exhibited tensile rupturing failures with the fibres oriented perpendicularly to the span providing little to no resistance (Figure 4.4a). The bidirectional fabric, having an even distribution of fibres placed both along and perpendicularly to the span, exhibited more of a fabric delamination (Figure 4.4b) failure with portions of the reinforcement sheets dislodging from the specimens at high strains.

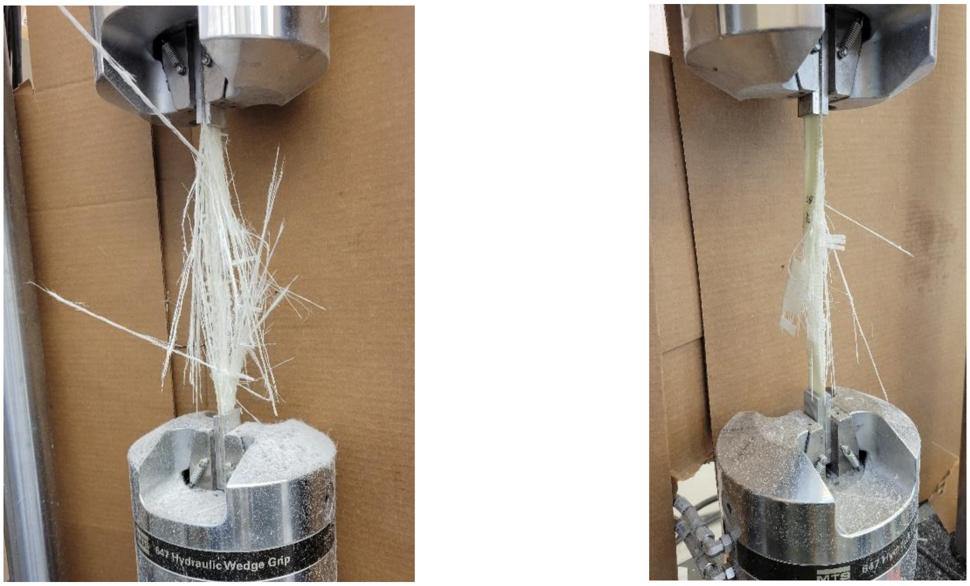

(a) Unidirectional fabric (b) Bidirectional fabric

Figure 4.4 - FRP Coupon Failure

Figure 4.5 shows representative stress-strain curves obtained experimentally for the six lay-ups investigated with the results tabulated in Table 4.3. The configurations made up entirely of unidirectional fibres behaved linearly up to an ultimate stress and strain which caused sudden tensile fibre ruptures.

The four and six bidirectional lay-ups behaved similarly, with a higher initial stiffness that slightly tapered away as the strain increased. The unidirectional fabric was shown to have higher stiffnesses when compared to the bidirectional fabric, with differences found within individual groups (i.e., unidirectional vs. bidirectional) that can be attributed to the amount of epoxy used when saturating the GFRP fabrics. The stress-strain curves detailing the ultimate strength and strains of each lay-up along with their associated standard deviation and coefficient of variation is provided in Appendix C.

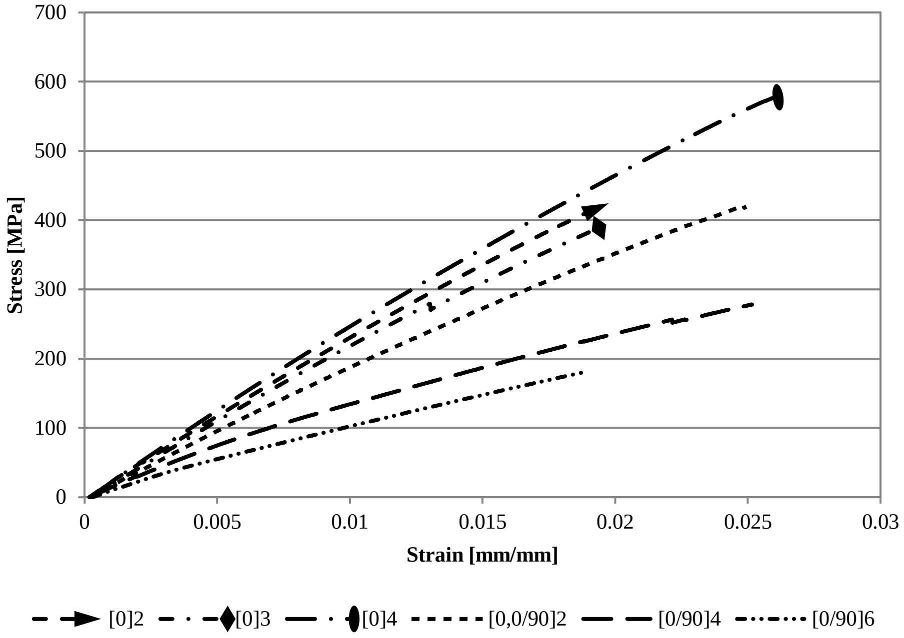

Figure 4.5 - Representative Stress-Strain Curves for FRP Coupons

Table 4.3 - Static Test Results of FRP Tension Coupons

Lay-up Configuration		MOE[a] (MPa)	f_{FRP}[b] (MPa)	ε_{FRP}[c] x 10^{-4} (mm/mm)
$[0]_2$	Average	23,507	434.6	204.0
	Std. Dev	730	14.8	8.0
	COV	0.03	0.03	0.04
$[0]_3$	Average	23,097	408.9	226.0
	Std. Dev	243	33.8	27.0
	COV	0.01	0.08	0.12
$[0]_4$	Average	25,146	561.0	255.0
	Std. Dev	821	19.9	7.0
	COV	0.03	0.04	0.03
$[0]_2\,[0/90]_2$	Average	17,361	428.2	246.0
	Std. Dev	715	31.4	14.0
	COV	0.04	0.07	0.06
$[0/90]_4$	Average	11,969	261.8	261.0
	Std. Dev	645	14.6	20.0
	COV	0.05	0.06	0.08
$[0/90]_6$	Average	9,910	190.9	221.0
	Std. Dev	392	8.3	29.0
	COV	0.04	0.04	0.13

[a] Tension modulus of elasticity

[b] Ultimate tensile strength

[c] Ultimate tensile strain

4.3 Characterization of Failure Modes for the Beams

The following section documents the behaviour and failure modes of the unreinforced and FRP reinforced glulam beams. Details of the general force-displacement plots along with the terminology used to describe the failure progression are initially discussed, followed by a thorough breakdown of the beam failures based on their reinforcement scheme and size.

The idealized resistance curve is shown in Figure 4.6, where the bending members behave elastically up to an ultimate load (P_{max}) and displacement ($\Delta_{P,max}$), referred to as maximum or peak resistance. Once the peak load is attained and the specimen experiences its first failure, an increasing or plateauing post-peak behaviour is observed. Depending on the reinforcement configurations and the quality of the member (i.e., presence of knots, direction of the grain), more than one peak can be experienced within the loading stage. The reported bending stiffness (K) is an average of the stiffnesses calculated using various instrumentation measuring the displacements and strains during the initial elastic portion of the resistance curve. The displacement-controlled loading protocol was used throughout the entire sample and loaded the bending members to failure. A 50% decrease from the maximum load was established as the ultimate failure by the author and is consistent with (D. N. Lacroix, 2017b). The major failure modes observed during the tests were simple tension, splintering tension, horizontal shear, and FRP delamination/slip. A simple tension failure is described as a direct rupture in the extreme wood tensile fibres. A splintering tension failure occurs when multiple slight tension failures occur within a high-bending stress region causing a staggering break in the tensile region of the bending specimen. A horizontal shear failure is described by the delamination or sliding of the compression and tension laminations along the length of the shear region. Reinforcement delamination or slip failure is when the bond between the wood and the FRP fails, ultimately inhibiting the composite action between both materials.

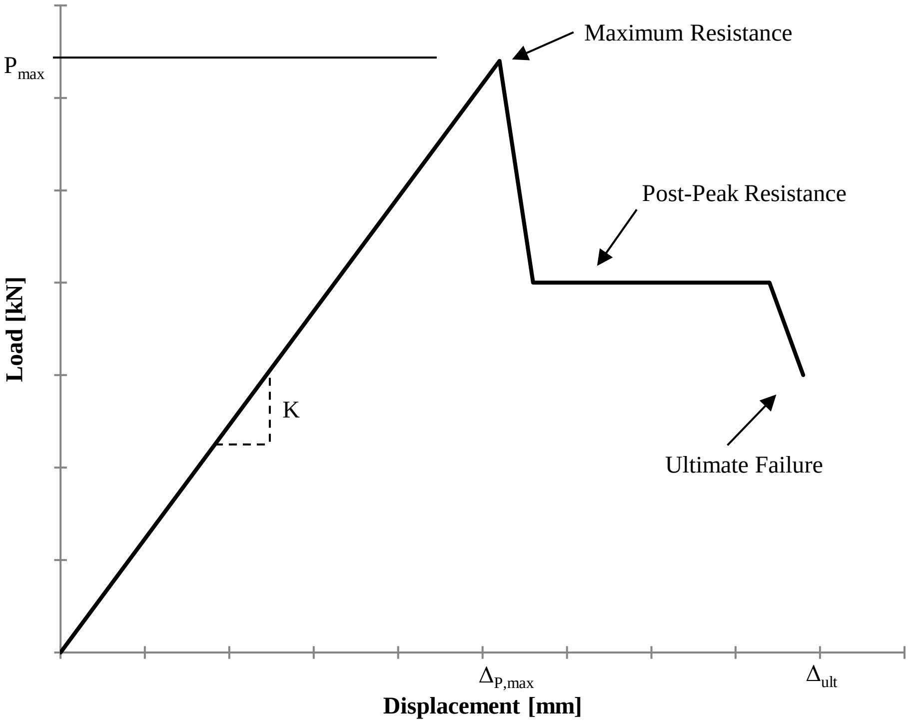

Figure 4.6 - Idealized Resistance Curve and Terminology

4.3.1 Unreinforced Glulam Beams

The five unreinforced glulam beams subjected to four-point bending loads all failed in tension. Specimens U-02 and U-05 experienced splintering tension failures, causing a ragged tension laminate containing wood fibres delaminating away from the surface (Figure 4.7). Specimen U-02 (Figure 4.7a) developed slight corner delamination propagating through the high-bending stress region which amplified with increasing load and finally reduced enough cross-sectional area to cause the specimen to fail. Figure 4.7b depicts the initial splintering failure of specimen U-05, which initiated on the tensile laminate and resulted in a ragged surface that was also amplified with increasing load until failure occurred within the high-bending stress region. Specimen U-04 failed in a brittle fashion due to cross-grain tension (Figure 4.8). Figure 4.8a and Figure 4.8b depict the specimen before and after the tensile failure, respectively. A detailed breakdown of the failure progression of unreinforced beams can be found in Appendix D.

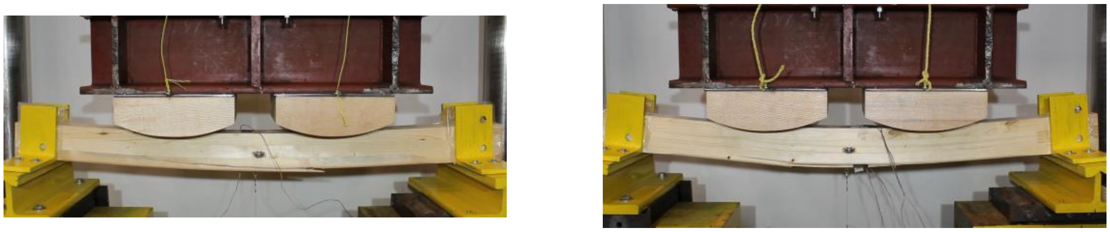

(a) U-02 (b) U-05

Figure 4.7 - Splintering Tension Failure of Unreinforced Beams

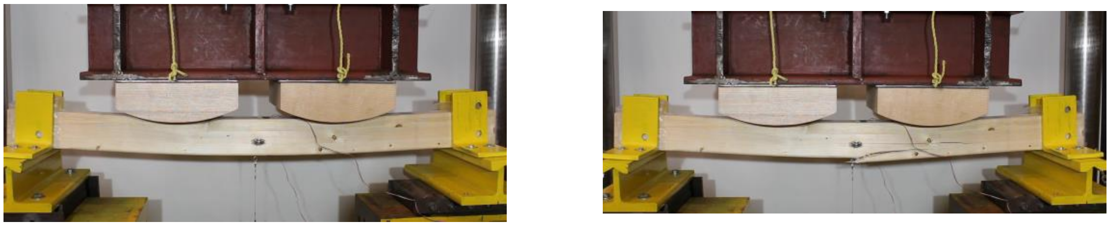

(a) U-04 (b) U-04

Figure 4.8 - Cross-grain Tension Failure of Unreinforced Beams

Prior to the termination of the test (i.e., before the ultimate tension failure), some compression folds were observed within the midspan of the beams (Figure 4.9). Figure 4.9a depicts a compression fold located directly above the tension failure. Figure 4.9b demonstrates the compression fold forming around a knot found near the compression face of specimen U-04.

(a) U-03

(b) U-04

Figure 4.9 - Compression Folds on Unreinforced Beams

Specimens U-01 and U-03 experienced simple tension failures that initiated from defects found in the high-bending stress region of the beams (Figure 4.10). Both tests were terminated once the initial failure occurred. Figure 4.10a and Figure 4.10c depict the simple tension failure of specimen U-01 which occurred at midspan. Similarly, Figure 4.10b and Figure 4.10d display the simple tension failure of specimen U-03, where both figures represent the front and back side faces of the failed specimen. The tension failure resulted in the separation of the tension laminate located within the high-bending stress region.

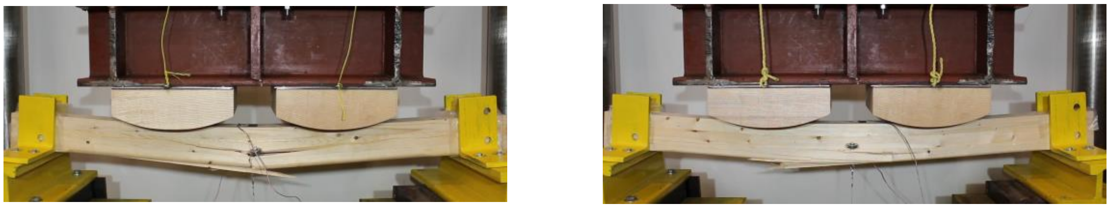

(a) U-01

(b) U-03

(c) Close-up of damage for U-01

(d) Close-up of damage for U-03

Figure 4.10 - Simple Tension Failure of Unreinforced Beams

4.3.2 Reinforced Glulam Beams

All specimens tested in stage 1 failed in shear. R1 beams experienced both horizontal shear and stress concentration failures. The horizontal shear failures, as shown in Figure 4.11 for the R1-02 and R1-03 specimens, initiated within the shear region and propagated through to the support faces. In both cases, the load decreased more than 50% from the maximum was recorded which terminated the tests.

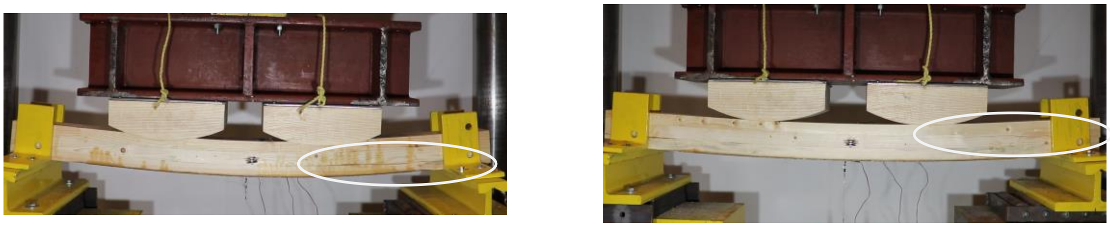

(a) R1-02 (b) R1-03

(c) Close-up of damage for R1-02 (d) Close-up of damage for R1-03

Figure 4.11 - Horizontal Shear Failures for R1 Beams

The stress concentration failure observed in specimen R1-02 occurred on the tensile face of the beam where the longitudinal reinforcement strip was terminated (Figure 4.12). The stress concentration caused perpendicular to grain tensile forces that exceeded the limit of the wood material, ultimately resulting in the propagation of failure across the length of the beam (Figure 4.12a). Figure 4.12b shows a close-up view of the failure, demonstrating the sudden rupture of wood fibres extending the width of the beam.

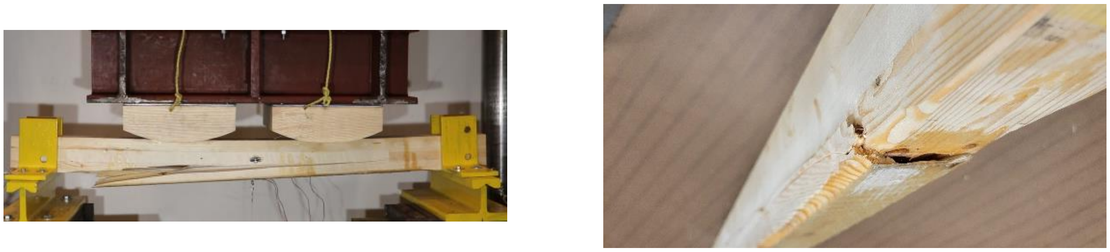

(a) R1-02 (b) Close-up of damage for R1-02

Figure 4.12 - Stress Concentration Failure for R1 Beams

A representative failure mode for reinforcement scheme 2 is shown in Figure 4.13 where a high-stress concentration located at the ends of the simple tension GFRP strips caused horizontal shear and tension perpendicular to grain stresses that failed the wood. It is important to note that in both of the specimens tested, the bond between the reinforcement and the wood remained intact, while the failure was entirely propagated throughout the wood material.

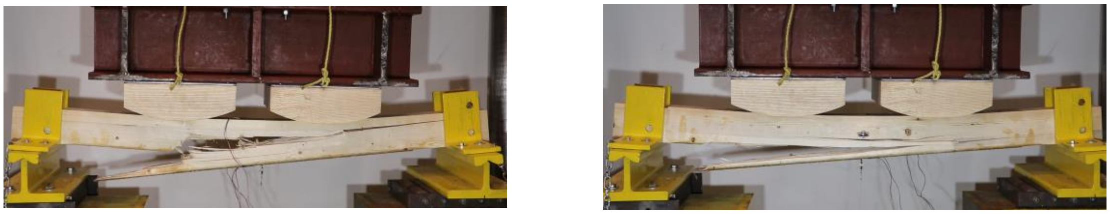

(a) R2-01 (b) R2-02

(a) Close-up of damage for R2-01 (d) Close-up of damage for R2-02

Figure 4.13 - Representative Failure Mode for R2 Beams

Figure 4.14 shows representative failure modes for reinforcement scheme 3. Only two specimens were tested, and both specimens experienced a different failure mode. R3-01 failed in horizontal shear, with the failure propagating through the support face as well as across the reinforcement located on the side faces of the beam (Figure 4.14a). The close-up of R3-01, as shown in Figure 4.14c, demonstrates an adequate bond between the wood tensile fibres and the reinforcement. The use of unidirectional fabric placed at 0° resulted in the majority of the fibres oriented along the span of the beams. In this case, the lack of fibres oriented perpendicular to the beams span resulted in little to no resistance in the transverse direction. Specimen R3-02 failed due to a stress concentration located at the end of the U-shaped reinforcement (Figure 4.14b). The partial confinement led to a brash tension failure in the tensile laminate that pushed away from the beam causing splitting within the FRP located on the side faces of the beam (Figure 4.14b). Again, from the close-up view for specimen R3-02 (Figure 4.14d), the stresses induced on the weak axis of the reinforcement caused significant damage.

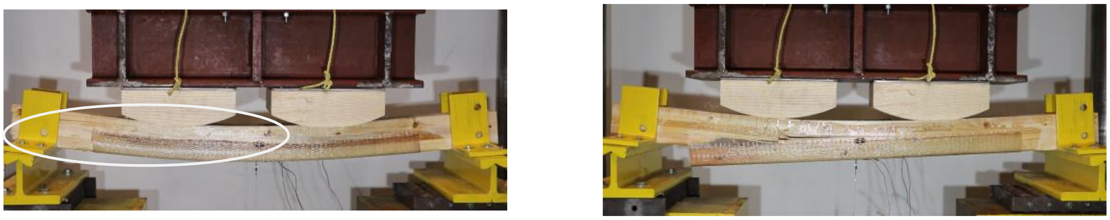

(a) R3-01 (b) R3-02

(c) Close-up of damage for R3-01 (d) Close-up of damage for R3-02

Figure 4.14 - Representative Failure Modes for R3 Beams

The representative failure mode for reinforcement scheme 4 is shown in Figure 4.15. The heavily reinforced specimens failed in a combination of horizontal shear and delamination of the reinforcement due to damage in the wood material. Figure 4.15a demonstrates the specimen at the time of failure, with the emphasis located within the left-most shear region where the GFRP delamination can be easily identified. The horizontal shear failure, which occurred simultaneously, is shown to propagate through the support face (Figure 4.15a and Figure 4.15b). An increase in load amplified the wood failures and created another horizontal shear plane directly above the original failure (Figure 4.15b).

(a) R4-01 (b) Close-up of damage for R4-01

Figure 4.15 - Representative Failure Mode for Reinforcement Scheme 4

Figure 4.16 shows the observed failure mode for reinforcement scheme 5. The addition of the GFRP hoops contained the ends of the simple tension strip and allowed for a tension failure to occur in the glulam. The initial tension failure for specimen R5-01 was located at a finger joint (FJ) located on the tensile laminate within the high-bending stress region (Figure 4.16a). The initial tension failure engaged the GFRP hoop, which is better displayed by the lighter colour circled in Figure 4.16a. The original tension failure at the FJ did not propagate across the entire bottom face of the beam. A large knot found on the tensile face of specimen R5-02 was responsible for the sudden brittle failure that occurred Figure 4.16b. The large knot created significant deviations in the grain pattern which resulted in tensile perpendicular to grain stresses that were greater than the material's capacity.


(a) R5-01

(b) R5-02

(c) Close-up of damage for R5-01

(d) Close-up of damage for R5-02

Figure 4.16 - Representative Failure Mode for Reinforcement Scheme 5

The representative failure mode for reinforcement scheme 6 is shown in Figure 4.17. The hoops contained the tension GFRP and allowed for a wood tensile failure. Specimen R6-01 failed due to cross-grain tension stresses experienced around a knot at midspan (Figure 4.17a and Figure 4.17b). The increase in load amplified the tension failure which pushed against the FRP, ultimately causing the reinforcement to de-bond from the wood and slip away from the GFRP hoops (Figure 4.17e). Contrarily, specimen R6-02 failed in simple tension at midspan in the second last tension laminate (Figure 4.17b). A close-up of the tension damage is shown in Figure 4.17d, where it is shown that the tensile failure caused horizontal shear failure planes at the intersection of the laminates (Figure 4.17d). Figure 4.17f shows the impact of the horizontal shear failures at the transverse hoop location. The lighter colour in the GFRP hoop implies the fabric was engaged and resisted the breakout force (i.e., contained the failure and prevented the debonding of the longitudinal reinforcement). Both R6 specimens were able to contain their damage within the hoops, however, the slipping of longitudinal GFRP reinforcement could not be avoided in either test.

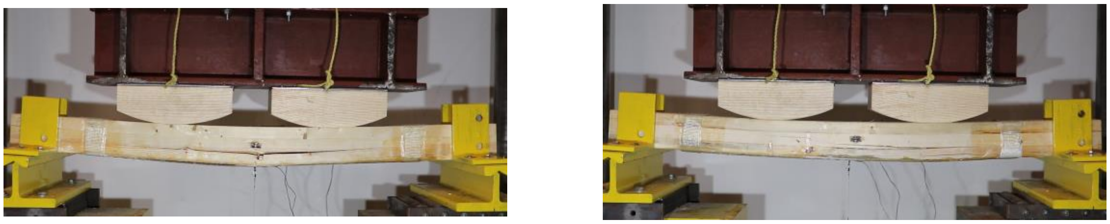

(a) R6-01 (b) R6-02

(c) Midspan tension damage for R6-01 (d) Midspan tension damage for R6-02

(e) Tension face of R6-01 (f) Shear region damage for R6-02

Figure 4.17 - Representative Failure Mode for Reinforcement Scheme 6

Figure 4.18 shows the observed failure mode for reinforcement scheme 7. R7 beams experienced early signs of FRP buckling in compression (Figure 4.18a), followed by tension failure in both the wood and FRP (Figure 4.18b). The damage for specimen R7-02 was localized to the midspan of the beam, where the beam first experienced compression folds (Figure 4.18a) and tension engagement of the reinforcement (Figure 4.18b). The addition of load amplified the damage and further engaged the FRP away from the failure zone (Figure 4.18c). Upon termination of the tests, the specimens were passed through the bandsaw in order to visually identify the wood damage inside the confinement reinforcement. As shown in Figure 4.18d, the wood damage is localized to a single plane experiencing some compressions folds and tensile fibre failures.

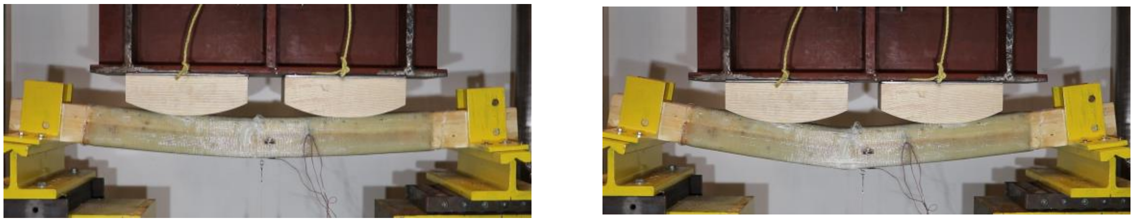
(a) Compression buckling of FRP R7-02 (b) Tension failure for R7-02


(c) Ultimate failure for R7-02 (d) R7-02 dissection

Figure 4.18 - Representative Failure Mode for Reinforcement Scheme 7

The failure modes observed in reinforcement scheme 8 were similar to the modes observed in scheme 7. Both R8-01 and R8-02 beams initially started failing near the left-most point load (Figure 4.19a and Figure 4.19b). The natural variability of the material and the pin-supported spreader beam emphasize the weaker locations on the beam. Once the failure plane is initiated (within the two load points) and the load amplifies, the displacement increases but the damage on the wood remains within that initial plane. Negligeable wood damage was recorded on specimen R8-01 (Figure 4.19c), where larger compression folds and tension rupture was apparent on specimen R8-02 (Figure 4.19d).

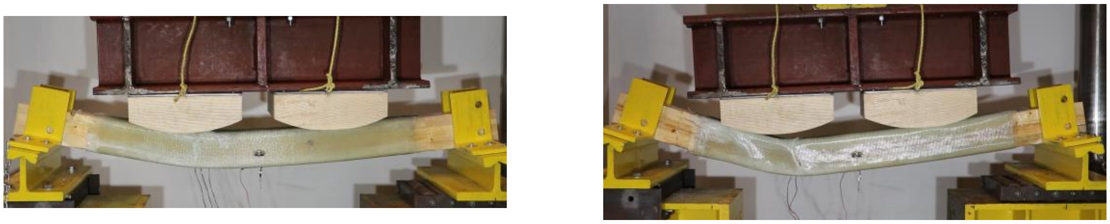

(a) R8-01 (b) R8-02

(c) R8-01 dissection (d) R8-02 dissection

Figure 4.19 - Representative Failure Mode for Reinforcement Scheme 8

The representative failure mode for R9 beams is shown in Figure 4.20. Both specimens tested failed due to cross-grain tension stresses that initiated from a knot located within the extreme tensile laminates. Specifically, for R9-02, a knot near midspan created a zone of high-tension perpendicular to grain which ultimately failed the specimen (Figure 4.20a). As the load increased, the cross-grained failure propagated to a splintering failure (Figure 4.20b) due to the confinement effect of the tension reinforcement anchors (i.e., not allowing the failed glulam to extend away from the specimen). It should be noted that the horizontal confinement action induced a horizontal shear failure once the member reached a certain post-peak displacement.

(a) Midspan tension failure for R9-02 (b) Close-up of splintering damage for R9-02

Figure 4.20 - Representative Failure Mode for Reinforcement Scheme 9

Figure 4.21 depicts the failure modes for reinforcement scheme 10. Specimen R10-01 failed in tension at the location of a knot near the point load (Figure 4.21a). The increase in load and displacement helped spread the tensile failure to the midspan of the beam and engaged the FRP fibres up to tensile failure (Figure 4.21c). Specimen R10-02 failed in horizontal shear and cross-grain tension simultaneously (Figure 4.21b). The location and source of the initial failure subjected the FRP anchor/shear reinforcement to high stresses and engaged the fabric up to the compression face. As the load increased, the stresses followed suit and formed a stress concentration in the FRP located at the edge of the beam (i.e., joining the compression and side face). The ultimate failure was achieved when the stresses in the FRP positioned on the side faces exceeded the limit of the material and tore off the beam (Figure 4.21d).

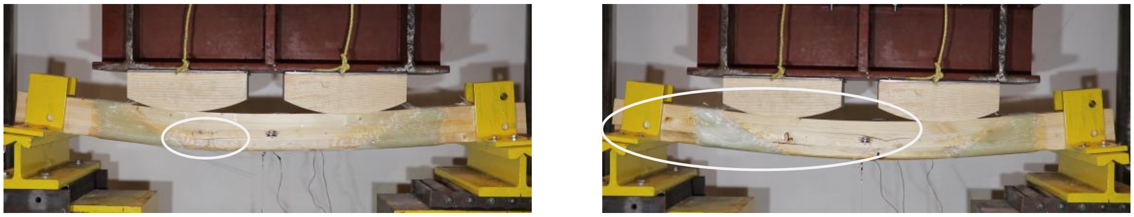

(a) R10-01 (b) R10-02

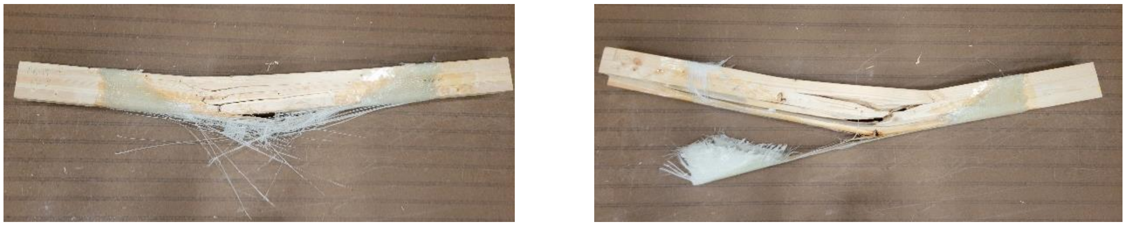

(c) R10-01 (d) R10-02

Figure 4.21 - Representative Failure Modes for Reinforcement Scheme 10

The failure mode for the 69 x 160 x 2280 mm^3 beams reinforced with longitudinal unidirectional sheets and bidirectional transverse hoops (i.e., reinforcement scheme 11) is shown in Figure 4.22. Both R11 beams initially failed in a splintering tension fashion, with the extreme tension fibres rupturing and pushing out onto the tension reinforcement. As shown in Figure 4.22a, the initial tension wood failure ruptured the bond between the reinforcement and the glulam near the failed area. As the load increased, the splintering tension failure amplified, creating a visibly damaged cross-section containing compression folds and complete rupture of tensile fibres (Figure 4.22b). The unidirectional GFRP reinforcement (applied longitudinally on the tension face of the glulam beams), did not yield due to the initial debonding at failure. The transversely applied GFRP hoops contained the tension strip and prevented total delamination from the glulam. However, as the midspan deflection continued to increase, the tensile stresses on the reinforcement strip caused significant slippage. Figure 4.22c depicts the slipping behaviour of the longitudinal reinforcement, where the reinforcement was initially placed underneath the outermost hoop and ended up near the innermost hoop.

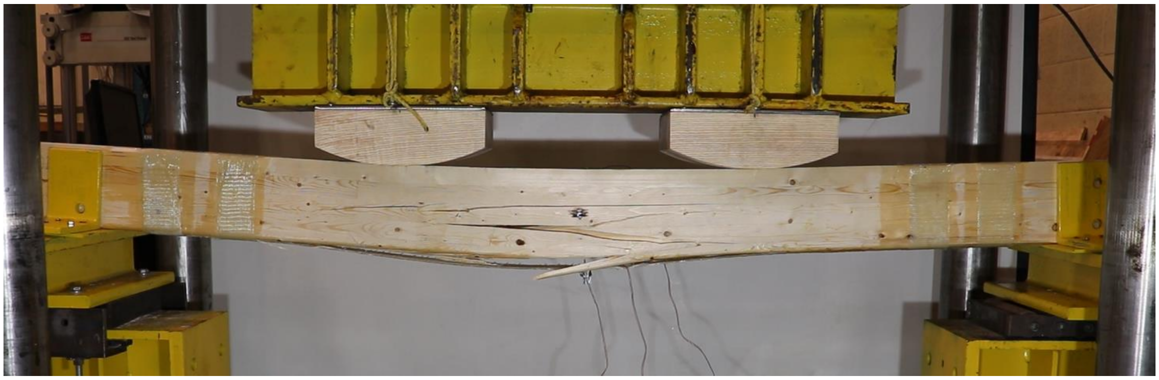

(a) Midspan splintering tension failure of R11-01

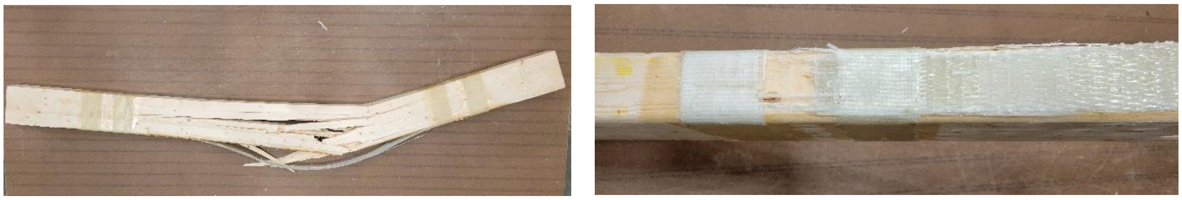

(b) Ultimate failure of R11-01

(c) Slipping of FRP on the tension face of R11-02

Figure 4.22 - Representative Failure Modes for Reinforcement Scheme 11

The representative failure mode for reinforcement scheme 12 is shown in Figure 4.23. The six layers of bidirectional tension reinforcement containing tapered confinement in the shear regions allowed both R12 beams to fail in simple tension. The initial tension failure occurred at the location of a knot found within the tensile laminates of the glulam beams. The tension reinforcement located in the high-bending stress region of beam R12-02 provided adequate reinforcement, causing the tensile failure to occur at a knot on the second last laminate (Figure 4.23a). The horizontal confinement provided by the shear reinforcement confined the tensile failure to the middle of the beam, allowing the initial tension failure to propagate through the depth of the beam instead of across to the shear and support regions (Figure 4.23b). The brash tensile failure of the outermost tensile laminate along with the compression folds located along the significantly damaged cross-section is shown in Figure 4.23c. The increase in load and displacement forced the tensile rupture of the reinforcement fibres, generating yielding and delamination damage within the high-bending stress region (Figure 4.23b and Figure 4.23c).

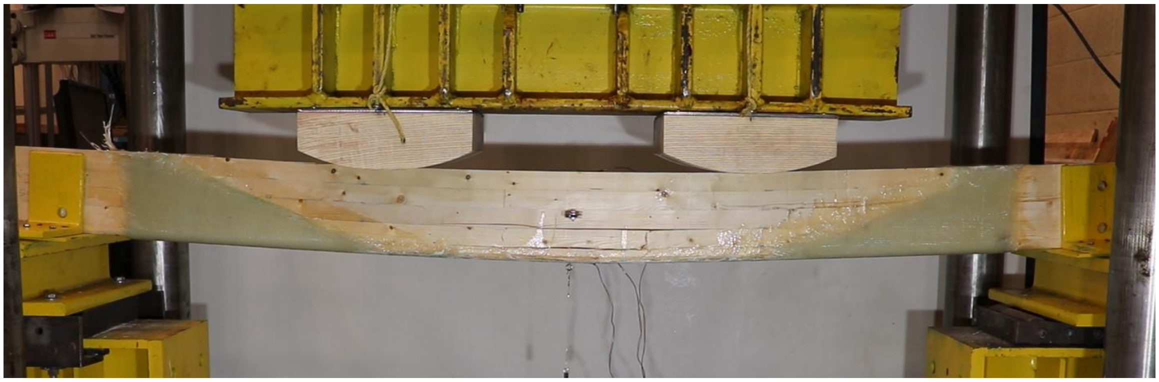

(a) Midspan tension failure of R12-02

(b) Ultimate failure of R12-01 (c) Close-up of damage for R12-02

Figure 4.23 - Representative Failure Modes for Reinforcement Scheme 12

4.4 Flexural Performance of Glulam Beams

4.4.1 Unreinforced Glulam Beams

The bending test results for the unreinforced glulam beams are presented in Table 4.4. P_{max} is the maximum force recorded by the actuator, $\Delta_{P,max}$ is equal to the string pot displacement at the time of maximum load. The strains, $\varepsilon_{t,max}$ and $\varepsilon_{c,max}$, represent the largest tensile and compressive strains recorded during the test. It should be noted that the strain readings were commonly lost past the initial peak in load (i.e., at loads greater than P_{max}). The modulus of rupture (MOR) was calculated based on the maximum load (P_{max}) and the beam geometry (e.g., span length, cross-sectional dimensions). The bending stiffness (K) was calculated as an average of the stiffnesses obtained from the 10% to 40% range of the maximum load. Distinct stiffnesses were calculated using the resistance curve, strain gauge data, and the shear-free deflection measurements.

Table 4.4 - Summary of Flexural Test Results of Unreinforced Beams

Specimen	**P_{max}[a] (kN)**	**$\Delta_{P,max}$[b] (mm)**	**MOR[e] (MPa)**	**K[f] (N/mm)**	**$\varepsilon_{t,max}$[c] x 10^{-4} (mm/mm)**	**$\varepsilon_{c,max}$[d] x 10^{-4} (mm/mm)**
U-01	27.9	26.4	45.8	1,620	38.7	-40.3
U-02	30.8	29.3	53.5	1,541	42.3	-61.2
U-03	36.8	24.3	64.5	1,731	48.3	-45.3
U-04	36.8	23.3	66.3	2,107	52	-41.6
U-05	31.9	29.8	57.2	1,510	58.4	-58.2
Average	32.8	26.6	57.4	1,702	47.9	-49.3
St. Dev.	3.5	2.6	7.5	216	7	8.7
COV	0.11	0.1	0.13	0.13	0.15	-0.18

[a] Maximum load resistance

[b] Displacement at maximum load

[c] Modulus of rupture

[d] Bending stiffness

[e] Maximum tensile strain

[f] Maximum compressive strain

The resistance curves for the five unreinforced beams are shown in Figure 4.24.

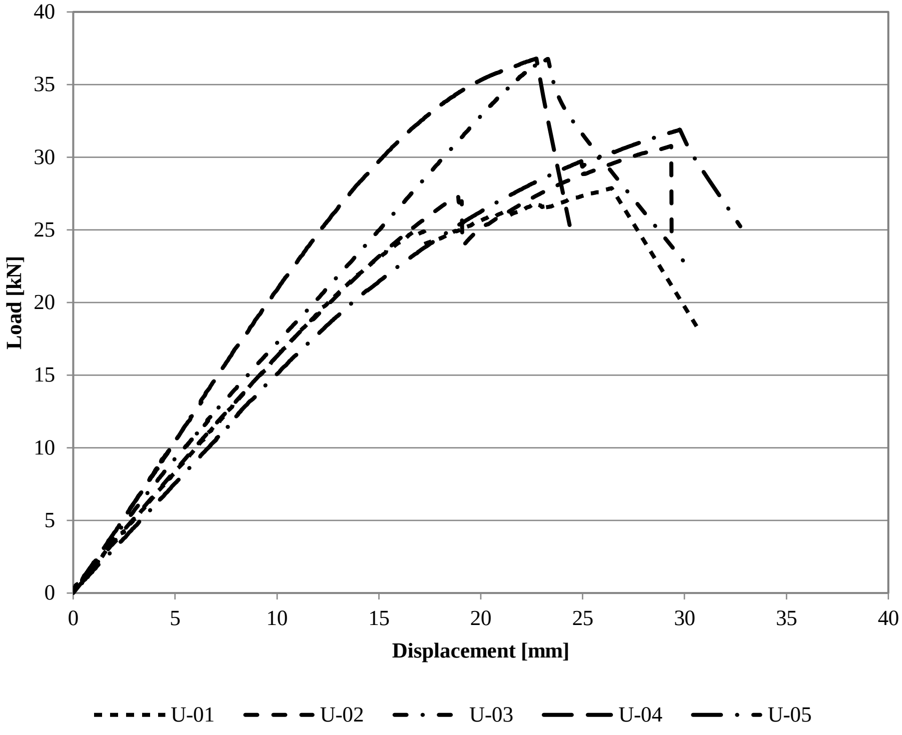

Figure 4.24 - Resistance Curves of Unreinforced Glulam Beams

4.4.2 Reinforced Glulam Beams

Table 4.5 presents the summary of the bending test results for the nine reinforced glulam beams statically tested in reinforcement Stage 1. An increase in maximum load (P_{max}) and stiffness (K) can be observed for most of the reinforced specimens. As previously stated in section 4.3.2, all stage 1 beams failed in shear, indicating that the increase in overall strength resulting from the reinforcement schemes developed came at the expense of the failure mode. The addition of reinforcement prevented the failure of wood tensile fibres observed during the unreinforced beam tests, which ultimately increased the shear stresses on the specimens. The shear stress increase resulted in even more brittle failures than the flexural failures experienced in the unreinforced beams. The ultimate tensile and compressive strains were recorded within the linear portion of the resistance curve.

Table 4.5 - Summary of Flexural Test Results of Reinforced Beams in Stage 1

Specimen	P_{max}^{a} (kN)	$\Delta_{P,max}^{b}$ (mm)	K^{c} (N/mm)	$\varepsilon_{t,max}^{d}$ x 10^{-4} (mm/mm)	$\varepsilon_{c,max}^{e}$ x 10^{-4} (mm/mm)	$\varepsilon_{FRP,max}^{f}$ x 10^{-4} (mm/mm)
Unreinforced [100][g]	32.8	26.0	1,702	47.9	-49.3	-
R1-01 [100]	32.1	12.8	2,544	31.2	-25.0	38.4
R1-02 [100]	35.2	24.1	1,783	54.3	-65.7	-
R1-03 [100]	36.8	19.5	2,082	45.3	-44.0	68.6
Average	34.7	18.8	2,137	34.7	-44.9	53.5
R2-01 [100]	44.4	27.4	2,459	58.2	-19.1	66.7
R2-02 [100]	50.0	25.8	2,499	44.1	-57.4	62.2
Average	47.2	26.6	2,479	51.2	-38.2	64.4
R3-01 [100]	42.9	21.5	2,277	45.0	-45.2	52.4
R3-02 [100]	39.6	29.1	1,976	59.4	-30.5	72.9
Average	41.2	25.3	2,126	52.2	-37.9	62.6
R4-01 [100]	46.8	35.1	2,259	42.6	-63.9	62.2
R4-02 [100]	46.9	19.5	2,844	39.1	-35.9	46.2
Average	46.8	27.3	2,552	40.8	-49.9	54.2

[a] Maximum load resistance

[b] Displacement at maximum load

[c] Bending stiffness

[c] Wood maximum tensile strain

[d] Wood maximum compressive strain

[e] FRP maximum tensile strain

[g] Average values of unreinforced beams

The bending test summary for the remaining sixteen reinforced beams tested in reinforcement Stage 2 is presented in Table 4.6. The summary table includes the results of the 69 x 160 x 2280 mm^3 (R11 and R12 beams) which cannot be compared to the smaller 69 x 100 x 1355 mm^3 unreinforced beams averaged at the beginning of the table. An increase of both strength (MOR) and stiffness (MOE) is generally observed for the reinforced beam A’s, relative to the unreinforced beams. The fully confined R7 and R8 beams experienced the largest increase in strength and stiffness, corresponding to 1.76 and 1.75 times that recorded for the unreinforced beams, respectively.

Table 4.6 - Summary of Flexural Test Results of Reinforced Beams in Stage 2

Specimen	**P_{max}[a] (kN)**	**$\Delta_{P,max}$[b] (mm)**	**K[c] (N/mm)**	**$\varepsilon_{t,max}$[d] x 10^{-4} (mm/mm)**	**$\varepsilon_{c,max}$[e] x 10^{-4} (mm/mm)**	**$\varepsilon_{FRP,max}$[f] x 10^{-4} (mm/mm)**
Unreinforced [100][g]	32.8	26.0	1,702	47.9	-49.3	-
R5-01 [100]	40.3	26.7	2,327	44.8	-11.4	59.8
R5-02 [100]	40.0	27.4	2,486	42.4	-27.8	56.7
Average	40.1	27.1	2,407	43.6	-19.6	58.3
R6-01 [100]	35.0	15.4	2,344	55.3	-26.9	70.9
R6-02 [100]	36.9	16.8	1,855	36.4	-38.0	40.3
Average	35.9	16.1	2,100	45.8	-32.4	55.6
R7-01 [100]	56.6	36.2	2,471	60.7	-43.5	70.9
R7-02 [100]	49.8	31.9	2,694	52.2	51.3	55.9
Average	53.2	34.0	2,583	56.4	3.9	63.4
R8-01 [100]	58.2	26.4	2,641	107.2	-45.2	-
R8-02 [100]	58.8	25.9	2,641	63.8	-34.8	69.4
Average	58.5	26.1	2,641	85.5	-40.0	69.4
R9-01 [100]	36.4	25.5	1,855	45.4	-45.6	55.2
R9-02 [100]	32.4	21.5	1,637	45.4	-	48.8
Average	34.4	23.5	1,746	45.4	-45.6	52.0
R10-01 [100]	47.2	31.8	2,385	52.4	-37.5	-
R10-02 [100]	44.3	36.2	1,921	61.1	-	80.3
Average	45.7	34.0	2,153	56.7	-37.5	80.3
R11-01 [160]	62.9	36.2	2,059	60.1	-43.8	-
R11-02 [160]	60.0	36.8	2,117	56.8	-48.1	51.7
Average	61.4	36.5	2,088	58.5	-46.0	51.7
R12-01 [160]	63.8	36.2	2,134	63.1	-44.5	-
R12-02 [160]	67.7	35.9	2,245	56.7	-42.6	59.7
Average	65.8	36.0	2,189	59.9	-43.5	59.7

[a] Maximum load resistance

[b] Displacement at maximum load

[c] Bending stiffness

[c] Wood maximum tensile strain

[d] Wood maximum compressive strain

[e] FRP maximum tensile strain

[g] Average values of unreinforced beams

4.4.3 Effect of the Reinforcement Configuration

The resistance curves corresponding to the reinforced beams in Stage 1 are shown in Figure 4.25. The general behaviour of the beams contains similarities that stem from the failure mode. Similar maximum loads are observed in Figure 4.25a and Figure 4.25b, with the main difference being the bending stiffness increase of the beams reinforced with four layers compared to the beams reinforced with only two layers of GFRP reinforcement. The horizontal shear and stress concentration failure occurred at comparable loads, explaining the small variances in maximum loads. The reinforcement was able to prevent the wood tensile failure observed in the unreinforced beams; however, the increased tensile strength was accompanied in another sudden failure mode. The resistance curves also visually demonstrate the brittle ultimate failure, having a linear behaviour up to maximum load with no post-peak resistance due to significant damage.

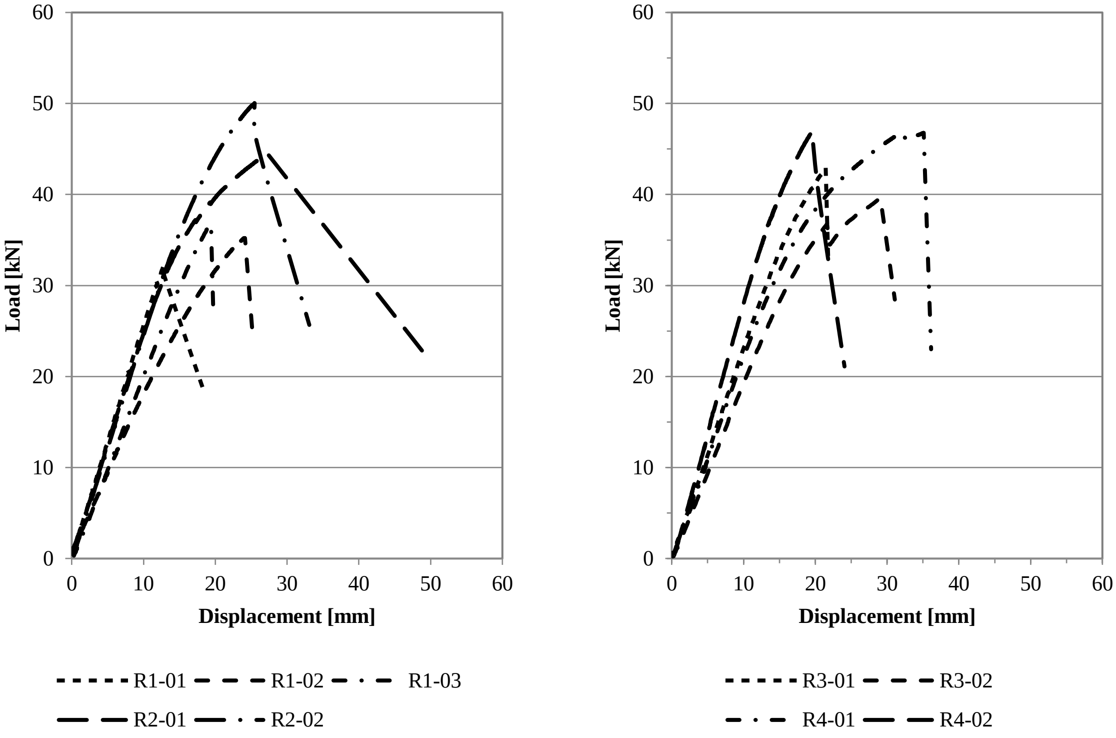

(a) R1 and R2 beams (b) R3 and R4 beams

Figure 4.25 - Resistance Curves of Reinforced Beams in Stage 1

Figure 4.26 depicts the twelve [100] beams tested in stage two, grouped based on their reinforcement configurations. R5 and R6 beams, containing unidirectional tensile reinforcement and transverse hoops, were observed to behave linearly up to maximum loads (Figure 4.26a) and failed suddenly in a combination of shear and flexure. The R6-02 specimen, indicating a lower bending stiffness in comparison to the group was deemed an outlier based on a large knot located on the tensile face of the beam. The resistance curves for the specimens containing full confinement reinforcement are grouped in Figure 4.26b. The four beams, displaying virtually identical bending stiffnesses (Figure 4.26b), differ from one another based on their initial failure mode. R7-02, the only specimen failing in flexure at the midspan of the beam, is observed to fail in a more ductile manner when compared to the rest of the group. The flexural failure (i.e., specimen R7-02) showed the best post-peak behaviour, capable of resisting larger loads at greater displacements. The fully confined specimens that failed in shear were able to resist larger loads (Figure 4.26b). The P_{max} increase came at the expense of the post-peak capabilities, with sheared members displaying little to no resistance past $\Delta_{P,max}$.

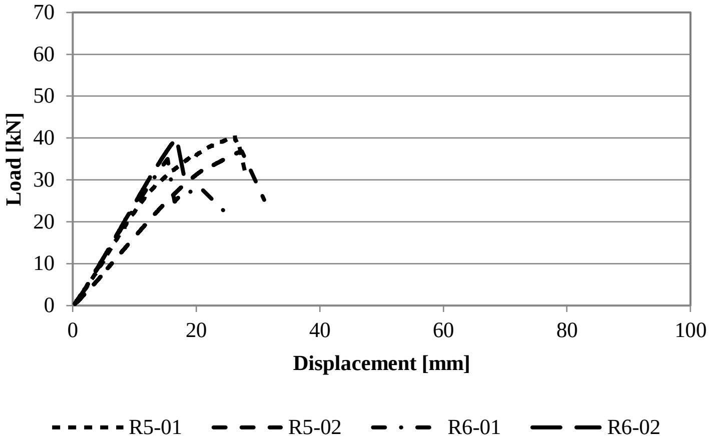

(a) R5 and R6 beams

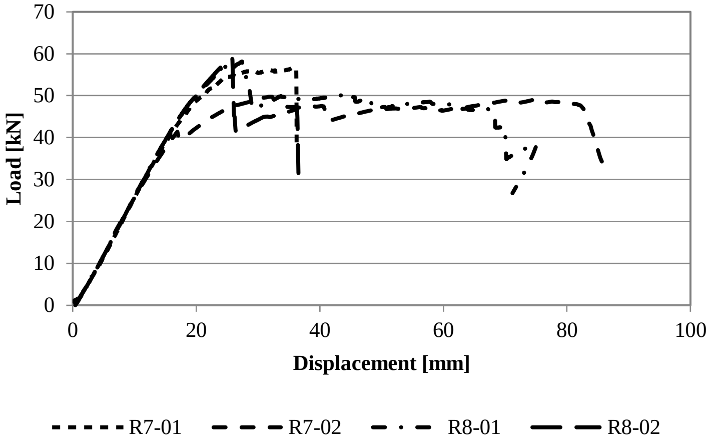

(b) R7 and R8 beams

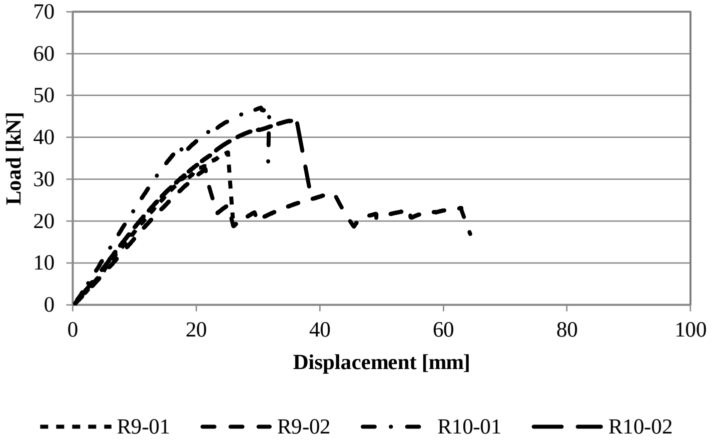

(c) R9 and R10 beams

Figure 4.26 - Resistance Curves of Reinforced [100] Beams in Stage 2

The resistance curves for the larger [160] beams (i.e., R11 and R12 beams) are displayed in Figure 4.27. Both reinforcement schemes created composite beams with relatively similar bending stiffnesses. A linear behaviour is observed in all four tests up to P_{max}, where flexural failures originating from defects found in the wood result in a sudden drop of resistance (Figure 4.27). Compression folds forming within the top face of the beams create a slight deviation from the linear elastic behaviour once the loads surpass roughly 80% of the maximum load. Significant post-peak resistance was observed in all four reinforced [160] beams, with Figure 4.27 displaying the resistance for both R12 beams. The R11 beams, reinforced using simple tension GFRP strips on the tension face along with transverse hoops, initially failed in flexure in the wood fibres causing the delamination of the GFRP within the high-bending stress region. The failure caused the string-pot to unfasten from the beam and ultimately ended the recording of useable data for the resistance curves, represented by dots on the resistance curves (Figure 4.27). The R11 beams did provide significant post-peak resistance, with a more detailed failure progression found in Appendix D.

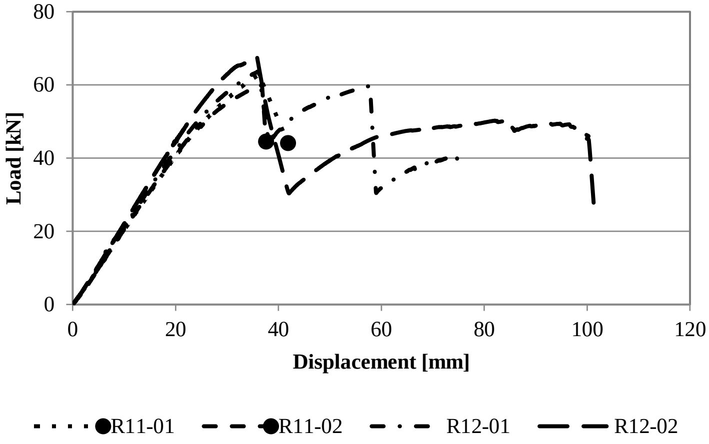

Note: ● End of useable displacement data.
Figure 4.27 - Resistance Curves of Reinforced [160] Beams in Stage 2

4.4.4 Summary of Bending Test Results

Finally, the general strength and stiffness summary for all experimentally tested beams are presented in Table 4.7. Grouped into the different stages, the resistance (P_{max}) and bending stiffness (K) are presented along with the initial failure mode.

Table 4.7 - Experimental Test Results Summary

Stage	**Specimen Type**	**Specimen Name**	**P_{max}[a] (kN)**	**K[b] (N/mm)**	**Failure Mode**
1	Unreinforced[c]	U-01 − U-05	32.8	1,702	Flexure
	Reinforced	R1-01; [100]	32.1	2,544	Shear
		R1-02; [100]	35.2	1,783	Shear
		R1-03; [100]	36.8	2,082	Shear
		R2-01; [100]	44.4	2,459	Shear
		R2-02; [100]	50.0	2,499	Shear
		R3-01; [100]	42.9	2,277	Shear
		R3-02; [100]	39.6	1,976	Shear
		R4-01; [100]	46.8	2,259	Shear
		R4-02; [100]	46.9	2,844	Shear
2	Reinforced	R5-01; [100]	40.3	2,327	Flexure
		R5-02; [100]	40.0	2,486	Shear and Flexure
		R6-01; [100]	35.0	2,344	Flexure
		R6-02; [100]	36.9	1,855	Shear and Flexure
		R7-01; [100]	56.6	2,471	Shear
		R7-02; [100]	49.8	2,694	Flexure
		R8-01; [100]	58.2	2,641	Shear
		R8-02; [100]	58.8	2,641	Shear
		R9-01; [100]	36.4	1,855	Shear and Flexure
		R9-02; [100]	32.4	1,637	Flexure
		R10-01; [100]	47.2	2,385	Flexure
		R10-02; [100]	44.3	1,921	Shear and Flexure
		R11-01; [160]	62.9	2,059	Flexure
		R11-02; [160]	60.0	2,117	Flexure
		R12-01; [160]	63.8	2,134	Flexure
		R12-02; [160]	67.7	2,245	Flexure

[a] Maximum resistance

[b] Bending stiffness

[c] Average values of unreinforced beams

Chapter 5

Analytical Model for Bending Strength

5.1 General

This chapter outlines the theory and methodology employed in the development of the material model used to predict the flexural behaviour of the glulam beams. The idealized stress-stress curves for the wood and GFRP materials, which were obtained from the experimental tests on coupons, are presented. The methodologies used to develop the moment-curvature and force-displacement curves of unreinforced and FRP-reinforced glulam beams are discussed in detail. Finally, the predictive model developed herein is verified against the predictions presented in Lacroix (2017).

5.2 Idealized Stress-Strain Relationship

Buchanan (1990) followed the work of Bazan (1980) and modified the stress-strain relationship established for clear wood by including reduction factors or strength effects. The modified (i.e., reduced) stress-strain relationship accounted for the naturally occurring defects and more accurately represented the in-grade commercial lumber behaviour.

The behaviour of wood subjected to tensile loads can be idealized as being linear elastic up to an ultimate tensile stress, f_t, and corresponding strain, ε_t. Contrarily, when subjected to compressive loads, the behaviour of wood can be assumed to be bilinear. The behaviour can be simplified to a positive linear response up to a compressive yielding stress, f_{cy}, and strain, ε_{cy}, followed by a negative linear response up to an ultimate compressive stress, f_{cu}, and strain, ε_{cu}. The slope of the descending branch, mE, is related to the compressive modulus of elasticity in the longitudinal direction (Buchanan, 1990). The stress-strain relationship used in this study is shown in Figure 5.1.

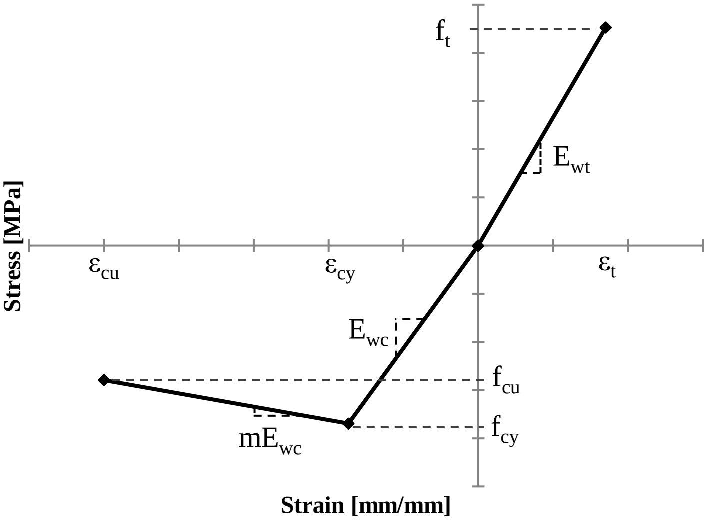

Figure 5.1 - Stress Distribution Proposed by Buchanan (1990)

5.2.1 Size Effects

The values used to define the stress-strain relationship of the wood material are size and specie dependent and can either be extracted from the literature (Barrett & Lau, 1994) or experimental coupon testing (Gentile et al., 2002; D. N. Lacroix, 2017b; Madsen & Buchanan, 1986). This study uses the results of a series of coupon tests done on clear samples that are further modified to include the size effect, a theorem that is based on the idea that material defects and their associated effect on the strength can be calculated based on the size of the coupon specimens (Buchanan, 1990). The compressive and tensile strength results obtained experimentally were modified for length and depth effects using Equations (5.1) and (5.2), respectively (Barrett & Lau, 1994; Buchanan, 1990).

$$f_c = f_{c,exp}\left(\frac{L_{c,exp}}{L_{ec}}\right)^{\frac{1}{k_1}}\left(\frac{d_{c,exp}}{d}\right)^{\frac{1}{k_2}} \tag{5.1}$$

$$f_t = f_{t,exp}\left(\frac{L_{t,exp}}{L_{ec}}\right)^{\frac{1}{k_1}}\left(\frac{d_{t,exp}}{d}\right)^{\frac{1}{k_2}} \tag{5.2}$$

where f_c is the modified compressive material model input yield strength, $f_{c,exp}$ is the average experimental compressive strength from the coupon tests, $L_{c,exp}$ is the average length of the compression coupon specimens, $d_{c,exp}$ is the average depth of the compression coupon specimens, $f_{t,exp}$ is the average experimental tensile strength obtained from the coupon tests, $L_{t,exp}$ is the average length of the tension coupon specimens, $d_{t,exp}$ is the average depth of the tension coupon specimens, L_{ec} is the equivalent stressed length in compression or tension, d is the average depth or width of the laminates composing the glulam section, k_1 is the size effect parameter for length, and k_2 is the size effect parameter for the depth.

Buchanan (1990) added that the load configuration also affects the strength of the specimens and is accounted for using Equation (5.3), where both equivalent stressed lengths can be determined for the simply supported beam loaded with two symmetrically placed loads.

$$L_{ec} = L\left(\frac{1 + \frac{a_1 k_1}{L}}{k_1 + 1}\right) \tag{5.3}$$

where L_{ec} is the equivalent stressed length, L is the span of the beam, a_1 is the distance between point loads, and k_1 is the length effect parameter.

The stress-strain relationship of the wood coupons tabulated in Table 4.1 and Table 4.2 are shown in Figure 5.2a and Figure 5.2b, respectively, and are used to develop the modified input strengths. The linear behaviour of the tension coupons resulted in an average failure stress of 89.3 MPa, which was divided by the tensile MOE of 13,288 MPa to extract the failure strain of 0.0067 mm/mm. The compression coupons experienced a linear behaviour up to peak resistance resulting in a maximum stress and strain of 40.4 MPa and 0.0038 mm/mm, respectively. All compression coupon specimens experienced some level of post-post resistance. As shown in Figure 5.2b, the assumed bilinear behaviour adequately represents the initial drop in resistance but fails to include the plateauing behaviour which occurs at larger strains. For the type of behaviour observed in this study, a trilinear idealization would better reflect the actual behaviour of the compression members. O'Callaghan et al. (2022), who investigated the effects of GFRP on the compressive behaviour of Spruce-Pine-Fir columns, also observed and reported the plateauing behaviour in the post-peak realm. However, the author chose to represent the compressive behaviour using a bilinear curve based on the fact that the plateau strains were significantly greater than the experimental strains observed in bending tests.

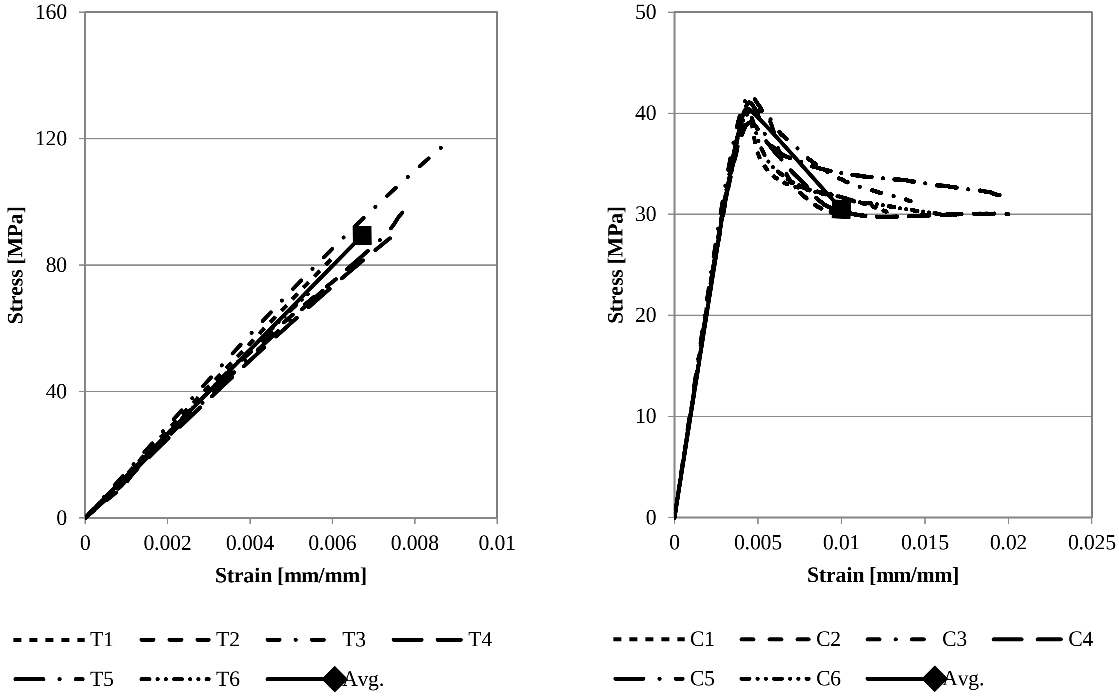

(a) Tension (b) Compression

Figure 5.2 - Experimental Stress-Strain Curves for the Wood Coupons

Table 5.1 presents the parameters used to determine the input model strength values. The length effect factors, k_1, of 10.00 and 5.88 were obtained from Barrett & Lau (1994) for compression and tension, respectively. The depth effect factors, k_2, of 69.61 for compression and 6.42 for tension were obtained using the approximation method outlined in (Madsen & Buchanan, 1986).

Table 5.1 - Model Input Strengths

Properties	**[100] Beam**		**[160] Beams**	
	Compression	**Tension**	**Compression**	**Tension**
Exp. strength: $f_{c,exp}$, $f_{t,exp}$	40.4	89.3	40.4	89.3
Coefficient of variations	0.02	0.18	0.02	0.18
Exp. length: $L_{c,exp}$, $L_{t,exp}$ [mm]	203.2	324.0	203.2	324.0
Length effect parameter, k_1	10.00	5.88	10.00	5.88
Depth effect parameter, $k_{2,a}$	-	6.4	-	6.4
Width effect parameter, $k_{2,b}$	69.6	6.4	69.6	6.4
Equivalent stressed length, L_e [mm]	472.7	516.3	756.4	826.0
Average depth of laminates, d_a [mm]	-	32.5	-	32.5
Average width of laminates, d_b [mm]	69		69	
Input model strength: f_{cy}, f_t [MPa]	36.9	45.2	35.2	41.8

Both depth and width averages are tabulated in Table 5.1 and represent the cross-sectional dimensions of the laminates composing the glulam section. It is important to note that only the width effect is considered in compression, which is due to the fact that the compression coupon specimens were thicker than one laminate (i.e., 50.8 mm > 32.5 mm) and therefore only modified in the width direction. Contrarily, the tension coupons were fabricated out of one single laminate which was reduced in both the depth and width direction, meaning the depth effect needed to be accounted for in both cross-sectional axes. The resulting stress-strain constitutive relationship for the four-point static loading used in this research program is presented in Figure 5.3. The strains associated with the maximum compressive and tensile stresses were calculated by dividing the input model strengths (i.e., Table 5.1) by the average experimental modulus of elasticity in compression or tension.

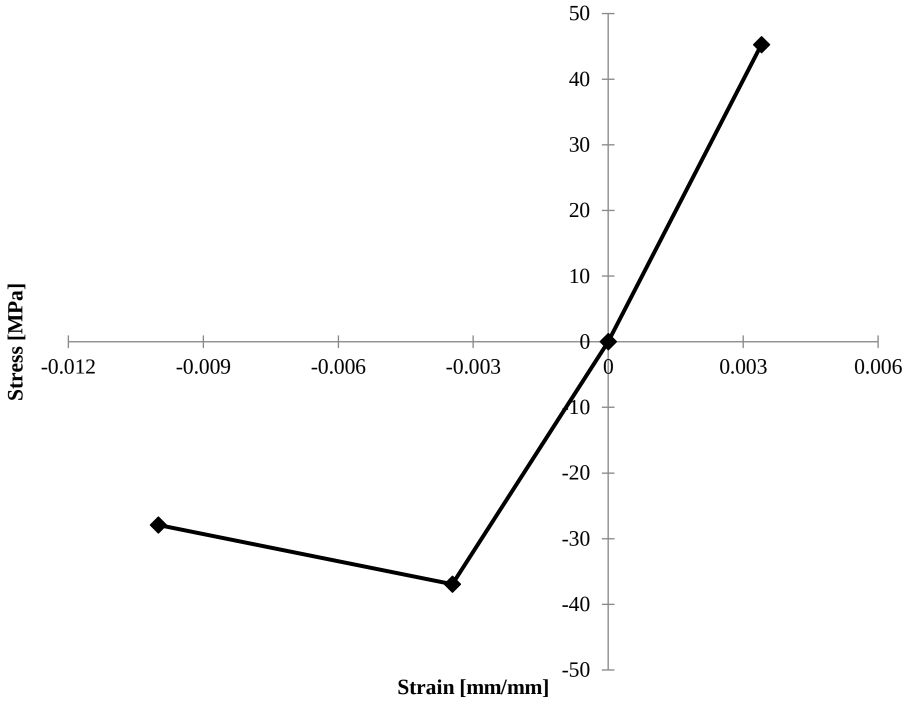

Figure 5.3 - Glulam Input Stress-Strain Relationship

The FRP stress-strain relationships tabulated Table 4.3 are used to model the reinforcing material as linear-elastic, using the average maximum stress and strain to develop the FRP input values shown in Figure 5.4. It should be noted that all FRP coupon specimens experienced slight decreases in stiffness as the strains increased, which is conservatively omitted in the modelling values (i.e., perfectly linear behaviour up to tensile fibre rupture).

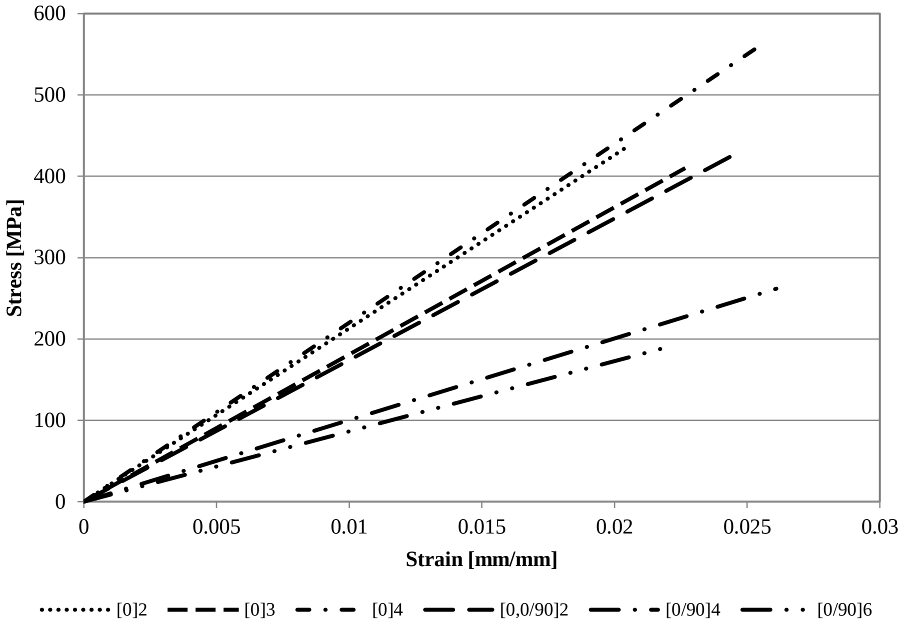

Figure 5.4 - FRP Input Stress-Strain Relationship

5.3 Moment Curvature Analysis

Reinforced timber has been the subject of multiple studies and as a result, different material models have been created to predict their bending capacity. As discussed in Chapter 2, common models are based on the cross-sectional analysis of the FRP-timber composite, with differences stemming from the constitutive laws applied in the timber's compression region. Previous research has also demonstrated that the existing models usually underestimate the member strength, thus some authors opted to keep their conservative values (e.g., Johns & Lacroix, 2000; Raftery & Harte, 2011) whereas others applied empirical strength factors to better fit the model output to the experimental data (e.g., Gentile et al., 2002; Lacroix, 2017; Wang et al., 2021; Yang et al., 2016). The material model presented in this chapter is based on the encouraging results previously performed on FRP-reinforced timber beams that allow for large deformations, and account for the softening compressive behaviour caused by the compression folds.

5.3.1 Unreinforced Beams

The cross-section, strain profile, stress distribution and resulting forces acting on the cross-section of the unreinforced member that has not exceeded the compression yield strain (i.e., $\varepsilon \leq \varepsilon_{cy}$) is shown in Figure 5.5. A linear distribution of stresses and strains are observed with the material idealized as linear elastic. The depth of the neutral axis is measured from the top of the compression face.

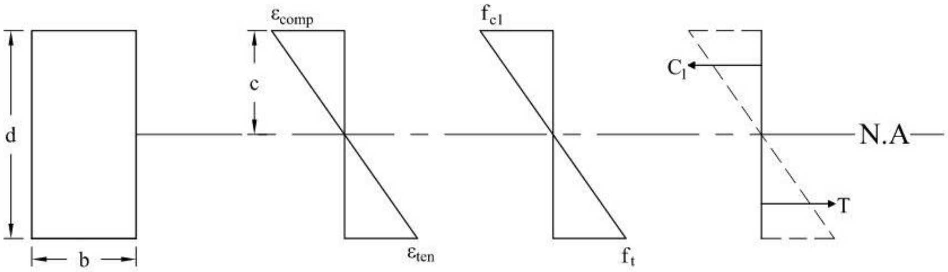

(a) Cross-section (b) Strain profile (c) Stress profile (d) Forces

Figure 5.5 - Unreinforced Glulam: Distribution of Strain, Stress, and Forces Prior to Compression Yielding

For the unreinforced glulam beams that have not reached the compressive yielding strain (Figure 5.5), the moment about the neutral axis can be calculated using Equations (5.4) – (5.6).

$$C_1 = \frac{E_{wc}\varepsilon_{comp}cb}{2} \tag{5.4}$$

$$T = \frac{E_{wc}\varepsilon_{ten}(d-c)b}{2} \tag{5.5}$$

$$M_{NA} = C_1\left(\frac{2c}{3}\right) + T\left[\frac{2(d-c)}{3}\right] \tag{5.6}$$

where ε_{comp} and ε_{ten} are the top and bottom strains representing the compression and tension strains, E_{wc} and E_{wt} are the compression and tension moduli of elasticity, c is the neutral axis depth measured from the top of the compression face, b is the member width, and d is the member depth.

The distribution of strains, stresses, and forces for the unreinforced glulam beams that have exceeded the compressive yielding strain (ε_{cy}) is shown in Figure 5.6, where the moment resistance about the neutral axis can be calculated using Equations (5.7) – (5.11).

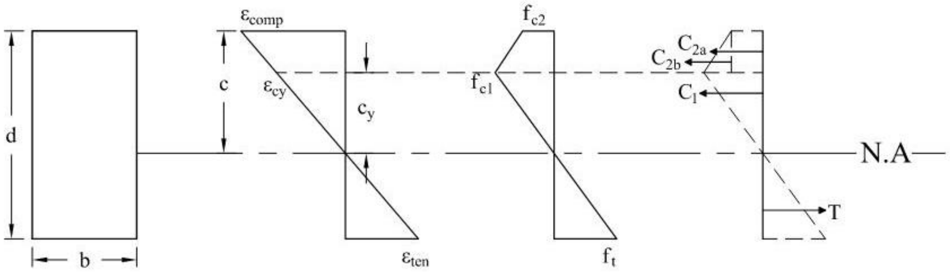

(a) Cross-section (b) Strain profile (c) Stress profile (d) Forces

Figure 5.6 - Unreinforced Glulam: Distribution of Strain, Stress, and Forces Post Compression Yielding

$$C_1 = \frac{E_{wc}\varepsilon_{cy}\left[\left(\frac{\varepsilon_{cy}}{\varepsilon_{comp}}\right)c\right]b}{2} \tag{5.7}$$

$$C_{2a} = \left[\varepsilon_{cy} - m\left(\varepsilon_{comp} - \varepsilon_{cy}\right)\right]\left[\left(1 - \frac{\varepsilon_{cy}}{\varepsilon_{comp}}\right)c\right]E_{wc}b \tag{5.8}$$

$$C_{2b} = \frac{\left[mE_{wc}\left(\varepsilon_{comp} - \varepsilon_{cy}\right)\right]\left[\left(1 - \frac{\varepsilon_{cy}}{\varepsilon_{comp}}\right)c\right]E_{wc}b}{2} \tag{5.9}$$

$$T = \frac{E_{wt}\varepsilon_{ten}(d-c)b}{2} \tag{5.10}$$

$$M_{NA} = C_1\left(\frac{2c_y}{3}\right) + C_{2a}\left(\frac{c_y + c}{2}\right) + C_{2b}\left(\frac{2c_y + c}{3}\right) + T\left[\frac{2(d-c)}{3}\right] \tag{5.11}$$

where c_y is the depth of the linear-elastic portion of the compression zone measured from the neutral axis, C_1, C_{2a}, C_{2b} are the compressive forces, and T is the tensile force acting over the cross-section.

When calculating the bending capacity of a wood member using experimental tensile stress results, a phenomenon referred to as the stress-distribution effect needs to be accounted for (Buchanan, 1990; Madsen & Buchanan, 1986). Research investigating the behaviour of timber beams subjected to bending stresses showed that the extreme tensile fibres strains exceeded those characterized by pure tension tests (Buchanan 1990). The extreme tensile bending stress, f_m, can be related to the uniaxial tensile stress, f_t, using Equation (5.12).

$$f_m = \left[\frac{d(1+k_3)}{d-c}\right]^{\frac{1}{k_3}} f_t \tag{5.12}$$

where d is the member depth, k_3 is the stress distribution factor, and c is the neutral axis depth measured from the compression face.

A moment-curvature VBA program was developed to generate the bending moment resistance of a cross-section having predefined dimensions and material stress-strain behaviours. A set of closed-form equations cannot be determined based on the failure stress being a function of the neutral axis; therefore, by increasing the compression strain and recording the moment resistance, a moment-curvature relationship can be generated until failure. Failure occurred once the program detected that the material strains for the wood in tension or compression and FRP were greater than the material limits determined experimentally. Two governing failure modes controlled the program; 1) the tensile strain in the wood exceeded the allowable bending tensile strain, or 2) the compressive strain in the wood exceeded the ultimate compressive strain. Figure 5.7 shows the representative moment-curvature program output for a 69 x 100 mm^2 cross-section having identical tension and compression moduli of elasticity. The primary vertical axis displays the moment resistance of the cross-section using a solid line. The secondary axis displays the depth of the neutral axis, measured from the bottom face, as a function of curvature. The entire depth range is presented on the secondary axis to better visualize the location of the neutral axis as the curvature increases.

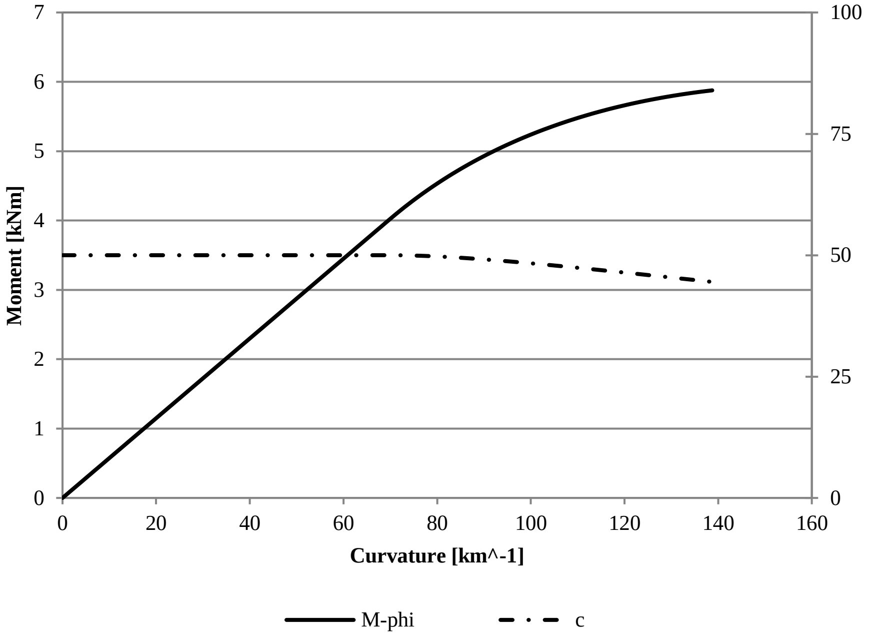

Figure 5.7 - Representative Moment-Curvature Analysis of Unreinforced Beams

5.3.2 Reinforced Beams

The moment-curvature VBA program was further developed to incorporate the FRP reinforcement. Two main assumptions were made during the analysis, namely, a perfect bond between the reinforcement and the wood fibres, and only the tensile stresses of the FRP were considered in the cross-section analysis (i.e., FRP does not contribute in compression). Figure 5.8 depicts the distribution of strains, stresses and forces acting on the rectangular cross-section reinforced with the U-shaped configuration.

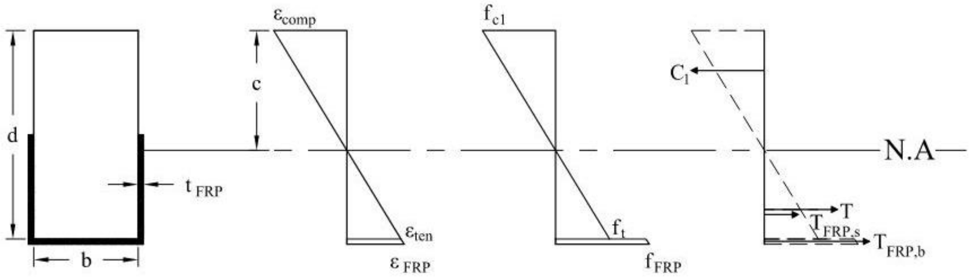

(a) Cross-section (b) Strain profile (c) Stress profile (d) Forces

Figure 5.8 - Reinforced Glulam: Distribution of Strain, Stress, and Forces Prior to Compression Yielding

For the reinforced glulam beams that have not reached the compressive yield strain (Figure 5.8), the resulting moment resistance about the neutral axis can be calculated using Equations (5.13) – (5.17).

$$C_1 = \frac{E_{wc}\varepsilon_{comp}cb}{2} \tag{5.13}$$

$$T = \frac{E_{wc}\varepsilon_{ten}(d-c)b}{2} \tag{5.14}$$

$$T_{FRPs} = E_{FRP}\varepsilon_{FRP}t_{FRP}(d-c+t_{FRP})b \tag{5.15}$$

$$T_{FRPb} = \frac{E_{FRP}(\varepsilon_{FRP}+\varepsilon_{ten})t_{FRP}b}{2} \tag{5.16}$$

$$M_{NA} = c_1\left(\frac{2c}{3}\right) + T\left[\frac{2(d-c)}{3}\right] + T_{FRPs}\left[\frac{2(d-c)}{3}\right] + T_{FRPb}\left(d-c+\frac{t_{FRP}}{2}\right) \tag{5.17}$$

where ε_{comp} and ε_{ten} are the top and bottom strains representing the compression and tension strains, E_{wc} and E_{wt} are the compression and tension moduli of elasticity, $T_{FRP,s}$ is the tension force from the FRP located on the sides of the member, $T_{FRP,b}$ is the tension force from the FRP located on the bottom face of the bending member, c is the neutral axis depth measured from the compression face, b is the member width, d is the member depth, and t_{FRP} is the FRP reinforcement thickness.

Similarly, the forces acting on the reinforced cross-section that exceeded the compressive yield strain (i.e., wood softening has occurred) is shown in Figure 5.9 and the resulting moment about the neutral axis can be calculated using Equations (5.18) – (5.24).

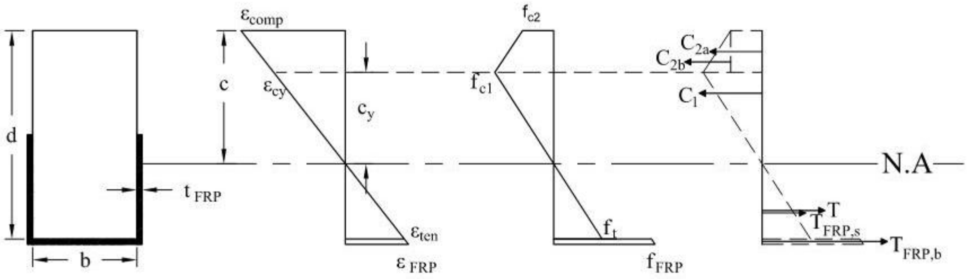

(a) Cross-section (b) Strain profile (c) Stress profile (d) Forces

Figure 5.9 - Reinforced Glulam: Distribution of Strain, Stress, and Forces Post Compression Yielding

$$C_1 = \frac{E_{wc}\varepsilon_{cy}\left[\left(\frac{\varepsilon_{cy}}{\varepsilon_{comp}}\right)c\right]b}{2} \tag{5.18}$$

$$C_{2a} = \left[\varepsilon_{cy} - m\left(\varepsilon_{comp} - \varepsilon_{cy}\right)\right]\left[\left(1 - \frac{\varepsilon_{cy}}{\varepsilon_{comp}}\right)c\right]E_{wc}b \tag{5.19}$$

$$C_{2b} = \frac{\left[mE_{wc}\left(\varepsilon_{comp} - \varepsilon_{cy}\right)\right]\left[\left(1 - \frac{\varepsilon_{cy}}{\varepsilon_{comp}}\right)c\right]E_{wc}b}{2} \tag{5.20}$$

$$T = \frac{E_{wc}\varepsilon_{ten}(d - c)b}{2} \tag{5.21}$$

$$T_{FRPs} = E_{FRP}\varepsilon_{FRP}t_{FRP}(d - c + t_{FRP})b \tag{5.22}$$

$$T_{FRPb} = \frac{E_{FRP}(\varepsilon_{FRP} + \varepsilon_{ten})t_{FRP}b}{2} \tag{5.23}$$

$$M_{NA} = C_1\left(\frac{2c_y}{3}\right) + \ + C_{2a}\left(\frac{c_y + c}{2}\right) + C_{2b}\left(\frac{2c_y + c}{3}\right) + T\left[\frac{2(d-c)}{3}\right] + T_{FRPs}\left[\frac{2(d-c)}{3}\right] + T_{FRPb}\left(d - c + \frac{t_{FRP}}{2}\right) \tag{5.24}$$

where c_y is the depth of the linear-elastic portion of the compression zone measured from the neutral axis, C_1, C_{2a}, C_{2b} are the compressive forces, $T_{FRP,s}$, $T_{FRP,b}$ are the tension forces from the reinforcement, and T is the tensile force acting over the cross-section.

As previously mentioned, the stress distribution effects in wood allowed for an increase in the maximum tensile stress when converting uniaxial stresses to bending stresses (Buchanan, 1990). This enhanced stress was further modified by Gentile et al. (2002), who introduced a factor that increases the allowable tensile stress based on results demonstrating the added benefit of the FRP placed along the extreme tensile fibres of the wood material. The reinforcement was shown to minimize the effects of defects found in the wood and allow for an increase in the tensile rupture strain, which was calculated by multiplying the allowable tensile stress by a factor, α_m. The enhanced tensile stress, $f_{m,r}$, is calculated using Equation (5.25).

$$f_{m,r} = \alpha_m \left[\frac{d(1 + k_3)}{d - c}\right]^{\frac{1}{k_3}} f_t \tag{5.25}$$

where α_m is the modification factor introduced by Gentile et al. (2002), d is the member depth, k_3 is the stress distribution factor, c is the neutral axis depth measured from the compression face, and f_t is the uniaxial tensile strength of the member.

The addition of FRP reinforcement added another possible failure mode to the moment-curvature program. Three failure modes now control the program; 1) the tensile strain in the wood exceeded the allowable bending tensile strain, 2) the compressive strain in the wood exceeded the ultimate compressive strain, or 3) the FRP strain exceeded its limit and the material ruptured. Figure 5.10 shows the representative moment-curvature plot for a 69 x 100 mm^2 cross-section strengthened with two layers of unidirectional fabric applied as U-shaped reinforcement having identical tension and compression moduli of elasticity. The primary vertical axis displays the moment resistance of the cross-section as a function of curvature while the secondary axis displays the depth of the neutral axis as a function of the curvature.

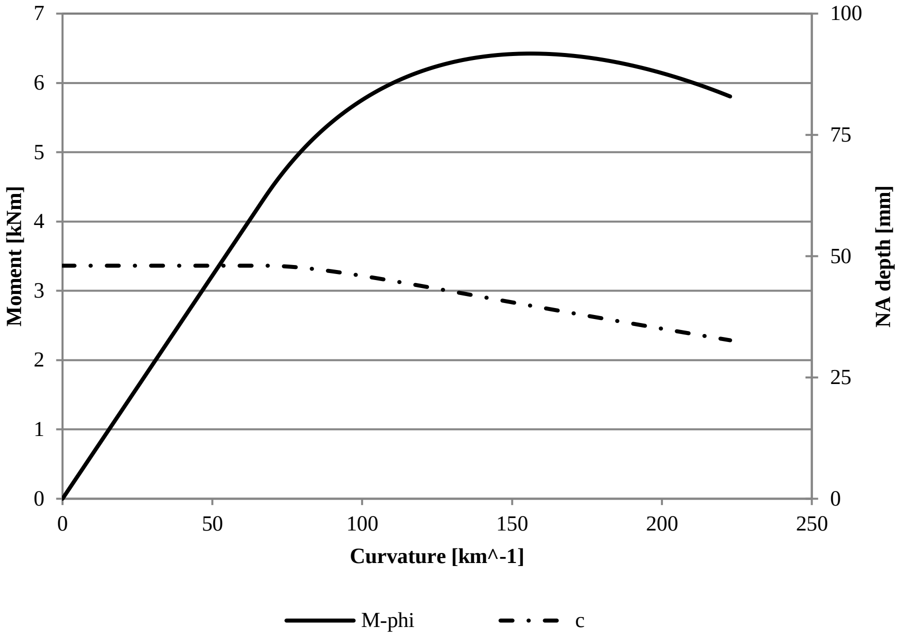

Figure 5.10 - Representative Moment-Curvature Analysis of Reinforced Beams

5.4 Development of Resistance Curves

It is common to represent the flexural behaviour of beams under the form of a resistance curve which visually represents the resistance as a function of displacement. In terms of material modelling and load predicting, generating a similar resistance displacement curve that allows for the comparison of theoretical versus experimental data helps researchers validate their models. The following sections describe the methodology used to derive the displacement equations and the general procedure followed to generate the resistance curve.

5.4.1 Derivation of the Displacement Equation for Linear Elastic Materials

The displacement equations for simply supported beams loaded at third points is presented in Figure 5.11 and are used to derive the equations from first principles.

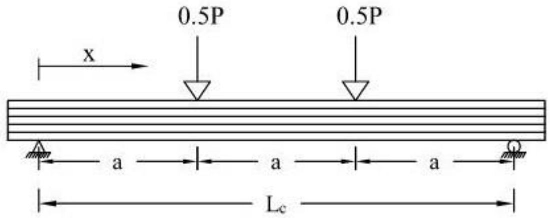

(a) Simple beam: Two equal concentrated loads symmetrically placed

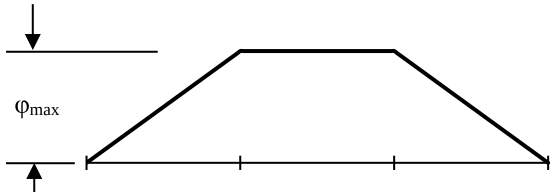

(b) Curvature, φ (1/m)

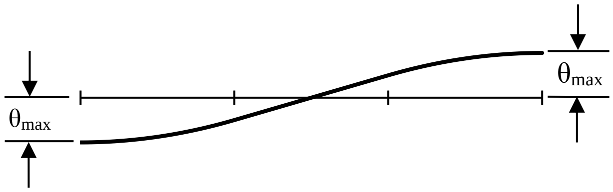

(c) Slope, θ (rad)

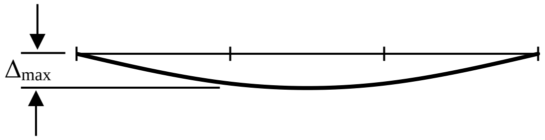

(d) Displacement, Δ (mm)

Figure 5.11 - Beam Diagrams for the Derivation of the Deflection Equation

Solving the basic differential equation of the elastic curve, a closed-form equation for the displacements of linear elastic materials was derived. With known boundary and continuity conditions, the integration constants were calculated in terms of curvature. When generating the resistance curve of the simply supported beam, only the midspan displacement was considered and calculated using Equation (5.26). The full derivation can be found in Appendix E.

$$\Delta_{max} = \frac{23a^2\varphi}{24} \tag{5.26}$$

5.4.2 Beam Displacements of Nonlinear Materials

As stated in Section 5.2, the stress-strain relationship of glulam is nonlinear, where the compressive behaviour is idealized as a bilinear with a descending branch. The displacement equation developed in Section 5.4.1 is only applicable for the linear-elastic portion of the stress-strain relationship. Once the compressive yield strain, ε_{cy}, is exceeded and further increased, the beam continues to deflect and causes geometrical nonlinearity in the member. This nonlinearity results in a curvature diagram that no longer matches the linear diagram shown in Figure 5.11b. To determine the midspan displacement of the yielded beam, a numerical integration VBA program was developed to graph the double integral of the curvature diagram. The program first determined the curvature along the beam based on the assigned midspan curvature and known moment-curvature. The curvature diagram for the beam experiencing compression yielding is shown in Figure 5.12.

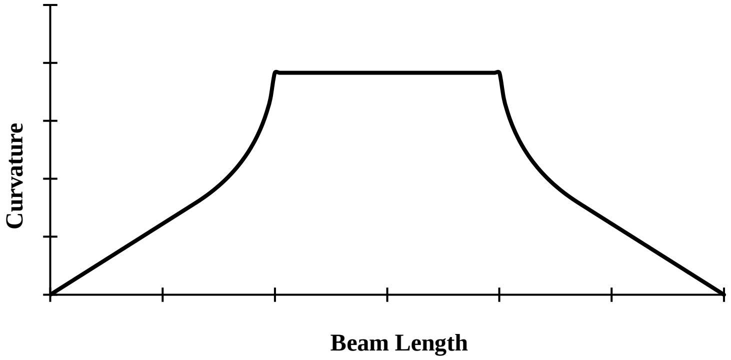

Figure 5.12 - Curvature Diagram of Yielded Beams

Based on the curvature diagram, the program was designed to numerically integrate using the trapezoidal rule, creating the slope and displacement graphs shown in Figure 5.13a and Figure 5.13b, respectively. Based on the loading type, a zero slope at midspan was used to determine the integration constant, which was used to calibrate the slope diagram and determine the shape of the displacement diagram.

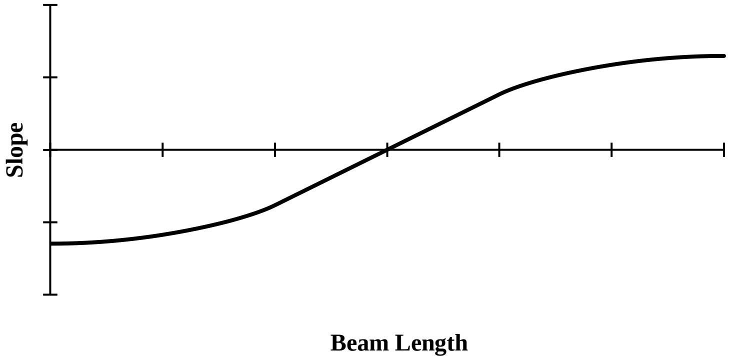

(a) Slope diagram

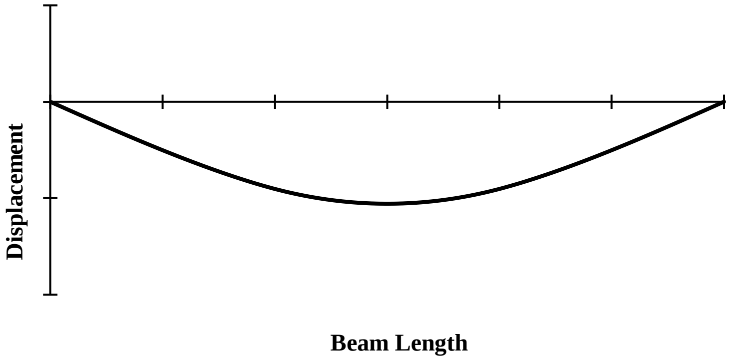

(b) Displacement diagram

Figure 5.13 - Slope and Displacement Diagrams of Yielded Beams

5.4.3 General Procedure

Based on the previously generated moment-curvature data, a program was developed to determine the members' force resistance as a function of displacement (i.e., the resistance curve). The beam diagrams shown in Figure 5.11 along with the procedures outlined in Section 5.4.1 and Section 5.4.2 were used to determine the resistance curves of unreinforced and reinforced beams.

The program followed a procedure that converted a discrete number of data points on the moment-curvature plot into their force-displacement equivalent. The force was calculated by determining the load required to produce a certain moment and the associated displacement was calculated by converting the curvature into a displacement based on the known moment-curvature behaviour. An example of the moment-curvature plot converted to its equivalent force-displacement behaviour is shown in Figure 5.14, representing a 69 x 100 mm^2 unreinforced glulam cross-section.

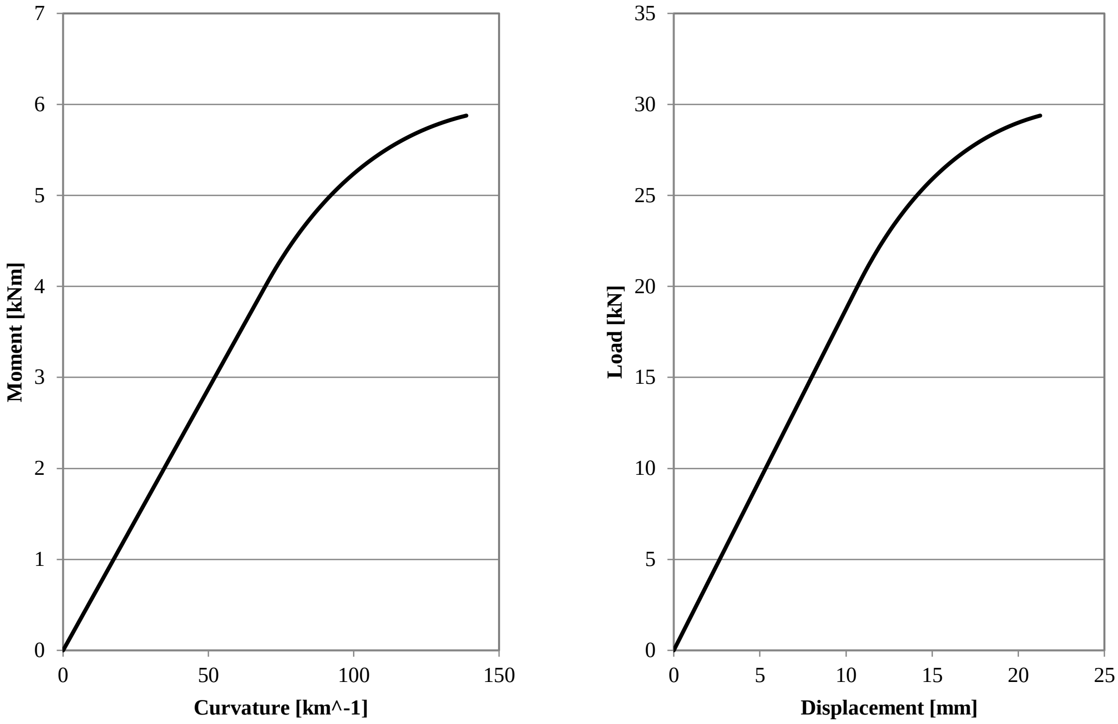

(a) Moment-curvature (b) Force-displacement

Figure 5.14 - Representative Moment-Curvature and Resistance Curve for Unreinforced Beams

5.5 Material Model Verification

In order to validate the accuracy of the proposed model, the resistance curves generated from the VBA program developed herein are compared against experimental and analytical results obtained in Lacroix (2017). The investigation is meant to validate the program by demonstrating similar results when comparing model outputs and their fit compared to experimental results.

Lacroix (2017) investigated the static and dynamic behaviour of FRP-reinforced glulam beams. Two cross-sectional beam sizes (i.e., 86 x 318 mm^2 and 137 x 222 mm^2) were considered for unreinforced and reinforced beams spanning 2,235 mm from support to support. Three different reinforcement schemes were investigated, which included a simple tension reinforcement, a U-shaped reinforcement, and full confinement (Lacroix 2017).

Wood is a viscoelastic material, meaning that the material properties are time-dependent, and the rate of loading can affect the material's behaviour (Lacroix 2017). When dynamic loading is applied to the beam, the strength increases both in tension and compression while maintaining the modulus of elasticity. Based on this, Lacroix (2017) considered four different material properties for both cross-sectional sizes as reproduced in Table 5.2.

Table 5.2 - Model Input Strengths for Lacroix (2017)

Properties	**B-[137]**		**B-[86]**	
	Static	**Dynamic**	**Static**	**Dynamic**
Tension:	13,288	13,288	8,298	8,298
E_t (MPa)	43.3	49.4	35.6	40.6
$f_{t,ult}$ (MPa)	0.00326	0.00372	0.00429	0.00489
$\varepsilon_{t,ult}$ (mm/mm)				
Compression:	7,102	7,102	7,743	7,743
E_c (MPa)	41.9	47.8	35	39.9
$f_{c,y}$ (MPa)	0.00590	0.00673	0.00452	0.00515
$\varepsilon_{c,y}$ (mm/mm)	30.2	34.4	28.8	32.7
$f_{c,ult}$ (MPa)	0.0156	0.0178	0.0147	0.0167
$\varepsilon_{c,ult}$ (mm/mm)	0.17	0.17	0.08	0.08
m	13,288	13,288	8,298	8,298
α	1.21			

The material properties used for the FRP reinforcement can be found in the original publication (Lacroix 2017). Lacroix (2017) summarized the model and experimental results, which was further developed to include the results from the developed VBA program. A comparison of resistance curves was also performed to further validate the program developed for this thesis project (Figure 5.15). Table 5.3 depicts the consistency between both models, with the average model to published result ratios of 1.01 for both the maximum load and the displacements. The results also demonstrate an accurate prediction of experimental results, with published model to experimental ratios of 0.97 and 0.99 for the maximum load and displacement, respectively (Lacroix 2017). A comparison of resistance curves was also performed to further validate the program created for this thesis project as shown in Figure 5.15.

Table 5.3 - Comparison of Model Predictions to Lacroix (2017) Results

Specimen	**Experimental Results**		**Lacroix (2017) Model**		**Model**		**P_{model} / $P_{Lacroix}$**	**Δ_{model} / $\Delta_{Lacroix}$**
	P_{max} (kN)	**$\Delta_{P,max}$**	**P_{max} (kN)**	**$\Delta_{P,max}$**	**P_{max} (kN)**	**$\Delta_{P,max}$**		
B1-[86]			175.7	19.7	177.2	19.9	1.01	1.01
B1.1-[86]			199.0	22.2	202.3	22.7	1.02	1.02
B2-[137]			152.4	25.5	151.0	25.3	0.99	0.99
B2.1-[137]			169.5	28.4	173.2	29.0	1.02	1.02
R1-1	196.7	32.9	186.3	31.4	191.4	32.0	1.03	1.02
R1-2	186.2	28.9						
R1-4.1	216.1	36.9	213.7	36.1	218.8	36.6	1.02	1.01
R2-1	206.3	32.6	186.3	31.4	191.4	32.0	1.03	1.02
R2-2	189.8	33.2						
R2-4.1	208	34.6	213.7	36.1	218.8	36.6	1.02	1.01
R3-1	214.3	38.5	199.2	33.3	197.7	32.8	0.99	0.98
R3-2	230.3	38.6						
R3-4.1	242.3	41.7	224.2	37.1	226.4	37.7	1.01	1.02
R4-1	242.2	40.3	236.5	38.3	230.9	37.5	0.98	0.98
R4-2	226.5	33.8						
R4-3.2	295.7	46.6	270.6	43.8	263.6	42.9	0.97	0.98
R4-4.1	274.6	43.5						
R6-B	234.3	38.9	212.1	36.0	212.9	36.2	1.00	1.01
R8-A	245.5	30.2	252.6	30.0	254.7	30.4	1.01	1.01
						Average	1.01	1.01
						St. Dev	0.02	0.02
						COV	0.017	0.015

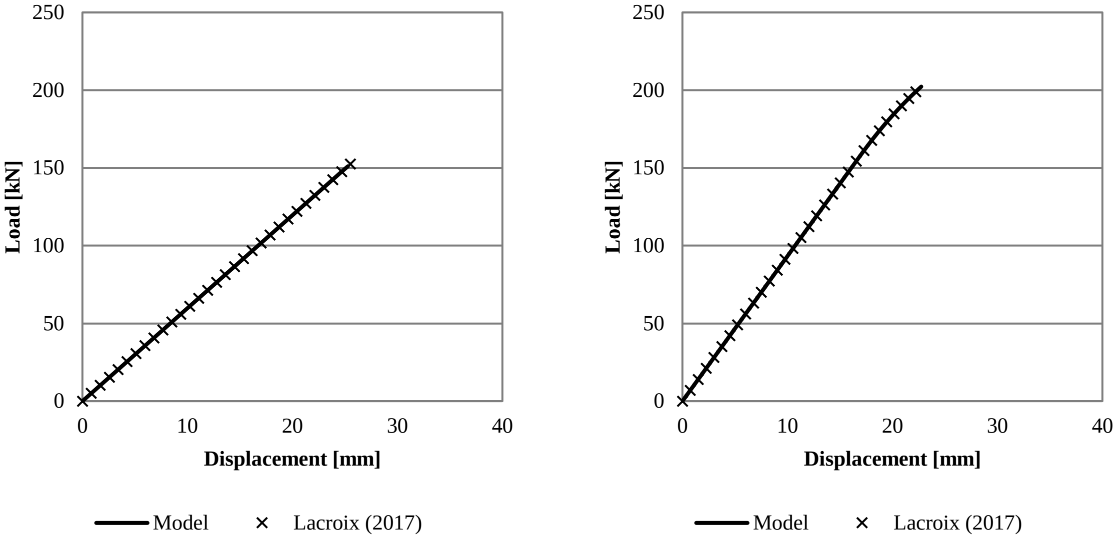

(a) Unreinforced; [137]

(b) Unreinforced dynamic; [86]

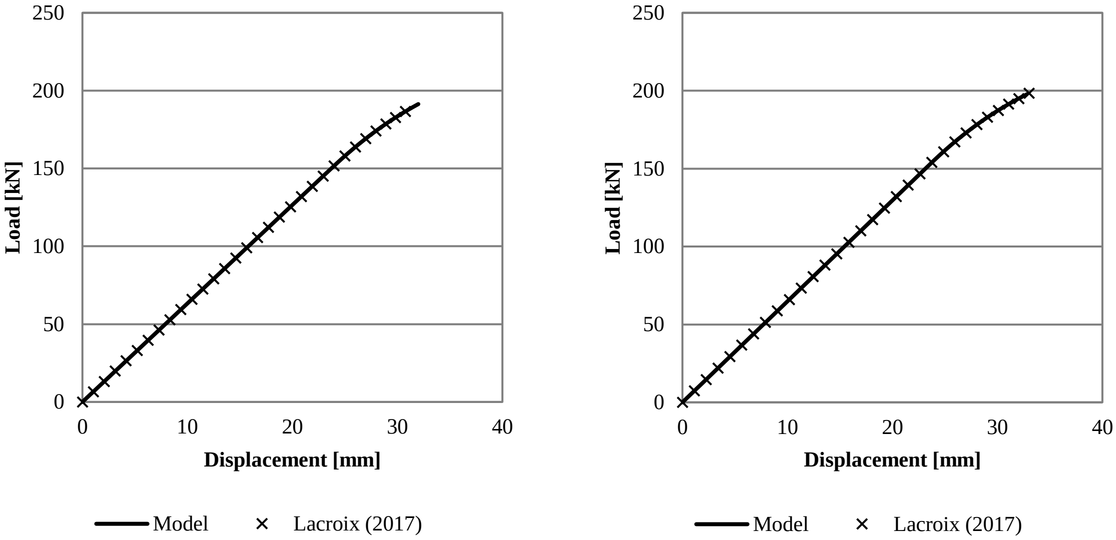

(c) Two layers simple tension; [137]

(d) Two layers U-shaped; [137]

Figure 5.15 - Comparison of Model to Published (Lacroix 2017) Resistance Curves

Chapter 6
Discussion

6.1 General

A total of thirty glulam beams were tested to failure under static four-point loading. The experimental program was divided into two stages investigating the flexural performance of GFRP reinforced beams. The following sections discuss the findings, specifically, the effects of simple tension and U-shaped reinforcement, the effects of transverse reinforcement in the shear region, and the relative performance of the partially and fully confined beams. In addition, the results from the material predictive model, which accounts for the reinforcement configurations and thickness of reinforcement provided, are presented.

6.1 Behaviour of Unreinforced Glulam Beams

A total of five unreinforced beams were tested to failure under four-point bending. The resistance curve of unreinforced beams is observed to behave in a linear fashion with some level of softening caused by compression yielding prior to the wood tensile failure. Since glulam beams consist of different laminates glue-pressed together, the variability and location of naturally occurring defects can lead to wood tensile failures occurring prior to the maximum resistance. As shown in Figure 6.1a, the U-01 and U-02 specimens both experienced some tensile failures prior to the maximum resistance which affected the remaining portion of the curves (i.e., increased softening which in turn increased the maximum displacement). The remainder of the unreinforced specimens shown in Figure 6.1b better represent the expected behaviour, with the resistance following a linear behaviour until the compression softening occurs. Although not uncommon to experience premature tensile failures, recognizing that the outermost tension failure does not always coincide with the peak load will be important in the comparison of the experimental data to that predicted by the material model. An example of the members experiencing tensile failures prior to achieving the maximum resistance is shown in Figure 6.2.

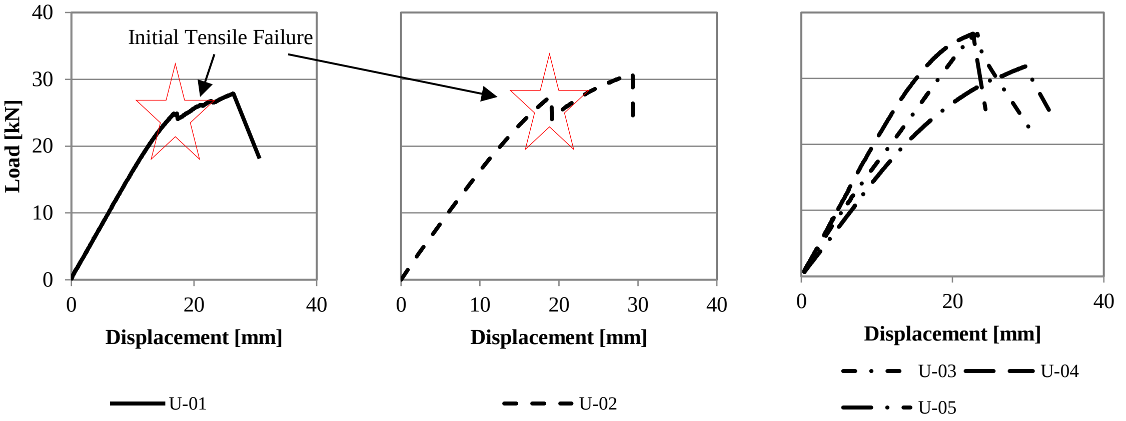

(a) Wood tensile failure prior to P_{max} (b) Elastic behaviour up to P_{max}

Figure 6.1 - Behaviour of Unreinforced Glulam Beams

(a) At initial failure

(b) At P_{max}

Figure 6.2 - Comparison of Initial Failure to Failure at P_{max} for the U-02

6.2 Effects of Simple Tension and U-shaped GFRP Reinforcement

Fourteen beams were tested destructively under four-point bending in stage 1 to investigate the effects of simple tension and U-shaped GFRP reinforcement on the flexural behaviour of glulam beams. Unidirectional fabric (i.e., 0°) was used in all reinforcement schemes considered in stage 1. Table 6.1 presents the average maximum load (P_{max}), displacement ($\Delta_{P,max}$), and bending stiffness (K) for the beams tested in stage 1 along with the increases observed for the reinforced beams compared to the control beams.

Table 6.1 - Effect of Simple Tension and U-shaped GFRP Reinforcement

Specimen Average	**P_{max}[a] (kN)**	**$\Delta_{P,max}$[b] (mm)**	**K[c] (N/mm)**	**P / $P_{unreinforced}$**	**Δ / $\Delta_{unreinforced}$**	**K / $K_{unreinforced}$**	**Failure Mode**
Unreinforced [100]	32.8	26.0	1,702	-	-	-	Flexure
R1 [100]	34.7	18.8	2,137	1.06	0.72	1.26	Shear
R2 [100]	47.2	26.6	2,479	1.44	1.02	1.46	Shear
R3 [100]	41.2	25.3	2,126	1.26	0.97	1.25	Shear
R4 [100]	46.8	27.3	2,552	1.43	1.05	1.50	Shear

[a] Average maximum load resistance
[b] Average displacement at maximum load
[c] Average bending stiffness

As shown in Table 6.1, an increase in maximum load and bending stiffness is observed for all reinforced beams on average. The addition of two unidirectional GFRP sheets applied longitudinally (i.e., R1) increased the capacity and stiffness of the beams on average by a factor of 1.06 and 1.26, respectively. Reinforcement scheme 2, which had four layers of unidirectional GFRP sheets applied on the tension face of the beam, demonstrated increases in resistance and stiffness on average by factors of 1.44 and 1.46, respectively. The displacement at maximum load for both simple tension reinforcement schemes (i.e., R1 and R2) did not proportionally increase relative to the unreinforced beams. All of the R1 beams failed at an average of 0.72 times less than that achieved in the unreinforced beam tests, whereas the R2 beams showed an increase of 1.02 times the displacement of unreinforced beams, which can be considered negligible. The significant difference in the change of resistance versus the change of maximum displacement observed in reinforcement schemes 1 and 2 can be attributed to a change in failure mode. The addition of simple tension reinforcement altered the failure mode from a wood tension failure to a horizontal shear failure or stress concentration failure located where the simple tension FRP reinforcement sheets were terminated. The FRP was shown to adequately increase the bending stiffness and reinforced the wood fibres, which allowed the specimens to support greater loads at smaller displacements. However, the undesirable change in failure mode did not allow the reinforcement to further increase the beams' bending performance. As such, the premature de-bonding caused by the wood failing in tension and pushing outwards on the FRP as reported by previous studies (e.g., Dorey & Cheng, 1996; Hernandez et al., 1997; Lacroix & Doudak, 2018; Sonti et al., 1996) was not observed.

Table 6.1 presents similar results for the beams reinforced with unidirectional GFRP sheets applied as U-shaped reinforcement (i.e., R3 and R4). When compared to the unreinforced beams, average resistance and stiffness increases of 1.26 and 1.25, respectively, were observed for the beams reinforced with two layers of U-shaped reinforcement (i.e., R3). R4 beams, which were reinforced with four layers of U-shaped GFRP, experienced average increases in resistance and stiffness of 1.43 and 1.50, respectively. The displacements at maximum loads for the R3 and R4 beams were not proportional to the capacity and stiffness increases as observed for the R1 and R2 beams. When compared to the unreinforced beams, a decrease of 0.03 times the displacement was observed for the R3 beams whereas a slight increase of 1.05 was observed for the R4 beams. Providing tension reinforcement that extended up to the mid-depth of the beam did not allow the beams to attain a flexural failure as the FRP-reinforced member failed in horizontal shear that propagated through the reinforcement fabric (Figure 6.3). Specimen R2-01 was able to resist larger loads at increased displacements (Figure 6.3a) when compared to the unreinforced average; however, these increases led to a horizontal shear failure initiating through the wood and extending out to the face of the GFRP (Figure 6.3b). The unidirectional fabric applied longitudinally (i.e., along the span of the beam) has the majority of the FRP fibres running parallel to the span, resulting in little to no reinforcement in the transverse direction which could have reinforced the beam against shear stresses.

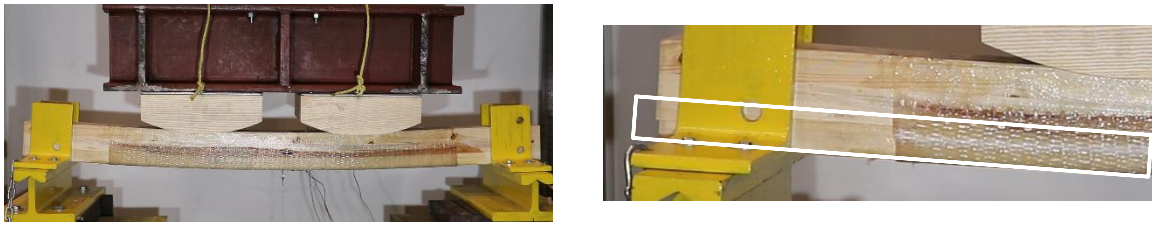

(a) At P_{max} (b) Initial failure

Figure 6.3 - Horizontal Shear Failure of R2-01

Previous research (e.g., Buell & Saadatmanesh, 2005; Lacroix, 2017) has shown that reinforced timber beams that fail in flexure experienced increased deflection at maximum resistance in the range of 1.37 to 2.91 compared to that of the unreinforced beams. The key component to achieving any ductility is to engage wood yielding in compression by strengthening the wood tensile fibres. Although FRP was provided, the configurations investigated herein were not able to engage the wood in compression. Rather, it changed the failure mode from wood failing on the tension side (e.g., simple tension, cross-grain tension, splintering tension) to horizontal shear, which is also considered a brittle failure mode. Hence, only the maximum resistance and stiffness benefited from the addition of FRP.

When comparing the effect of U-shaped reinforcement (i.e., R3 and R4) to the simple tension configuration (i.e., R1 and R2), the overall flexural behaviour of the specimens is very similar (Figure

6.4). As shown in Figure 6.4a, the specimens reinforced with 2 layers of U-shape reinforcement (i.e., R3) increased in resistance and displacement at maximum resistance in comparison to the R1 beams (i.e., two layers of simple tension) by an average of 1.19 and 1.35, respectively. On the other hand, the specimens tested with 4 layers of reinforcement did not benefit from the U-shaped configuration in comparison to the simple tension. As shown in Figure 6.4b, negligeable differences are observed in the two reinforcement configurations (i.e., 4 layers of simple tension vs. 4 layers of U-shaped). The maximum capacity of the four layer U-shaped beams (i.e., R4) was on average approximately equal to the maximum resistance observed for the four layer simple tension (i.e., R2) beams, whereas the displacement at maximum resistance and stiffnesses were observed to be slightly higher than the R2 beams by an average of 1.02 and 1.03, respectively.

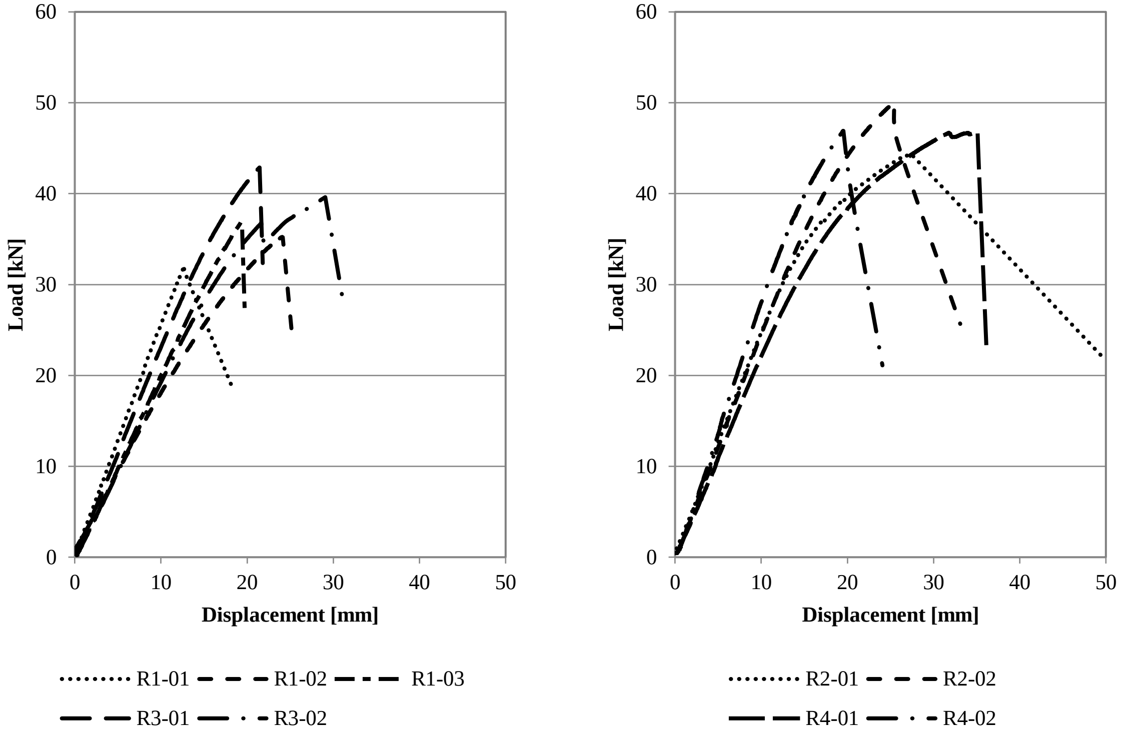

(a) Two layers of reinforcement

(b) Four layers of reinforcement

Figure 6.4 - Comparison of Simple Tension and U-shaped Reinforcement Configurations

The reinforcement schemes investigated in stage 1 have been examined in past research programs on different cross-sectional dimensions and span lengths and it has been shown that the beams reinforced with simple tension reinforcement are prone to premature failures resulting from de-bonding of the reinforcement (Dorey & Cheng, 1996; Lacroix & Doudak, 2018; Moody et al., 1983; Sonti et al., 1996).

While the research program in this thesis included the simple tension reinforcement as a base case to evaluate the behaviour of FRP-reinforced beams having a shear span-to-depth (a/d) ratio of 4, no such premature failure was observed in this study due to the fact that the presence of horizontal shear and stress concentration failures were prominent.

Various factors can be identified as possible reasons for these unwanted failure modes. For unreinforced beams, the ASTM D198 "Standard Test Methods of Static Tests of Lumber in Structural Sizes" standard recommends a span-to-depth (a/d) ratio of 4-6 for tests aiming to determine flexural strength properties and states that specimens with a/d ratios of 2.5 would produce a significant number of shear failures (ASTM, 2021). As previously stated, the current study chose a shear span-to-depth ratio of 4 which falls on the lower end of the recommended range. For all unreinforced specimens, wood tension-dominated failure (e.g., simple tension, cross-grain tension, splintering tension) was observed. However, the increase in wood tensile strength provided by a 2% reinforcement ratio (i.e., the smallest ratio investigated) proved significant enough to alter the failure mode from flexure to shear. The provided FRP reinforcement contributed to stiffening the beams, thereby allowing for greater loads to be sustained at smaller tensile wood strains which ultimately lead to the horizontal shear failure. Based on the current observations, the stress concentration failures can be attributed to the development length or the length of the reinforcement extending beyond the loading points. Although the main purpose of the reinforcement is to increase the tensile capacity of the beam at locations of large bending stresses, in order to remain effective, the reinforcement is required to be adequately anchored or bonded, to allow the transfer of stresses. Figure 6.5 shows a representative failure mode for the beams reinforced with simple tension reinforcement in the current study compared to what has traditionally been reported in the literature. Minimal deflection was observed at maximum loads (Figure 6.5a), where the sudden stress concentration failure (Figure 6.5b) resulted in a complete loss of load-carrying capacity. It is important to note that an adequate bond was maintained between the wood and FRP, with the failure initiating and extending solely through the wood material. The failure mode observed in stage 1 is entirely different from what has been observed in the literature where the wood was observed to fail and push outwards on the FRP thereby causing premature de-bonding (Figure 6.5c).

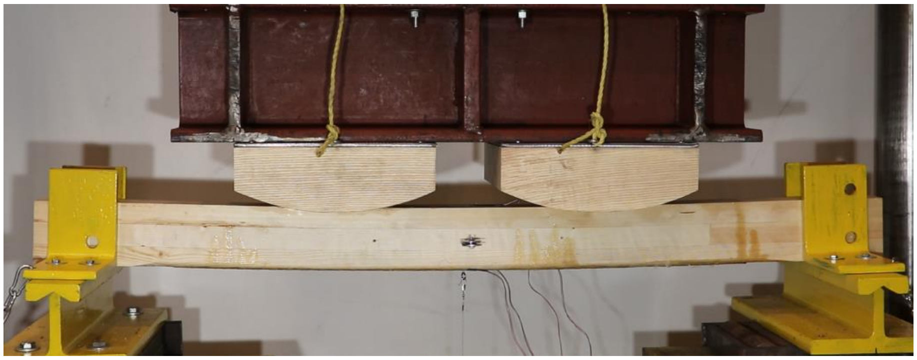

(a) R1-01 at P_{max}

(b) R1-01 at initial failure

(c) Representative example of premature de-bonding of FRP due to the wood (Lacroix, 2017)

Figure 6.5 - Stress Concentration Failure of R1-01

The configurations investigated in stage 1 clearly show the importance of considering the effect of the FRP reinforcement, the span-to-depth ratio of the reinforced beam as well as the length of the FRP reinforcement provided as they all significantly impact the observed failure mode (e.g., shear). Lacroix et al. (2021) have also reported similar observations for light-frame walls reinforced with FRP under simulated blast load for which the quantity of reinforcement was significant enough to change from a flexural failure mode at the mid-span of the studs to a bearing failure at the supports. Although there are significant studies on the development length of FRP for concrete members, there are no guidelines for wooden members.

6.3 Effect of Transverse GFRP Reinforcement

The second stage of the experimental program investigated reinforcement schemes aimed at addressing the undesirable failure modes observed in the prior stage (e.g., horizontal shear and stress concentrations). The horizontal shear and stress concentration failures observed in stage 1 were addressed in stage 2 by providing partial-length GFRP confinement (e.g., Figure 6.6a and Figure 6.6b) and full-length GFRP confinement (Figure 6.6c).

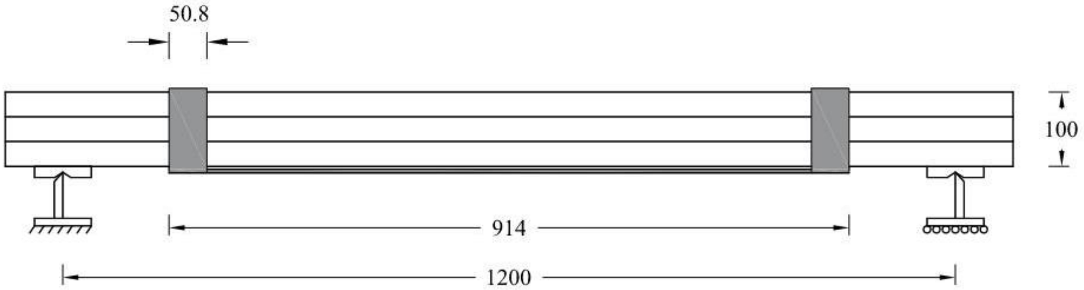

(a) Partial confinement - Hoops

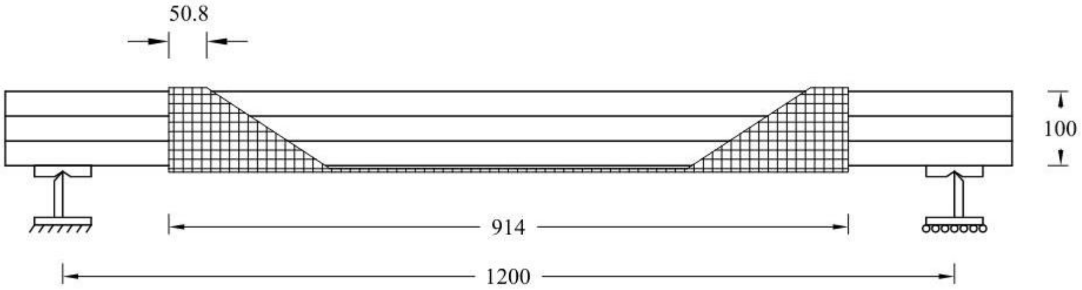

(b) Partial confinement - Tails

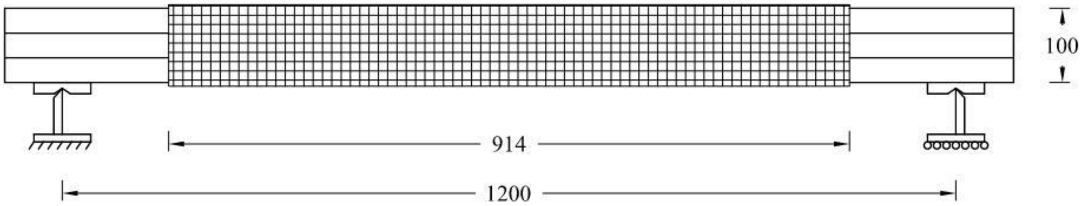

(c) Full confinement

Figure 6.6 - Transverse Reinforcement Provided in Stage 2

The main purpose of providing longitudinal reinforcement is to increase the tensile strength of the composite bending member to allow for a more ductile failure mode. Lacroix & Doudak (2018) investigated the effects of localized confinement located within the high-bending stress region and although it was observed to adequately confine the high-bending stress region, the failure extended into the outer shear regions causing the de-bonding of the simple tension and U-shaped reinforcement. Experimental tests conducted on fully confined beams (i.e., extending along the entire length of the beam) were carried out by Lacroix and Doudak (2020) with the intention of preventing the shear region de-bonding failure previously observed. By providing full-length confinement reinforcement composed of multi-directional fabrics applied in various configurations, the authors were able to observe significant ductility increases of up to 3.6 times that were obtained for the unreinforced specimens. In an effort to address some of the accessibility issues related to fully confined beams, the confinement reinforcement applied in the shear region developed in this research program is based on the previous research demonstrating the need for FRP anchoring outside of the high-bending stress regions to allow for the transfer and retention of stresses.

Table 6.2 presents the results from the reinforced beams tested in stage 2 (e.g., R5 – R10) and includes the results of the unreinforced and reinforced beams tested in stage 1 for comparison.

Table 6.2 - Effect of Transverse GFRP Reinforcement

Specimen Average	**P_{max}[a] (kN)**	**$\Delta_{P,max}$[b] (mm)**	**K[c] (N/mm)**	**Failure Mode**
Unreinforced [100]	32.8	26.0	1,702	Flexure
R1 [100]	34.7	18.8	2,137	Shear
R2 [100]	47.2	26.6	2,479	Shear
R3 [100]	41.2	25.3	2,126	Shear
R4 [100]	46.8	27.3	2,552	Shear
R5-01, R6-01 [100]	37.6	21.0	2,336	Shear and Flexure
R5-02, R6-02 [100]	38.4	22.1	2,104	Shear and Flexure
R7 [100]	53.2	34.0	2,583	Flexure
R8 [100]	58.5	26.1	2,641	Flexure
R9 [100]	34.4	23.5	1,746	Shear and Flexure
R10 [100]	45.7	34.0	2,153	Shear and Flexure

[a] Average maximum load resistance
[b] Average displacement at maximum load
[c] Average bending stiffness

Reinforcement schemes 5 and 6 investigated the effects of providing transversely applied GFRP hoops confining the ends of simple tension reinforcement (Figure 6.6a). As shown in Table 6.2, the addition of GFRP hoops confining the two simple tension reinforcement sheets (i.e., R5-01 and R6-01) increased the capacity and stiffness by average factors of 1.14 and 1.37, respectively, when compared to the unreinforced beams. When compared to the beams comprised solely of two layers of longitudinal reinforcement (i.e., R1), the addition of hoops increased the average resistance, displacement at maximum resistance, and stiffness by factors of 1.08, 1.12, and 1.09, respectively. It should be noted that in addition to the aforementioned increases, the specimens detailed with the transverse hoops were able to prevent the stress concentration failures that proved to be detrimental in stage 1.

The specimens reinforced with four layers of simple tension and transverse hoops (i.e., R5-02 and R6-02) did not benefit from the additional reinforcement. When comparing the R5-02 and R6-02 beams to those solely comprised of simple tension reinforcement (i.e., R1 and R2) referred to in Table 6.2, no significant increase in terms of load-carrying capacity or midspan displacement is observed. Despite this observation, the presence of GFRP hoops allowed the beams to fail in wood tension or a combination of wood tension and shear. As shown in Figure 6.7, the stress concentration failure associated with specimen R2-01 (Figure 6.7a) is significantly more prominent than that observed for the specimen having identical tension reinforcement with the addition of the hoops (Figure 6.7b).

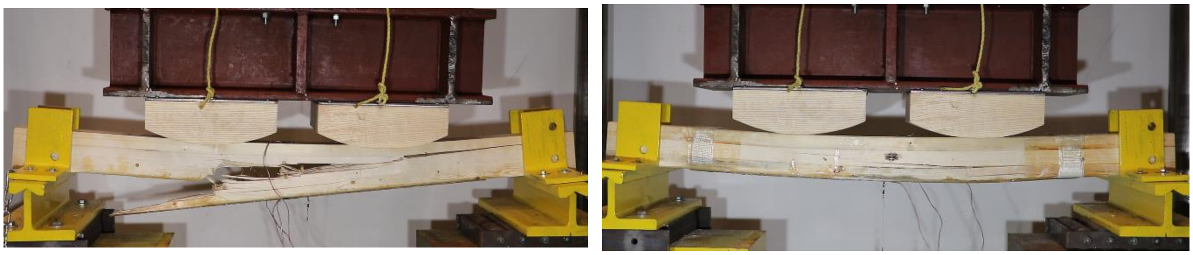

(a) R2-01 (b) R6-02

Figure 6.7 - Confinement Effect of GFRP Hoops

To demonstrate the potential of the GFRP reinforcement, fully confined reinforcement configurations were designed and tested to compare against the control specimens. The R7 and R8 beams, each comprising of a minimum of two layers of bidirectional (0/90°) confinement, were shown to benefit the most in terms of strength, stiffness, and ductility. The specimens having two layers of U-shaped tension and two layers of confinement reinforcement (i.e., R7) increased in resistance, displacement at maximum resistance, and stiffness by average factors of 1.62, 1.31, and 1.52, respectively, when compared to the unreinforced control beams. Similar resistance and stiffness increases were observed for the specimens reinforced with four layers of confinement sheets (i.e., R8). As shown in Table 6.2, the R8 beams were able to carry the largest load, with an average increase of 1.78 relative to the unreinforced beams. The primary benefit of providing confinement reinforcement that spans beyond the high-bending stress region is that the FRP was able to contain the wood damage to a small area. As shown in Figure 6.8a, the severely damaged beam was able to resist the loading with the help of the reinforcement surrounding the damaged area. Figure 6.8b further demonstrates the reinforcement ability to localize the failure to a cross-section, with little to no damage observed in the wood outside of this region.

(a) Confined beam subjected to bending loads

(b) Dissected beam

Figure 6.8 - Contained Wood Damage

The fully confined beams (i.e., R7 and R8) also improved the post-peak behaviour of the beams. As shown in Figure 6.9, all fully reinforced beams demonstrated some level of post-peak behaviour that exceeded the brittle failure behaviour observed for the U-shaped reinforcement (R3) and unreinforced (U) beams. This increased post-peak resistance can be attributed to the fact that the full-length confinement contained the damage to a small area, thereby forcing the failure to happen in a localized region as opposed to following the path of least resistance and propagating throughout the beam.

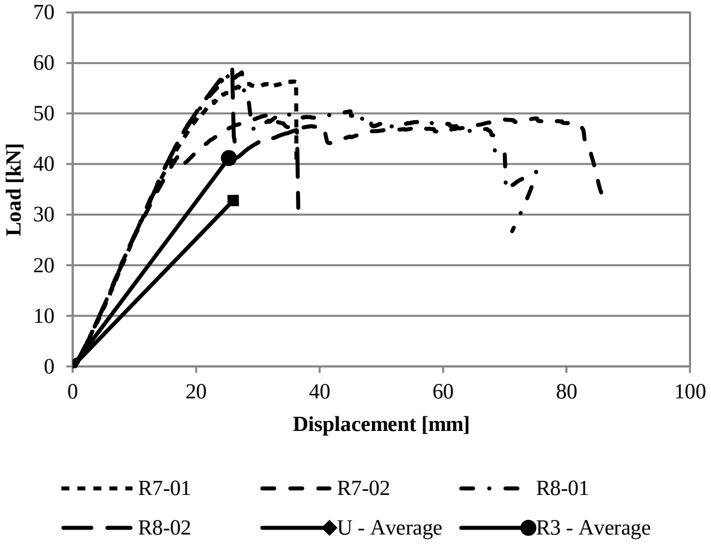

Figure 6.9 - Post-Peak Behaviour of Fully Confined Beams

Although the full-length confinement demonstrated significant improvements on the behaviour, this configuration would not be achievable for many in-situ rehabilitation projects having accessibility constraints. Future studies would need to investigate the benefit of more heavily reinforced beams, where a certain confinement reinforcement ratio could be used to better optimize the FRP.

Intermediate reinforcement schemes were thus designed and evaluated to address the accessibility issues along with benefiting from the confinement reinforcement as observed for the R7 and R8 beams. By providing simple tension reinforcement in the high-bending stress region that extended up to the compression face in the shear region (Figure 6.6b), the reinforcement configurations (i.e., R9 and R10) were able to increase the tensile strength at midspan and address the undesirable failure modes observed in the shear regions. The specimens reinforced with four layers of bidirectional (0/90°) reinforcement tails (i.e., R10) demonstrated significant potential. As shown in Table 6.2, the tail reinforcement increased the resistance, displacement at maximum resistance, and stiffness by average factors of 1.40, 1.31, and 1.26, respectively, when compared to the unreinforced beams. When compared to the R1 specimens tested in stage 1, the tail reinforcement configuration contributed to an increase in resistance and displacement at maximum resistance by average factors of 1.32 and 1.81, respectively. Figure 6.10 compares the reinforced beams comprised of tail reinforcement (i.e., R10) to the average result of the beams reinforced with two layers of simple tension.

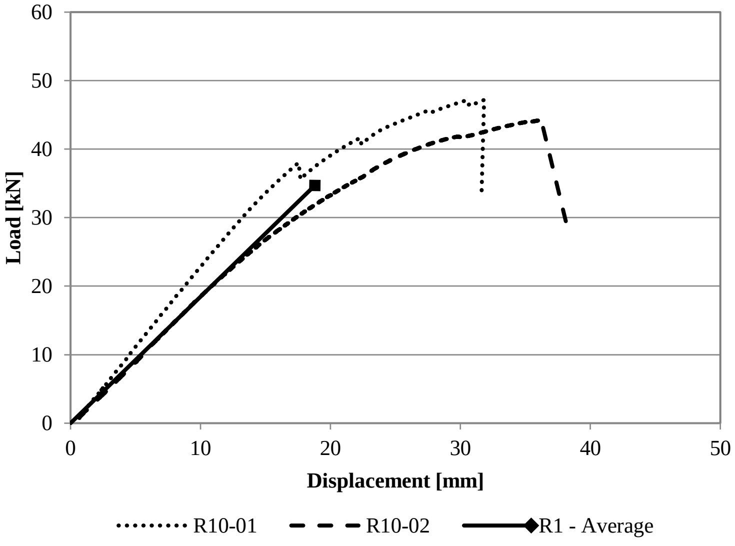

Figure 6.10 - Comparison of Tail Reinforcement to Simple Tension

As shown in Figure 6.10, higher loads and larger displacements were attained for the R10 beams when compared to the R1 beams. The confinement reinforcement provided in the shear region strengthened the beams and allowed the engagement of more wood yielding in compression, therefore allowing the resistance curve of the R10 beams to extend past the R1 average. Although larger displacements were attained, the failure mode was still a brittle one with little to no post-peak resistance in comparison to R7 and R8. Nonetheless, the tail configuration prevented the undesirable failure modes observed in beams reinforced with simple tension (Figure 6.11a), with the damage remaining within the shear region confinement regions (Figure 6.11b). The rupture of GFRP fabric shown in Figure 6.11b represents not only a good bond between the wood and the reinforcement but also indicates that the amount of reinforcement was adequate in providing resistance without overcompensating which has been shown to result in brittle failures (Figure 6.11a). The comparison of the four layer bidirectional (0/90°) GFRP tail to the two layer unidirectional (0°) GFRP simple tension was based on the fact that the bidirectional fabric is assumed to only have half of the FRP fibres are oriented in the longitudinal direction of the beam span when compared to the unidirectional fabric. By comparing the average composite bending stiffness of the two configurations, a negligible difference was calculated between the two (Table 6.2) which demonstrates a similar initial behaviour that can be used to validate the potential of the tail reinforcement.

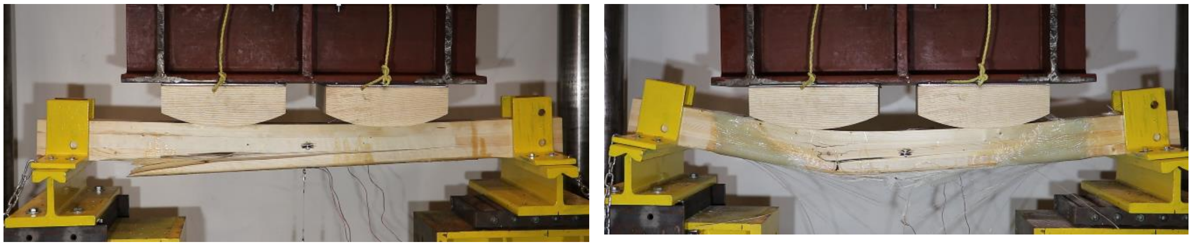

(a) R1-01; Stress Concentration

(b) R10-01; Flexure

Figure 6.11 - Failure Mode Comparison of Tail Reinforcement to Simple Tension

The two beams reinforced with two layers of unidirectional (0°) simple tension and two layers of tail GFRP fabric (i.e., R9) were deemed outliers based on the bending stiffness and a series of unfortunate events that occurred during the application process. As shown in Figure 6.12, the average resistance curve for the R9 beams have a bending stiffness that more closely resembles the stiffness observed for the unreinforced beams. Based on both R9 and R1 reinforcement configurations having two layers of simple tension fabric along with the two extra bidirectional layers in the R9 configurations, the difference in bending stiffness was determined to be caused by both material variability and application errors. During the application process of the R9 beams, a previous GFRP layup was removed from the specimens due to improperly mixed epoxy. The specimens were resurfaced, and the application of the two unidirectional simple tension and bidirectional tails were then reapplied with a proper mix of epoxy. Although precautionary measures were taken to avoid bond failure, the adhesion between the wood and reinforcing material did not create the composite behaviour otherwise documented in this research program. Figure 6.13a depicts the lack of proper bonding that occurred on specimen R9-01, where the circled area represents a smooth surface between the wood and the reinforcement that should not be present if the two materials were adequately bonded together. An example of a failed specimen that had an adequate bond is shown in Figure 6.13b, where the delamination of the FRP away from the specimen resulted in the rupture of wood fibres connected to the reinforcement. This evidence validates the importance of the application process and the need for an adequate bond.

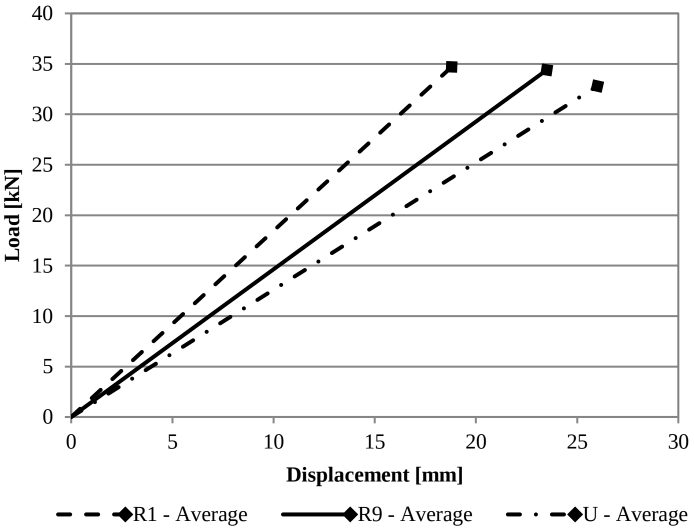

Figure 6.12 - R9 Results Compared to Simple Tension and Unreinforced Beam Averages

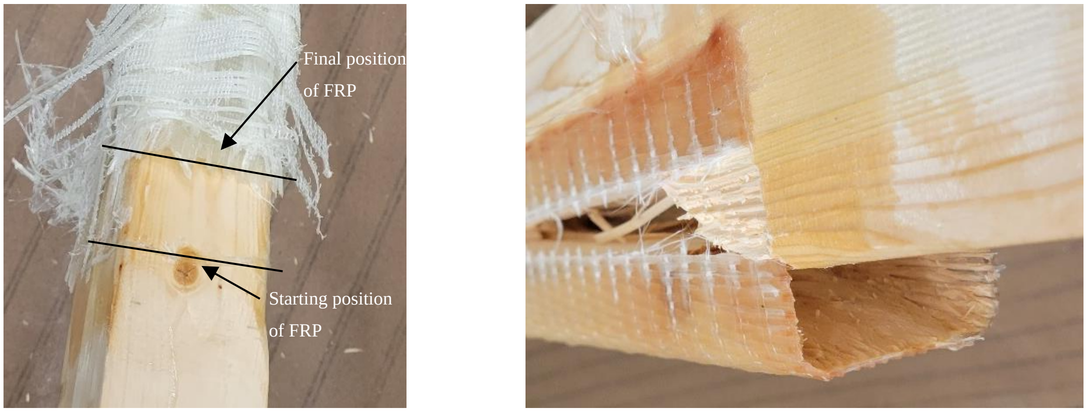

(a) Improper bond (b) Adequate bond

Figure 6.13 - Bond Failure

6.4 Effect of Beam Depth

The effect of beam depth was investigated on two schemes involving partial-length confinement, as shown in Figure 6.14. Due to the larger span, two transverse hoops were provided to confine the simple tension reinforcement (Figure 6.14a) as it was assumed that a single hoop on either side would not have been sufficient. The second reinforcement scheme considered is that consisting of the tail reinforcement as shown in Figure 6.14b. The reinforcement configurations developed for the [160] beams were designed to produce reinforcement ratios equal to the ratios used for the reinforced [100] beams. The three layers of unidirectional (0°) simple tension reinforcement provided in R11 beams resulted in a reinforcement ratio of 2%, which is comparable to the 2% reinforcement ratio calculated for [100] beams reinforced with two layers of simple tension (i.e., R1). The six layer reinforcement configuration made up entirely of bidirectional (0/90°) tails (i.e., R12) resulted in a reinforcement ratio of 2.5%, which is comparable to the ratio of 2.6% calculated for the four layers of GFRP tails provided in the R10 beams.

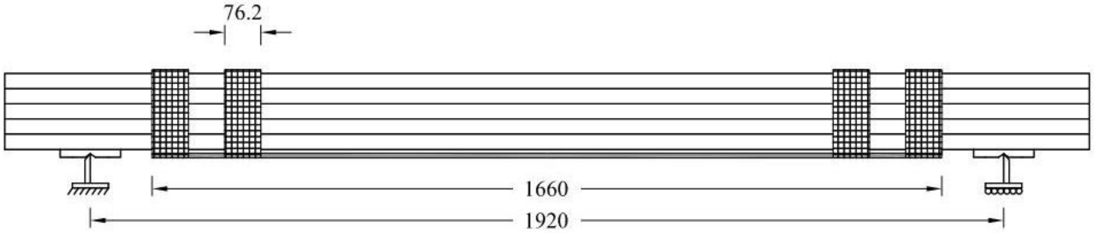

(a) Partial confinement - Hoops

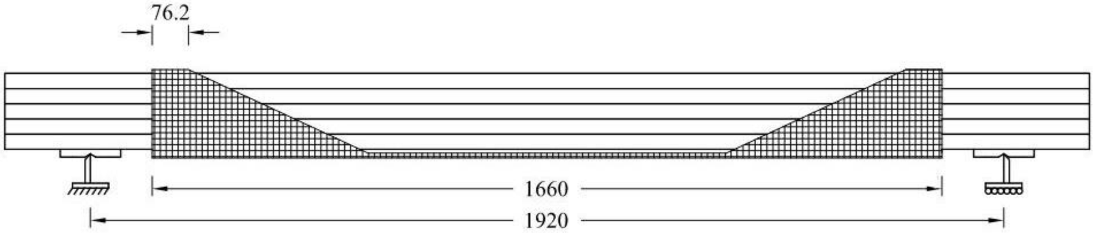

(b) Partial confinement - Tails

Figure 6.14 - Reinforcement Schemes Investigated on the [160] Beams

Due to the limited quantity of available beam length having a cross-sectional dimension of 69 x 160 mm^2 (i.e., [160] beams), no unreinforced beams were tested to failure. Aiming to extract data on the unreinforced specimens, a non-destructive loading protocol was developed such that all of the beams were loaded up to 10 kN and then unloaded. The results from the non-destructive and destructive testing are presented in Table 6.3.

Table 6.3 - Unreinforced and Reinforced Bending Stiffnesses for [160] Beams in Stage 2

Specimen	**P_{max}[a] (kN)**	**$\Delta_{P,max}$[b] (mm)**	**K_U[c] (N/mm)**	**K_R[d] (N/mm)**	**Failure Mode**
R11-01 [160]	62.9	36.2	1,699	2,059	Flexure
R11-02 [160]	60.0	36.8	1,734	2,117	
Average	61.4	36.5	1,717	2,088	
R12-01 [160]	63.8	36.2	1,807	2,134	Flexure
R12-02 [160]	67.7	35.9	1,867	2,245	
Average	65.8	36.0	1,837	2,190	

[a] Maximum load resistance
[b] Displacement at maximum load
[c] Unreinforced bending stiffness
[d] Reinforced bending stiffness

The reinforcement schemes for the [160] beams were effective in preventing premature de-bonding of the GFRP tension reinforcement and to allow the beams to failure in flexure. Figure 6.15 shows representative failure modes of reinforcement schemes 11 and 12.

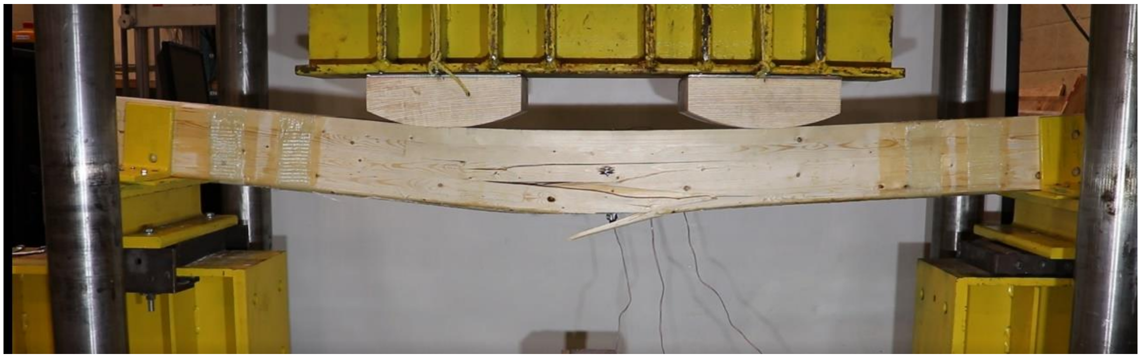

(a) Partial confinement - Hoops

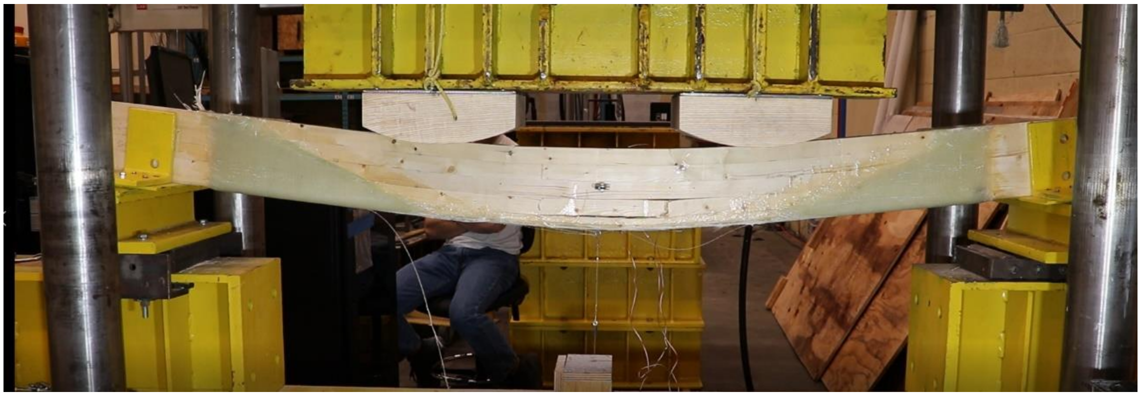

(b) Partial confinement - Tails

Figure 6.15 - Representative Failure Modes for the [160] Beams

The reinforcement scheme using the tail reinforcement (R12) has shown promising results by not only providing increased stiffness compared to the unreinforced beams, but also by providing some level of post-peak resistance in comparison to the reinforcement schemes with only the transverse hoops as shown in Figure 6.16. Whereas the hoops were effective in preventing premature debonding, they did not contribute to any sustained post-peak resistance. Therefore, the concept of using a hybrid between simple tension reinforcement and full-length confinement in the form of a “tail” reinforcement scheme shows significant potential for applications where full access to a member is not possible despite having tested only two specimens. The “tail” configuration also contributes to a decrease in FRP fabric as well as required epoxy, thereby reducing the overall cost of the reinforcement or rehabilitation.

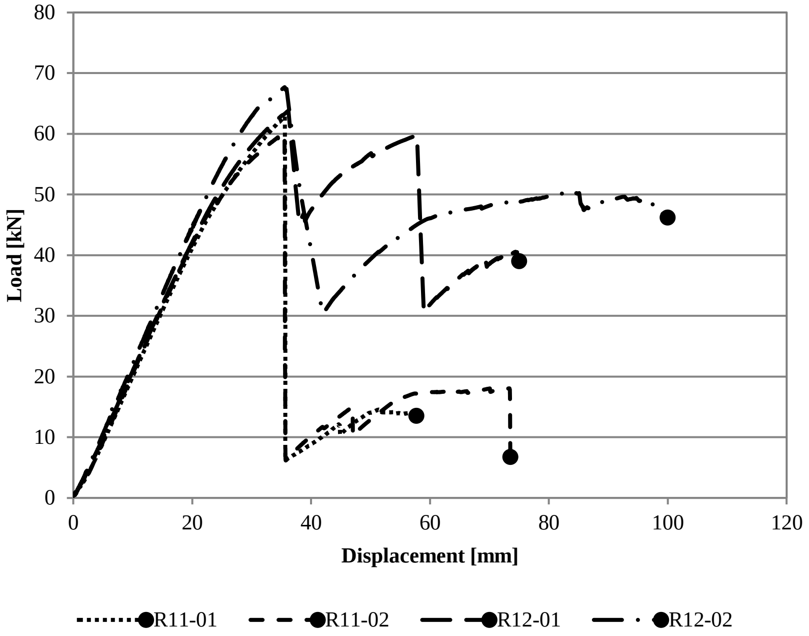

Note: ● End of useable displacement data.
Figure 6.16 - Resistance Curves of Reinforced [160] Beams in Stage 2

Table 6.4 summarizes the bending stiffness increases for the reinforcement configurations that have comparable reinforcement ratios. The results show that the stiffness increases provided by the reinforcement for the deeper [160] beams are less pronounced than those calculated for the [100] beams. Ductility ratios ranging from 2.08 to 2.78 were attained for the tail configurations.

Table 6.4 - Effect of Beam Depth on Bending Stiffness

Specimen Average	**K[a] (N/mm)**	**$K_{reinforced}$ / $K_{unreinforced}$**
Unreinforced [100]	1,702	-
R1 [100]	2,137	1.26
R10 [100]	2,153	1.26
Unreinforced [160]	1,777	-
R11 [160]	2,088	1.18
R12 [160]	2,189	1.23

[a] Average bending stiffness

6.5 Modelling the Behaviour of Unreinforced and Reinforced Glulam Beams

The non-linear material model developed in Chapter 5 was used to generate the moment-curvature curves of unreinforced and FRP-reinforced glulam beams was used to predict the experimental flexural resistance curves. The experimental flexural tests were used to measure the increase in the wood tensile failure strain in FRP-reinforced beams compared to unreinforced to obtain the α_m modification factor for the analytical model. Additionally, the wood tensile and compressive stress-strain relationships were obtained from uniaxial tests conducted on coupon specimens. The resistance curves were then developed for unreinforced and reinforced beams and compared to the experimental curves.

6.5.1 Effect of FRP Reinforcement on the Strain Distribution

The presence of FRP as reinforcement of wooden flexural members has been shown to increase the wood tensile failure strain when compared to unreinforced members (Table 4.5 and Table 4.6). This phenomenon was initially brought forth by Johns and Lacroix (2000), who experimentally observed that the reinforcing material helps to bridge local defects found on the wood and promotes greater wood tensile strains. The improved tensile capacity of reinforced wood was then incorporated into various material models through the use of a factor, α_m, which is intended to better predict the failure strain of bending specimens that fail due to wood fibre rupture. (Gentile et al., 2002; Lacroix, 2017; Yang et al., 2016a). The lack of research surrounding the phenomenon, unfortunately, requires researchers to determine their own factors based on experimental or theoretical results (i.e., fitting data). A value of 1.3 for α_m has previously been used successfully in the past by researchers investigating the behaviour of FRP and steel reinforced timber beams (e.g., Gentile et al., 2002; Yang et al., 2016b). More recently, Lacroix and Doudak (2020) experimentally determined the enhanced strain capability of FRP-reinforced wood by comparing the ultimate tensile strain obtained from coupon tests to the ultimate tensile strain obtained by strain gauges during bending tests of reinforced beams. The authors reported an average increase in wood tensile failure strain of 1.21 in flexure when the beams are reinforced with FRP (Lacroix, 2017; Lacroix & Doudak, 2018; Lacroix & Doudak, 2020).

The experimental average failure strains obtained in this research program are summarized in Table 6.5. To determine the α_m factor associated with the presented data set, only the specimens that failed in flexure were considered. The average of every reinforced scheme is shown in Table 6.5 to further illustrate that the beams that failed in shear did not benefit from the enhanced tensile strain provided by the FRP. An average factor, α_m, of 1.17 was obtained for both [100] and [160] specimens when considering the specimens that failed in flexure only. Individual strain distributions for the entire set of specimens tested throughout this research program are presented in Appendix F.

Table 6.5 - Wood Tensile Failure Strain

Specimen	**Average Wood Tensile Failure Strain, $\varepsilon_{t,max}$ x 10-4 (mm/mm)**		**Reinforced / Unreinforced**	**Failure Mode**
	Unreinforced	**Reinforced**		
U; [100]	47.9			Flexure
R1; [100]		34.70	0.72	Shear
R2; [100]		51.10	1.07	Shear
R3; [100]		52.20	1.09	Shear
R4; [100]		40.80	0.85	Shear
R5; [100]		43.60	0.91	Flexure
R6; [100]		45.80	0.96	Flexure
R7; [100]		56.40	1.18	Flexure
R8; [100]		85.50	1.78	Flexure
R9; [100]		45.40	0.95	Flexure
R10; [100]		56.70	1.18	Flexure
R11; [160]		56.80	1.19	Flexure
R12; [160]		59.90	1.25	Flexure
		Average =	1.09 (1.17)*	

*Omitting all specimens that failed in shear

6.5.2 Predicting the Behaviour of Unreinforced Beams

The flexural behaviour of unreinforced glulam beams can be predicted by conducting a moment-curvature analysis and determining the resulting resistance curve using the procedure described in Chapter 5. The results are presented in Table 6.6 and the resistance curves are shown in Figure 6.17.

Table 6.6 - Comparison of Model to Experimental Results for Unretrofitted Beams

Specimen	**Experimental**		**Model**		**Model / Experimental**	
	P_{max} (kN)	**$\Delta_{P,max}$ (mm)**	**P_{max} (kN)**	**$\Delta_{P,max}$ (mm)**	**P_{max}**	**$\Delta_{P,max}$**
U-01; [100]	24.9	17.2	30.7	15.3	1.23	0.89
U-02; [100]	27.0	18.9			1.14	0.81
U-03; [100]	36.8	24.3			0.84	0.63
U-04; [100]	36.8	23.3			0.83	0.66
U-05; [100]	31.9	29.8			0.96	0.51
				Average	1.00	0.70
				St. Dev	0.16	0.13
				COV	0.16	0.19

Ratios of 1.00 and 0.70 were determined for the maximum resistance and displacement of the unreinforced beam. The discrepancy found for the displacement at maximum load can be attributed to the variability in the wood properties used as input to the material model, which were obtained from coupons tested experimentally. Based on the results, it can be seen that while the wood tensile failure strain governs the failure mode and that the model predicted a tension failure strain that was lower than that occurring in the experimental tests.

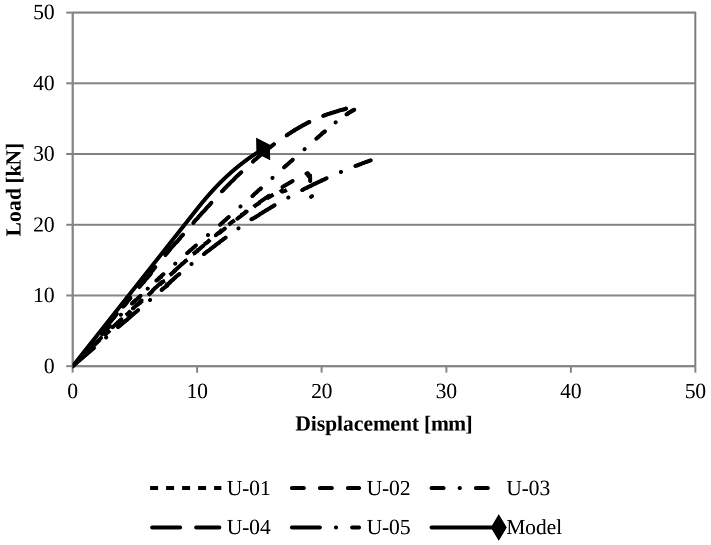

Figure 6.17 - Prediction of Unreinforced Beams

6.5.3 Predicting the Behaviour of Reinforced Beams

Following the procedure outlined in Chapter 5, the resistance curves can be predicted for the reinforced beams. The results for the reinforced beams in stage 1, comprising of simple tension and U-shaped reinforcement schemes are summarized in Table 6.7. The previously mentioned shear failures observed for the reinforced beams in stage 1 were accounted for in the material model by using an α_m factor of one. The FRP provided no wood tensile strain enhancement requiring the use of a modification factor greater than one.

Table 6.7 - Comparison of Model to Experimental Results for Retrofitted Beams in Stage 1

Specimen	**Experimental**		**Model**		**Model / Experimental**	
	P_{max} (kN)	**$\Delta_{P,max}$ (mm)**	**P_{max} (kN)**	**$\Delta_{P,max}$ (mm)**	**P_{max}**	**$\Delta_{P,max}$**
R1-01; [100]	32.1	12.8	35.2	16.7	1.10	1.31
R1-02; [100]	35.2	24.1			1.00	0.69
R1-03; [100]	36.8	19.5			0.96	0.86
R2-01; [100]	44.4	27.4	39.4	18.4	0.89	0.67
R2-02; [100]	50.0	25.8			0.79	0.71
R3-01; [100]	42.9	21.5	36.8	17.6	0.86	0.82
R3-02; [100]	39.6	29.1			0.93	0.61
R4-01; [100]	46.8	35.1	41.0	20.0	0.88	0.57
R4-02; [100]	46.9	19.5			0.87	1.02
				Average	0.92	0.81
				St. Dev	0.09	0.22
				COV	0.10	0.27

Predicted to experimental ratios of 0.93 were obtained for both the maximum resistance and the displacement, with the representative resistance curves shown in Figure 6.18.

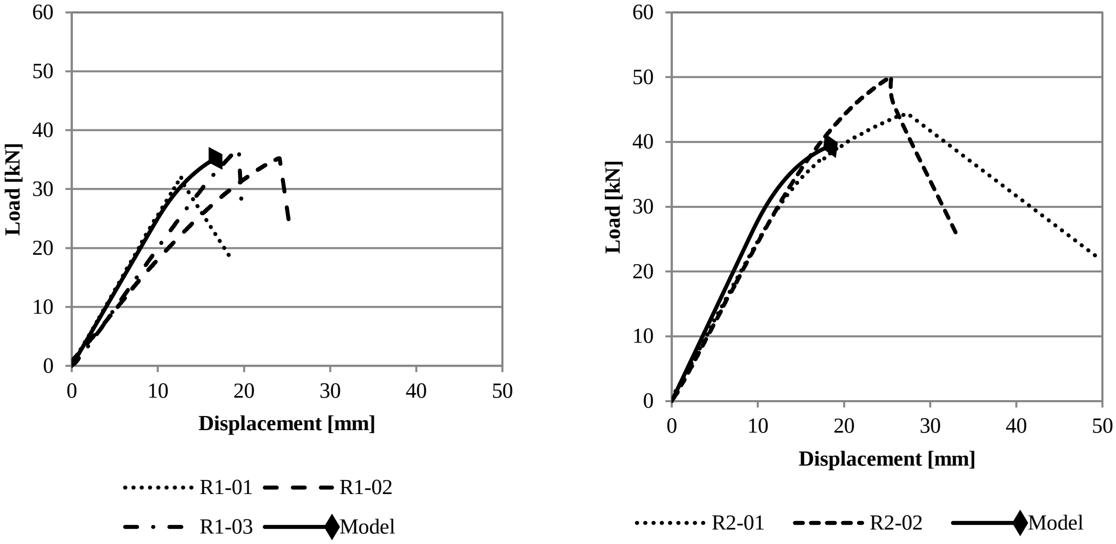

(a) R1 beams

(b) R2 beams

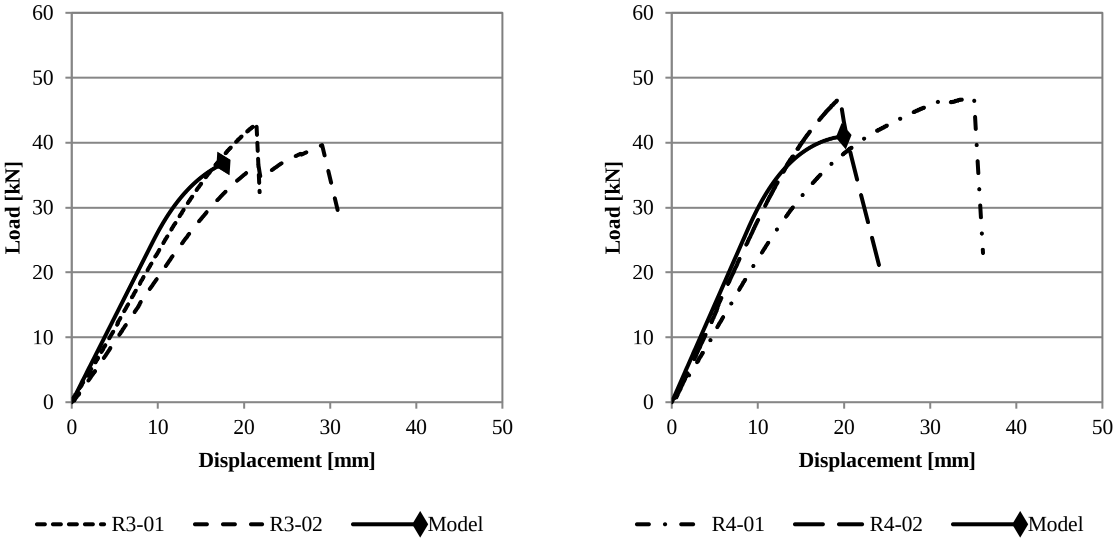

(c) R3 beams

(d) R4 beams

Figure 6.18 - Prediction of Reinforced Beams in Stage 1

The results of the beams reinforced with unidirectional simple tension GFRP sheets and transversely applied GFRP hoops (i.e., R5 and R6 beams) are summarized in Table 6.8. Predicted to experimental ratios of 0.98 and 0.87, respectively, were obtained for both the maximum resistance and the displacement. The representative resistance curves are shown in Figure 6.19. The reinforced beams used an α_m factor of one based on the failure mode being partially governed by shear failures. The model results are identical to the R1 and R2 beams for simple tension reinforcement because the model does not incorporate the shear resistance provided by the GFRP hoops.

Table 6.8 - Comparison of Model to Experimental Results for R5 and R6 Beams in Stage 2

Specimen	**Experimental**		**Model**		**Model / Experimental**	
	P_{max} (kN)	**$\Delta_{P,max}$ (mm)**	**P_{max} (kN)**	**$\Delta_{P,max}$ (mm)**	**P_{max}**	**$\Delta_{P,max}$**
R5-01; [100]	40.3	26.7	35.2	16.7	0.87	0.63
R6-01; [100]	35.0	15.4			1.01	1.09
R5-02; [100]	36.9	27.4	39.4	18.4	1.07	0.67
R6-02; [100]	40.0	16.8			0.98	1.09
				Average	0.98	0.87
				St. Dev	0.07	0.22
				COV	0.07	0.26

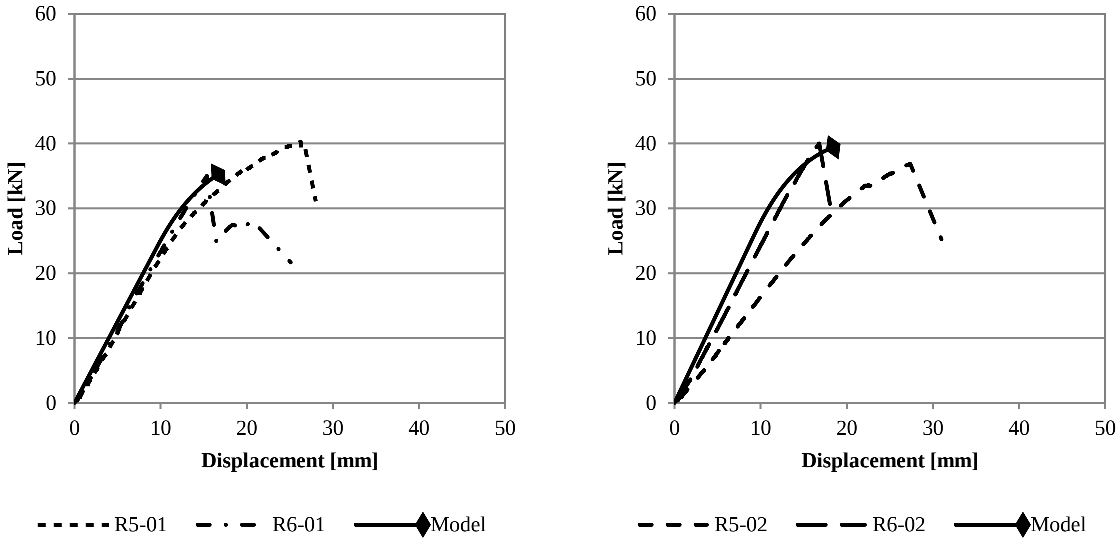

(a) Two layers of simple tension reinforcement (a) Four layers of simple tension reinforcement

Figure 6.19 - Prediction of R5 and R6 Beams in Stage 2

The results of the beams reinforced with simple tension reinforcement tails (i.e., R9 and R10 beams) are summarized in Table 6.9. Predicted to experimental ratios of 0.93 and 0.66 were obtained for both the maximum resistance and the displacement, respectively. The representative resistance curves are shown in Figure 6.19. The R9 beams used an α_m factor of 1 based on the observed decrease in the wood tensile failure strain presented in Table 1.5 and the R10 beams used an α_m factor of 1.18.

Table 6.9 - Comparison of Model to Experimental Results for R9 and R10 Beams in Stage 2

Specimen	Experimental		Model		Model / Experimental	
	P_{max} (kN)	$\Delta_{P,max}$ (mm)	P_{max} (kN)	$\Delta_{P,max}$ (mm)	P_{max}	$\Delta_{P,max}$
R9-01; [100]	32.4	21.5	36.1	16.9	1.14	0.95
R9-02; [100]	36.4	25.5			1.02	0.80
R10-01; [100]	47.2	31.8	36.6	20.3	0.75	0.61
R10-02; [100]	44.3	36.2			0.80	0.54
				Average	0.93	0.66
				St. Dev	0.13	0.08
				COV	0.14	0.12

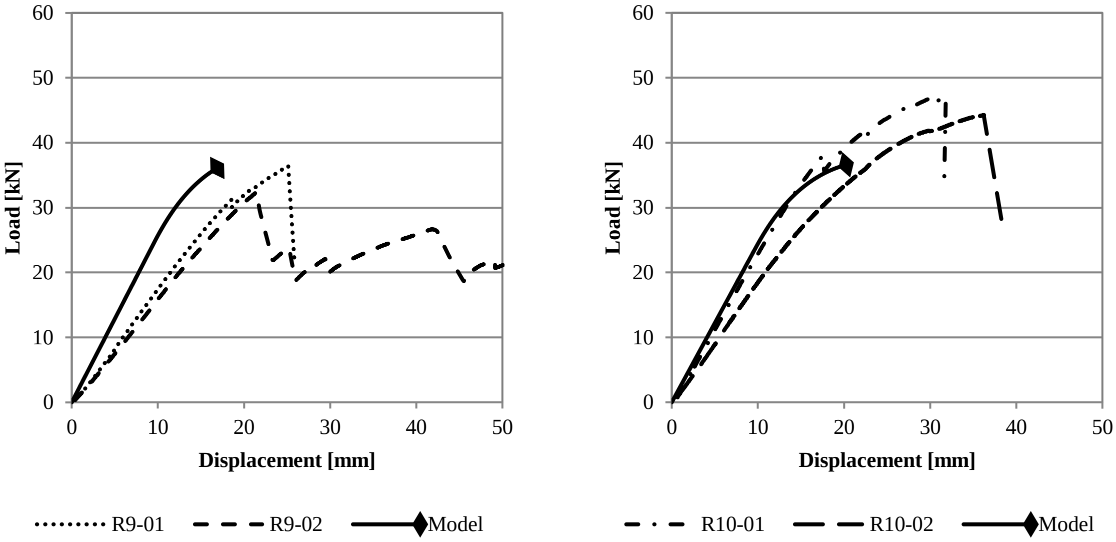

(a) R9 beams (b) R10 beams

Figure 6.20 - Prediction of R9 and R10 Beams in Stage 2

The large discrepancy associated with the R9 beams are discussed in greater detail in Section 6.3. In terms of model validation, the resistance curve for the beams reinforced with two layers of U-shaped reinforcement and two layers of full confinement (i.e., R7) was generated and is shown in Figure 6.21. The model only considers the FRP subjected to tensile stresses, resulting in identical model inputs used for the R9 and R7 beams. Although shown to significantly underpredict the maximum resistance (Figure 6.21), the model adequately predicts the behaviour associated with the first 50% of the curve. Based on the resistance curves shown in Figure 6.21, it can be assumed that the confined beams benefited from the FRP in compression and did not fail in wood yielding as per the model results. These findings help further prove that the R9 beams did not adequately bond to the reinforcement (i.e., any comparisons to the material model should not be scrutinized) and that future investigation is required to better incorporate the entire compressive behaviour of both the wood and FRP in the material model.

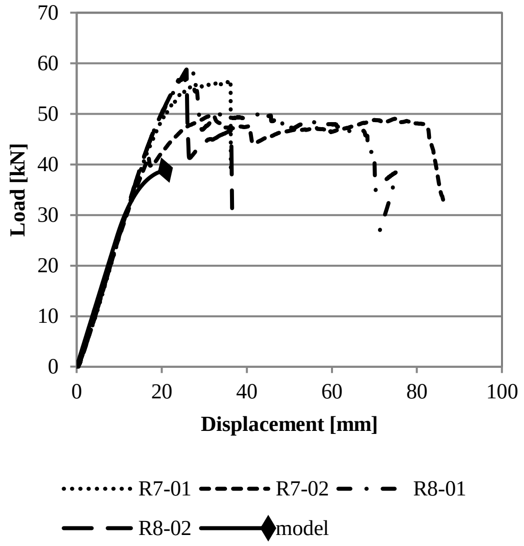

Figure 6.21 - Prediction of R7 Beams in Stage 2

The results of the [160] beams reinforced with simple tension reinforcement (i.e., R11) and tails (i.e., R12) are summarized in Table 6.10. Predicted experimental ratios of 0.93 and 0.72, respectively, were obtained for both the maximum resistance and the displacement. The representative resistance curves are shown in Figure 6.19. The R11 and R12 beams used an α_m factor of 1.19 and 1.25, respectively.

Table 6.10 - Comparison of Model to Experimental Results for R11 and R12 Beams in Stage 2

Specimen	**Experimental**		**Model**		**Model / Experimental**	
	P_{max} (kN)	**$\Delta_{P,max}$ (mm)**	**P_{max} (kN)**	**$\Delta_{P,max}$ (mm)**	**P_{max}**	**$\Delta_{P,max}$**
R11-01; [160]	62.9	36.2	56.7	30.6	0.90	0.84
R11-02; [160]	60.0	36.8			0.94	0.83
R12-01; [160]	63.8	36.2	55.4	31.6	0.87	0.87
R12-02; [160]	67.7	35.9			0.82	0.88
				Average	0.88	0.86
				St. Dev	0.05	0.02
				COV	0.05	0.02

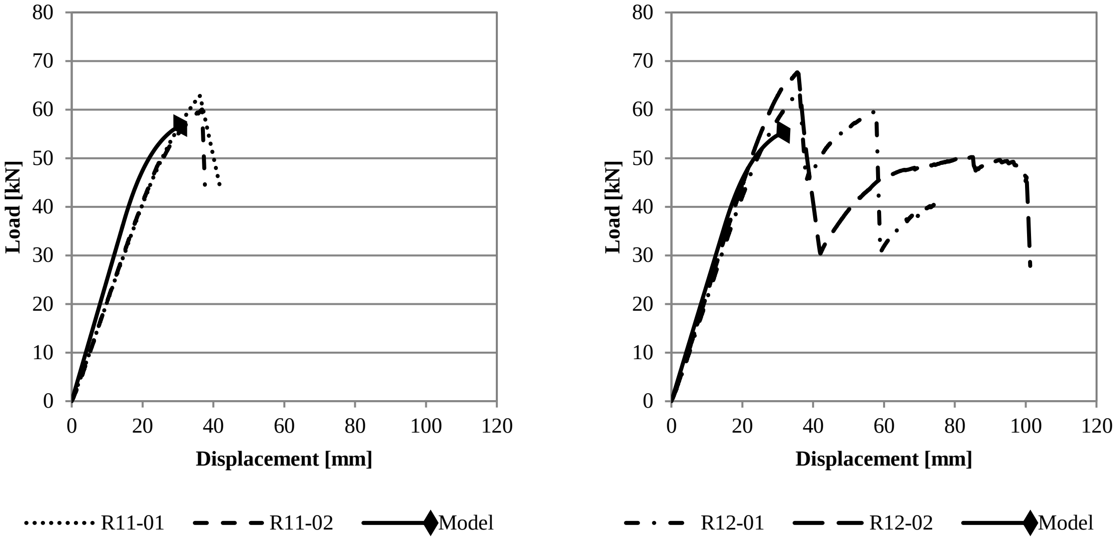

(a) R11 beams (b) R12 beams

Figure 6.22 - Prediction of R11 and R12 Beams in Stage 2

A summary of the model to experimental strength ratios is presented in Table 6.11.

Table 6.11 - Summary of Model to Experimental Strength Ratios

Specimen	**Experimental**		**Model**		**Model / Experimental**	
	P_{max} (kN)	**$\Delta_{P,max}$ (mm)**	**P_{max} (kN)**	**$\Delta_{P,max}$ (mm)**	**P_{max}**	**$\Delta_{P,max}$**
U-01; [100]	27.9	26.4	30.7	15.3	1.10	0.58
U-02; [100]	30.8	29.3			1.00	0.52
U-03; [100]	36.8	24.3			0.84	0.63
U-04; [100]	36.8	23.3			0.83	0.66
U-05; [100]	31.9	29.8			0.96	0.51
R1-01; [100]	32.1	12.8	35.2	16.7	1.10	1.31
R1-02; [100]	35.2	24.1			1.00	0.69
R1-03; [100]	36.8	19.5			0.96	0.86
R2-01; [100]	44.4	27.4	39.4	18.4	0.89	0.67
R2-02; [100]	50.0	25.8			0.79	0.71
R3-01; [100]	42.9	21.5	36.8	17.6	0.86	0.82
R3-02; [100]	39.6	29.1			0.93	0.61
R4-01; [100]	46.8	35.1	41.0	20.0	0.88	0.57
R4-02; [100]	46.9	19.5			0.87	1.02
R5-01; [100]	40.3	26.7	35.2	16.7	0.87	0.63
R6-01; [100]	36.9	27.4			1.01	1.09
R5-02; [100]	35.0	15.4	39.4	18.4	1.07	0.67
R6-02; [100]	40.0	16.8			0.98	1.09
R7-01; [100]	56.6	36.2	38.9	20.8	0.69	0.57
R7-02; [100]	49.8	31.9			0.78	0.65
R8-01; [100]	58.2	26.4	-	-	-	-
R8-02; [100]	58.8	25.9			-	-
R9-01; [100]	32.4	21.5	36.1	16.9	1.11	0.79
R9-02; [100]	36.4	25.5			0.99	0.66
R10-01; [100]	47.2	31.8	36.6	20.3	0.78	0.64
R10-02; [100]	44.3	36.2			0.83	0.56
R11-01; [160]	62.9	36.2	56.7	30.6	0.90	0.84
R11-02; [160]	60.0	36.8			0.94	0.83
R12-01; [160]	63.8	36.2	55.4	31.6	0.87	0.87
R12-02; [160]	67.7	35.9			0.82	0.88
				Average	0.93	0.77
				St. Dev	0.12	0.19
				COV	0.13	0.24

Chapter 7
Conclusions

7.1 Summary and Conclusions

The current research effort investigated the effects of GFRP sheets applied as tension reinforcement on the bending behaviour of glulam beams. Initially, a series of coupon tests for both the glulam and FRP material was conducted to determine the uniaxial stress-strain relationship of the materials. The first phase of full-scale four-point bending tests investigated the behaviour of unreinforced and reinforced glulam beams with simple or U-shaped GFRP tension reinforcement. The purpose of this phase was to determine relative increases when using the reinforcement and to better understand the failure modes associated with the reinforced beams. The configurations in the second phase of the full-scale four-point bending tests were targeted at preventing undesirable failure modes observed in the FRP-reinforced glulam beams observed in the first phase. The following conclusions can be drawn from the current research study:

- The use of FRP sheets applied as simple tension and U-shaped reinforcement successfully increased the resistance and stiffness of glulam beams subjected to four-point loading. Providing two layers of simple tension and U-shaped reinforcement resulted in average resistance increases of 1.06 and 1.26, respectively. The addition of FRP reinforcement from two to four layers of simple tension and U-shaped reinforcement contributed to an increase in resistance by average factors of 1.36 and 1.14, respectively.

- The addition of FRP reinforcement increased the ultimate resistance of the members; however, all simple tension and U-shaped reinforced beams failed in shear. This failure was in part attributed to the fact that the a/d ratio of 4 allowed the shear stress in the members to exceed the wood limit as well as to the development length of the FRP which resulted in stress concentrations that led to perpendicular to grain tension stresses causing failure.

- The shear failure was addressed through transversely applied GFRP fabric that provided shear reinforcement and anchoring for the tensile reinforcement. The addition of GFRP hoops located at the end of the simple tension reinforcement helped contain the wood failure and prevented the brittle stress concentration failure observed for the simple tension and U-shaped reinforced beams. The “tails” configuration prevented premature de-bonding, thereby allowing the beam to fail in flexure while also contributing to some level of post-peak resistance in the deeper beams.

- The addition of partial confinement through the “tail” reinforcement scheme not only resulted in increased strength and stiffness but also contributed to improved post-peak behaviour with ductility with ratios ranging from 2.08 to 2.78 for the [160] beams. At shorter spans, the tails prevented premature debonding of the FRP but ultimately failed in a combination of flexure and shear, thereby resulting in limited post-peak resistance.
- The addition of FRP to the glulam beams contributed to an increased wood tensile failure strain when compared to the unreinforced specimens only when the FRP-reinforced glulam member failed in flexure. For flexure, an average increase of 1.17 was observed which is in line with previous studies. No increases were observed for specimens that failed in shear.
- A material predictive model capable of predicting the flexural behaviour of the beams up to maximum resistance with reasonable accuracy was developed. The novelty of the current model is in its implementation where the moment-curvature analysis is conducted by iterating on the compressive strain as opposed to Lacroix (2017). Prior to predicting the resistance curves, the model was validated against results from Lacroix (2017).

Despite the effort to provide a comprehensive understanding of the behaviour of FRP-reinforced glulam beams, the current study has limitations. It should be noted that despite the numerous configurations investigated, only two replicas of each configuration were tested, although it did provide significant insight on the parameters to investigate in future studies. Also, the predictions from the material model rely on the accuracy of the constitutive material relationships, which were carefully obtained through experimental tests. Also, the material model is limited in predicting the flexural failure and cannot be used to predict whether or not the shear failure governs.

Recommendations for Future Work

Based on the research described in this thesis, it is recommended to investigate:

- Different span-to-depth ratios, layups, FRP development lengths, and cross-section sizes to further validate the findings from the current study as well as to better inform designers.

- Develop the material model to include different failure modes as well as the effect of varying FRP profiles along the length to better represent the flexural behaviour. Additionally, include the post-peak behaviour in the material model.
- Conduct parametric analyses to better understand the relationship between the wood and FRP properties.

References

ACI Committee 440. (2007). *400R-07 Report on Fiber-Reinforced Polymer (FRP) Reinforcement for Concrete Structures* (ACI Committee 440, Ed.; Issue Report 440.2R-08). ACI.

Akbiyik, A., Lamanna, A. J., & Hale, W. M. (2007). Feasibility investigation of the shear repair of timber stringers with horizontal splits. *Construction and Building Materials*, *21*(5). https://doi.org/10.1016/j.conbuildmat.2006.03.004

Aratake, S., Morita, H., & Arima, T. (2011). Bending creep of glued laminated timber (glulam) using sugi (Cryptomeria japonica) laminae with extremely low Young's modulus for the inner layers. *Journal of Wood Science*, *57*(4), 267–275. https://doi.org/10.1007/s10086-011-1175-0

ASTM. (2012). Standard Practice for Establishing Characteristic Values for Reinforced Glued Laminated Timber (Glulam) Beams Using Mechanics-Based Models. In *ASTM D7199-12* (p. 11). American Society for Testing and Materials. https://doi.org/10.1520/D7199-07R12

ASTM. (2014). Standard Test Method for Tensile Properties of Polymer Matrix Composite Materials. In *ASTM D3039-14* (p. 13). American Society for Testing and Materials.

ASTM. (2021a). Standard Test Methods for Small Clear Specimens of Timber. In *ASTM D143-21* (p. 31). American Society for Testing and Materials.

ASTM. (2021b). Standard Test Methods of Static Tests of Lumber in Structural Sizes. In *ASTM D198-21a* (p. 27). American Society for Testing and Materials. https://doi.org/10.1520/D0198-21A

Augustin, S., & Fell, D. (2015). *Wood as a Restorative Material in Healthcare Environments*. www.fpinnovations.ca.

Bakis, C. E., Bank, L. C., Brown, V. L., Cosenza, E., Davalos, J. F., Lesko, J. J., Machida, A., Rizkalla, S. H., & Triantafillou, T. C. (2002). Fiber-Reinforced Polymer Composites for Construction—State-of-the-Art Review. *Journal of Composites for Construction*, *6*(2). https://doi.org/10.1061/(ASCE)1090-0268(2002)6:2(73)

Bank, L. C. (2006). *COMPOSITES FOR CONSTRUCTION: Structural Design with FRP Materials*. John Wiley & Sons.

Barrett, J. D., & Lau, W. (1994). *Canadian Lumber Properties*. Canadian Wood Council.

Bazan, I. M. M. (1980). *Ultimate bending strength of timber beams: Vol. Ph.D.*

Buchanan, A. H. (1990). Bending Strength of Lumber. *Journal of Structural Engineering*, *116*(5). https://doi.org/10.1061/(ASCE)0733-9445(1990)116:5(1213)

Buell, T. W., & Saadatmanesh, H. (2005). Strengthening timber bridge beams using carbon fiber. *Journal of Structural Engineering*, *131*(1), 173–187. https://doi.org/doi:10.1061/(ASCE)0733-9445(2005)131:1(173)

Bulleit, W. M. (1984). Reinforcement of Wood Materials: A Review. *Wood and Fiber Science*, *16(3)*, 391–397.

Canada, N. R. (2020). *Green Construction through Wood (GCWood) Program*. https://Www.Nrcan.Gc.ca/Science-and-Data/Funding-Partnerships/Funding-Opportunities/Forest-Sector-Funding-Programs/Green-Construction-through-Wood-Gcwood-Program/20046.

Canadian Standards Association (2015). *CSA O177 Qualification code for manufacturers of structural glued-laminated timber*

Canadian Standards Association. (2019a). *CSA O86:19 Engineering design in wood*.

Canadian Standards Association. (2019b). *CSA S6:19 Canadian Highway Bridge Design Code*.

Corradi, M., Mouli Vemury, C., Edmondson, V., Poologanathan, K., & Nagaratnam, B. (2021). Local FRP reinforcement of existing timber beams. *Composite Structures*, *258*. https://doi.org/10.1016/j.compstruct.2020.113363

Davids, W. G., Nagy, E., & Richie, M. C. (2008). Fatigue Behavior of Composite-Reinforced Glulam Bridge Girders. *Journal of Bridge Engineering*, *13*(2), 183–191. https://doi.org/10.1061/(ASCE)1084-0702(2008)13:2(183)

Dorey, A. B., & Cheng, J. J. R. (1996a). Glass Fiber Reinforced Glued Laminated Wood Beams. In *Canada-Alberta Agreement Documents* (Issue Canada-Alberta Partnership Agreement in Forestry Report 147,). Natural Resources Canada, Canadian Forest Service, Northern Forestry Centre.

Dorey, A. B., & Cheng, J. J. R. (1996b). The behavior of GFRP glued laminated timber beams. In M. M. El-Badry (Ed.), *Adv. Comp. Mat. in Bridges and Struct. II* (pp. 787–794). The Canadian Society for Civil Engineering.

El-Hacha, R., & Rizkalla, S. (2004). Near-Surface-Mounted Fiber-Reinforced Polymer Reinforcements for Flexural Strengthening of Concrete Structures. *ACI Structural Journal*, *101*(5). https://doi.org/10.14359/13394

Fell, D. R. (2010). *Wood in the human environment : restorative properties of wood in the built indoor environment*. https://open.library.ubc.ca/collections/ubctheses/24/items/1.0071305

Frey, W. (2020). *Wood buildings can boost health and productivity: expert*. https://canada.constructconnect.com/joc/news/projects/2020/11/wood-buildings-can-boost-health-and-productivity-expert

Gasparri, E., & Aitchison, M. (2019). Unitised timber envelopes. A novel approach to the design of prefabricated mass timber envelopes for multi-storey buildings. *Journal of Building Engineering*, *26*, 100898. https://doi.org/10.1016/j.jobe.2019.100898

Gentile, C., Svecova, D., & Rizkalla, S. H. (2002). Timber Beams Strengthened with GFRP Bars: Development and Applications. *Journal of Composites for Construction*, *6*(1). https://doi.org/10.1061/(ASCE)1090-0268(2002)6:1(11)

Gentry, T. R. (2011). Performance of Glued-Laminated Timbers with FRP Shear and Flexural Reinforcement. *Journal of Composites for Construction*, *15*(5). https://doi.org/10.1061/(ASCE)CC.1943-5614.0000206

Glisovic, I., Pavlovic, M., Stevanovic, B., & Todorovic, M. (2017). Numerical Analysis of Glulam Beams Reinforced with CFRP Plates. *Journal of Civil Engineering and Management*, *23*(7). https://doi.org/10.3846/13923730.2017.1341953

Green, M., & Taggart, J. (2017). *TALL WOOD BUILDINGS DESIGN, CONSTRUCTION AND PERFORMANCE*.

Hernandez, R., Davalos F., J., Sonti, S. S., Kim, Y., & Moody C., R. (1997). *Strength and stiffness of reinforced yellow-poplar glued laminated beams* (Issue FPL-RP-554). U.S. Department of Agriculture, Forest Service, Forest Products Laboratory.

Hota, G. V. S., Vijay, P. V., & Abhari, R. S. (2010). Glass Fiber Reinforced Polymer Strengthening and Evaluation of Railroad Bridge Members. *Structural Engineering International*, *20*(4). https://doi.org/10.2749/101686610793557627

International Code Council. (2021). *International Building Code*.

Johns, K. C., & Lacroix, S. (2000). Composite reinforcement of timber in bending. *Canadian Journal of Civil Engineering*, *27*(5). https://doi.org/10.1139/cjce-27-5-899

Karacabeyli, E., & Gagnon, S. (2019). *Canadian CLT Handbook* (2019 Edition). Special Publication SP-532E.

Kim, K.-H. E., & Andrawes, B. (2016). Compression behavior of FRP strengthened bridge timber piles subjected to accelerated aging. *Construction and Building Materials*, *124*, 177–185. https://doi.org/10.1016/j.conbuildmat.2016.07.020

Lacroix, D., & Doudak, G. (2020). Towards enhancing the post-peak performance of glued-laminated timber beams using multi-directional fibre reinforced polymers. *Engineering Structures*, *215*. https://doi.org/10.1016/j.engstruct.2020.110680

Lacroix, D. N. (2017). *Investigating the Behaviour of Glulam Beams and Columns Subjected to Simulated Blast Loading (PhD Thesis)*. University of Ottawa.

Lacroix, D. N., & Doudak, G. (2018). Experimental and Analytical Investigation of FRP Retrofitted Glued-Laminated Beams Subjected to Simulated Blast Loading. *Journal of Structural Engineering*, *144*(7), 04018089. https://doi.org/10.1061/(ASCE)ST.1943-541X.0002084

Lacroix, D., Viau, C., Battelli, E., & Doudak, G. (2021). Enhancing the performance of light-frame wood studs using glass fibre-reinforced polymers. *Engineering Structures*, *245*, 112973. https://doi.org/10.1016/J.ENGSTRUCT.2021.112973

Lacroix, D., Viau, C., & Doudak, G. (2018). Design Considerations for Glulam Beams and Columns Under High Strain-Rates. *CSCE 2018 Annual Conference*, 10.

Lefebvre, D., & Richard, G. (2014). Design and construction of a 160-metre-long wood bridge in Mistissini, Quebec. *WCTE 2014 - World Conference on Timber Engineering, Proceedings*.

Legg, C., & Tingley, D. (2020). *Timber Bridge Best Practices and the State of the Industry in Atlantic Canada*.

Legg, M., & Bradley, S. (2016). Measurement of stiffness of standing trees and felled logs using acoustics: A review. *The Journal of the Acoustical Society of America*, *139*(2), 588–604. https://doi.org/10.1121/1.4940210

Lei Win, T. (2021). *How much carbon does the construction industry emit? | World Economic Forum*. https://www.weforum.org/agenda/2021/01/planet-warming-emissions-buildings-construction-climate-goals-risk/

Madsen, B., & Buchanan, A. H. (1986). Size effects in timber explained by a modified weakest link theory. *Canadian Journal of Civil Engineering*, *13*(2), 218–232. https://doi.org/10.1139/l86-030

Moses, & Brown & Co. (2017). *Ontario Wood Bridge Reference Guide*. Canadian Wood Council.

Naturally Wood – *What Is Plywood? How Is Plywood Made?* (2022). Retrieved April 1, 2022, from https://www.naturallywood.com/products/plywood/

Nelson, T. (2020). *France Wants All Public Buildings to Be Made of at Least 50% Wood by 2022*. Https://Www.Architecturaldigest.Com/Story/France-Wants-All-Public-Buildings-to-Be-Made-of-at-Least-50-Wood-by-2022.

NLGA. (2017). *National Lumber Grades Authority (NLGA) - Standard Grading Rules for Canadian Lumber*. http://nlga.org/en/publications-for-download/

NRC. (2021). *The State of Mass Timber in Canada 2021 | Canadian Forest Service Publications | Natural Resources Canada*. https://cfs.nrcan.gc.ca/publications?id=40364

NRCC. (2022). *National Building Code of Canada*. Ottawa, ON: The Council

O'Callaghan, R. (2021). *Effects of GFRP Reinforcement on the Compressive Behaviour of Square SPF Timber Columns* [Master's Thesis]. University of Waterloo.

O'Callaghan, R. B., Lacroix, D., & Kim, K. E. (2022). Experimental investigation of the compressive behaviour of GFRP wrapped spruce-pine-fir square timber columns. *Engineering Structures*, *252*, 113618. https://doi.org/10.1016/j.engstruct.2021.113618

Orlowski, K. (2019). Assessment of Manufacturing Processes for Automated Timber-Based Panelised Prefabrication. *Buildings*, *9*(5), 125. https://doi.org/10.3390/buildings9050125

Philip A. Ritchie Le-Wu Lu and Guy M. Conelly, D. A. T. (1990). External Reinforcement of Concrete Beams Using Fiber Reinforced Plastics. *ACI Structural Journal*, *88*(4). https://doi.org/10.14359/2723

Plevris, N., & Triantafillou, T. C. (1992). FRP-Reinforced Wood as Structural Material. *Journal of Materials in Civil Engineering*, *4*(3). https://doi.org/10.1061/(asce)0899-1561(1992)4:3(300)

Province of British Columbia. (2009). *Wood First Act*. Https://Www.Bclaws.Gov.Bc.ca/Civix/Document/Id/Complete/Statreg/00_09018_01.

Raftery, G. M., & Harte, A. M. (2011). Low-grade glued laminated timber reinforced with FRP plate. *Composites Part B: Engineering*, *42*(4). https://doi.org/10.1016/j.compositesb.2011.01.029

Raftery, G. M., & Harte, A. M. (2013). Nonlinear numerical modelling of FRP reinforced glued laminated timber. *Composites Part B: Engineering*, *52*, 40–50. https://doi.org/http://dx.doi.org/10.1016/j.compositesb.2013.03.038

Ramage, M. H., Burridge, H., Busse-Wicher, M., Fereday, G., Reynolds, T., Shah, D. U., Wu, G., Yu, L., Fleming, P., Densley-Tingley, D., Allwood, J., Dupree, P., Linden, P. F., & Scherman, O. (2017). The wood from the trees: The use of timber in construction. *Renewable and Sustainable Energy Reviews*, *68*. https://doi.org/10.1016/j.rser.2016.09.107

Rosa García, P., Escamilla, A. C., & Nieves González García, M. (2013). Bending reinforcement of timber beams with composite carbon fiber and basalt fiber materials. *Composites Part B: Engineering*, *55*, 528–536. https://doi.org/10.1016/j.compositesb.2013.07.016

Sartori, T., & Crocetti, R. (2016). Prefabricated timber-concrete composite floors. *European Journal of Wood and Wood Products*, *74*(3), 483–485. https://doi.org/10.1007/s00107-016-1007-4

Schober, K.-U., Harte, A. M., Kliger, R., Jockwer, R., Xu, Q., & Chen, J.-F. (2015). FRP reinforcement of timber structures. *Construction and Building Materials*, *97*, 106–118. https://doi.org/10.1016/j.conbuildmat.2015.06.020

Sonti, S. S., GangaRao, H. V. S., & Superfesky, M. C. (1996). Rehabilitation and strengthening of glulam stringers for bridge superstructures. In H. Saadatmanesh & M. R. Ehsani (Eds.), *First International Conference on Composites in Infrastructures*. University of Arizona.

Su, J., Leroux, P., Lafrance, P.-S., Berzins, R., Gratton, K., Gibbs, E., & Weinfurter, M. (2021). *Fire testing of rooms with exposed wood surfaces in encapsulated mass timber construction*.

Svecova, D., & Eden, R. J. (2004). Flexural and shear strengthening of timber beams using glass fibre reinforced polymer bars — an experimental investigation. *Canadian Journal of Civil Engineering*, *31*(1). https://doi.org/10.1139/l03-069

Wacker, J. P., Dias, A. M. P. G., & Hosteng, T. K. (2020). 100-Year Performance of Timber–Concrete Composite Bridges in the United States. *Journal of Bridge Engineering*, *25*(3), 04020006-1-04020006–04020009. https://doi.org/10.1061/(ASCE)BE.1943-5592.0001513

Wang, Y., Hou, Q., Xu, T., Qu, S., & Zhang, B. (2021). The bending-shear behaviors of steel reinforced fast-growing poplar glulam beams with different shear-span ratios. *Construction and Building Materials*, *300*, 124008. https://doi.org/10.1016/j.conbuildmat.2021.124008

Yang, H., Liu, W., Lu, W., Zhu, S., & Geng, Q. (2016). Flexural behavior of FRP and steel reinforced glulam beams: Experimental and theoretical evaluation. *Construction and Building Materials*, *106*, 550–563. https://doi.org/http://dx.doi.org/10.1016/j.conbuildmat.2015.12.135

Zhang, W., Song, X., Gu, X., & Tang, H. (2012). Compressive Behavior of Longitudinally Cracked Timber Columns Retrofitted Using FRP Sheets. *Journal of Structural Engineering*, *138*(1), 90–98. https://doi.org/10.1061/(ASCE)ST.1943-541X.0000423

Appendices

Appendix A

Test Results of Wood Compression Coupons

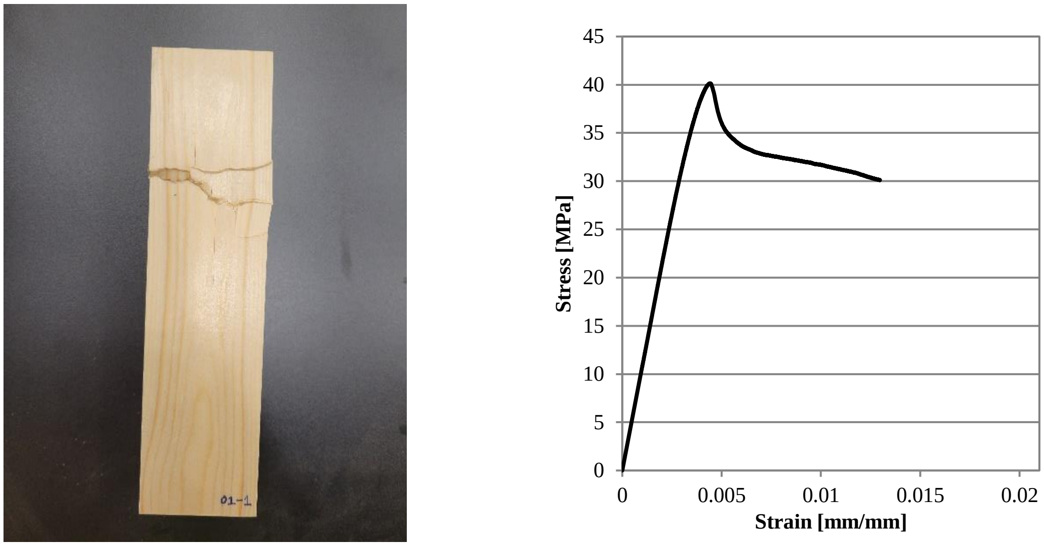

(a) Ultimate failure (b) Stress-strain behaviour

Figure A.1 - Experimental Result for C1

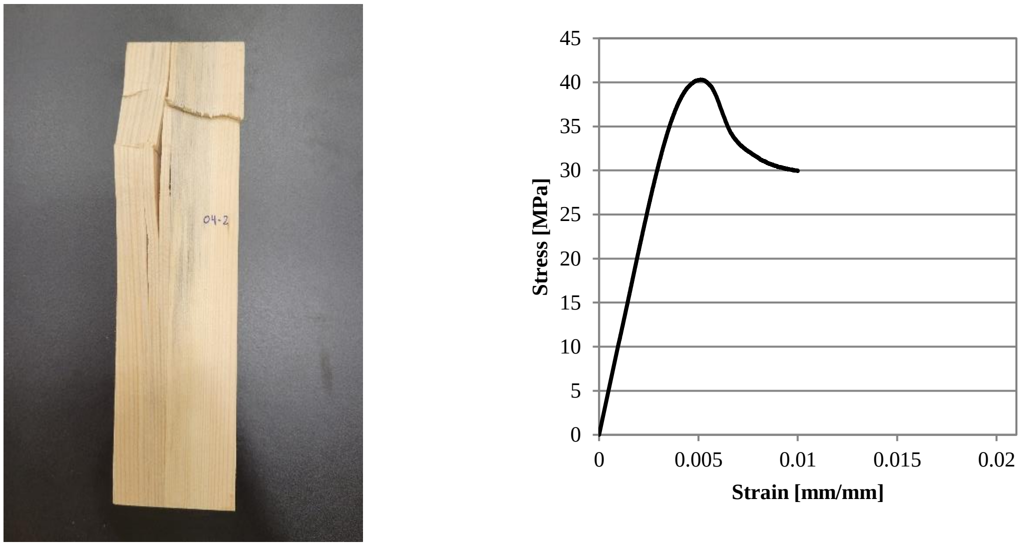

(a) Ultimate failure (b) Stress-strain behaviour

Figure A.2 - Experimental Result for C2

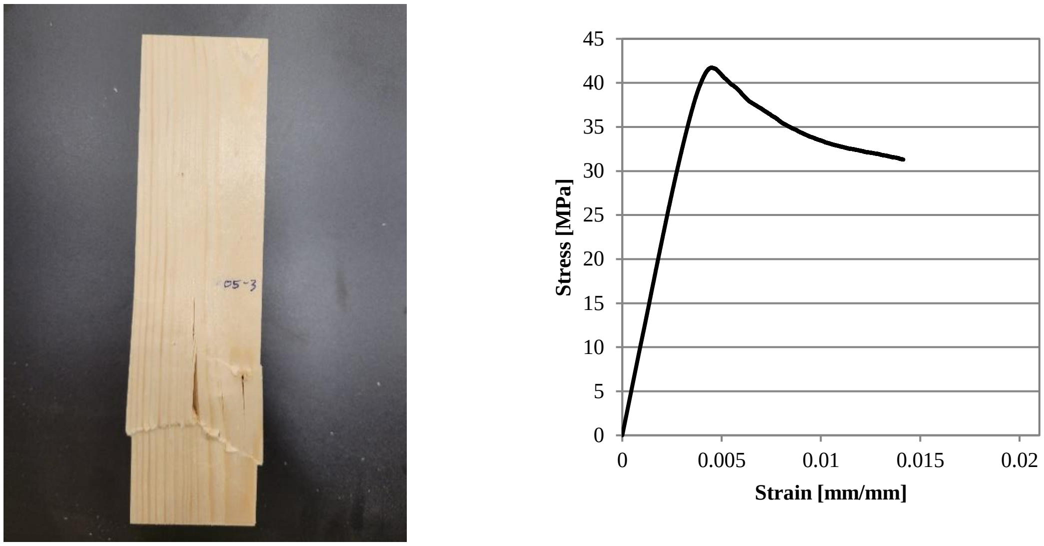

(a) Ultimate failure (b) Stress-strain behaviour

Figure A.3 - Experimental Result for C3

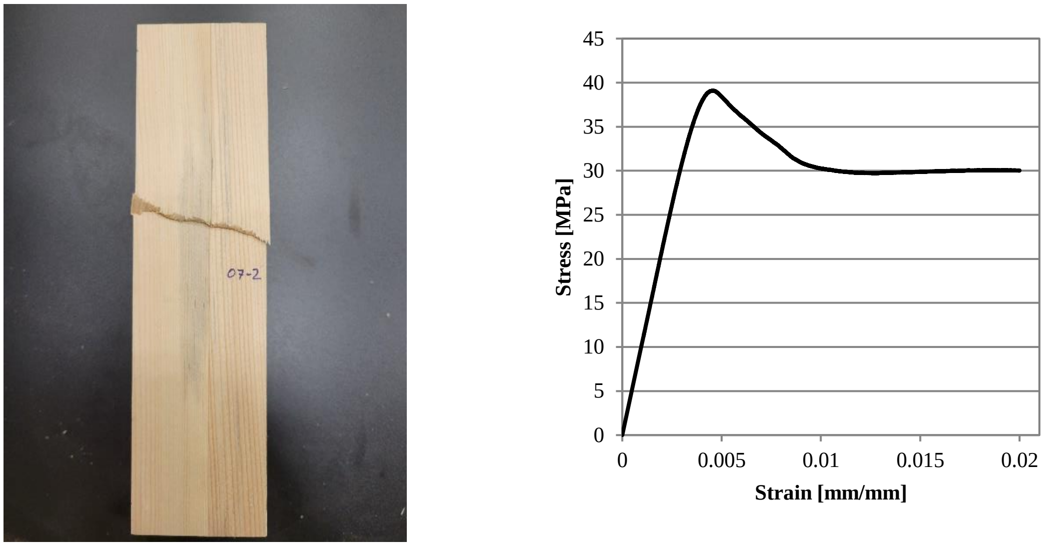

(a) Ultimate failure (b) Stress-strain behaviour

Figure A.4 - Experimental Result for C4

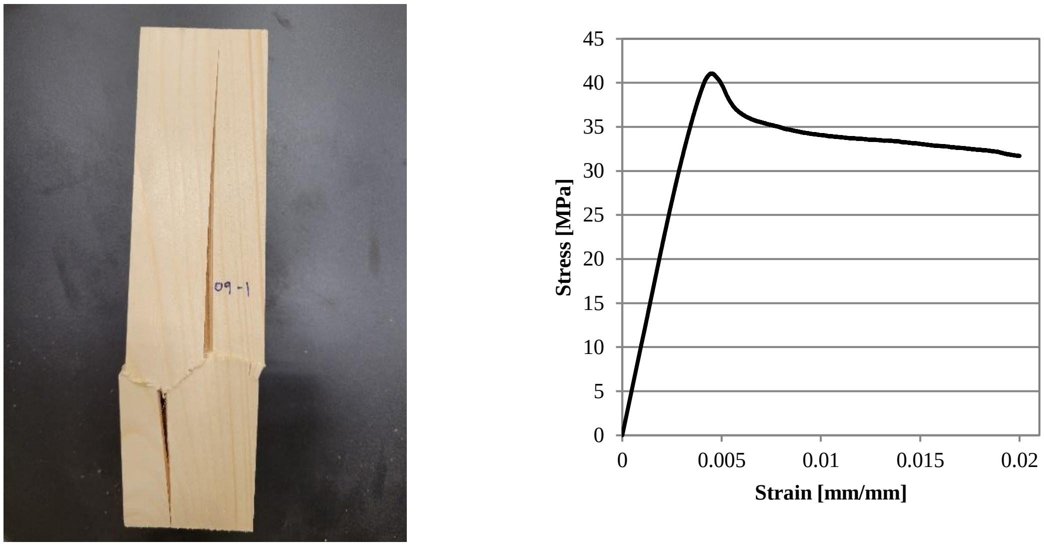

(a) Ultimate failure (b) Stress-strain behaviour

Figure A.5 - Experimental Result for C5

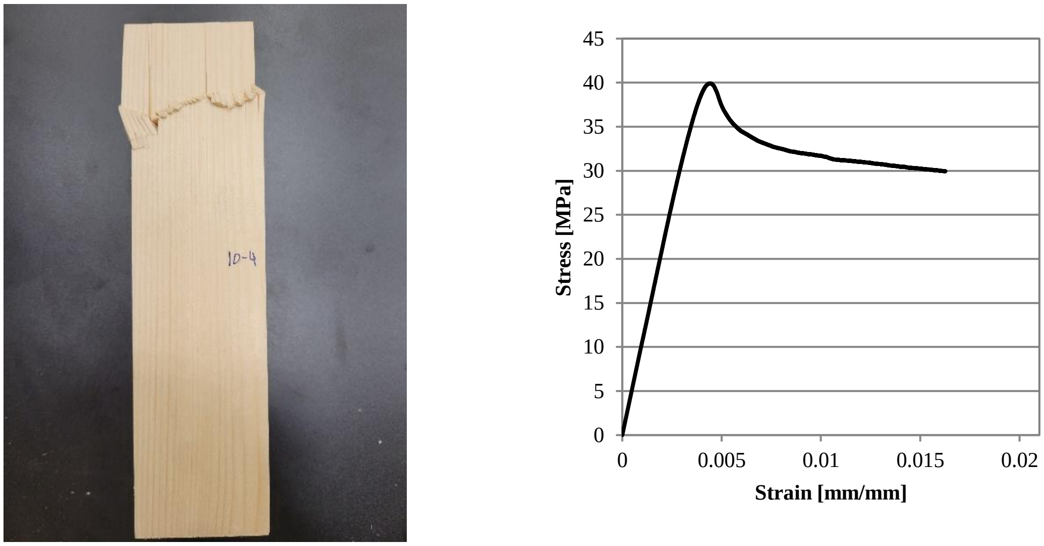

(a) Ultimate failure (b) Stress-strain behaviour

Figure A.6 - Experimental Result for C6

Appendix B

Test Results of Wood Tension Coupons

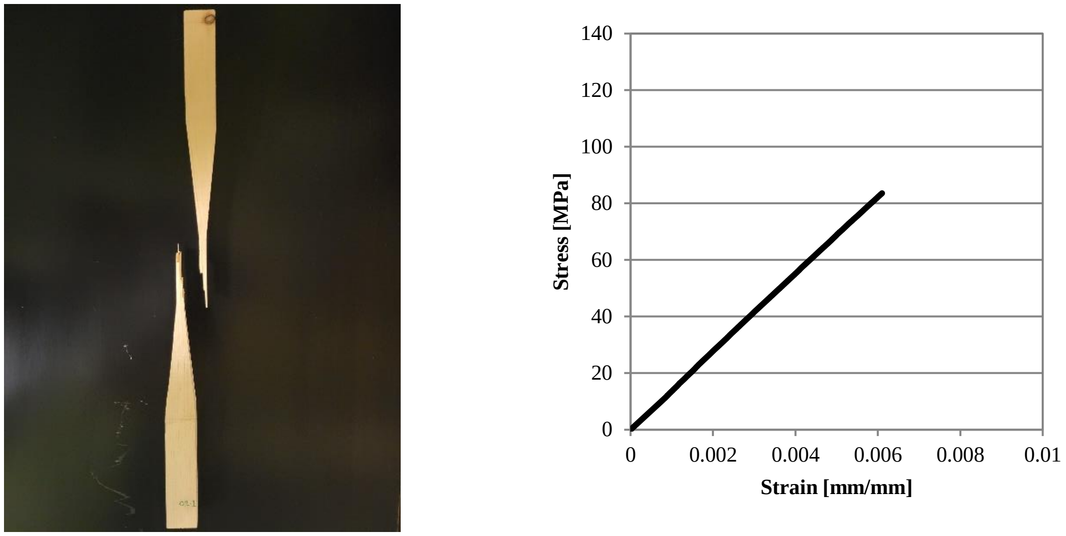

(a) Ultimate failure (b) Stress-strain behaviour

Figure B.1 - Experimental Result for T1

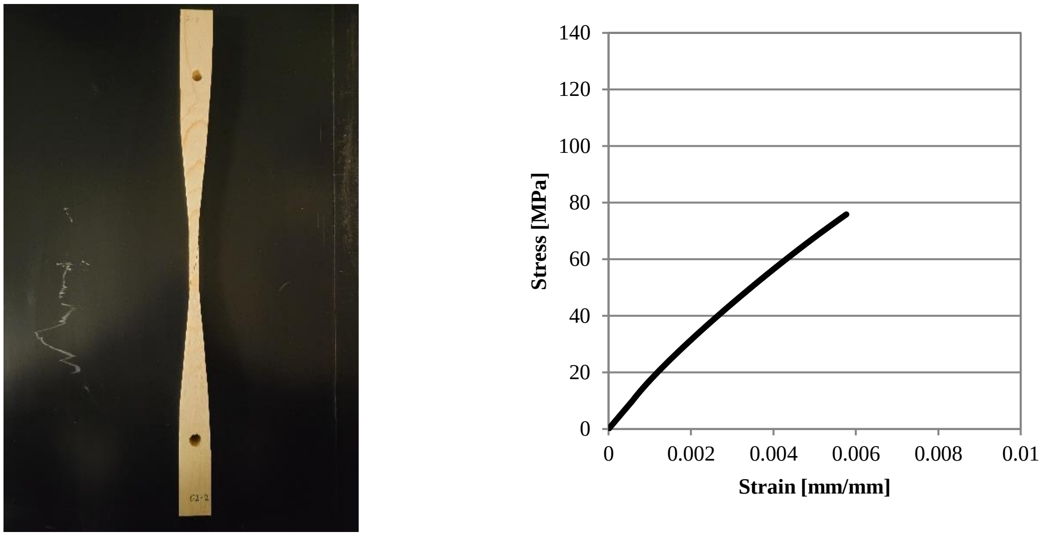

(a) Ultimate failure (b) Stress-strain behaviour

Figure B.2 - Experimental Result for T2

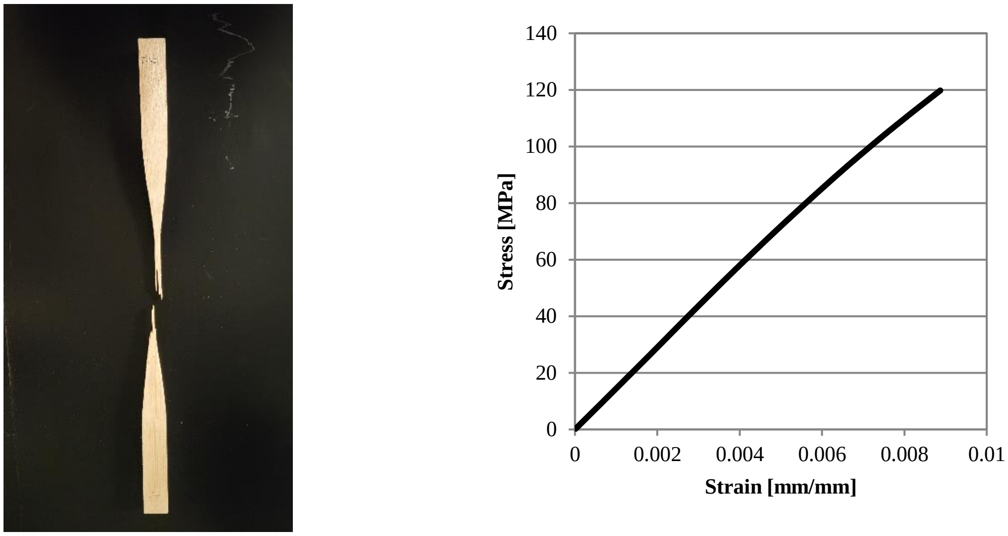

(a) Ultimate failure (b) Stress-strain behaviour

Figure B.3 - Experimental Result for T3

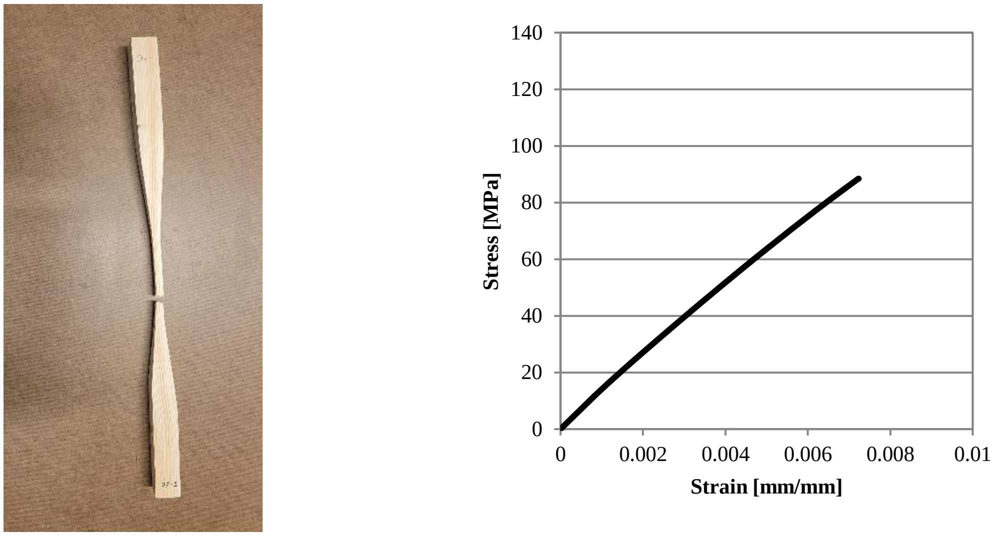

(a) Ultimate failure (b) Stress-strain behaviour

Figure B.4 - Experimental Result for T4

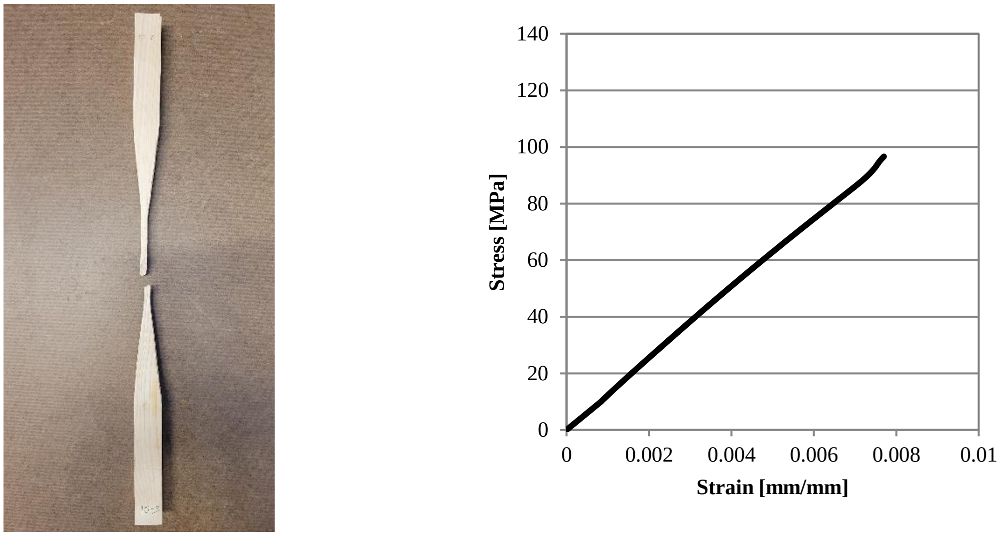

(a) Ultimate failure (b) Stress-strain behaviour

Figure B.5 - Experimental Result for T5

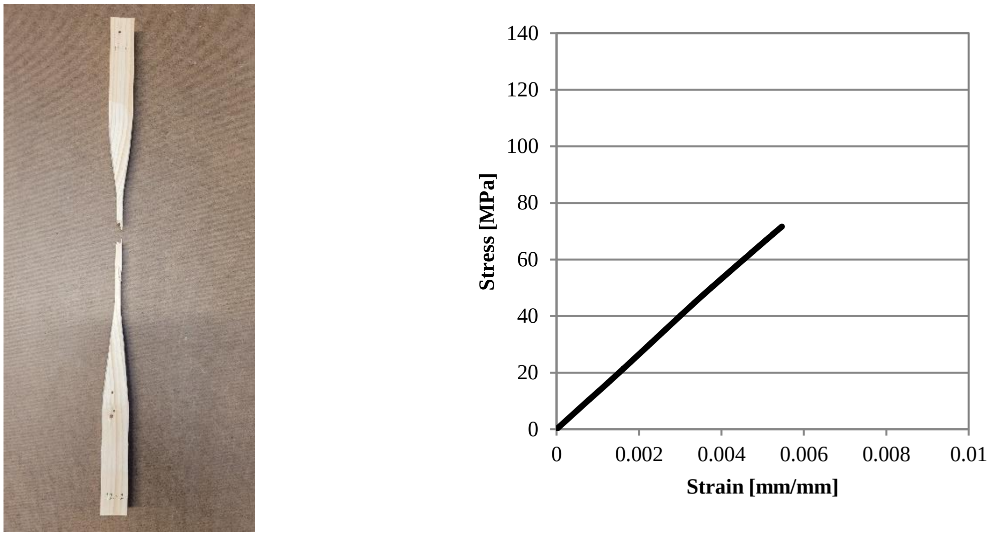

(a) Ultimate failure (b) Stress-strain behaviour

Figure B.6 - Experimental Result for T6

Appendix C

Test Results of FRP Tension Coupons

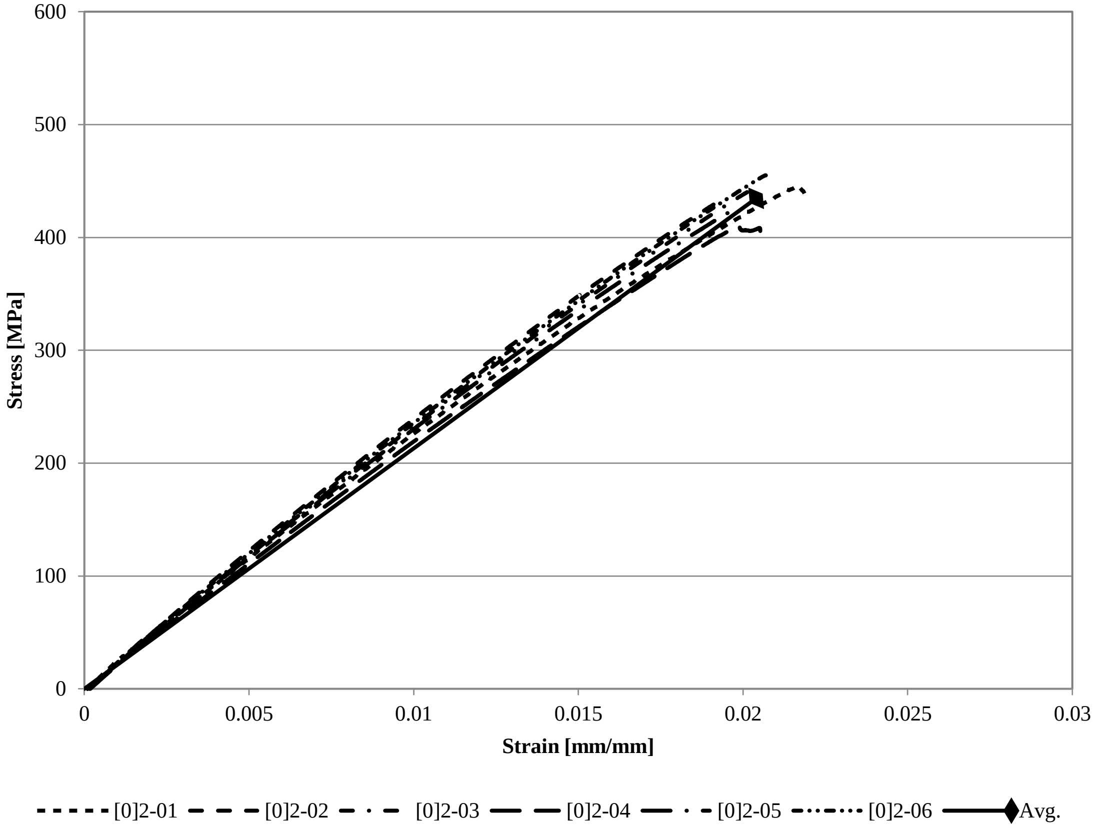

Figure C.1 - Experimental Stress-Strain Curves of GFRP $[0]_2$ Coupons

Table C.1 - Summary of Results for GFRP $[0]_2$

Specimen	A (mm^2)	MOE (MPa)	f_{tu} (MPa)	ε_{tu} (mm/mm)
01	55.15	22,960	444.95	0.0218
02	55.93	24,477	431.47	0.0193
03	57.53	23,838	442.10	0.0203
04	60.77	22,204	409.68	0.0206
05	58.61	23,793	424.56	0.0198
06	57.60	23,773	455.09	0.0207
Average	57.60	23,507	434.64	0.0204
Std. Dev	1.82	730	14.80	0.0008
COV	0.03	0.03	0.03	0.04

[a] Average cross-sectional area
[b] Tension modulus of elasticity
[c] Ultimate tensile strength
[d] Ultimate tensile strain

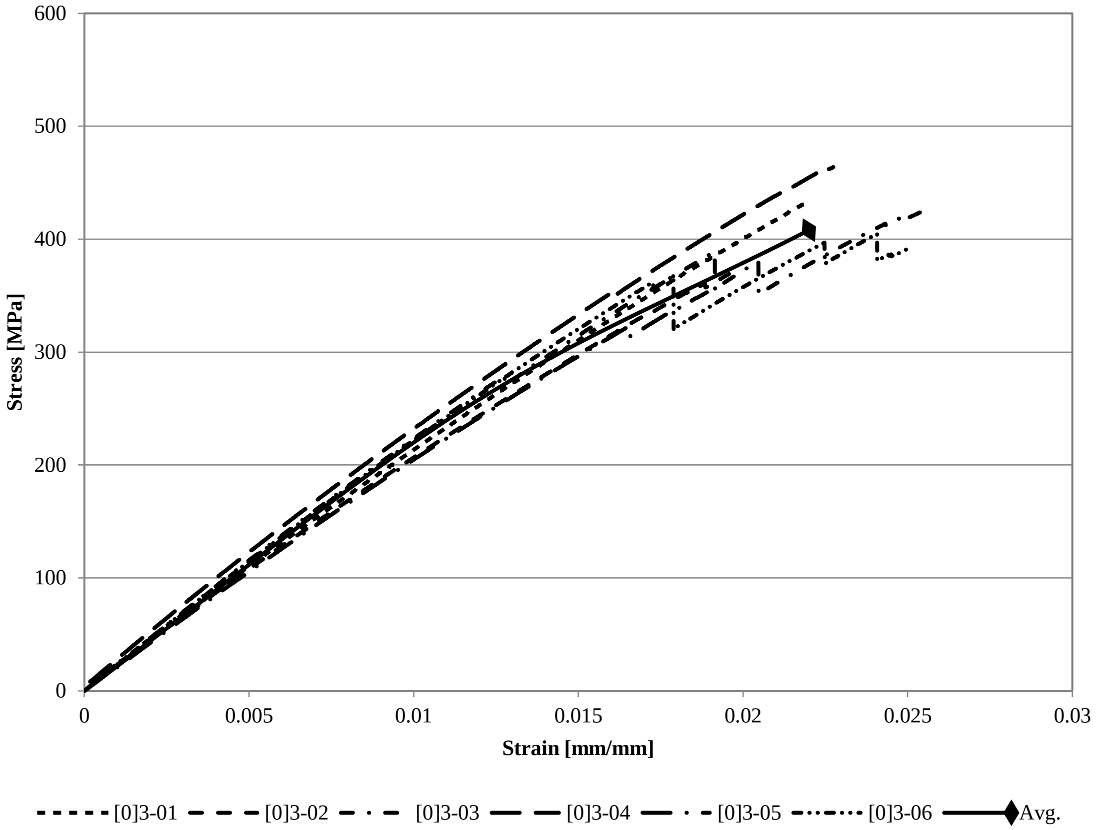

Figure C.2 - Experimental Stress-Strain Curves of GFRP $[0]_3$ Coupons

Table C.2 - Summary of Results for GFRP $[0]_3$

Specimen	A (mm^2)	MOE (MPa)	f_{tu} (MPa)	ε_{tu} (mm/mm)
01	88.47	23,085	430.99	0.0221
02	98.50	23,237	369.16	0.0200
03	92.88	23,189	424.28	0.0268
04	93.60	23,436	463.88	0.0230
05	95.45	22,651	374.22	0.0189
06	98.84	22,985	390.88	0.0248
Average	94.62	23,097	408.90	0.0226
Std. Dev	3.55	243	33.80	0.0027
COV	0.04	0.01	0.08	0.12

[a] Average cross-sectional area
[b] Tension modulus of elasticity
[c] Ultimate tensile strength
[d] Ultimate tensile strain

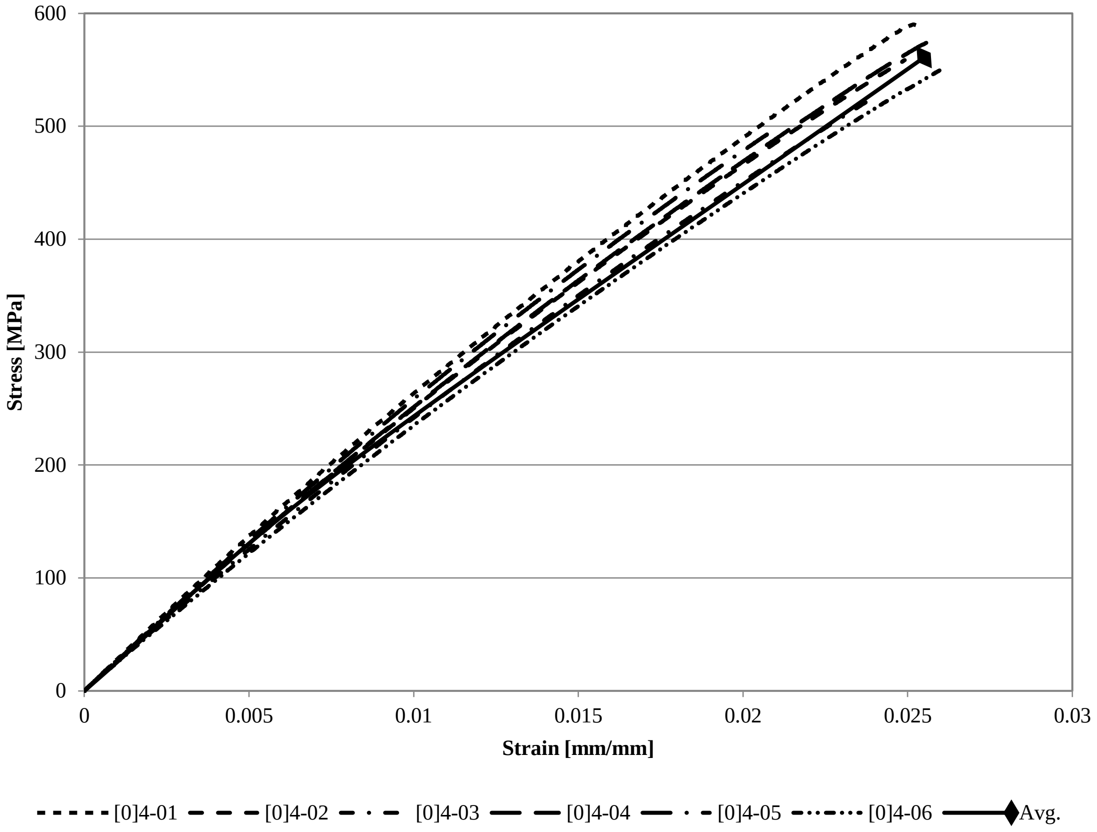

Figure C.3 - Experimental Stress-Strain Curves of GFRP $[0]_4$ Coupons

Table C.3 - Summary of Results for GFRP $[0]_4$

Specimen	**A (mm^2)**	**MOE (MPa)**	**f_{tu} (MPa)**	**ε_{tu} (mm/mm)**
01	102.53	26,584	590.15	0.0255
02	105.13	25,116	558.48	0.0251
03	113.95	24,247	527.65	0.0242
04	106.10	25,239	578.69	0.0261
05	104.22	25,545	559.12	0.0256
06	110.27	24,147	551.65	0.0263
Average	107.03	25,146	560.96	0.0255
Std. Dev	3.89	821	19.88	0.0007
COV	0.04	0.03	0.04	0.03

[a] Average cross-sectional area

[b] Tension modulus of elasticity

[c] Ultimate tensile strength

[d] Ultimate tensile strain

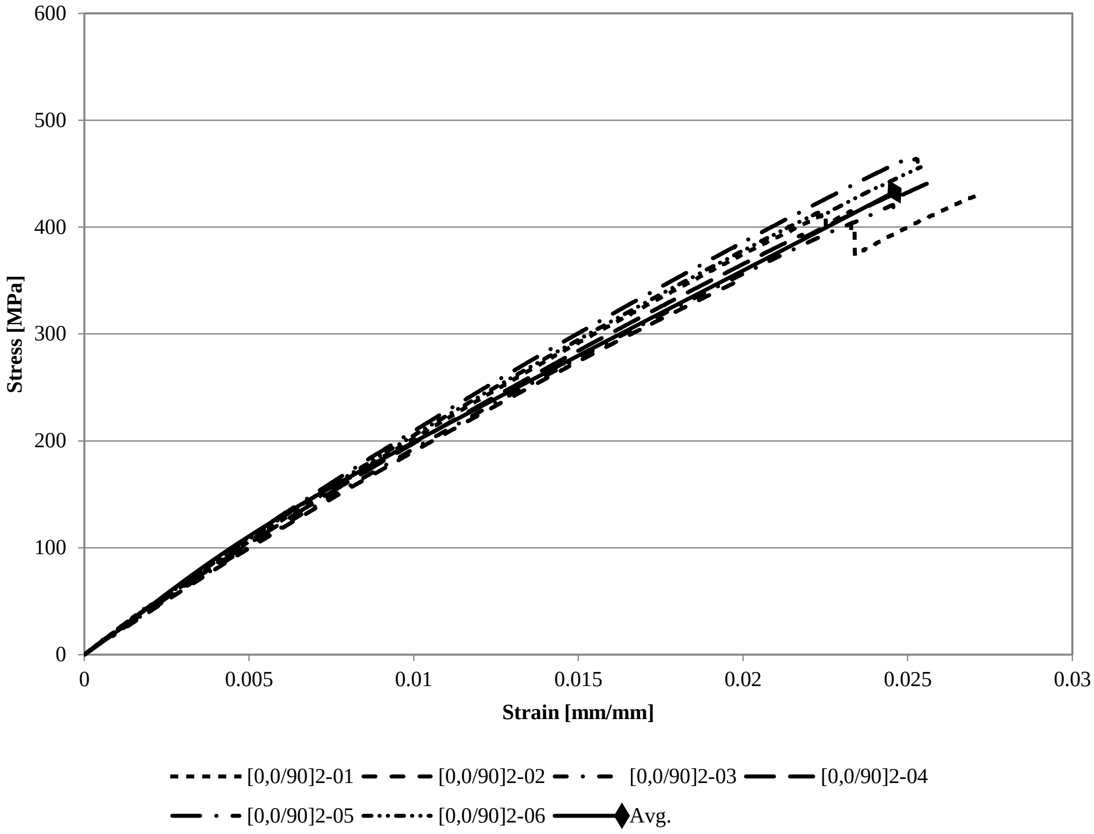

Figure C.4 - Experimental Stress-Strain Curves of GFRP [0, 0/90]$_2$ Coupons

Table C.4 - Summary of Results for GFRP [0, 0/90]$_2$

Specimen	**A (mm^2)**	**MOE (MPa)**	**f_{tu} (MPa)**	**ε_{tu} (mm/mm)**
01	91.02	17,802	414.87	0.0236
02	95.97	16,274	369.85	0.0221
03	95.61	16,709	420.67	0.0249
04	94.57	17,162	443.99	0.0260
05	88.58	18,340	463.89	0.0256
06	90.52	17,880	455.83	0.0256
Average	92.71	17,361	428.19	0.0246
Std. Dev	2.80	715	31.43	0.0014
COV	0.03	0.04	0.07	0.06

[a] Average cross-sectional area

[b] Tension modulus of elasticity

[c] Ultimate tensile strength

[d] Ultimate tensile strain

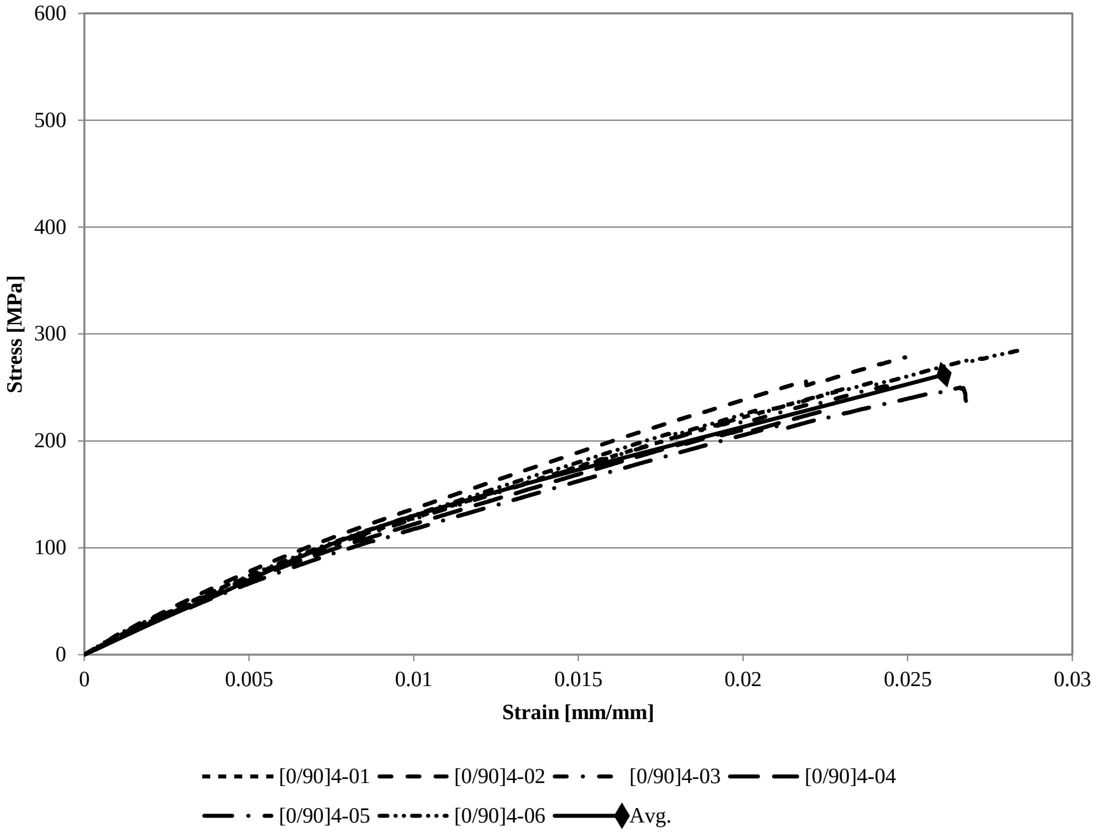

Figure C.5 - Experimental Stress-Strain Curves of GFRP [0/90]$_4$ Coupons

Table C.5 - Summary of Results for GFRP [0/90]$_4$

Specimen	**A (mm^2)**	**MOE (MPa)**	**f_{tu} (MPa)**	**ε_{tu} (mm/mm)**
01	79.20	12,512	245.75	0.0231
02	79.75	11,364	278.15	0.0251
03	82.82	11,570	252.62	0.0248
04	86.26	12,311	259.77	0.0276
05	83.87	11,148	249.96	0.0270
06	79.29	12,910	284.57	0.0293
Average	81.87	11,969	261.80	0.0261
Std. Dev	2.66	645	14.56	0.0020
COV	0.03	0.05	0.06	0.08

[a] Average cross-sectional area

[b] Tension modulus of elasticity

[c] Ultimate tensile strength

[d] Ultimate tensile strain

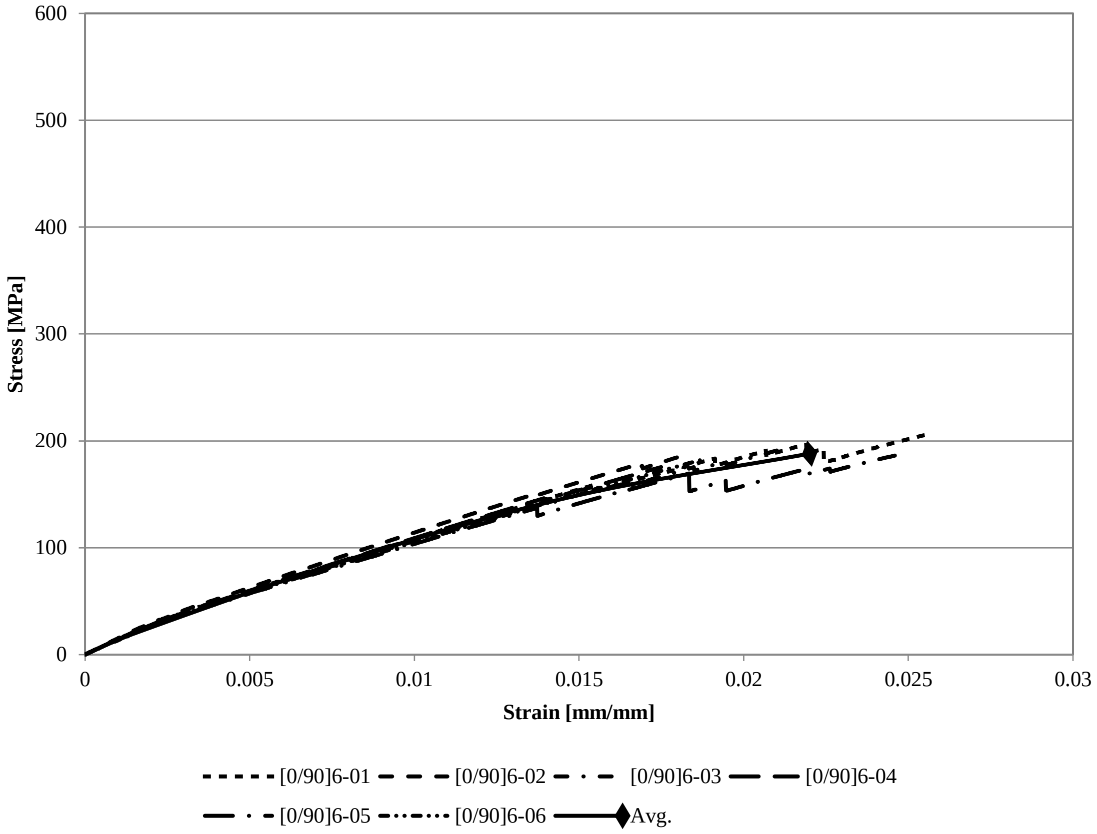

Figure C.6 - Experimental Stress-Strain Curves of GFRP $[0/90]_6$ Coupons

Table C.6 - Summary of Results for GFRP $[0/90]_6$

Specimen	A (mm^2)	MOE (MPa)	f_{tu} (MPa)	ε_{tu} (mm/mm)
01	127.04	9,900	207.32	0.0260
02	129.66	10,715	185.28	0.0181
03	123.95	9,663	192.51	0.0216
04	132.83	9,950	192.30	0.0233
05	135.05	9,483	186.24	0.0248
06	131.15	9,749	181.71	0.0190
Average	129.95	9,910	190.89	0.0221
Std. Dev	3.66	392	8.29	0.0029
COV	0.03	0.04	0.04	0.13

[a] Average cross-sectional area

[b] Tension modulus of elasticity

[c] Ultimate tensile strength

[d] Ultimate tensile strain

Appendix D

Failure Progression of Unreinforced and Reinforced Glulam Beams

Specimen Name: U-01 **Reinforcement Scheme: Unreinforced**

(1) Start of test

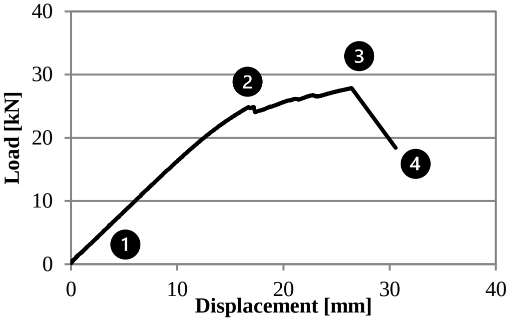

(2) Initial failure

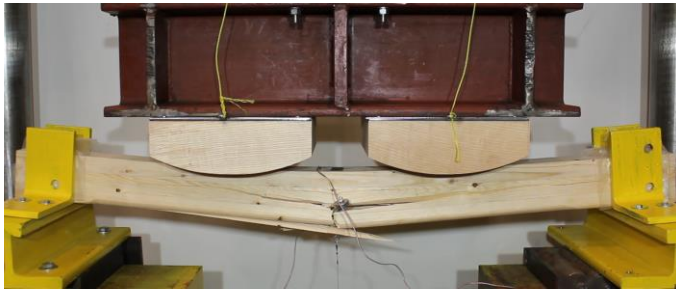

(4) Ultimate failure

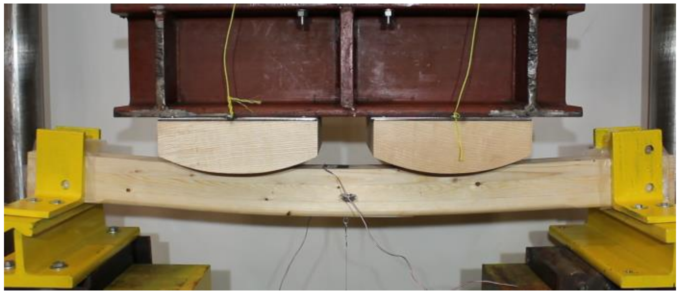

(3) Maximum load (P_{max})

Figure D.1 - Failure Progression of Control Beam U-01

Specimen Name: U-02 **Reinforcement Scheme: Unreinforced**

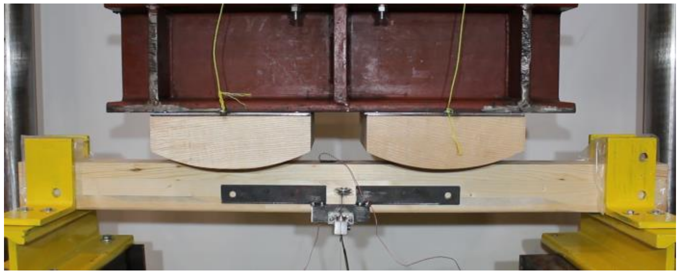

(1) Start of test

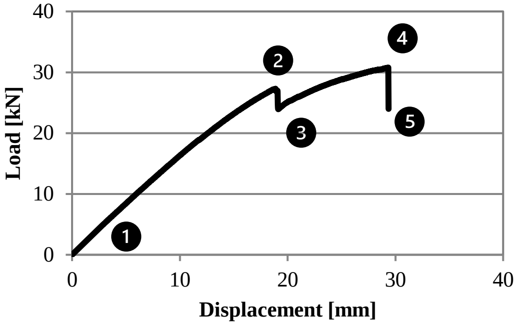

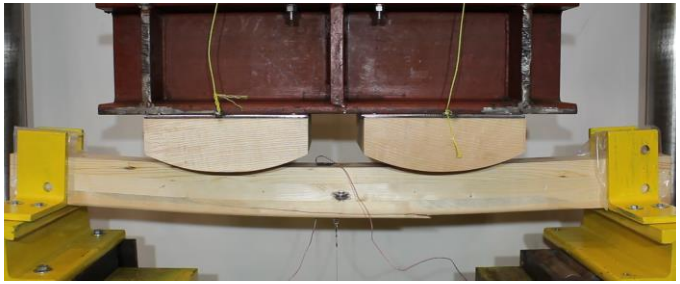

(2) Initial failure

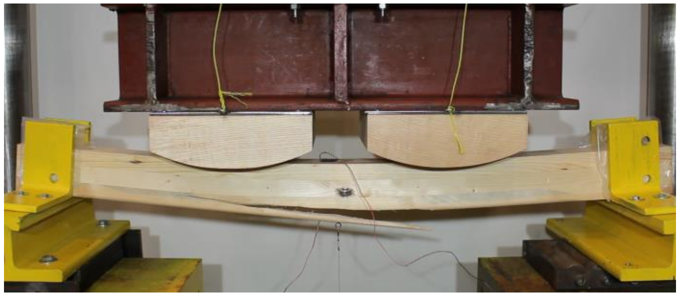

(4) Maximum load (P_{max})

(3) Propagation of initial failure

(5) Ultimate failure

Figure D.2 - Failure Progression of Control Beam U-02

Specimen Name: U-03 **Reinforcement Scheme: Unreinforced**

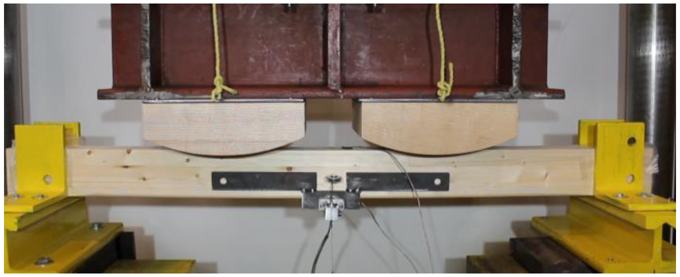

(1) Start of test

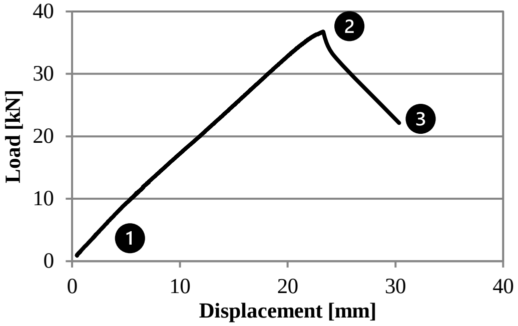

(2) Maximum load (P_{max})

(3) Ultimate failure

Figure D.3 - Failure Progression of Control Beam U-03

Specimen Name: U-04 **Reinforcement Scheme: Unreinforced**

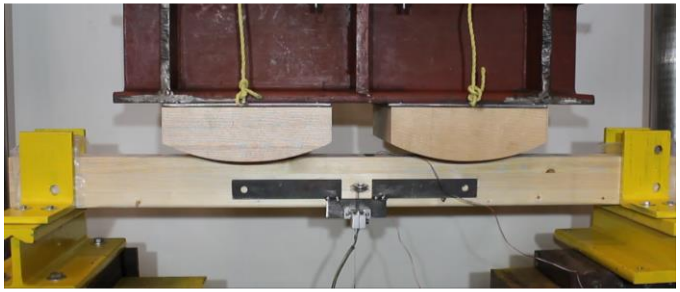

(1) Start of test

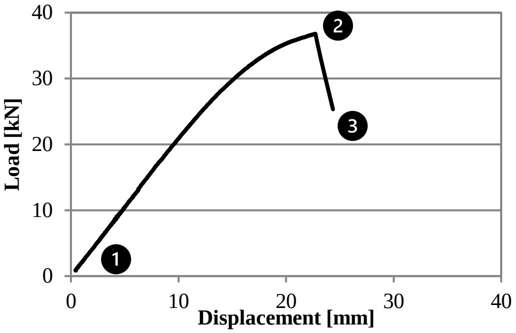

(2) Maximum load (P_{max})

(3) Ultimate failure

Figure D.4 - Failure Progression of Control Beam U-04

Specimen Name: U-05 **Reinforcement Scheme: Unreinforced**

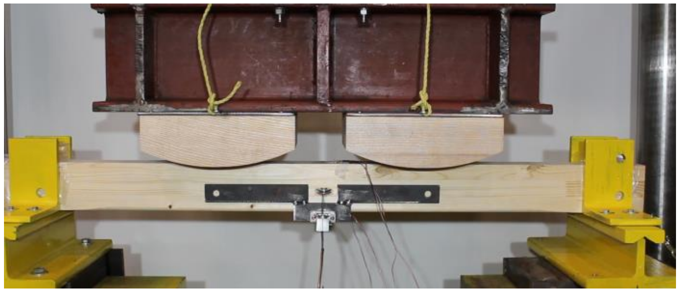

(1) Start of test

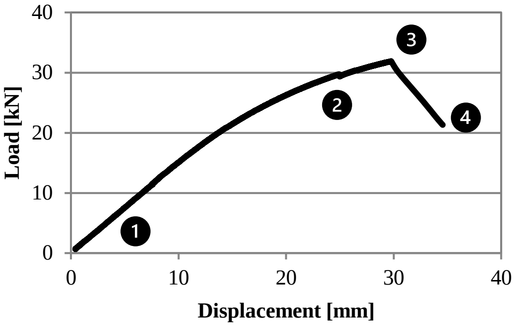

(2) Initial rupture of wood tension fibres

(4) Ultimate failure

(3) Maximum load (P_{max})

Figure D.5 - Failure Progression of Control Beam U-05

Specimen Name: R1-01 **Reinforcement Scheme: S[0]$_2$**

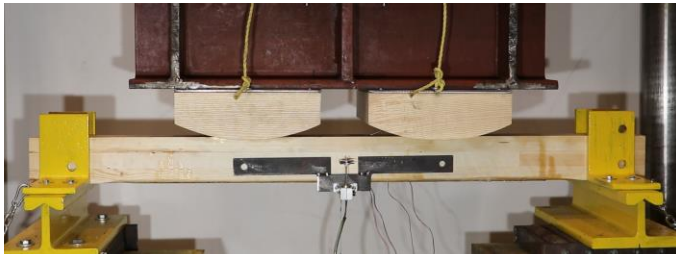

(1) Start of test

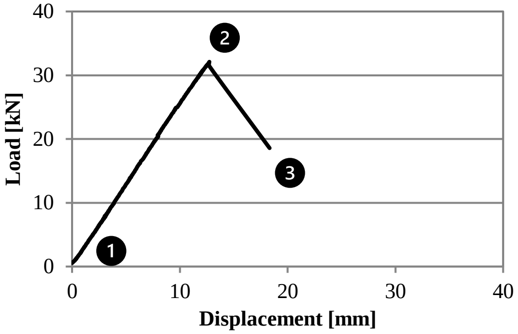

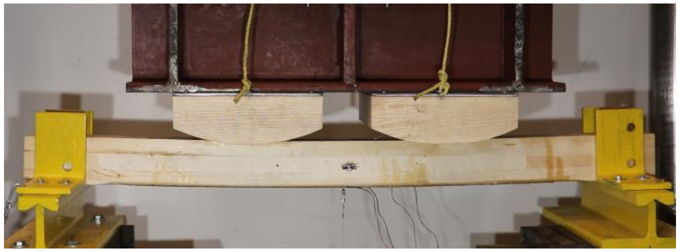

(2) Maximum load (P_{max})

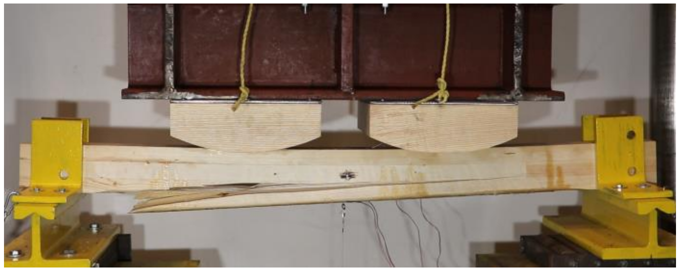

(3) Ultimate failure

Figure D.6 - Failure Progression of Reinforced Beam R1-01

Specimen Name: R1-02 **Reinforcement Scheme: S[0]$_2$**

(1) Start of test

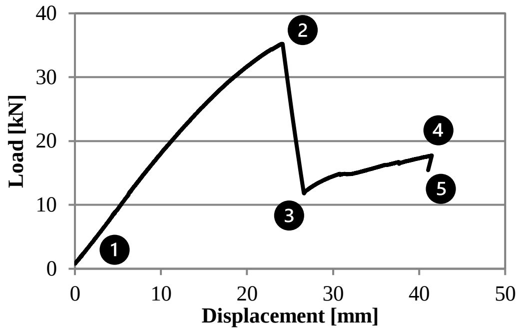

(2) Maximum load (P_{max})

(4) Second increase in load

(3) Horizontal shear failure

(5) Ultimate failure

Figure D.7 - Failure Progression of Reinforced Beam R1-02

Specimen Name: R1-03 **Reinforcement Scheme: $S[0]_2$**

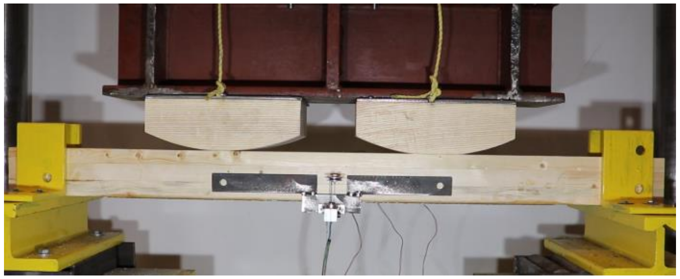

(1) Start of test

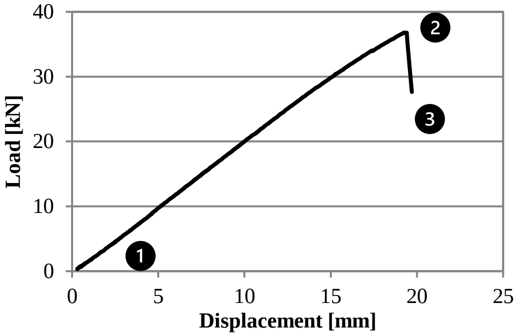

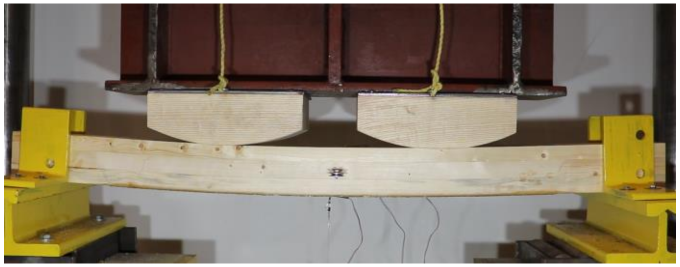

(2) At maximum load (P_{max})

(4) Ultimate failure – horizontal shear in shear region

Figure D.8 - Failure Progression of Reinforced Beam R1-03

Specimen Name: R2-01 **Reinforcement Scheme: $S[0]_4$**

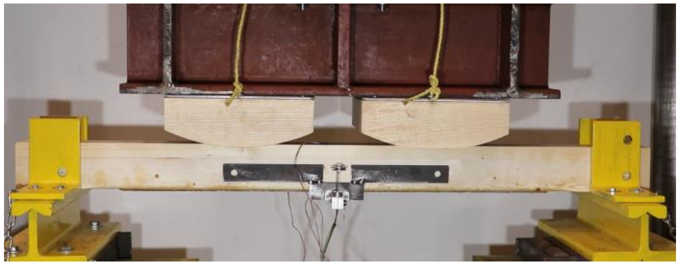

(1) Start of test

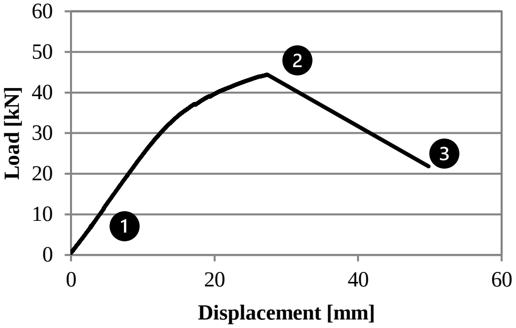

(2) Maximum load (P_{max})

(3) Ultimate failure

Figure D.9 - Failure Progression of Reinforced Beam R2-01

Specimen Name: R2-02 **Reinforcement Scheme: S[0]$_4$**

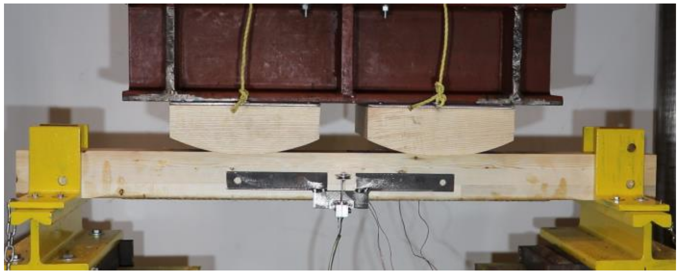

(1) Start of test

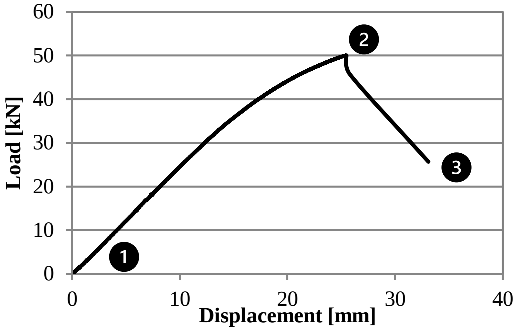

(2) Maximum load (P_{max})

(3) Ultimate failure

Figure D.10 - Failure Progression of Reinforced Beam R2-02

Specimen Name: R3-01 **Reinforcement Scheme: $U[0]_2$**

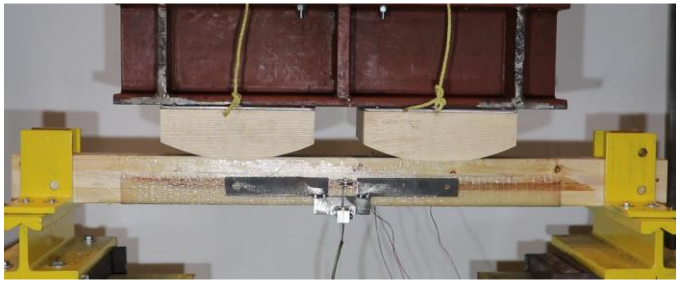

(1) Start of test

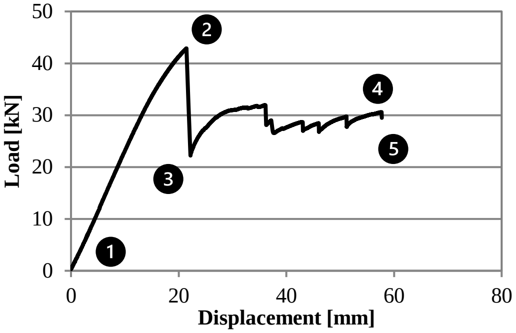

(2) Maximum load (P_{max})

(4) Shear failure propagating along the beam

(3) Horizontal shear failure

(5) Ultimate failure

Figure D.11 - Failure Progression of Reinforced Beam R3-01

Specimen Name: R3-02 **Reinforcement Scheme: $U[0]_2$**

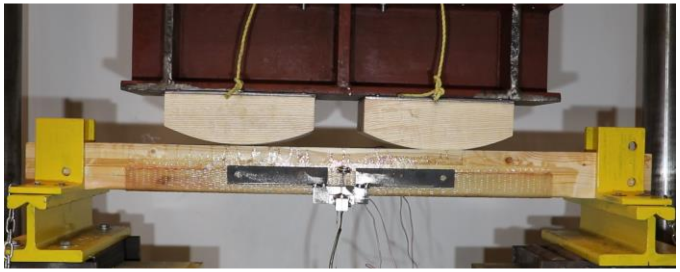

(1) Start of test

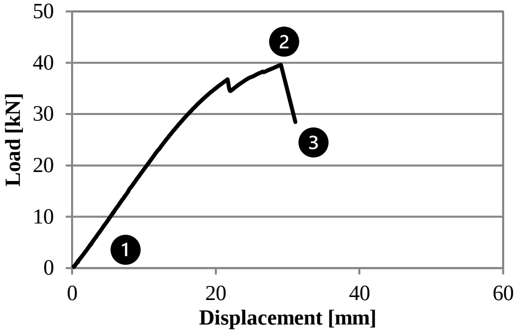

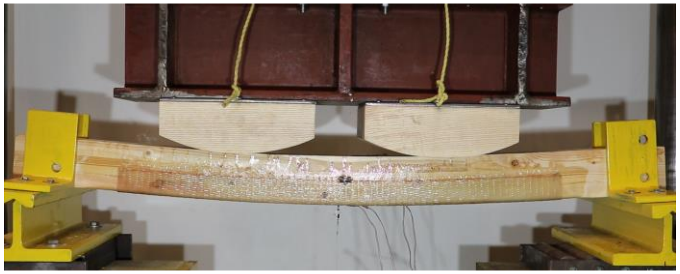

(2) Maximum load (P_{max})

(3) Ultimate failure

Figure D.12 - Failure Progression of Reinforced Beam R3-02

Specimen Name: R4-01 **Reinforcement Scheme: $U[0]_4$**

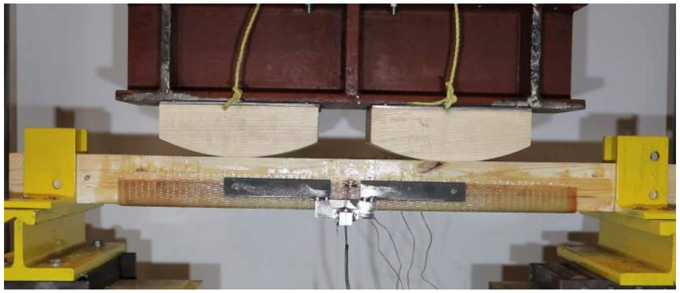

(1) Start of test

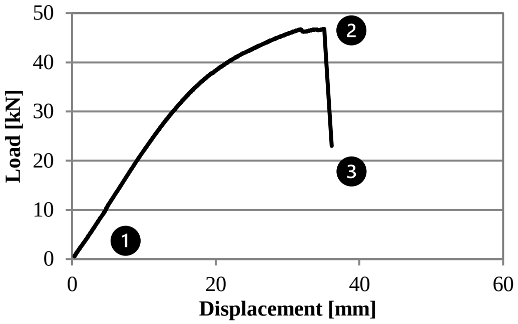

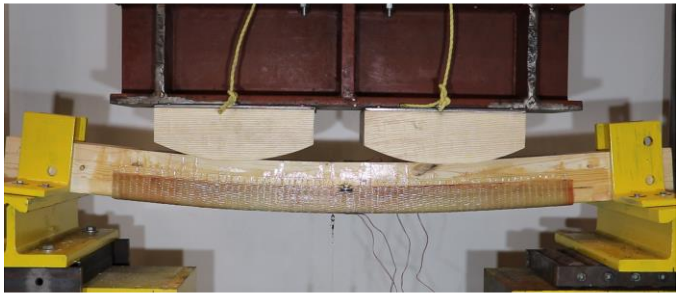

(2) Maximum load (P_{max})

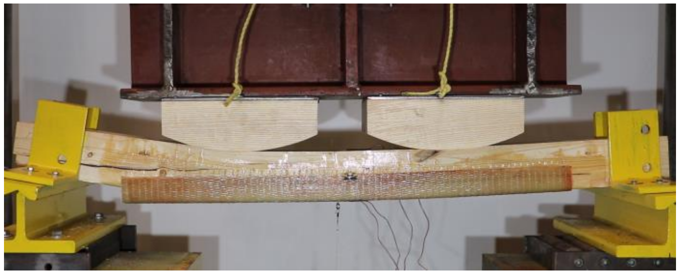

(3) Ultimate failure

Figure D.13 - Failure Progression of Reinforced Beam R4-01

Specimen Name: R4-02 **Reinforcement Scheme: $U[0]_4$**

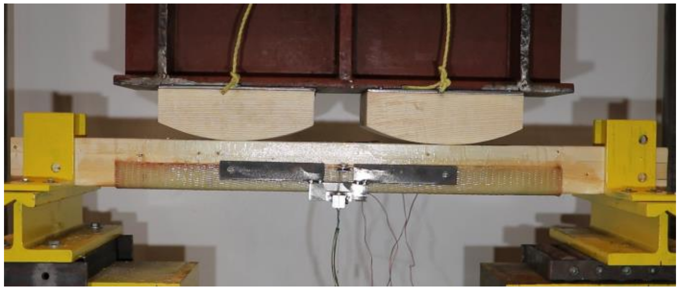

(1) Start of test

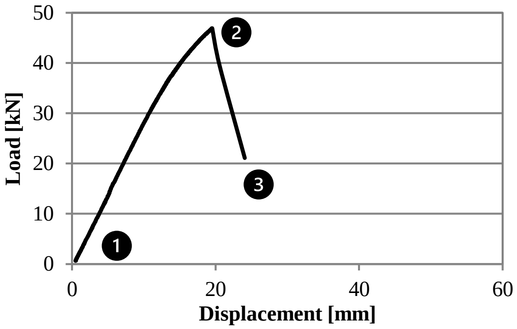

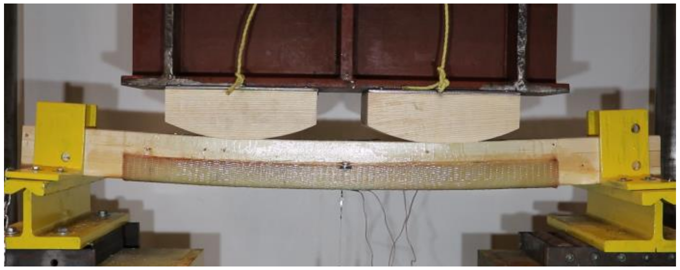

(2) Maximum load (P_{max})

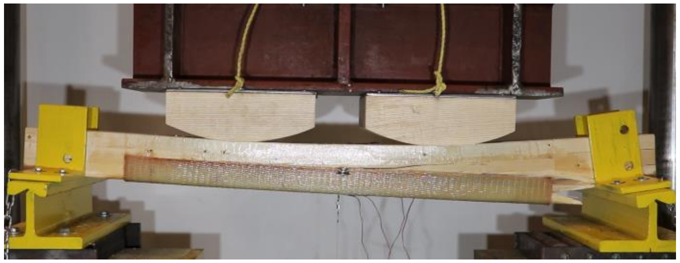

(3) Ultimate failure

Figure D.14 - Failure Progression of Reinforced Beam R4-02

Specimen Name: R5-01 **Reinforcement Scheme: S[0]$_2$ H[0]$_2$**

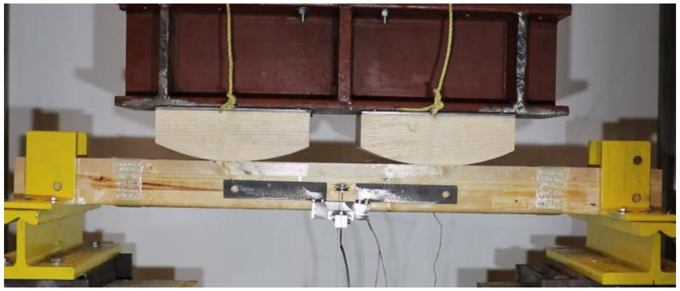

(1) Start of test

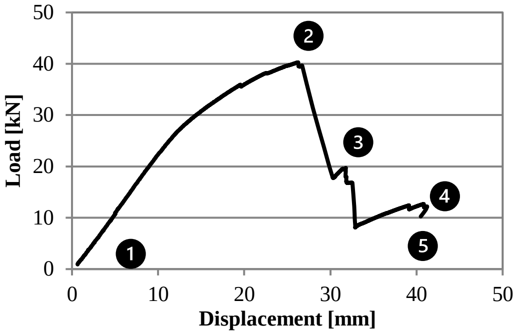

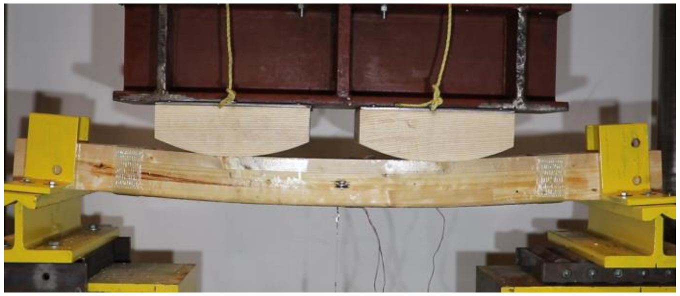

(2) At maximum load (P_{max})

(4) Shear failure propagating throughout laminates

(3) Failure initiating in the tension laminate and extending to the shear hoop

(5) Ultimate failure

Figure D.15 - Failure Progression of Reinforced Beam R5-01

Specimen Name: R5-02 **Reinforcement Scheme: S[0]$_4$ H[0]$_2$**

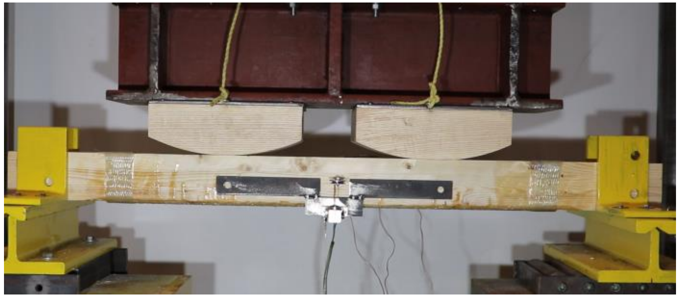

(1) Start of test

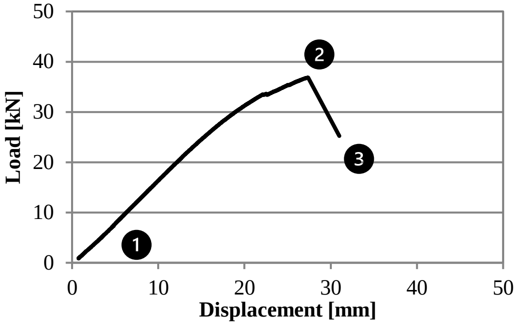

(2) At maximum load (P_{max})

(3) Ultimate failure – large knot on tension face of the wood

Figure D.16 - Failure Progression of Reinforced Beam R5-02

Specimen Name: R6-01 **Reinforcement Scheme: $S[0]_2$ $H[0]_2$**

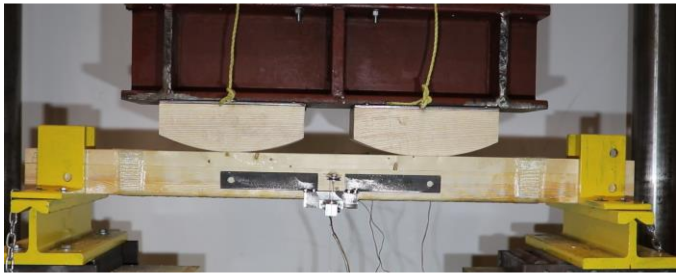
(1) Start of test

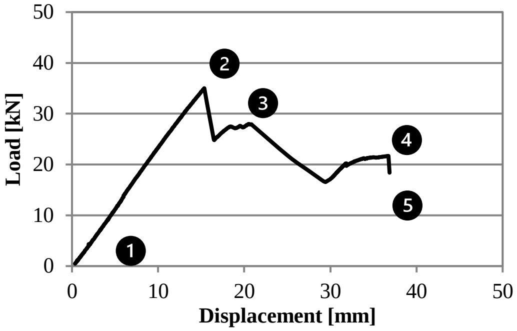

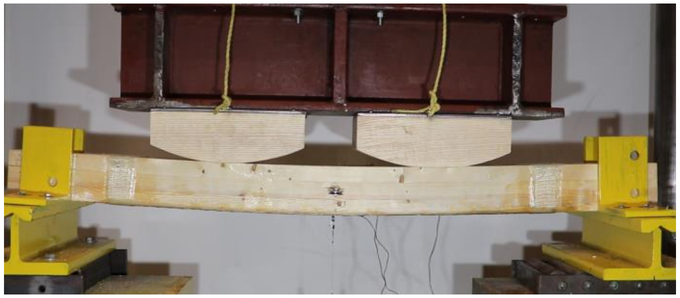
(2) At maximum load (P_{max})


(4) Wood failure propagating through laminates


(3) Wood tensile failure near midspan

(5) Ultimate failure

Figure D.17 - Failure Progression of Reinforced Beam R6-01

Specimen Name: R6-02 **Reinforcement Scheme: $S[0]_4\ H[0/90]_2$**

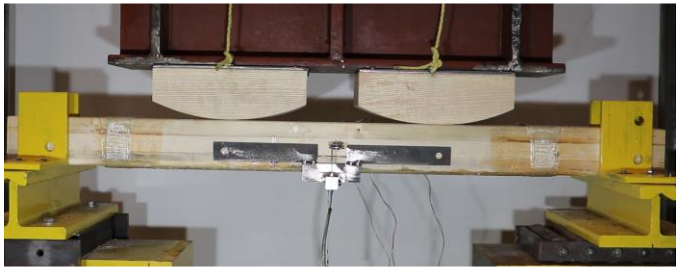

(1) Start of test

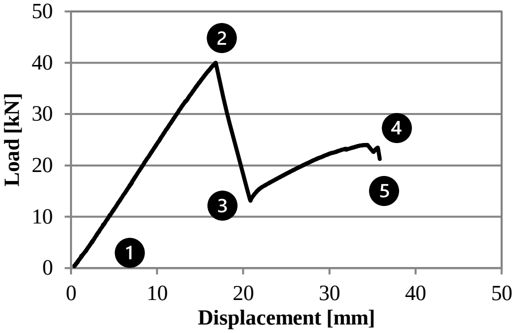

(2) At maximum load (P_{max})

(4) Wood failure propagating through laminates

(3) Wood tensile and shear failure extending to shear hoop

(5) Ultimate failure

Figure D.18 - Failure Progression of Reinforced Beam R6-02

Specimen Name: R7-01 **Reinforcement Scheme: U[0]$_2$ C[0/90]$_2$**

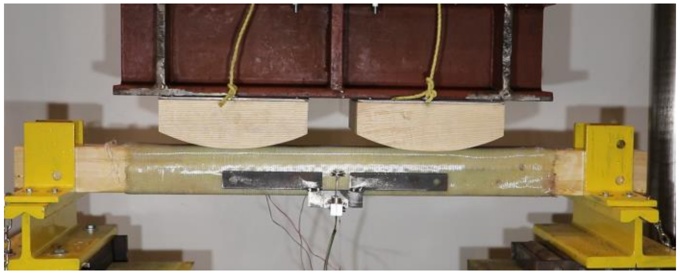

(1) Start of test

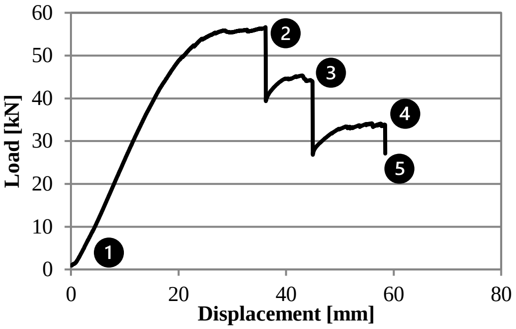

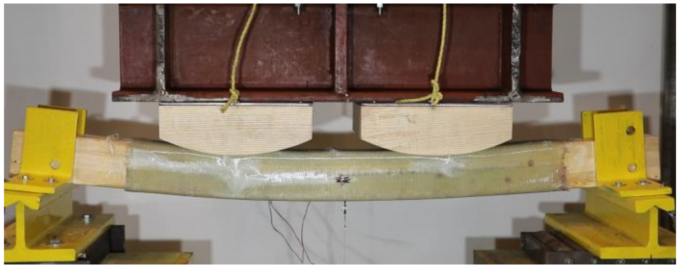

(2) FRP compression failure at maximum load (P_{max})

(4) FRP and wood failure propagation at third load peak

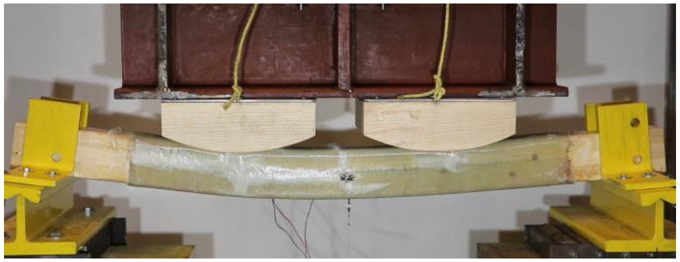

(3) FRP failure propagation and wood compression failure

(5) Ultimate failure

Figure D.19 - Failure Progression of Reinforced Beam R7-01

Specimen Name: R7-02 **Reinforcement Scheme: U[0]$_2$ C[0/90]$_2$**

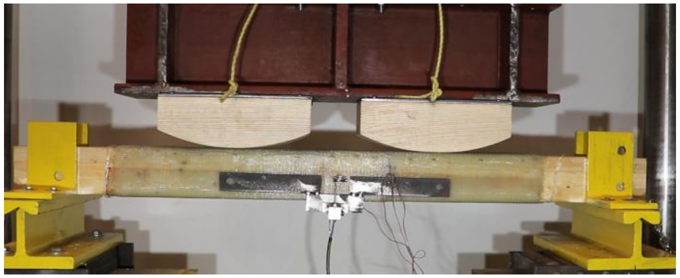

(1) Start of test

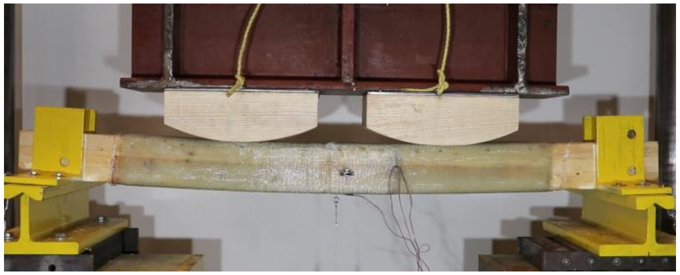

(2) Initial buckling of the FRP in compression at midspan

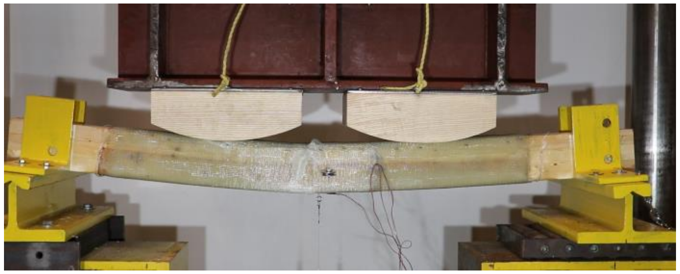

(3) FRP tension failure at maximum load (P_{max})

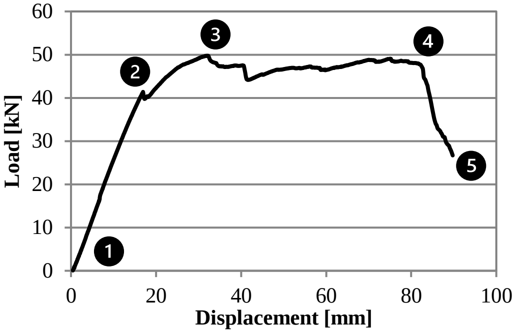

(4) FRP failure propagation and wood (tension and compression) failure confined at midspan

(5) Ultimate failure

Figure D.20 - Failure Progression of Reinforced Beam R7-02

Specimen Name: R8-01 **Reinforcement Scheme: C[0/90]$_4$**

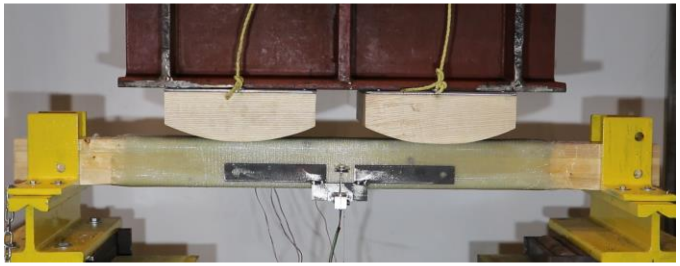

(1) Start of test

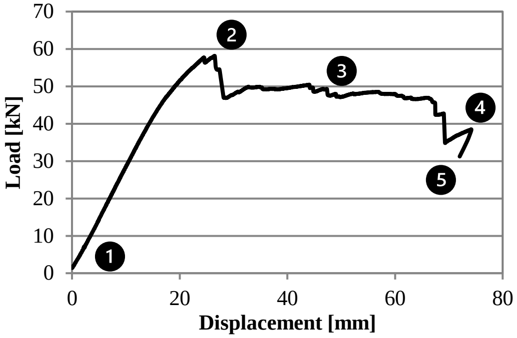

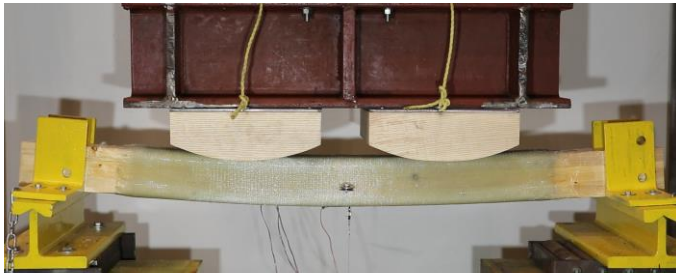

(2) Initial buckling of the FRP in compression near point load at maximum load (P_{max})

(4) FRP failure propagation and wood (tension and compression) failure confined near the leftmost point load

(3) FRP compression failure propagation within confined region

(5) Ultimate failure

Figure D.21 - Failure Progression of Reinforced Beam R8-01

Specimen Name: R8-02 **Reinforcement Scheme: C[0/90]$_4$**

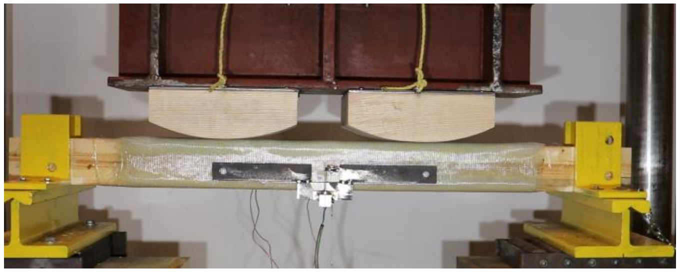

(1) Start of test

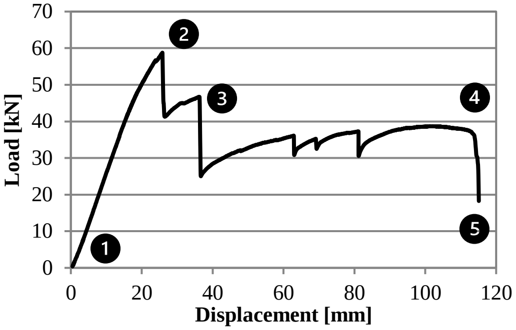

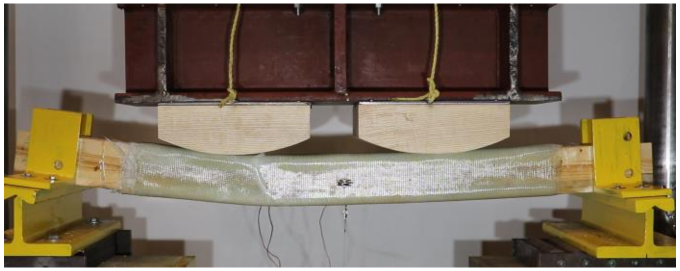

(2) FRP tension and compression failure near leftmost point load at maximum load (P_{max})

(4) FRP failure propagation and wood (tension and compression) failure confined near the leftmost point load

(3) FRP failure propagation within confined region

(5) Ultimate failure

Figure D.22 - Failure Progression of Reinforced Beam R8-02

Specimen Name: R9-01 **Reinforcement Scheme: $S[0]_2$ $TA[0/90]_2$**

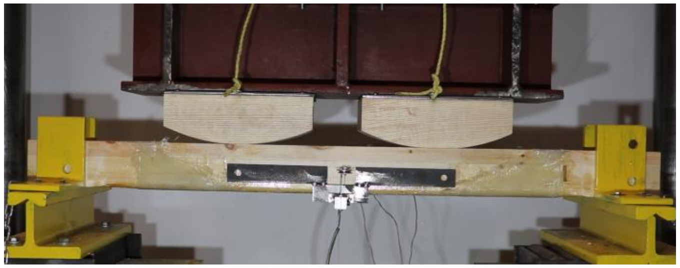

(1) Start of test

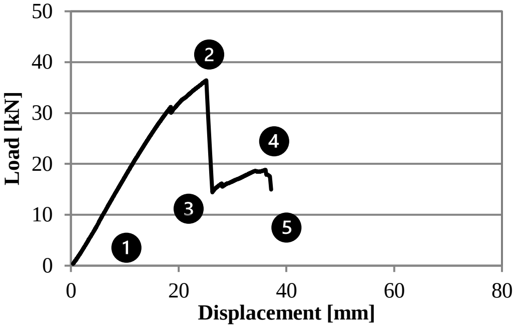

(2) At maximum load (P_{max})

(4) Propagation of shear failure near the midspan

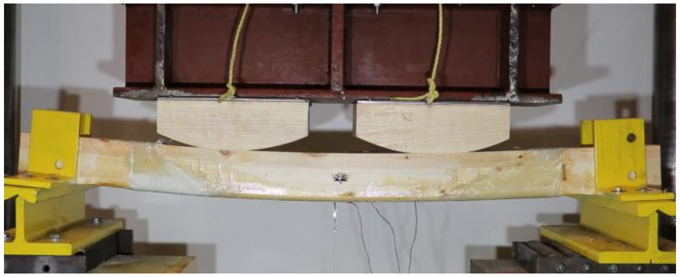

(3) Failure in the shear region

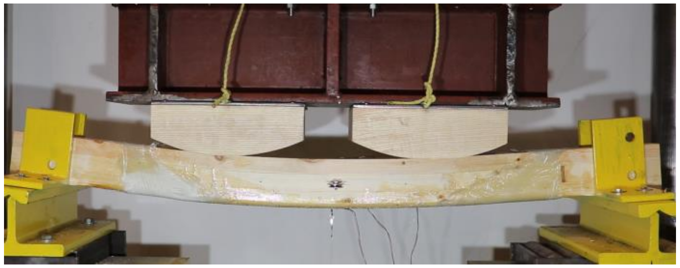

(5) Ultimate failure

Figure D.23 - Failure Progression of Reinforced Beam R9-01

Specimen Name: R9-02 **Reinforcement Scheme: S[0]$_2$ TA[0/90]$_2$**

(1) Start of test

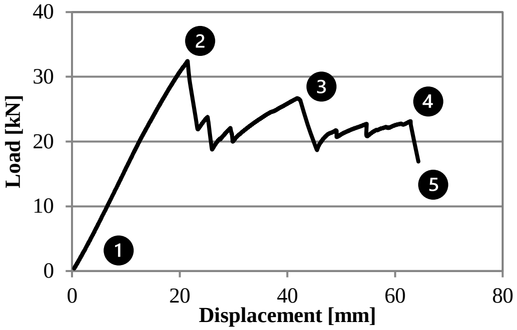

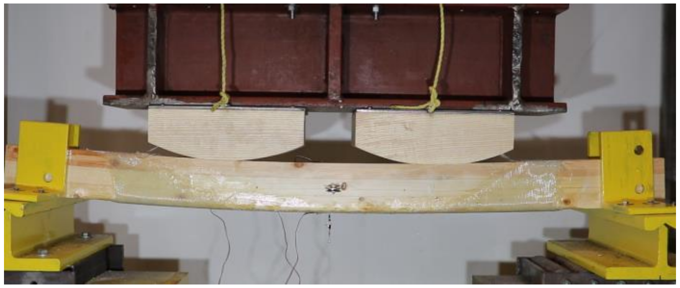

(2) At maximum load (P_{max})

(4) Failure propagating into the shear region

(3) Failure initiating within the wood tension fibres

(5) Ultimate failure

Figure D.24 - Failure Progression of Reinforced Beam R9-02

Specimen Name: R10-01 **Reinforcement Scheme: TA[0/90]$_4$**

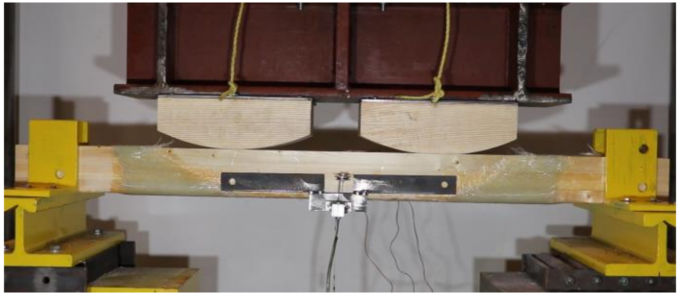

(1) Start of test

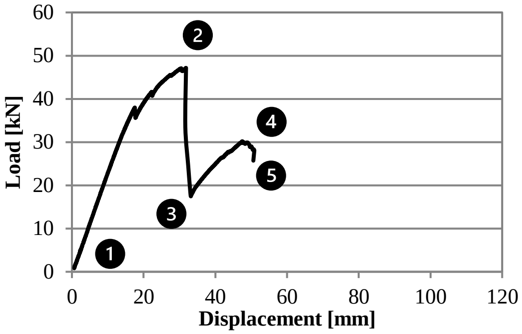

(2) At maximum load (P_{max})

(4) Propagating wood failure and initiating of FRP rupture

(3) Wood tensile failure under the point load

(5) Ultimate failure

Figure D.25 - Failure Progression of Reinforced Beam R10-01

Specimen Name: R10-02 **Reinforcement Scheme: TA[0/90]$_4$**

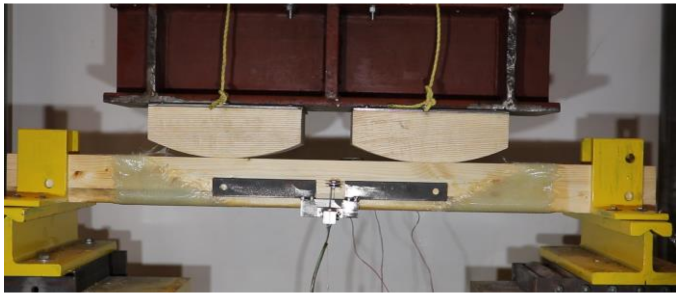

(1) Start of test

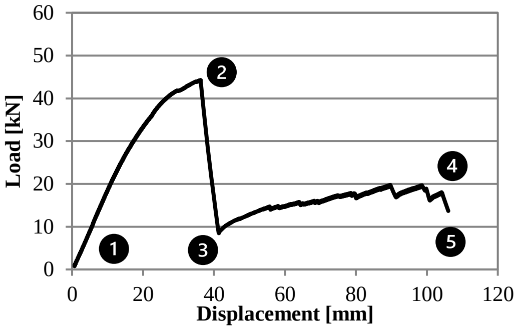

(2) At maximum load (P_{max})

(4) Propagating wood failure and engagement of FRP shear reinforcement

(3) Wood tensile and shear failure

(5) Ultimate failure

Figure D.26 - Failure Progression of Reinforced Beam R10-02

Specimen Name: R11-01 **Reinforcement Scheme: $S[0]_3\ H[0/90]_2$**

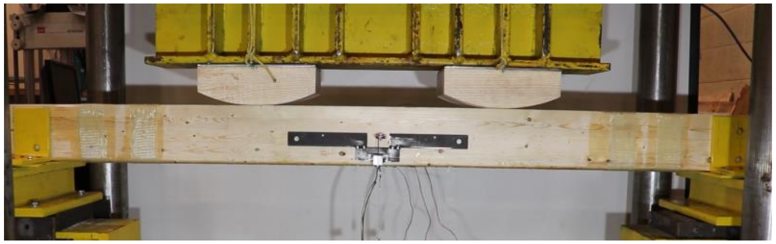

(1) Start of test

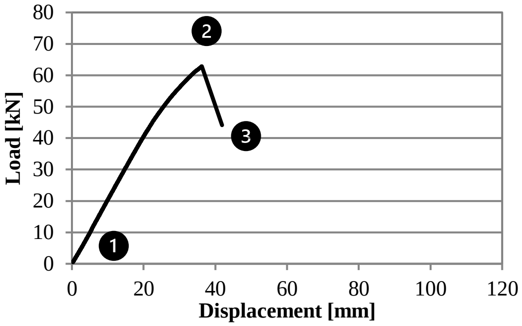

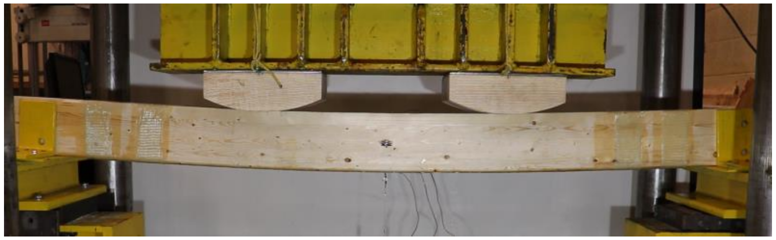

(2) At maximum load (P_{max})

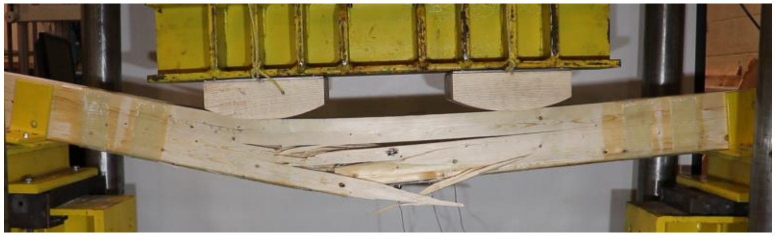

(4) Propagating wood tensile failure (Data unavailable)

(3) Wood tensile failure *String pot disconnects

(5) Ultimate failure

Figure D.27 - Failure Progression of Reinforced Beam R11-01

Specimen Name: R11-02 **Reinforcement Scheme: S[0]$_3$ H[0/90]$_2$**

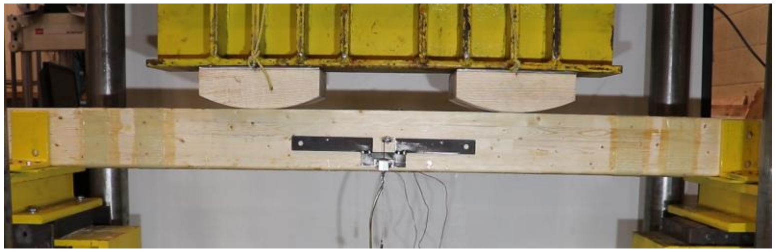

(1) Start of test

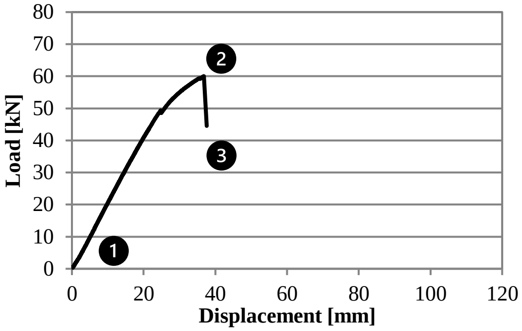

(2) At maximum load (P_{max})

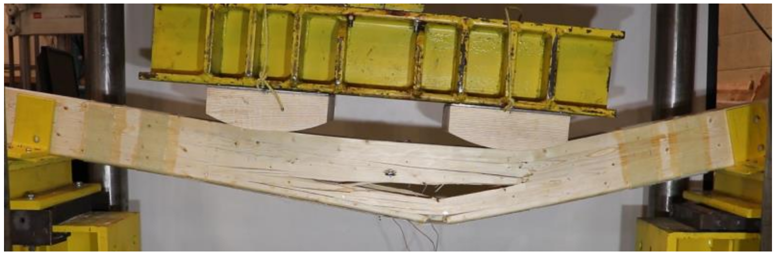

(4) Propagating wood failure and engagement of FRP shear reinforcement

(3) Wood tensile at finger joint *String pot disconnects

(5) Ultimate failure

Figure D.28 - Failure Progression of Reinforced Beam R11-02

Specimen Name: R12-01 **Reinforcement Scheme: TA[0/90]$_6$**

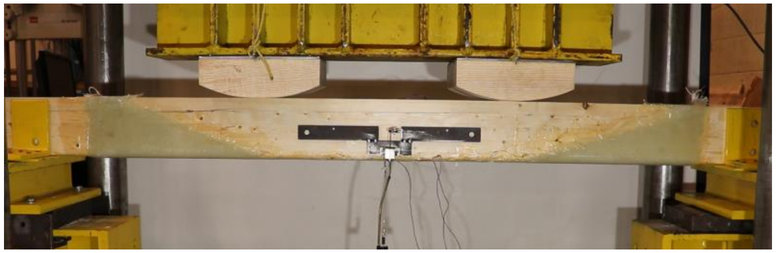

(1) Start of test

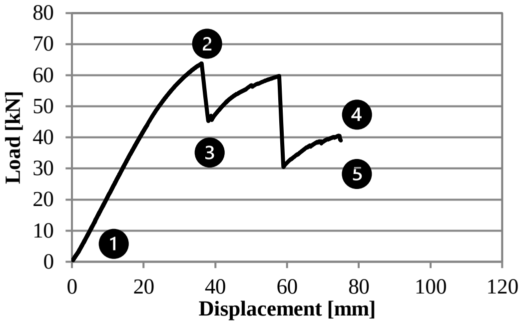

(2) At maximum load (P_{max})

(4) Propagating wood tension and FRP failure

(3) Wood tensile failure and FRP rupture

(5) Ultimate failure

Figure D.29 - Failure Progression of Reinforced Beam R12-01

Specimen Name: R12-02 **Reinforcement Scheme: TA[0/90]$_6$**

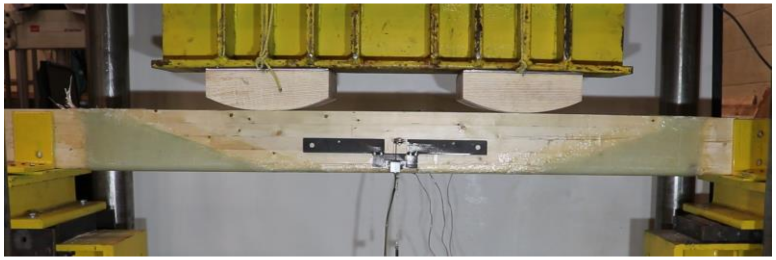

(1) Start of test

(2) At maximum load (P_{max})

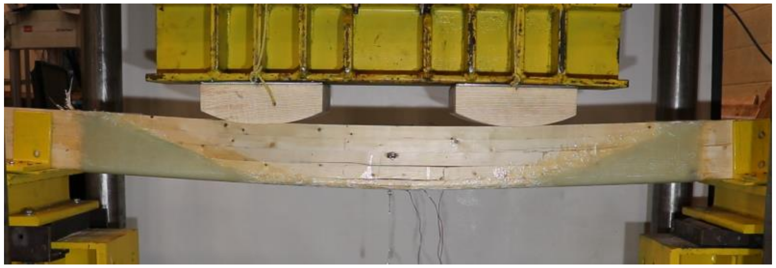

(3) Wood tensile failure

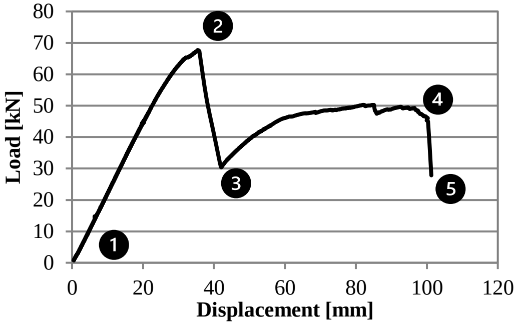

(4) Propagating wood failure and commencement of FRP tensile rupture

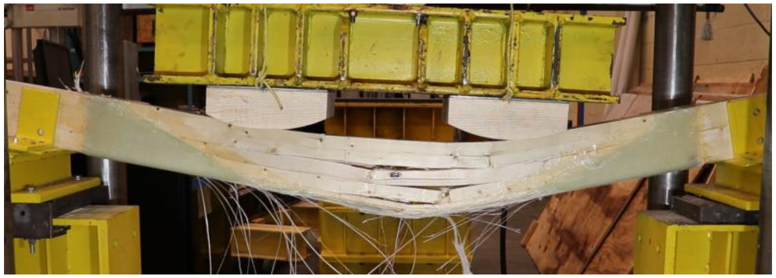

(5) Ultimate failure

Figure D.30 - Failure Progression of Reinforced Beam R12-02

Appendix E

Derivation of Displacement Equations for Resistance Curve

This appendix provides the derivation of the displacement equations of a beam subjected to four-point bending loads. The equations are kept in terms of the curvature, φ, which differentiates from the typical displacement equations developed based on the loading and bending stiffness. This method was chosen to allow for the midspan displacement to be calculated based on the moment-curvature data previously calculated in Section 5.3. The beam diagrams used as basis for the derivation are shown in Figure E.1.

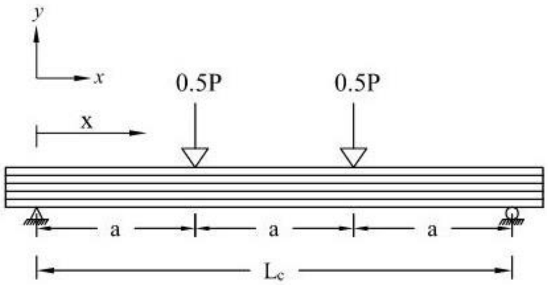

(a) Simple beam - Two equal concentrated loads symmetrically placed

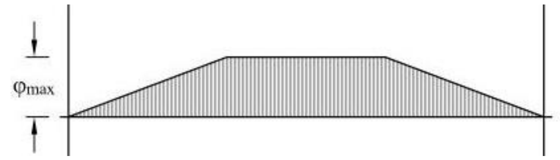

(b) Curvature, φ (1/m)

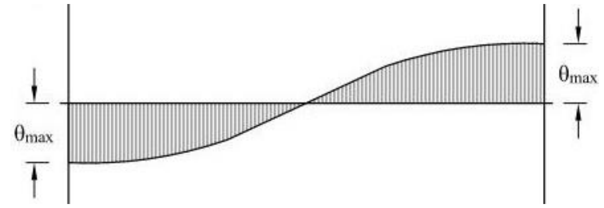

(c) Slope, θ (rad)

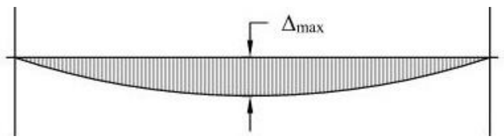

(d) Displacement, Δ (mm)

Figure E.1 - Beam Diagrams for Deflection Derivation

Establishing a rectangular coordinate system originating at the pin support (Figure E.1a), we can double integrate the differential equation of the elastic curve (Eq. (E.1) in terms of x for both coordinate sets considered on the beam (i.e., x < a, x > a and x < 2a).

$$\frac{d^2\Delta}{dx^2} = \frac{M}{EI} = \varphi \tag{E.1}$$

For $x < a$;

$$\frac{d^2\Delta_1}{dx^2} = \frac{\varphi_m x}{a}$$

$$\frac{d\Delta_1}{dx} = \frac{\varphi_m x^2}{2a} + C_1$$

$$\Delta_1 = \frac{\varphi_m x^3}{6a} + C_1 x + C_2 \tag{E.2}$$

For $x > a$ and $x < 2a$;

$$\frac{d^2\Delta_2}{dx^2} = \varphi_m$$

$$\frac{d\Delta_2}{dx} = \varphi_m x + C_3$$

$$\Delta_2 = \frac{\varphi_m x^2}{2} + C_3 x + C_4 \tag{E.3}$$

Four boundaries and continuity conditions are used to determine the constants of integration, namely, the displacement at the support is zero ($\Delta_1 = 0$ at x = 0), the slope at midspan is zero ($\theta_2 = 0$ at x = 1.5a), and the continuity of the slope ($\theta_1 = \theta_2$ at x = a) and displacement ($\Delta_1 = \Delta_2$ at x = a) at the location of load points. Applying these conditions yields:

i) $\Delta_1 = 0$ when $x = 0$;

$$C_2 = 0$$

ii) $\frac{d\Delta_2}{dx} = 0$ when $x = \frac{3\text{a}}{2}$;

$$C_3 = \frac{-3\varphi_m a}{2}$$

iii) $\frac{d\Delta_1}{dx} = \frac{d\Delta_2}{dx}$ when $x_1 = \text{x}_2 = a$;

$$\frac{\varphi_m a}{2} + C_1 = \varphi_m a - \frac{3\varphi_m a}{2}$$

$$C_1 = -\varphi_m a$$

iv) $\Delta_1 = \Delta_2$ when $x_1 = \text{x}_2 = a$;

$$\frac{\varphi_m a^2}{6} - \varphi_m a^2 = \frac{\varphi_m a^2}{2} - \frac{3\varphi_m a^2}{2} + C_4$$

$$C_4 = \frac{\varphi_m a^2}{6}$$

Therefore, substituting the integration constants into Equations (E.2) and (E.3) yields:

For $x < a$;

$$\frac{d^2\Delta_1}{dx^2} = \frac{\varphi_m x}{a}$$

$$\frac{d\Delta_1}{dx} = \frac{\varphi_m}{2a}(x^2 - 2a^2)$$

$$\Delta_1 = \frac{\varphi_m}{6a}(x^3 - 6a^2 x) \tag{E.4}$$

And for $x > a$ and $x < 2a$;

$$\frac{d^2\Delta_2}{dx^2} = \varphi_m$$

$$\frac{d\Delta_2}{dx} = \varphi_m\left(x - \frac{3a}{2}\right)$$

$$\Delta_2 = \frac{\varphi_m}{6}(3x^2 - 9ax + a^2) \tag{E.5}$$

Considering we are solely focused on determining the midspan deflection, we can compute the deflection by substituting $x = 1.5a$ into Equation (E.5), resulting in:

$$\Delta_{max} = \frac{23a^2\varphi}{24}$$

where a is the shear span, and φ is the midspan curvature calculated in the moment-curvature analysis.

Appendix F

Force Displacement and Strains

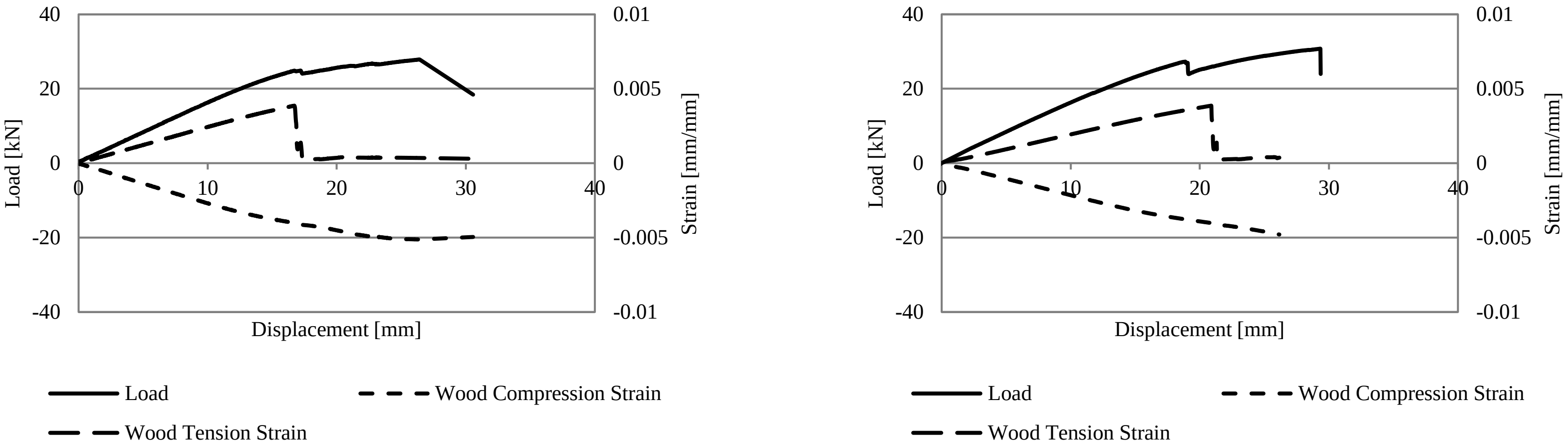

U-01

U-02

Figure E.2 - Strain Distribution for U-01 and U-02 Beams

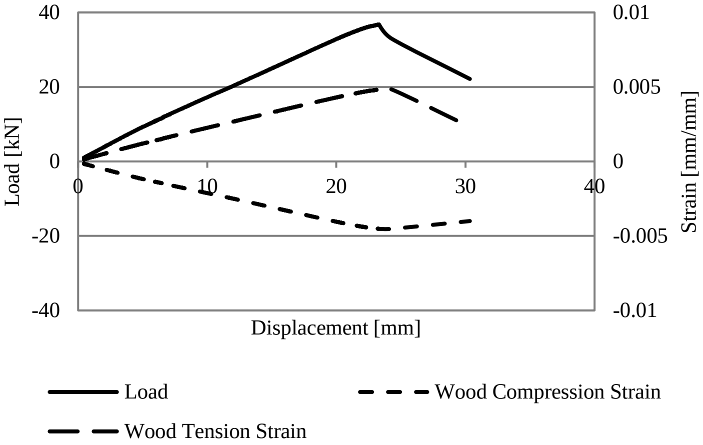

U-03

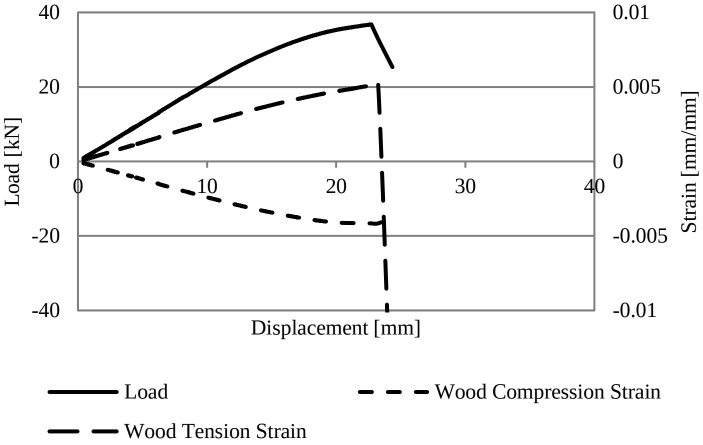

U-04

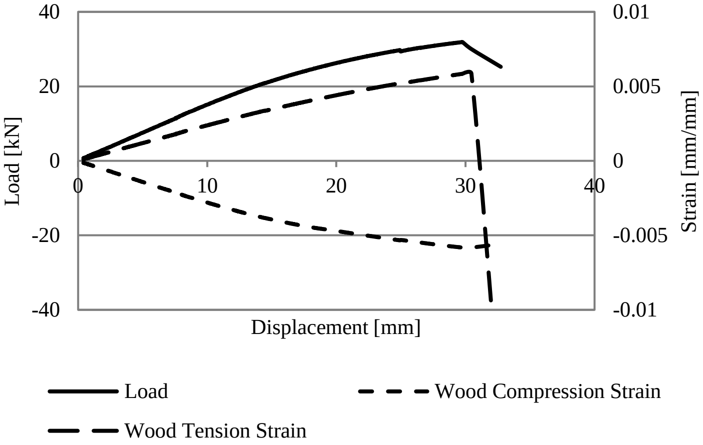

U-05

Figure E.3 - Strain Distribution for U-02 – U-05 Beams

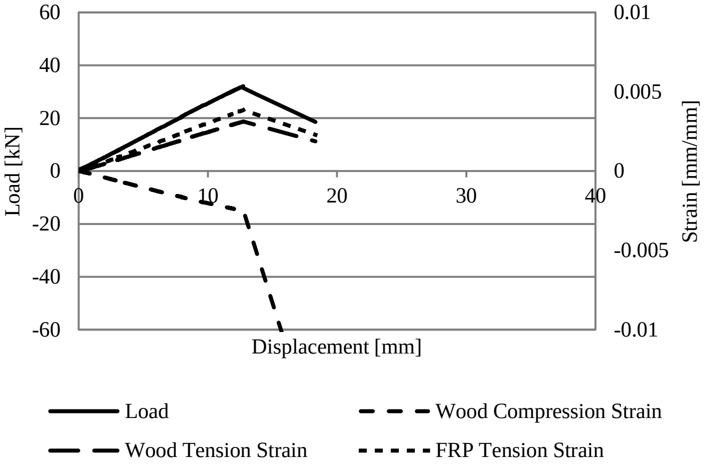

R1-01

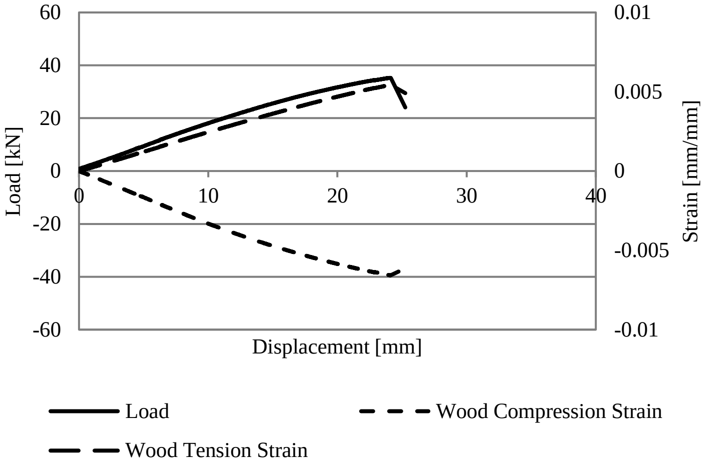

R1-02

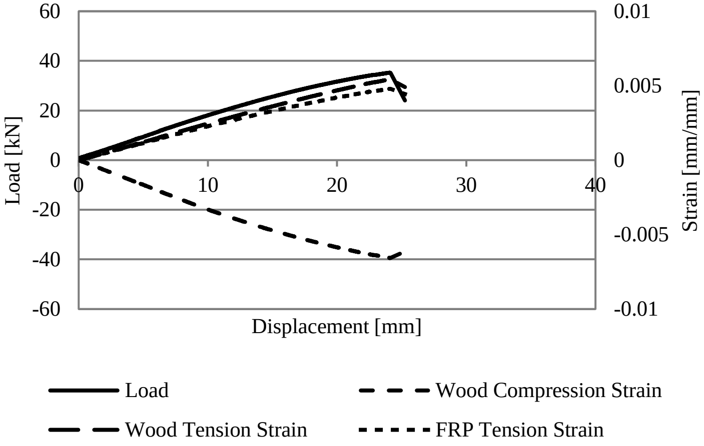

R1-03

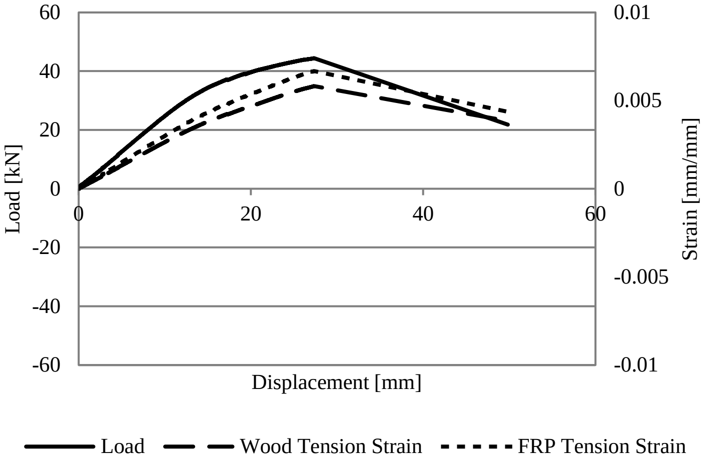
60
40
20
0
-20
-40
-60
0.01
0.005
0
-0.005
-0.01
0
20
40
60
Load [kN]
Strain [mm/mm]
Displacement [mm]
Load
Wood Tension Strain
FRP Tension Strain

R2-01

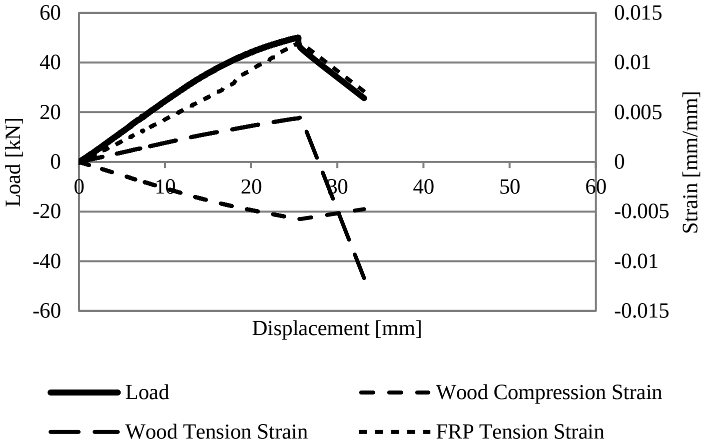
60
40
20
0
-20
-40
-60
0.015
0.01
0.005
0
-0.005
-0.01
-0.015
0
10
20
30
40
50
60
Load [kN]
Strain [mm/mm]
Displacement [mm]
Load
Wood Compression Strain
Wood Tension Strain
FRP Tension Strain

R2-02

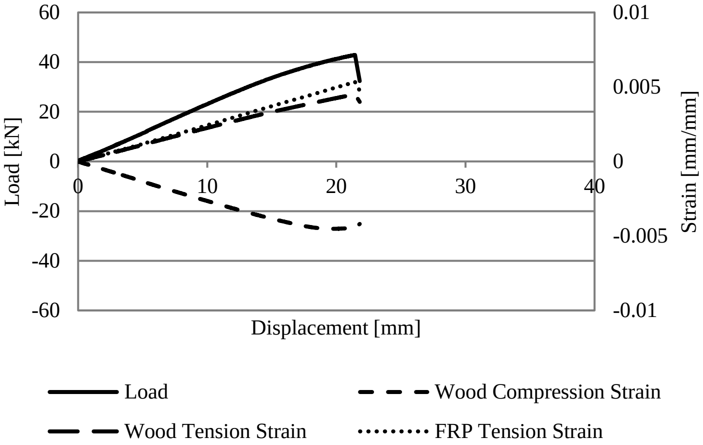

R3-01

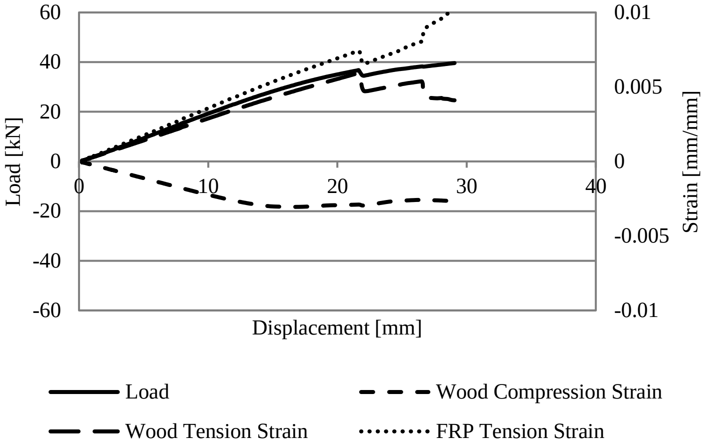

R3-02

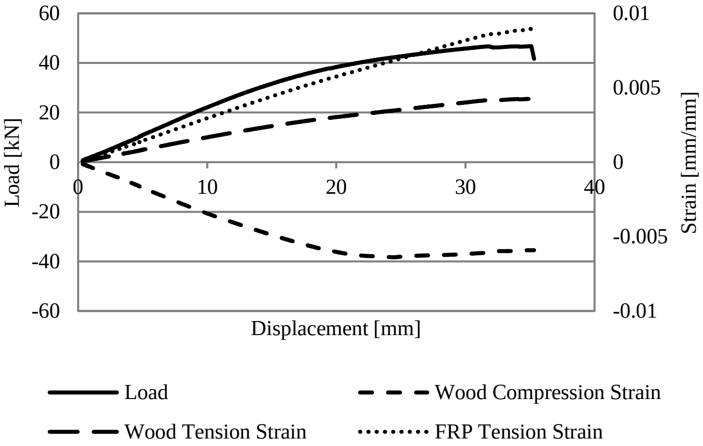

R4-01

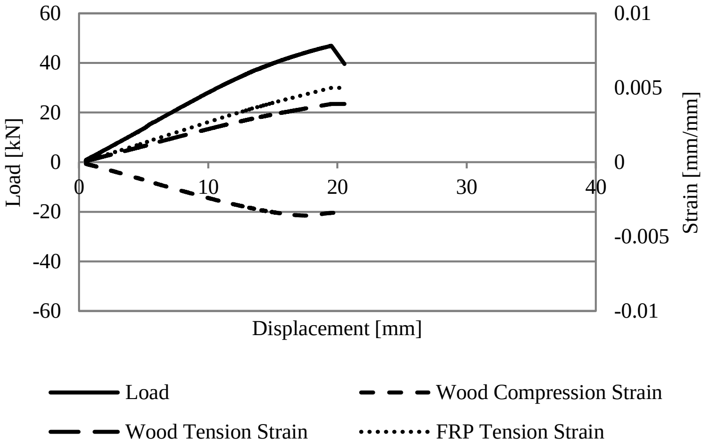

R4-02

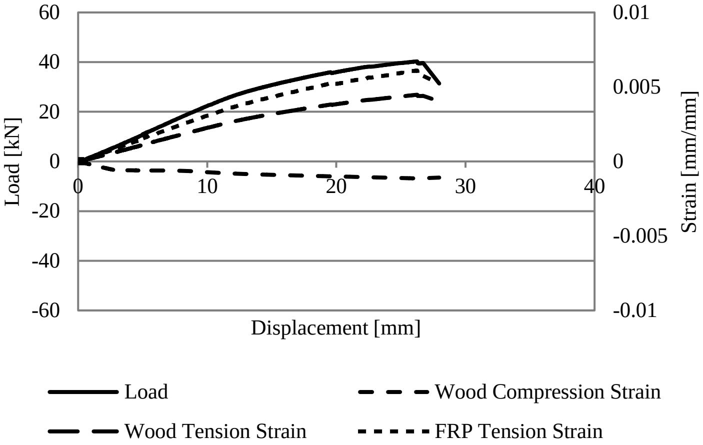

R5-01

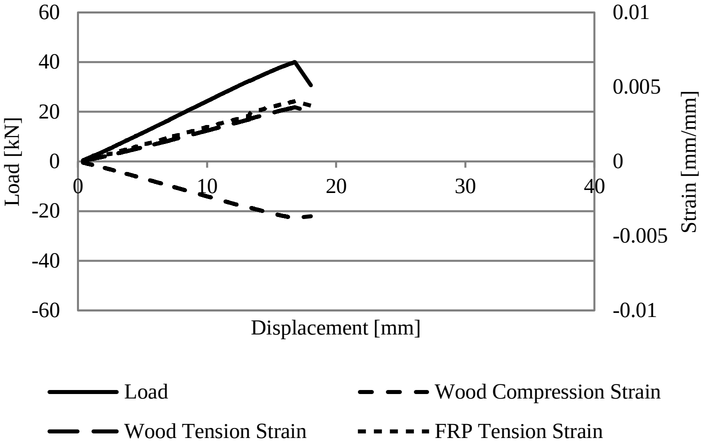

R5-02

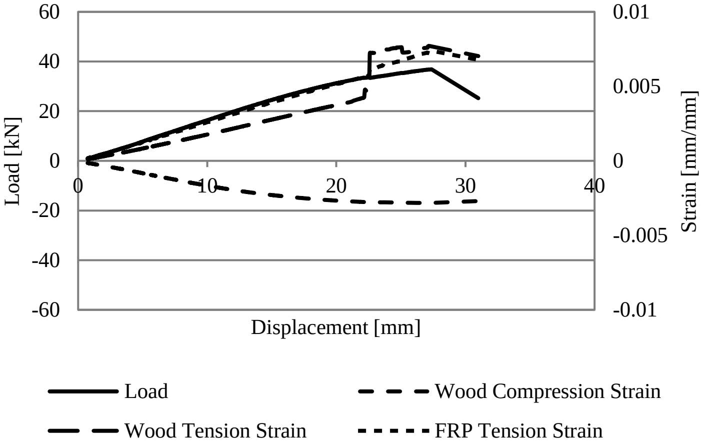

R6-01

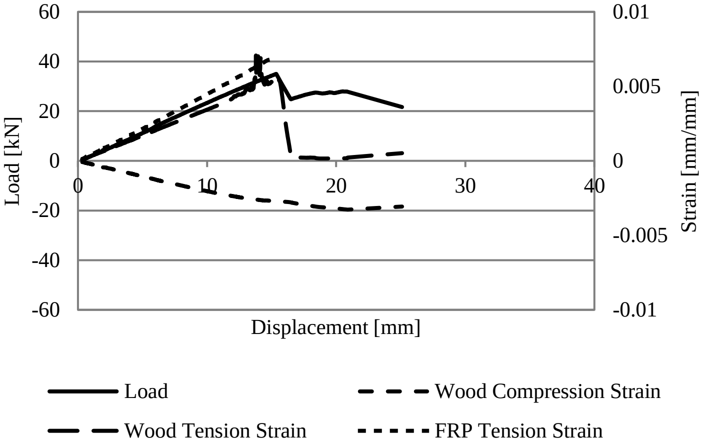

R6-02

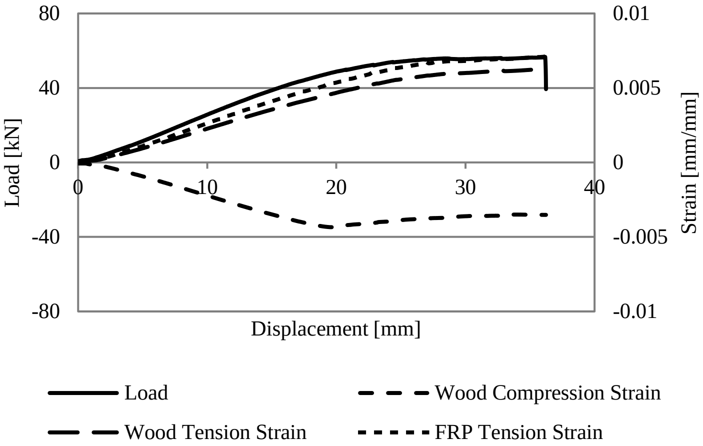

R7-01

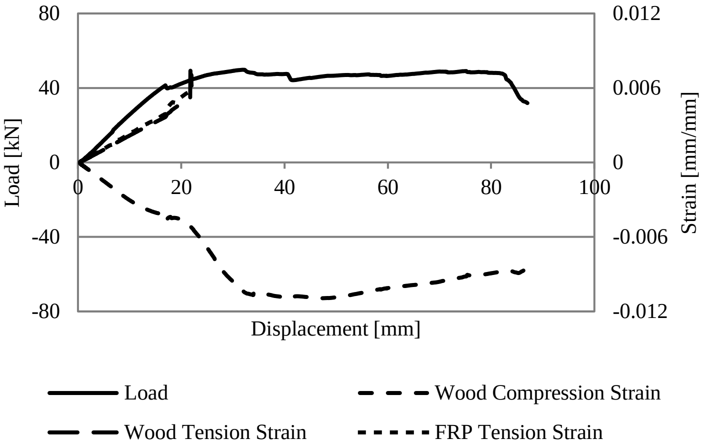

R7-02

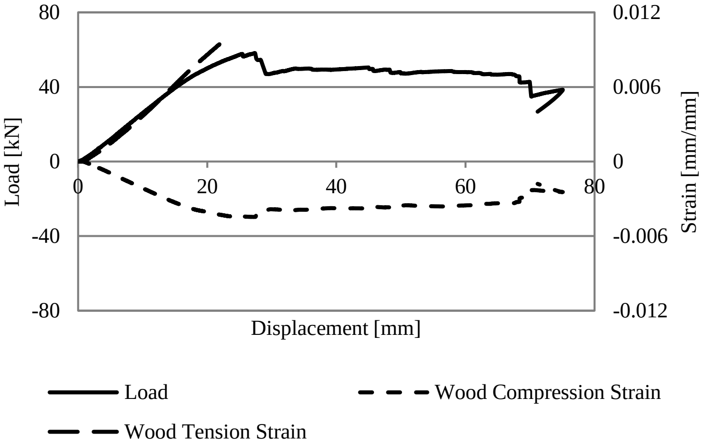

R8-01

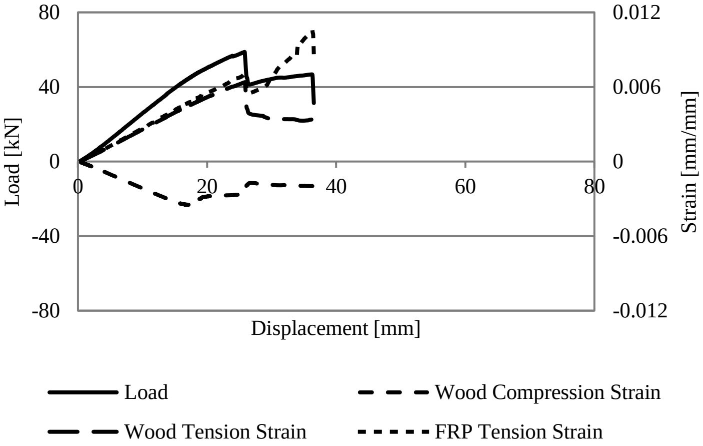

R8-02

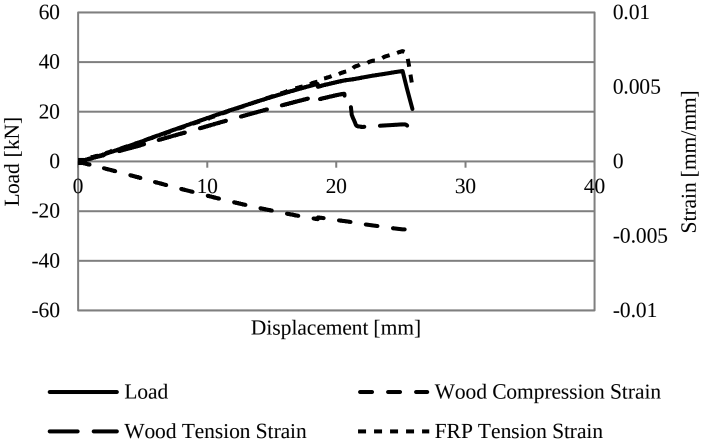

R9-01

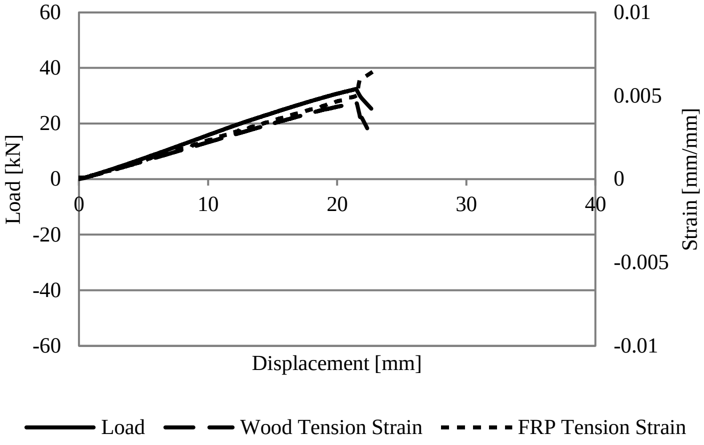

R9-02

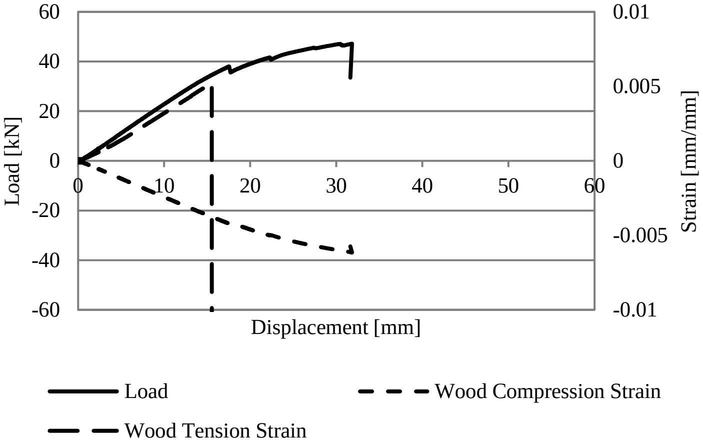

R10-01

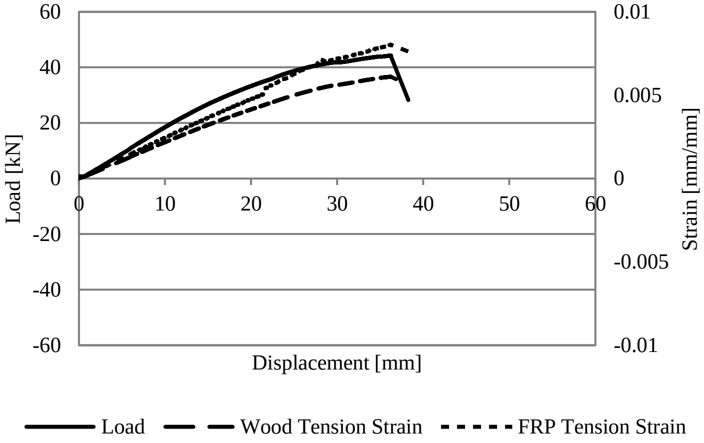

R10-02

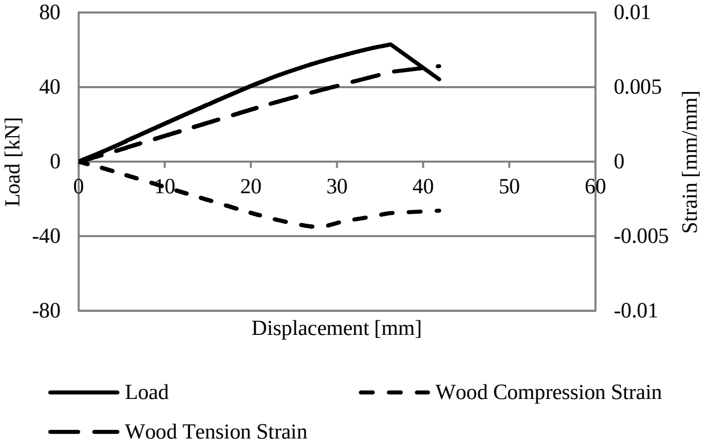

R11-01

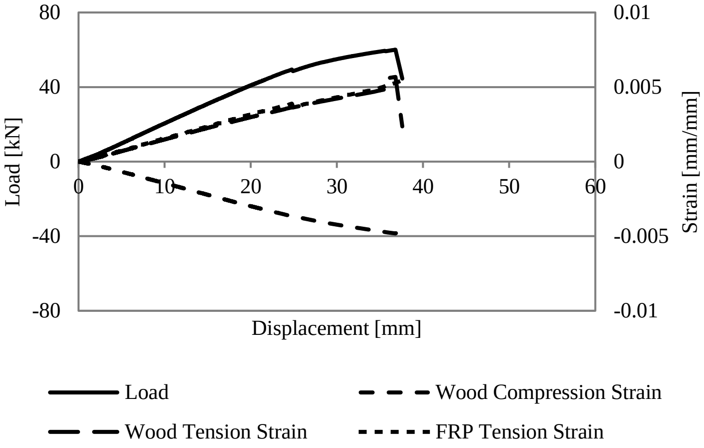

R11-02

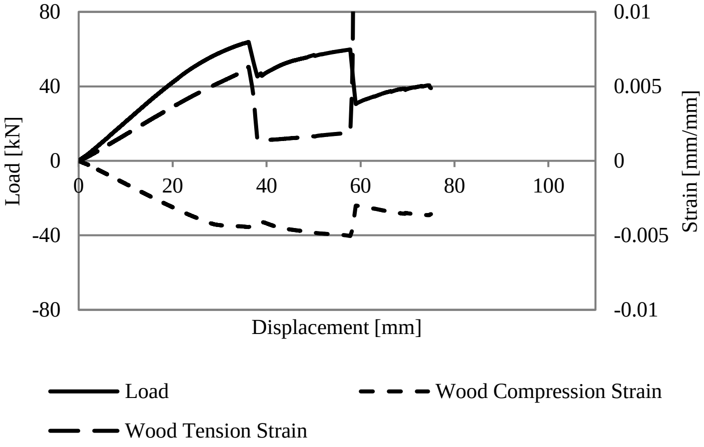

R12-01

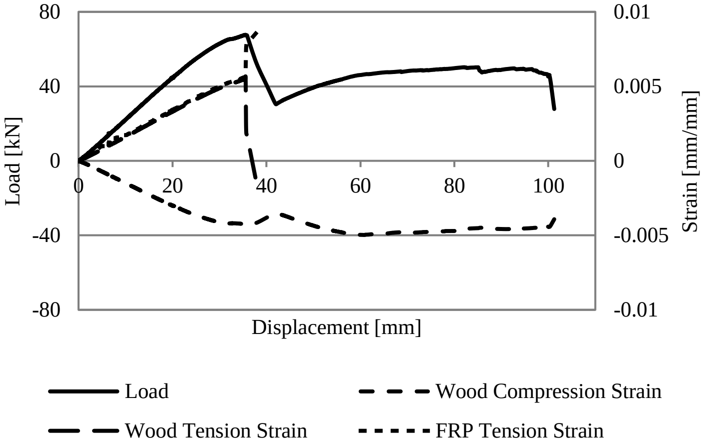

R12-02